Simultaneous Tandem Polymerizations for Facile Synthesis of Polymer Brushes

Dissertation
zur Erlangung des akademischen Grades

Doktor der Naturwissenschaften

im Promotionsfach Chemie
Am Fachbereich Chemie, Pharmazie, Geographie und Geowissenschaften
der Johannes Gutenberg-Universität
in Mainz

vorgelegt von

Katharina Erika Irmgard Kluthe
geboren in Heidelberg

Mainz 2022

1. Berichterstatter: [redacted]

2. Berichterstatter: [redacted]

Tag der mündlichen Prüfung: 31.01.2022

The work forming the basis for this dissertation has been conducted between September 2017 and December 2020 in at the MAX PLANCK INSTITUTE FOR POLYMER RESEARCH in Mainz in the research group of [redacted]. I hereby declare that I wrote the dissertation submitted without any unauthorized external assistance and used only sources acknowledged in the work. All textual passages which are appropriated verbatim or paraphrased from published and unpublished texts as well as all information obtained from oral sources are duly indicated and listed in accordance with bibliographical rules. In carrying out this research, I complied with the rules of standard scientific practice as formulated in the statutes of JOHANNES GUTENBERG-UNIVERSITY MAINZ to insure standard scientific practice.

To my Family

TABLE OF CONTENTS

Abstract

Polymer brushes' physical properties and therefore their possible applications are sensitively dependent on the composition and two- or three-dimensional arrangement of their constituent polymer segments. For a wide application, their synthesis must therefore be robust, reliable and precise. However, high grafting densities of brush copolymers represent great steric challenges to the synthetic chemist. Current synthetic routes rely on a stepwise polymerization of the two monomers but often lead to incomplete conversion or low grafting densities. This dissertation presents a method to overcome the steric challenges by conducting the polymerizations of both monomers in a single step *via* orthogonal polymerization techniques. Two systems are presented to yield molecular bottlebrushes and binary mixed surface-initiated polymer brushes.

Molecular bottlebrushes were synthesized in a one-pot, one-step polymerization. Through the combination of two orthogonal polymerization techniques, ring opening metathesis polymerization and ring opening polymerization (ROMP and ROP), the backbone and side chains were synthesized at the same time. Herein, ROMP of a strained cyclic olefin was catalyzed by the Third Generation Grubbs catalyst to produce the backbone chain. The heat-activated 2,4-dihydro-2,4,5-triphenyl-1,2,4-triazol-3-ylidene catalyzed ROP of L-lactide was shown to simultaneously produce the side chains. Mutual compatibility of the two catalysts was demonstrated. Molecular bottlebrushes were synthesized with different lengths of poly (L-lactide) side chains and various poly (N-(hydroxyl ethyl)-cis-5-norbornene-exo-2,3-dicarboximide) backbone lengths. It was shown that short molecular bottlebrushes can be synthesized with very narrow dispersities of both backbone and side chains, with high or complete conversions. Kinetic investigations were conducted to prove the simultaneous nature of the synthetic approach. Characterization of the bottlebrushes proved that narrow molecular weight distributions were achieved in both backbone and side chains.

The mutually orthogonal combination of atom transfer radical polymerization (ATRP) and ROP was employed to synthesize amphiphilic binary mixed brushes. A Y-shaped bifunctional initiator was synthesized to enforce maximal mixing at a molecular level and

ensure covalent attachment of the chains. The bifunctional initiator was deposited onto silicon wafers *via* alcoholysis. A suitable orthogonal catalytic system was established, and reaction conditions tuned to afford simultaneous growth of poly (2-(dimethylamino) ethyl methacrylate) and poly (ε-caprolactone) chains. Stannous octoate was employed together with PMDETA-ligated copper (I) bromide to allow simultaneous ROP and ATRP respectively. Binary mixed brushes were then grown off the functionalized surface in a single polymerization step. The brushes were investigated by ToF-SIMS to prove successful polymerization and grafting homogeneity. AFM investigations allowed to show brush reorganization to adapt to selective solvents. Cycling through solvent adaptations proved the covalent attachment of both chains.

Zusammenfassung

Die einzigartigen Eigenschaften von Polymerbürsten und ihre vielseitigen Anwendungsgebiete sind empfindlich von ihrer molekularen Zusammensetzung sowie der zwei-und dreidimensionale Anordnung der Polymersegmente abhängig. Um zuverlässig Polymerbürsten mit den gewünschten Eigenschaften herstellen zu können, muss ihre Synthese sowohl robust, zuverlässig als auch präzise sein. Die intrinsisch hohen sterischen Ansprüche stellen den Polymerchemiker aber vor synthetische Schwierigkeiten: die verbreiteten Synthesewege beruhen auf der schrittweisen Polymerisation von zwei unterschiedlichen Monomeren und leiden meist unter niedrigen Umsätzen oder geringen Pfropfdichten. Die hier dargelegte Arbeit präsentiert einen Lösungsansatz, der die hohen sterischen Ansprüche umgeht, indem beide Polymerisationen simultan in einer Eintopfsynthese geführt werden. Diese Methode wurde angewandt, um zwei dicht gepfropfte Polymerarchitekturen zu synthetisieren: molekulare Bürsten und gemischte binäre Oberflächenbürsten.

Molekulare Polymerbürsten konnten erfolgreich in einer Eintopfsynthese hergestellt werden. Durch die orthogonale Kombination von zwei mechanistisch unterschiedlichen Polymerisationsmethoden — ringöffnende Polymerisation und ringöffnende Metathese Polymerisation (ROP und ROMP) — wurden Rückgrat und Seitenketten in nur einem Schritt polymerisiert und verknüpft. Die Polymerisation eines cyclischen Olefins mit hoher Ringspannung und ROP-Initiator Funktion wurde durch den Grubbs Katalysator dritter Generation kontrolliert, um das Rückgratpolymer zu synthetisieren. Gleichzeitig wurde ein thermisch aktiviertes N-heterocyclisches Carben eingesetzt um die Polymerisation von L-Lactid zu katalysieren. Molekulare Verknüpfungen zwischen Seitenketten und Rückgratpolymer wurden durch die ROP-Initiatorfunktion des Rückgratmonomers erreicht. Molekulare Polymerbürsten mit unterschiedlichen Rückgrat-und Seitenkettenlängen konnten einfach synthetisiert werden. Bei kurzen Rückgratlängen wurden vollständige Umsätze mit niedrigen Dispersitäten erreicht. *In-situ* ^{1}H NMR kinetische Studien belegten, dass beide Polymerisationen gleichzeitig stattfinden. AFM Aufnahmen und selektive Rückgratdepolymerisierung zeigten die enge Molekulargewichtsverteilung der Seitenketten.

Durch den orthogonalen Einsatz von ATRP und ROP, konnten im zweiten Teil der Arbeit amphiphile, binäre gemischte Oberflächenpolymerbürsten in nur einem Schritt synthetisiert werden. Ein dreiarmiges Linker-Molekül wurde synthetisiert, das sowohl ROP- als auch ATRP-Initiatorfunktionalitäten mit einem Silyletheranker kovalent verknüpft. Der Linker wurde über die Silyletherfunktionalittät auf Silikonwafer aufgebracht. Auf diese Weise konnte sichergestellt werden, dass die ATRP und ROP Ketten auf molekularer Ebene gemischt sind, sowie kovalent an die Waferoberfläche gebunden wurden. Katalysatoren, Monomere und Reaktionsbedingungen konnten so eingestellt werden, dass zeitgleich DMAEMA *per* ATRP und ε-Caprolacton *per* ROP polymerisiert werden konnte. Mit diesem System wurden mit amphiphilen, binären gemischten Polymerbürsten funktionalisierte Wafer in nur einem Schritt hergestellt. Die Waferoberflächen wurden mit ToF-SIMS und XPS untersucht, um die erfolgreiche Synthese zu belegen, sowie die Homogenität der Oberfläche zu etablieren. AFM Aufnahmen belegten, dass die binären Polymerbürsten sich spontan in selektiven Lösemittel reversibel organisieren.

Acknowledgments

There are many who helped me along the way on this journey. I want to take this opportunity to thank them.

First, I wish to thank my thesis supervisors. [redacted] for his role in guiding my thesis, my personal development and our many informative conversations. I thank [redacted] for the opportunity to work as part of her research group, and [redacted] and [redacted] for welcoming me to their research group at the University of Florida.

A particular thanks goes to my many colleagues at the Max Planck Institute for Polymer Research who helped me along the way [redacted] for his enthusiastic help for all NMR measurements, methods and explanations, for his ever joyous mood, kind encouragement and the many coffees. He also conducted the *in-situ* ^{1}H NMR measurements used in the bottlebrush experiments. A further thanks to [redacted] for the ToF-SIMS measurements and multivariate data analysis. He kindly conducted all ToF-SIMS measurements discussed in the surface brushes chapter. Another goes to the wonderful women at the polymer analytics laboratories who measured my hundreds of GPC samples: [redacted] who fractioned off samples, developed HPLC systems and conducted LS measurements. I appreciate the help of [redacted] for solid state NMR measurements. I am very grateful to [redacted] for conducting AFM and contact angle measurements of the grafted wafers. To [redacted] for all other AFM measurements. I thank [redacted] for his discussions and explanations and [redacted] for the TGA and DSC measurements, as well as her help synthesizing the linker. [redacted] for the SEM measurements and his jokes [redacted] for the XPS measurements, his friendly hellos and proactive help. A big thanks also for the technical staff. Above all to [redacted].

My friends, my parents, and my brothers who put up with my complaints, my frustrations and worst of all my excitement. I am forever grateful for their patience and

understanding. Among them, I want to thank my dear [redacted] in particular. Words cannot express the gratitude for my family [redacted] for their constant support in all matters of life.

Abbreviations

ADMET	Acyclic diene metathesis
AFM	Atomic force microscopy
AP	Anionic polymerization
ATRP	Atom transfer radical polymerization
AGET ATRP	Activators generated by electron transfer ATRP
ARGET ATRP	Activators regenerated by electron transfer ATRP
ATR	Attenuated total reflection
BB	(Molecular) bottle brush
CL	Caprolactone
CNT	Carbon nano tube
COSY	Correlated spectroscopy
CRP	Controlled radical polymerization
CTA	Chain transfer agent
d	Doublet
δ	Chemical shift
DBU	1,8-Diazabicyclo[5.4.0]undec-7-en
DFT	Density functional theory
DMAEMA	Dimethyl amino ethyl methacrylate
DMAP	4-dimethylaminopyridine
DMF	N,n'-dimethyl formamide
DMSO	Dimethyl sulfoxide
DOSY	Diffusion ordered spectroscopy
DSC	Dynamic scanning calorimetry
DTRP	Degenerative-transfer radical polymerizations
DTT	1,3,4-triphenyl-4,5-dihydro-1H-1,2,4-triazole-5-ylidene
EBiB	2-ethyl bromoisobutyrate
EGMA	Ethylene glycol methacrylate
et al.	And others

EtOH	Ethanol
eq.	Equivalents
FoV	Field of View
FRP	(Free) radical polymerization
Grubbs-I	Grubbs' First Generation Catalyst
Grubbs-II	Grubbs' Second Generation Catalyst
Grubbs-III	Grubbs' Third Generation Catalyst
GPC	Gel Permeation chromoatography
HBIB	2-Hydroxyethyl 2-bromoisobutyrate
HONDC	N-(hydroxyl ethyl)-cis-5-norbornene-*exo*-2,3-dicarboximide
HV	High vacuum
Inimer	Monomer with (orthogonal) initiating functionality
IPr	1,3-bis(2,6-bis(diphenylmethyl)-4-methylphenyl)imidazo-2-ylidene
IR	Infrared (spectroscopy)
LLA	L-lactide (dilactide
MA	Methacrylic acid
MALDI	Matrix assisted laser desorption ionization
MBP	Mixed binary brush polymer
Me	Methyl-
MM	Macromonomer
MMA	Methyl methacrylate
M_n	Number average molar mass
MeOH	Methanol
MPC	2-Methacryloyloxyethyl phosphorylcholine
MTBD	7-Methyl-1,5,7-triazabicyclo[4.4.0]dec-5-ene
M_w	Weight average molar mass
MWD	Molecular weight distribution
MVA	Multivariate analysis
ν	Wavenumber
NBE	Norbornene
NBO	5-Norbornene-2-ol
NBM	5-Norbornene-2-methanol
NCA	N-Carboxy-alpha-amino acid anhydrides
NIPAM	N-Isopropyl acrylamide
NMF	Non-negative matrix factorization

NMP	Nitroxide mediated polymerization
NMR	Nuclear magnetic resonance spectroscopy
ODMA	Octadecyl methacrylate
PAA	Poly acrylic acid
PC	Principle component
PDI	Polydispersity index
PDMS	Poly dimethyl siloxane
PEG	Poly ethylene glycol
PEO	Poly ethylene oxide
Ph	Phenyl
ppm	Parts per million
PSF	Poly(styrene)-*stat*-poly(2,3,4,5,6-pentafluorostyrene)
R	Organic rest
RAFT	Reversible addition fragmentation
RoI	Region of interest
ROMP	Ring opening metathesis polymerization
ROP	Ring opening polymerization
RDRP	Reversible deactivation radical polymerization
RP	Free/ conventional radical polymerization
RT	Room temperature
SAM	Self-assembled monolayer
SIMes	1,3-dimesitylimidazolin-2-ylidene
$Sn[Oct]_2$	Stannous octoate
SRMP	Stable-radical mediated polymerization
St	Styrene
TBD	1,5,7-Triazabicyclo[4.4.0]dec-5-ene
TFA	Trifluoroacetic acid
T_g	Glass transition temperature
T_m	Melting temperature
ToF-SIMS	Time of flight secondary ion mass spectrometry
TGA	Thermogravimetric analysis
THF	Tetrahydrofuran
ToF	Time of Flight
2VP	2-vinyl-pyrolidone

1 INTRODUCTION

From packaging[1], over water purification[2], to surgical implants[3], synthetic polymers have found their way into virtually all aspects of modern life. Their widespread use stems from the accuracy with which polymeric material properties can be tuned to satisfy application requirements[4]. Leveraging structure-property relationships allows to strategically address macroscopic properties by selecting appropriate monomers. This powerful platform is expanded by the ability to combine polymers consisting of different monomeric units. A sharp distinction should be drawn between approaches that seek to control material properties by combining two different polymeric materials and those that impart material properties on a molecular level. Among the former count the controlled preparation of supramolecular structures, polymer blends and polymer composites. Molecular polymer engineering on the other hand concerns itself with controlling constituents and configurations of polymers on a molecular level. The most basic building block for molecular polymer engineering are segments of like monomers. Like or unlike segments can then in turn be arranged into entities with various complexities by molecular attachment into one-, two- or three-dimensional arrays. Such structures include the groups of block polymers, graft polymers, star polymers and dendritic polymers. To synthesize these complex architectures, synthetic polymer chemists rely on employing a range of controlled polymerization techniques[4].

1.1 Polymerization Techniques

Polymerization techniques can be divided into three distinct mechanistic classes: *chain growth polymerizations, polycondensations* and *polyadditions*[5]. Polycondensations and polyadditions are often classed under the general term of step growth polymerizations to reflect their shared kinetic profiles but IUPAC discourages this use[6]. Both in polycondensations and polyadditions, chain growth occurs in a step-wise manner. These two systems can be described using the FLORY equal reactivity assumption, where every reactive group has an equal probability of reacting, independent of the chain length[7]. In chain growth polymerizations, growth of the polymer chain occurs exclusively through the addition of a monomer to the active center, with regeneration of the active center within each growth step[5].

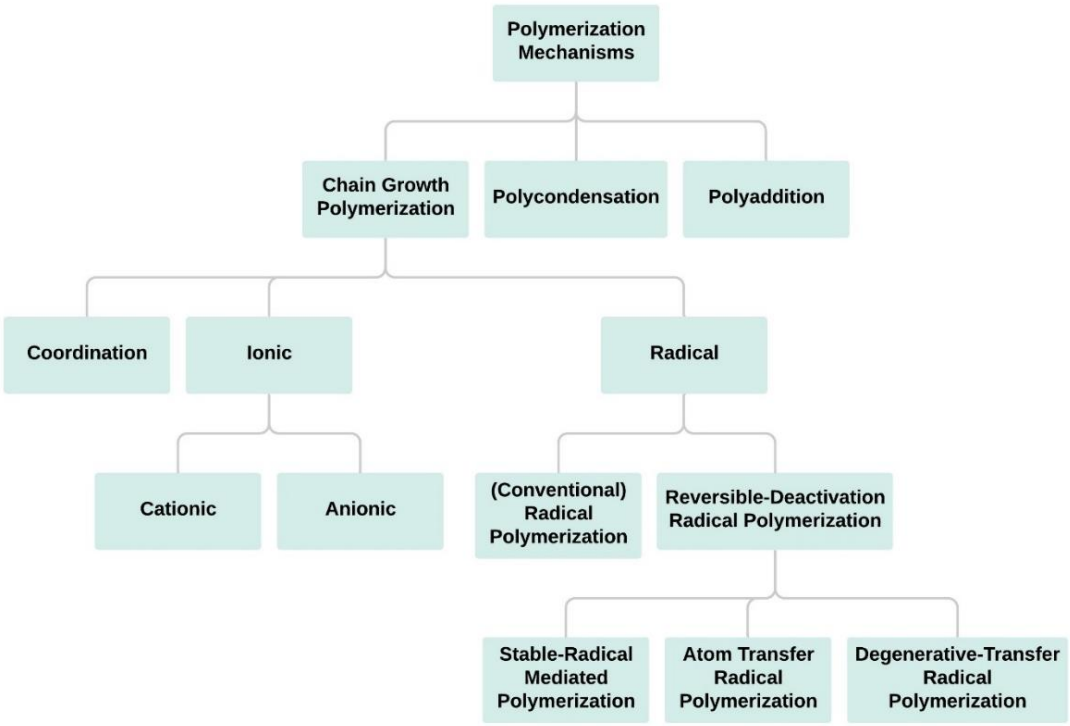

Figure 1-1: Overview of selected Polymerization Mechanisms.

1.1.1 Radical Polymerizations

Radical polymerizations are classed among chain growth polymerizations where the active center is a radical species[5]. They can be divided into “free radical polymerization” and “controlled/living radical polymerization”. IUPAC discourages the use of these terms and suggest the less ambiguous handles of *radical polymerization* (RP) and *reversible-deactivation radical polymerization* (RDRP) respectively.[8] Nonetheless, the two

discouraged terms remain in widespread use in literature, reflecting the handy associations triggered by the terms.

As chain growth polymerizations, the kinetic profiles of RPs are characterized by the three component steps of *initiation, propagation* and *termination*, with some systems also portraying chain transfer[5]. Most commonly, RP is initiated by thermally labile peroxide or azoinitiators that produce two primary radicals. Alternatively, photoinitiators are excited through UV irradiation and then undergo homolysis to yield two primary radicals[9]. The initiator-derived radicals then proceed to react with a monomer, completing the initiation step. Radical addition of further monomer (propagation) produces the growing polymer chain and retains the radical active site at the chain end[5]. The concentration of the chain carriers (radicals) is usually treated according to the steady state approximation as propagation is much faster than initiation[4]. The life time of an individual radical is short and limited by the combination of two radicals, resulting in termination of both radicals. RP is a robust process, tolerating protic solvents, trace impurities of oxygen, inhibitors and other impurities. This robustness and the large number and diversity of monomers polymerizable *via* this technique have contributed to place RP in a dominant position in industry[10]. Yearly production of RP derived polymers with thousands of compositions exceeds 100 million metric tons[11]. However, polymers produced *via* RP are usually characterized by large molecular weight distributions and the degree of architectural control is limited[5].

Over the last decades, considerable progress has been made overcoming the limitations of RPs through the advent of RDRPs[12]. In allusion to an idealized case of anionic polymerizations, the discouraged term "*living radical polymerization*" is meant to convey the virtual absence of termination or irreversible chain transfer reactions. This goal is achieved *via* introduction of additives that mediate a reversible conversion of propagating radicals into an inactive (*dormant*) state and a reactivation into the same active center within the lifetime of the polymerizing chain[13]. Reaction conditions can be selected to convert the majority of growing chains into a dormant state. By this approach the concentration of active radicals that participate in propagation is reduced. The dormant chain ends are unable to participate in bi-radical coupling and hence the occurrence of termination is dramatically suppressed (although never completely absent)[14]. The reversibility of the inactivation extends the life time of individual propagating chains and so it is possible to synthesize block copolymers by sequential addition of monomers[14]. If the rate of interconversion is fast relative to the rate of co-propagation, all chains are able to grow at the same rates. If, in addition to the above conditions, an equilibrium between active and dormant sites can be reached rapidly and initiation is much faster than propagation, molecular weight distributions of the resulting polymeric products become very narrow. Indeed in an ideally controlled RDRP, the chain

length distribution would be expected to follow a negative binomial distribution derived from the number-average degree of polymerization and the chain transfer constant[15]. Usually, when using the term *controlled radical polymerization*, one refers to the control over molecular weight, resulting narrow molecular weight distributions, the retention of a well-defined end group and the ability to extend the chain end by addition of additional or a second monomer[12].

Various systems have been established to achieve RDRP that portray many of these attributes. Particularly noteworthy classes of RDRP include *stable-radical-mediated polymerizations* (SRMP) *atom-transfer radical polymerizations* (ATRP) and *degenerative-transfer radical polymerizations* (DTRP)[12]. Their primary differences lie within the process through which the reversible deactivation is mediated and shall briefly be outlined.

In SRMP, propagating radicals may reversibly couple with a persistent (stable) radical[5]. The most commonly employed stable radicals are aminoxyl radicals with the general structure $R_2N\text{-}O^{\bullet}$, often referred to as *nitroxyl* radicals. Consequently, SRMP are usually called *nitroxyl-mediated polymerizations* (NMP, although IUPAC discourages the term[6]). Sterically hindered alkoxyamines without α-hydrogens undergo homolytic fission of the C-O bond during initiation to produce a carbon primary radical that can react with monomers and an aminoxyl radical. The resonance of the 2-center 3-electron N-O system stabilizes the radical. The steric bulk and absence of α-hydrogens impede disproportionation[16]. Excellent control can be achieved through the exploitation of the *persistent radical effect*[17], where the aminoxyl radical is persistent and the carbon radicals (primary radical or chain ends) are transient. The rapid coupling of the persistent radical with active chain ends to from dormant chain ends results in the low incidence of termination reaction. Due to the reversibility of aminoxyl coupling, the active centers can be regenerated and the polymerization proceeds until the monomer is depleted. Polymerization of styrene and its derivatives is well-controlled. Methacrylate based monomers however suffer from preferential disproportionation between stable radical and active chain end over reversible addition. As a result, NMP of methacrylic monomers are typically uncontrolled and do not result in nitroxide terminated polymer chains, necessary for block polymer formation[16].

ATRP achieves a reversible deactivation by transfer of atoms or groups, typically (but not exclusively) mediated by transition metals[18]. Most commonly, the transferable group are halogen radicals[19]. Various initiation methods have been developed for ATRP. In "*normal*" ATRP, initiators are alkyl halides with a high propensity towards homolytic fission of the C-X bonds to yield a carbon radical and a halogen radical. The carbon radical proceeds to react with monomers in propagation steps, while the halogen radical undergoes a concerted inner

shell electron transfer reaction with the activator transition metal complex LM^n, which is hereby oxidized to form the deactivator $LM\text{-}X^{n+1}$. The deactivator in turn can undergo homolytic fission of the M-X bond, regenerating the activator complex and the halogen radical, making the process reversible. The halogen radical can then combine with an active chain end, producing a dormant halogen-terminated chain carrier[18].

In DTRP, deactivation of the active radicals occurs *via* the degenerative transfer of groups or atoms. Notable polymerization techniques include *reversible-addition-fragmentation chain-transfer polymerization* (RAFT) or *iodine transfer polymerization*[12]. After addition of primary radicals to monomers, active sites react with the RAFT agent, to form a radical adduct. The adduct fragments in a second (rapid) step to form a dormant macro-RAFT agent and a new propagating radical to react with more monomer. The chain transfer is both rapid and reversible, allowing for a homogeneous chain growth with low termination reactions[20]. The molecular weight distributions of RAFT-derived polymers depends on the initiating efficiency of the primary radical source but narrow dispersities have been reported for a wide range of monomers, owing to the excellent functional group tolerance[20].

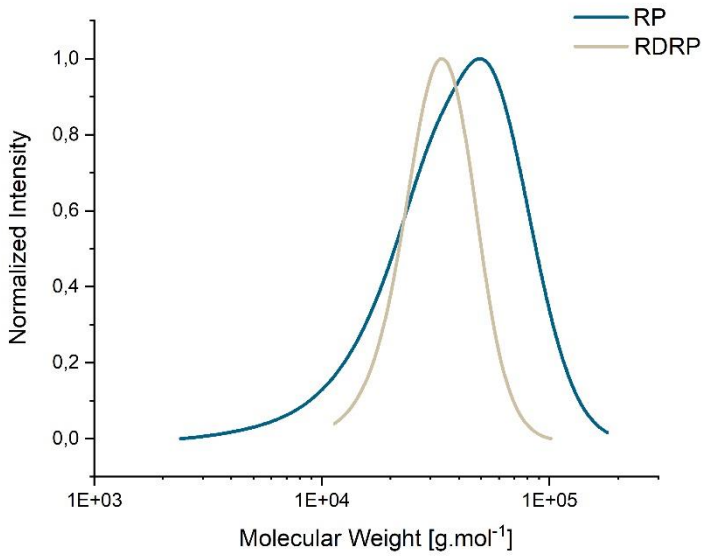

Figure 1-2: GPC traces contrasting the typical molecular weight distributions of RP-derived polymer with a large dispersity and the much more narrowly distributed RDRP-derived polymer (both polystyrene, reacted for the same time at the same temperature and concentration, note the logarithmic scale).

1.1.2 Ring Opening Polymerization

Ring opening polymerization (ROP) is sometimes classed as its own category along with chain polymerization and step growth polymerization as one in three overarching polymerization modes[5]. However, such a categorization can be misleading as it implies a unified mechanistic theme. ROP can proceed *via* an anionic pathway, cationically, zwitterionically or through a coordination-insertion mechanism. What binds all ROP into one distinct group of polymerizations is not the identity of the active propagating species but the high ring strain of its exclusively cyclic monomers[14].

Monomers that are routinely polymerized *via* ROP include the industrially important class of ethylene and propylene oxides, *N-carboxy-alpha-amino acid anhydrides* (NCA's) as well as cyclic esters, amines, sulfides, siloxanes, ethers, acetals and amides[21]. Whether or not a monomer can be polymerized depends on thermodynamic and kinetic considerations[5]. The entropic loss associated with polymerization implies that the enthalpic component must be sufficiently large to afford polymerization. The thermodynamic driving force in ROP is alleviation of ring strain. Whether the monomer's ring strain is sufficiently large depends mainly on geometric factors[5]. Heats of combustion can be used to determine ring strain in a homologous series of monomers. Generally speaking, ring strain is greatest for three- and four-membered rings, and drops sharply for five-, six- or seven-membered rings. As a general rule, ROP of six-membered rings is not observed[21]. The primary driving force for larger rings is angular strain. In addition to being thermodynamically favorable, ROP of a specific monomer must also be kinetically feasible. If the monomers contain bulky groups for example, polymerization may be thermodynamically but not kinetically feasible, as steric clash is greater in a linear chain than in cyclic monomer[5]. Finally, for polymerization to occur, monomer (and potentially catalyst) must provide a mechanistic pathway. Heteroatoms in cyclic monomers for example provide a site for nucleophilic or electrophilic attack by the initiator species.[21]

A notable class of heterocyclic monomers are cyclic esters and carbonates like L-lactide, glycolide or ε-caprolactone (see Chart 1-1). Aliphatic polyesters constitute an attractive class of polymers due to their (bio-)degradability. In contrast to polyesters produced by polycondensation, ROP allows to target high molecular weights, complex architectures and achieve specific end-groups. Depending on the reaction conditions and catalysts employed, cyclic esters can be polymerized cationically or anionically or *via* coordination-insertion polymerization. ROP of cyclic esters may be conducted in solution, in bulk[22], in emulsion[23,24] or in dispersion[25]. In contrast to other cyclic compounds, ring strain in six-membered cyclic lactones is greater than for five-membered lactones[26]. As a consequence, ROP of the former group is routinely achieved while the latter is not observed[27].

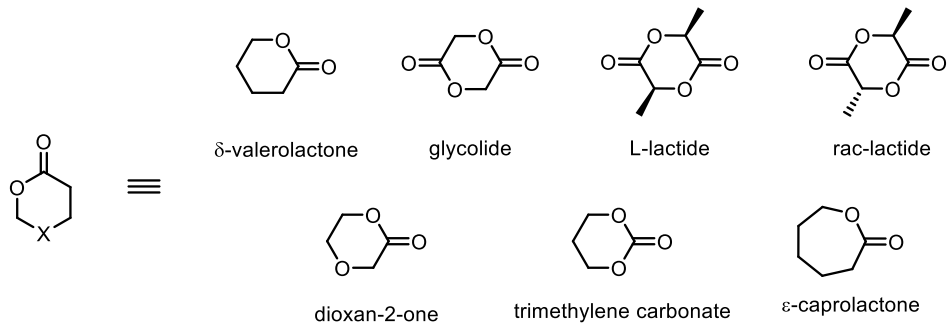

Chart 1-1: Selection of cyclic ester and carbonate monomers that readily undergo ROP.

Anionic ring opening polymerization of cyclic lactones is initiated by bases or LEWIS bases. Propagation proceeds *via* one of two mechanistic pathways: either via alkyl-oxygen or acyl-oxygen cleavage giving either a carboxylate or alkoxide as a polymerizing chain end[28]. Cyclic lactones or lactides larger than four-membered rings react exclusively *via* the propagating anion's attack on the carbonyl carbon, resulting in acyl-oxygen scission and producing an alkoxide as the propagating species[29]. The active species is negatively charged, although reaction conditions and nature of counter ion and solvent determine the ionic or covalent character of the chain end. High molecular weights can be achieved although the incidence of backbiting can be high. Conversely, cationic polymerization involves the formation of a positively charged initiator followed by nucleophilic attack of the monomer. An oxonium ion or acylium ion (formed by unimolecular ring opening of the oxonium ion) is formed as the active propagating species[30]. Both cationic and anionic ROP lead to a covalent attachment of the initiating species on one chain end and the active center on the other chain end, as is typical for ionic chain polymerizations. As such, propagation steps can be summarized as $I(M_i)^-$ -> $I(M_{i+1})^-$ -> $I(M_{i+2})^-$ etc. for anionic pathways and $I(M_i)^+$-> $I(M_{i+1})^+$ -> $I(M_{i+2})^+$ etc. for cationic pathways, i.e. they proceed *via* macroanions and macrocations respectively. In contrast to linear ionic polymerizations, activated monomer (cationic as well as anionic) are also possible but the delineations between the two paths may be fluid. Diazabicycloundecene (DBU) catalyzed ROP of LLA for example can occur via an ionic or activated monomer pathway, depending on the relative concentrations of initiator and catalyst[31].

Zwitterionic pathways are possible for certain combinations of monomers and catalysts.[32–34] Of these, the initiator-free zwitterionic polymerization of cyclic lactones, effected by N-heterocyclic carbenes (NHCs) deserve particular notice. NHCs are a group of persistent carbenes whose inherently high BRØNSTED basicity and nucleophilicity[35]. Their tunable steric constraints allow for applications as ligands for metal-organic catalysts or as organocatalysts in a wide range of organic transformations. The synthetically (and

occasionally commercially) available NHCs fall into the four major groups of thiazol-, triazol-, imidazole-, and imidazolin-2-ylidenes. Chart 1-2 provides an overview of these four groups with a representative example of each of catalysts with (bio-) synthetic importance.

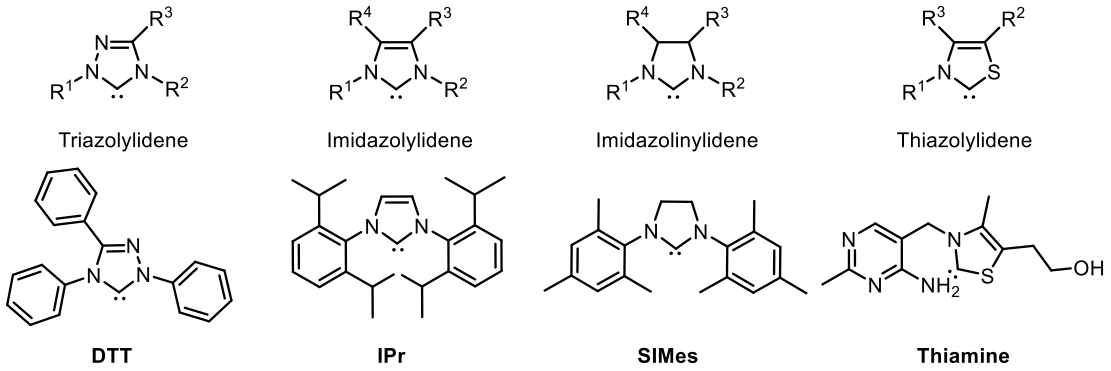

Chart 1-2: N-heterocyclic carbenesused in organic synthesis fall into the four classes of triazolylidenes with 1,3,4-triphenyl-4,5-dihydro-1H-1,2,4-triazole-5-ylidene (DTT) as representative, imidazolylidenes, for example 1,3-bis(2,6-bis(diphenylmethyl)-4-methylphenyl)imidazo-2-ylidene (Ipr), the saturated imidazolinylidenes like 1,3-dimesitylimidazolin-2-ylidene (SIMes) and thiazolylidene like the vitamin B_1 coenzyme thiamine.

Following the pioneering work by HEDRICK, WEYMOUTH, et al.[36], NHCs have gained widespread attention as highly active catalysts for the ROP of cyclic lactones. Employing NHC catalysts allows to synthesize high molecular weight polyesters rapidly under mild conditions. L-lactide for example can be polymerized at room temperature and atmospheric pressure within 15 min[23,37]. A range of other lactones has been successfully polymerized by the help of NHC catalysts, such as glycolide[38,39], rac-lactide[40,41], β-butyrolactone[38] or ε-caprolactone[42]. They can also be employed in the polymerization of cyclic carbonates and cyclic carbosiloxanes[43]. Notably, the use of organocatalysts allows to afford polymers without trace amounts of metal catalyst remaining in the product. Particularly in biomedical or electronic applications, residual metal adversely affects material performance[44]. By rationally designing steric hindrance and chirality in the NHC catalyst, polymers with controlled tacticity can be produced[41].

Coordination ROP are distinct from ionic ROP as they propagate *via* insertion of monomer into the bond between initiator and polymer chain[45]. For this reason, coordination polymerizations are also referred to as insertion polymerization[14]. The initiating species is commonly called the “catalyst” but in contrast to true catalysts, it is not split off from the active site after each reaction step but remains attached like an initiator. Despite the technically incorrect use of the term catalyst, its ubiquitous employment in literature permits its adoption as a pragmatic handle in the following. In the absence of transfer reactions, every one initiator

results in one polymer chain. As a consequence, polymers produced by coordination-insertion have one chain end derived from the initiator (or its quenching product) and one monomer-derived chain end.

1.1.3 Ring Opening Metathesis Polymerization

Ring opening metathesis polymerization (ROMP) can be thought of as a special case of coordination ROP. Much like other ROP, the driving force for ROMP is the alleviation of ring strain[46]. Alternatively, ROMP can be classed based on its mechanism as a polymer-forming metathesis reaction[5] together with *acyclic diene methathesis* (ADMET) and *ring expansion metathesis polymerization* (REMP). Metatheses are exchange and disproportionation reactions of carbon-carbon multiple bonds mediated by late transition metal compounds *via* the carbene pathway. The early, poorly defined heterogeneous catalysts based on transition metal halides were highly active but were limited to fairly stable compounds. The combined work of SCHROCK[47,48] and GRUBBS[49–53] led to the arrival of well-defined homogeneous catalysts capable of tolerating more sensitive functional groups (see Chart 1-3). Particularly the catalysts developed by GRUBBS and coworkers showed excellent functional group tolerance. Through introduction of NHC ligands, the catalysts of later generations retained their functional group tolerance and gained excellent activity[12].

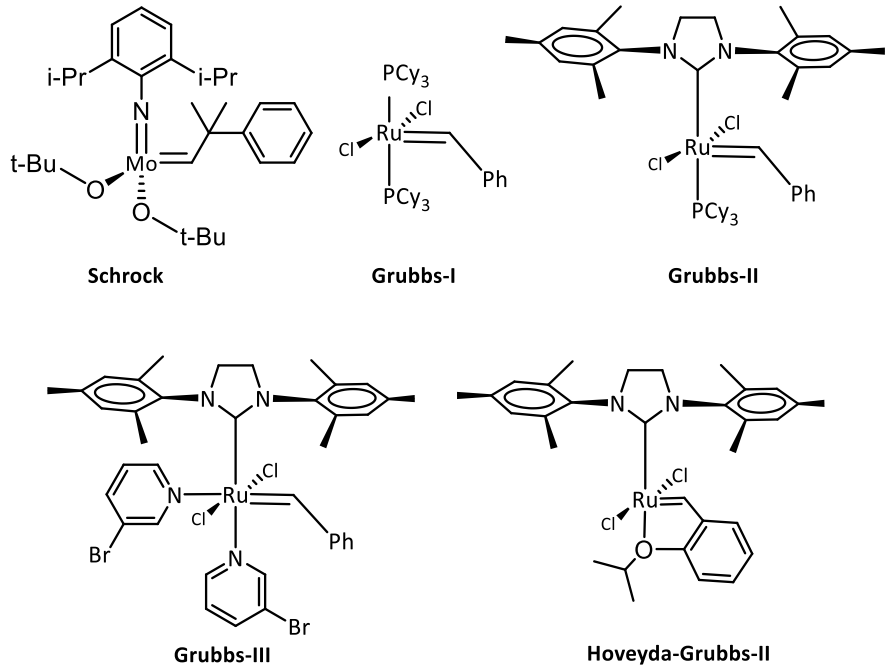

Chart 1-3: Well-defined metathesis catalysts: SCHROCK's catalyst(Schrock), GRUBBS' catalyst of first (Grubbs-I), second (Grubbs-II) and third generation (Grubbs-III) and the Second Generation HOVEYDA-GRUBBS catalyst (Hoveyda-Grubbs-II).

The ability of metathesis catalysts to effect intramolecular arrangements as well as addition reactions between two compounds mean that ROMP is accompanied by intermolecular and intramolecular chain-transfer reaction[54]. With decreasing initial monomer concentration, the competition of dimer/trimer formation over polymerization increases. As a consequence of greater side reactions, polymer dispersities increase[54]. Nonetheless, through the highly active Grubbs catalysts, ROMP is routinely employed yielding very narrowly distributed polymer of various geometries. The fast initiation of particularly the later generation GRUBBS type catalysts allows to yield narrowly distributed polymers of various architectures[12].

Monomers are exclusively strained cyclic olefins. In contrast to cationic or matallocene-mediated polymerizations, ROMP products of cyclic olefins retain the monomer's unsaturation in the main chain. The probability of a monomer to undergo ROMP is again sensitively dependent on ring size, geometric considerations and substitution patterns. Only rings with sufficient ringstrain (45 kcal.mol^{-1}) can be polymerized through ROMP. A selection of ROMP-able monomers in provided in Chart 1-4. Cyclobutene and many of its substituted analogues polymerize readily, polymerized by a range of catalysts. Unsaturated five-membered rings have sufficient ring strain to undergo ROMP but their reactivity depends on the type and location of substitution. Unsubsituted cyclopentene ROMP products constitute an industrially important synthetic rubber source, while 2-substituted cyclopentene monomers do not undergo ROMP at all. 3- and 4- substituted cyclopentene monomers polymerize well, unless part of a cyclohexane or benzene ring[4]. Norbornene and its 5,6-subsitituted analogues make up an important class of ROMP monomers due to their high ring strain and versatile functionalization options[55]. Cyclohexene or cycloheptene do not undergo ROMP at all. Functional groups must be compatible with the catalyst but the high tolerance of Grubbs type catalysts accommodates for a diverse set of functionalities.

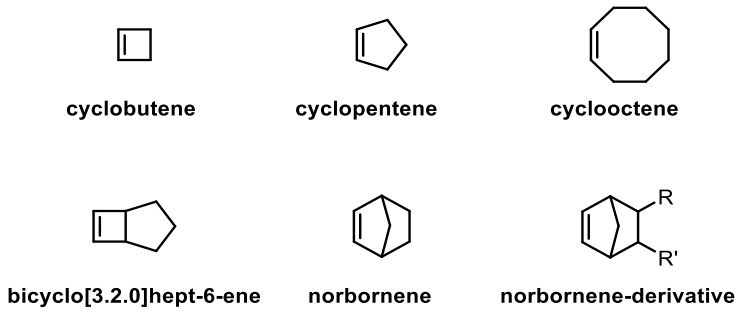

Chart 1-4: Selection of strained olefinic monomers suitable for ROMP.

1.2 Polymer Brushes

Since the advent of controlled polymerization techniques enabled their synthesis, polymer brushes have enjoyed a large share of material scientists' attention[56]. They are dense macromolecular assemblies where one chain end is tethered to an interface. The interface may be a liquid-liquid interface in melt or solution such as those found in micelles and membranes or an impenetrable interface such as a solid surface. Brushes may be covalently tethered or adsorbed *via* intermolecular interactions such as hydrophilic, hydrophobic, LONDON-dispersion, dipolar or π-stacking interactions[57]. Covalently grafted brushes can be handily categorized into one-, two- or three-dimensional brushes (see Figure 1-3). One-dimensional brushes are polymers grafted off another polymer chain. They are also referred to as graft polymers[6]. Two-dimensional graft polymers are tethered to a flat surface and called surface brushes. Similarly, three-dimensional brushes are attached to concave or convex surfaces such as grafted nanoparticles or porous substrates like membranes.

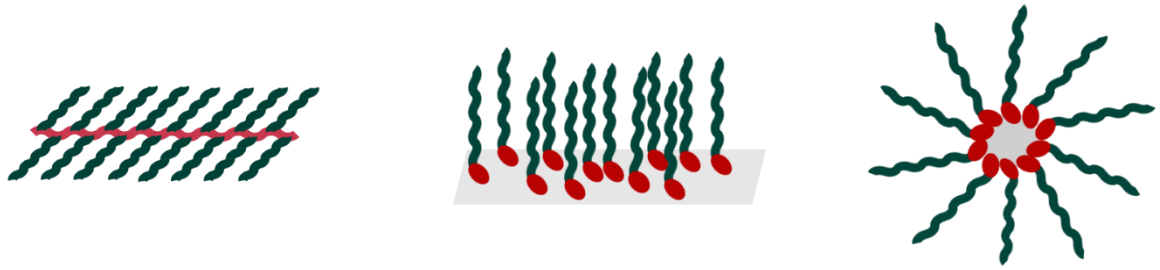

Figure 1-3: Covalent brushes at impenetrable interfaces from one to three-dimensional geometries.

Sufficiently dense grafting of polymer chains in combination with the mobility restriction imposed by the attachment of one chain-end results in equilibrium conformations distinct from the random-walk configurations found in polymer melts or solution[58]. The high density at the tethering site results in a strong overlap of the individual chains, raising the monomer-monomer interaction energy. As a consequence, the chains stretch away normal to the surface, minimizing the interaction energy at the expense of the elastic free energy. Stretching increases the layer thickness while reducing monomer concentration within the brush. Due to their stretched conformation and the high steric crowding, individual chains of a polymer brush show decreased mobility in contrast to polymer chains in solution or melt. As a consequence, their mechanico-chemical properties can differ dramatically. For a dense brush, the extended polymer chain length (L) scales as a function of degree of polymerization

(N). For a polymer chain in solution, the random walk conformation allows to predict the radius of gyration (R_g) scaling with degree of polymerization by $R_g \sim N^{1/2}$.[59]

1.2.1 Surface Brushes

Polymer brushes have enjoyed significant growth in interest from both a fundamental and an applications perspective. Surface brushes have been intensely studied by polymer physicists as an accessible model for complex polymeric systems such as micelles, polymersomes or polymers at interfaces. Their practical applications are inspired by the ability to change a material's surface properties while leaving the bulk properties unchanged. The thin polymer layer allows to tune wettability, colloidal stabilization[60], compatibilization with polymer/biological matrices[61,62], fouling resistance and nonspecific binding of biomolecules[63–66]. Particular within the medical field, this surface engineering approach enjoys a multitude of applications. Polymer brushes are grafted onto medical devices or implants to avoid fouling due to bio adsorption, achieve compatibilization with tissues, reduce friction of implants or contact lenses, allow selective protein adsorption or encourage tissue adhesion[67–75]. They can be employed as a new class of adhesive materials[76,77] or as a lubricant[67]. The high steric demands further restricts accessibility of solvent or other molecules to the surface. Patterned surface brushes have been employed as reactive ion etching resists for substrates used in the semiconducting industry[78].

Brushes have been used to alter surfaces of various geometries. Grafting at spherical nanoparticles has been employed to stabilize colloidal solution against flocculation by employing a polymer that preferentially interacts with solvent rather than other colloid surfaces[79]. Both experiments and simulations found that the stabilization effect is sensitive to grafting density and grafted chain length[80]. Additionally, zeta potentials of inorganic nanoparticles can be tuned through the introduction of charged polymer chains[63]. Polymer brushes on silica gel allow to develop tailored chromatographic devices[81]. In the presence of solvents, polymer chains adapt according to their solvophilicity. In a good solvent, interaction with solvent molecules is maximized and interaction with other polymer chains is minimized. As a consequence, the polymer chains are highly extended. In the presence of a bad solvent, interactions with solvent molecules are minimized and the brushes collapse.

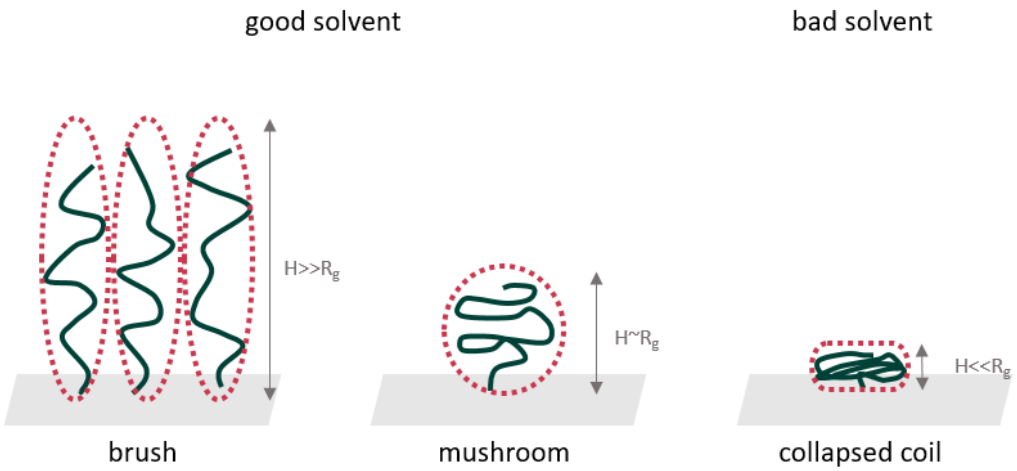

Figure 1-4: Schematic representation of polymer chains tethered to a surface. Left: densely grafted brush in a good solvent. Center: Polymer chain in a good solvent (mushroom). Right: collapsed polymer chain in a bad solvent.

Depending on grafting density and chain length, grafted polymers may adopt one of three conformations: (stretched) brush, mushroom and collapsed coil (or pancake). (see Figure 1-4). The grafting density of polymer brushes (σ) can be calculated (see Equation 1-1) by knowing the chains' density (ρ), their dry brush thickness (H), multiplied by AVOGADRO's constant (N_A) and dividing by the chains' number averaged molecular weight.

$$\sigma = \rho H N_A / M_n$$

Equation 1-1

The tethered density parameter (Σ) can be determined to predict homopolymer brush conformations. This dimensionless parameter is defined by surface density and the polymer's radius of gyration (R_g) (see Equation 1-2). At low tethered densities ($\Sigma << 1$), the chains are present as collapsed coils (also known as pancake regime). As the tethered density approaches unity, a mushroom conformation is adopted. Although the two former conformations are also commonly referred to as polymer brushes, only high grafting densities ($\Sigma >> 1$) lead to the proper brush regime.

$$\Sigma = \sigma \pi R_g^2$$

Equation 1-2

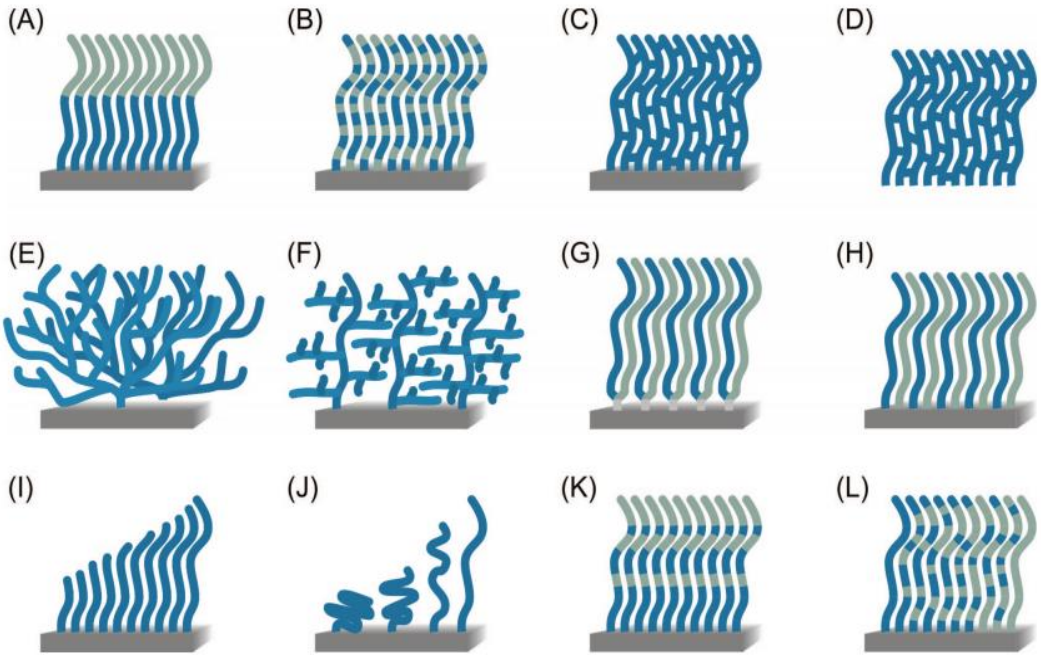

Figure 1-5: Overview of different polymer brush architectures that can be prepared via surface-initiated controlled radical polymerization. (A) block copolymer brushes; (B) random copolymer brushes; (C) cross-linked polymer brushes; (D) free-standing polymer brushes; (E) hyperbranched polymer brushes; (F) highly branched polymer brushes; (G) Y-shaped binary mixed polymer brushes; (H) standard binary mixed brushes; (I) molecular weight gradient polymer brushes; (J) grafting density gradient polymer brushes; (K, L) chemical composition gradient polymer brushes. Reproduced with permission from[82] Copyright ©2009 American Chemical Society.

Analogous to polymers in melt or solution, a range of polymeric architectures can be targeted. Homopolymeric brushes were synthesized with highly homogeneous chain lengths[83], chain length gradients[84] and grafting density gradients[85,86]. Employing inimers as (co) monomers allows to target highly branched (arborescent)[87] or hyper-branched architectures[88]. Employing cross linking agents permits to crosslink the brushes and subsequently remove them from the surface to yield free-standing brushes[8990]. Grafting from a cross-linked monolayer[91] or nanosheet results in polymer carpets[92]. Copolymers include two-layer brushes (grafted diblock copolymers)[93], statistical copolymers[94], and gradient copolymers (along the grafted chain[95,96] as well as laterally[97]).

Mixed polymer brushes (MPBs) are surface brushes containing two or more, different homopolymer chains. Binary brushes are surface brushes containing polymer chains of two monomers (see Figure 1-5 G and H), ternary brushes contain three types of polymer etc.. They are distinct from grafted di- or triblock copolymers (see Figure 1-5, A), or grafted statistical or gradient copolymers in that the grafts are different homopolymers, but mixed on a molecular level. They may be arranged either randomly or alternating on a surface.

Mixed brushes show a host of intriguing phase behaviors when the two grafted polymers (A and B) are immiscible. The FLORY-HUGGINS theory of polymer mixing predicts that enthalpic and entropic considerations drive two immiscible polymers to undergo spontaneous phase separation. The covalent connection between immiscible blocks found in amphiphilic copolymers precludes a macroscopic demixing and gives rise to a diverse set of nanoscopic phase structures. The conformations adopted by immiscible block copolymers are dictated by their molecular weights, volume fractions and FLORY-HUGGINS interaction parameter (χ). Much like block copolymers, MPB's grafted with immiscible homopolymers are precluded from macroscopic phase separation by their covalent attachment to the surface. This attachment introduces a set of additional parameters influencing the phase morphology: grafting density, symmetry of chain length, polymer ratios and surface geometry all impact the brush behavior.

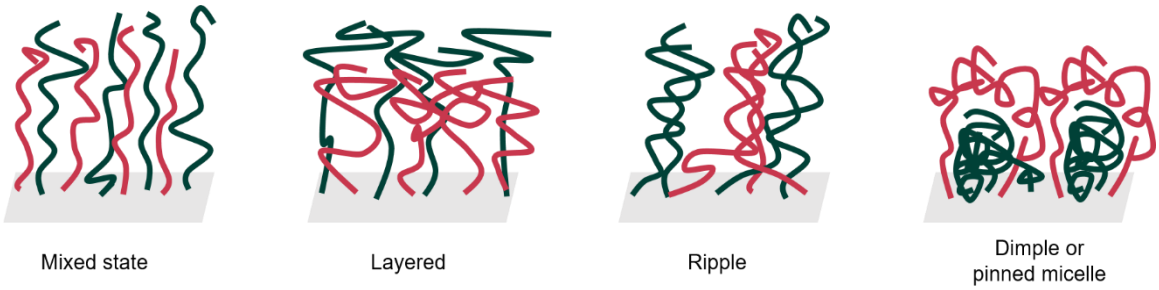

Figure 1-6: Schematic representation of nanoscopic structures adopted by immiscible mixed brushes.

Figure 1-6 schematically shows a set of nanoscopic morphologies, binary mixed brushes may adopt: the mixed state, layered, ripple or dimple phases. These can be adopted in melt, in non-selective solvent or in selective solvent. In the mixed state, interaction between the different polymers is maximized. This structure is adopted if steric hindrance precludes adoption of an energetically more favorable structure, the FLORY-HUGGINS immiscibility parameter is low or if interactions with a non-selective solvent are greater than polymer-polymer interactions, leading to a chain-extended form.

Layered morphologies are the result of a vertical phase separation. The two immiscible polymers segregate perpendicular to the surface, while remaining laterally homogeneous. Mixed brushes adopt this structure if polymer A has greater affinity to the substrate. Another factor favoring a layered conformation is the relative chain length of the two polymers. Intuitively, if polymer B is significantly longer than polymer A, the top phase is rich in polymer B (see Figure 1-7 c)).

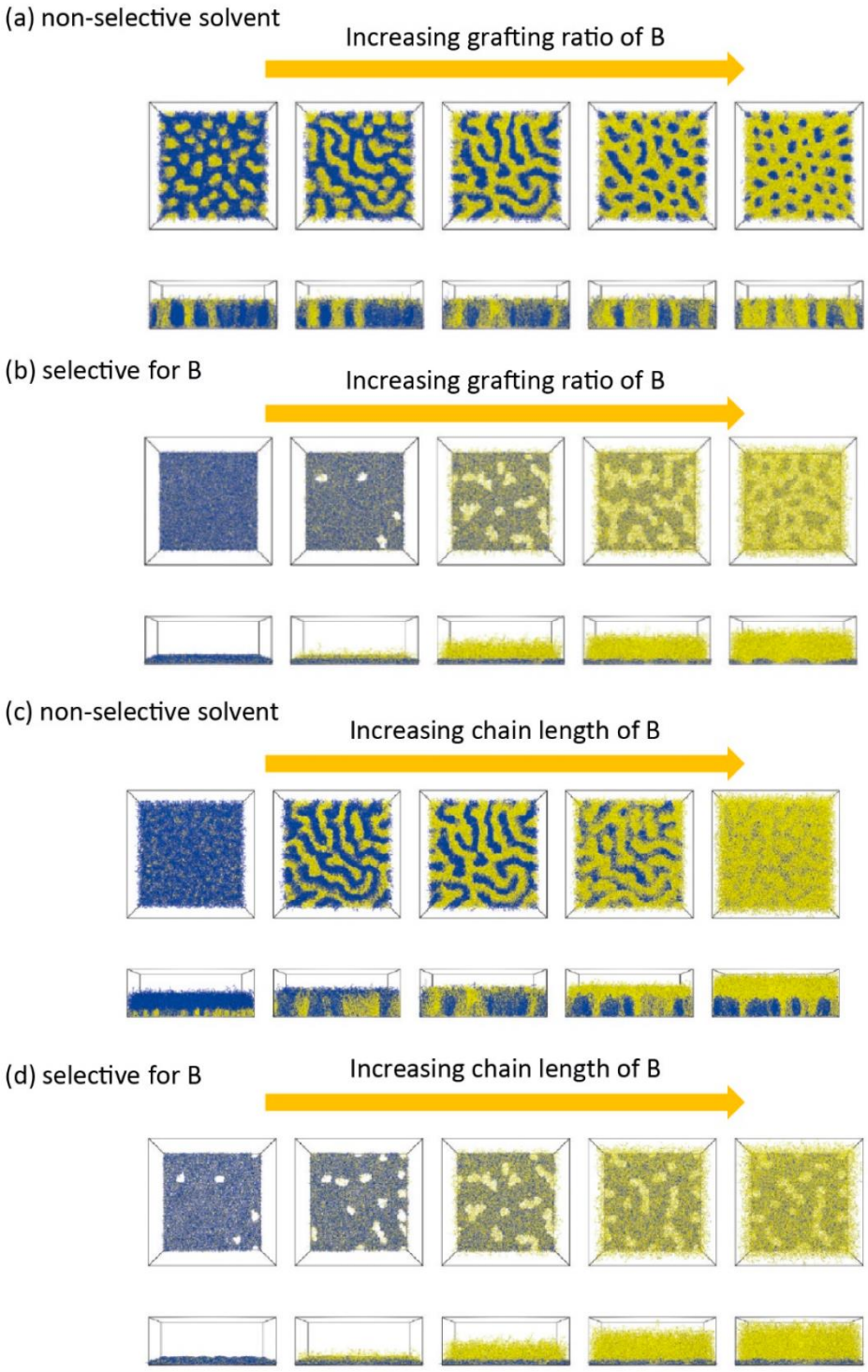

Figure 1-7: Simulation results on mixed polymer brushes (MPBs) composed of two incompatible polymers A (blue) and B (yellow). Top view and side view of MPBs with increasing grafting density of B and fixed grafting density of A in (a) non-selective good solvent and (b) selective solvent for B. The middle images represent equal grafting ratios of two components. Top view and side view of MPBs with increasing chain length of B and fixed chain length of A in (c) non-selective good solvent and (d) selective solvent for B. The middle images represent equal chain lengths of two components. (Reproduced with permission from Reference[98], Copyright 2009, American Chemical Society) and [99].

Ripples can be observed both in melt or non-selective solvents and results from a lateral phase separation. In this case, phases enriched in one polymer alternate on the surface with phases enriched with the other. These two-dimensional structures have well-defined length scales that are controlled by the molecules' extension. The domain size was found to be twice the root-mean-square end-to-end distance of the polymer chains[98]. The immiscibility parameter predicts whether the domains are discreet or gradual in nature. The lateral distributions of the ripples and their morphology depends strongly on the grafting ratio between polymer A and B. Figure 1-7 a) shows the simulation results of binary brushes adopting different ripple topologies as a function of increasing grafting ratio[98]. At low grafting ratios, polymer A is a continuous phase with small domains of polymer B. At equal grafting ratio, the ripples appear as meandering stripes and at high grafting ratios, polymer B forms the continuous surface composition with dotted polymer A domains. AFM measurements allow to visualize ripple structures by tracing the indentations between domains, if the cantilever interacts selectively with one polymer or if rheological differences prevail. The morphologies were predicted by self-consistent field calculations. With increasing incompatibility, the brushes undergo a phase change from disordered melt into laterally segregated cylindrical domains (i.e. ripples)[100]. Experimental investigations confirmed the presence of these ripples. Through the use of AFM and plasma etching, MINKO et al.[101] confirmed that the phase separation extends normal to the surface. The group synthesized random mixed PMMA and poly(styrene-stat- pentafluorostyrene) (PSt/PFS) brushes on silica wafers. Plasma etching was employed to remove the brush layer by layer, exploiting the two brushes disparate etching rates. XPS measurements were used to monitor atomic composition as a function of etching depth. AFM measurements were conducted after every etching step to assess surface topology.

Dimple structures portray both lateral and vertical separations. They occur both in selective and non-selective solvents. When the immiscibility parameter for polymers A and B is sufficiently large, and the solvent is poor, the ripple phase undergoes a phase transition to minimize interaction with the solvent. Two distinct dimple phases may be observed: a symmetrical dimple structure with alternating A and B dimples or dimple A in a matrix of B (and vice versa). The resulting morphology can be thought of as the grafted versions of micelles, with polymer A forming a core and polymer B providing a shell. For highly symmetric and narrowly distributed chains, these arrays are predicted to show long-scale periodic order on the surface. However in experiment, such long-range order has never been observed. The schism between theory and practice may be due to (i) fallacious parameters used for the modeling or (ii) due to randomness of the grafting sites. The lateral, and vertical segregations are depicted in Figure 1-6 d).

The range of MPB morphologies that can be targeted has important implications on the surface properties. But even more importantly, covalently attached MPB's binary brushes have the ability to adapt to various external stimuli through cooperative changes of their conformation. Being able to externally control various physical properties is the corner stone of material scientists' endeavor to develop new types of sensors, switches or microatentuators. As a consequence, binary brushes and their phase transitions have been intensely studied both in theory as well as experimentally. The best explored stimulus-response is that to solvent selectivity. Simulations showed that for a binary brush — solvent system defined by the polymer incompatibility (χ) and solvent selectivity (ξ), a phase diagram comprising ripples, dimples and disordered phases can be constructed (see Figure 1-8)[100]. At low incompatibilities, the binary brush is present as a disordered state, irrespective of the solvent selectivity. However as incompatibility increases, a non-selective solvent leads to a phase transition yielding the formation of ripples. A solvent selective for polymer A will result in a dimple B state and vice versa. At very large values of χ, only dimple states are observed. Müller and Wang98 simulated binary brushes of various grafting ratios, chain lengths and solvent slectivities to yield three-dimensional conformations that help to visualize the phase transition. The binary brush system in Figure 1-7 switches from ripple (a) to dimple (b) formation when exposed to a solvent selective for polymer B. The height profiles are a useful pictorial tool to visualize the lateral and vertical phase separations. The blue polymer A is collapsed near the surface while clearly showing a laterally segregated distribution.

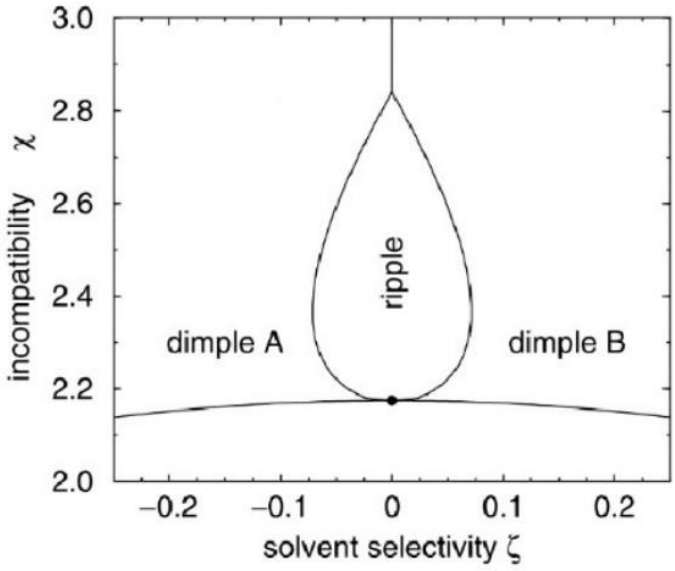

Figure 1-8: Phase diagram as a function of incompatibility (χ) and solvent selectivity (ξ). Reproduced with Permission from [100]. Copyright 2002 American Physical Society.

Various groups have observed such phase transitions in experiment. For example, STAMM et al[102]. synthesized binary brushes consisting of high molecular PSt and Poly 2-vinylpyridene (P2VP) chains. The group observed the formation of "ripples" in non-selective solvent. However when exposing the brushes to a selective solvent (toluene is selective for PSt and acidified water for P2VP), the incompatibility of the other block led to a rearrangement of the brushes, as evidenced by XPS and contact angle measurements. When exposed to acidified water, the surface was rich in P2VP, while when exposed to toluene, styrene moved to the surface. This switching of polymer brushes[103] was further investigated by TSUKRUK et al.[104] The group synthesized Y-shaped mixed brushes at a sparse grafting density and showed that at modest chain lengths (30-40 units), the dissimilar polymer chains led to a spontaneous phase separation with 30 nm-100 nm domains at a height of 1.8 nm to 2.3 nm. The shorter chain lengths led to a smoother surface and pinned micelle structures rather than ripples. The micelle structure could be inverted by immersion into selective solvents.

In addition to solvent responsiveness, mixed polymer brushes and their adaptive responses have also been studied under a range of other stimuli, among which pH, ion strength, temperature and humidity. Poly acrylic acid and Poly 2-vinyl-pyridine (PAA/P2VP) binary brushes have been synthesized and their response was monitored as pH was modulated. The pK_as of the two polymers dictate that PAA is negatively charged at high pH, while P2VP is positively charged at low pH. The charged chains lead to electrostatic repulsion and hence a selective stretched out conformation[105]. Similarly, PEO/PAA mixed brushes were synthesized on gold substrate and by modulation of the ion strength, a swollen or collapsed conformation of the PAA chain could be achieved. At high ion strengths, the deprotonated PAA enters a salted regime and collapses, while PEO remains stretched out. By this approach, protein adsorption and desorption could be modulated[106,107]. By grafting a temperature responsive polymer such as Poly N- isopropyl acrylamide (PNIPAM), mixed polymer brushes can undergo phase changes by externally controlling temperature. PS/PNIPAM brushes were synthesized and when increasing the temperature to above PNIPAM's lower critical solution temperature (LCST), the polymer transitioned from coil to globule and the surface turned opaque[108].

The adaptive nature of mixed binary brushes explains the vast range of their applications. Binary brushes have been explored for microfluidic devices[109], responsive colloids[110], smart coatings[111], protein adsorption[112–114] and for smart drug delivery systems[115].

1.2.2 Molecular Brushes

Molecular bottlebrushes (BBs) are a type of densely grafted macromolecule. IUPAC defines graft macromolecules as "a macromolecule with one or more species of block connected to the main chain (backbone) as side chains, these side chains having constitutional or configurational features that differ from those in the main chain."[6] The primary polymer poly(A) to which the poly(B) chains are attached is also called the backbone, main chain or graft(ing) substrate. Poly(B) is then referred to as either side chains, pendant chains, branches or grafts[5]. For a graft polymer to be classed as a molecular BB, particularly high grafting densities must be achieved. In particular, the distance between two grafting points along the backbone must be smaller than the characteristic dimension of the grafted side chain[116]. Such high grafting densities lead to high steric interactions between the side chains. The covalent bonding, meanwhile preclude detachment of the side chains. These conflicting properties confer two determining physical factors to BBs in general. First they lead to a stretching out and stiffening of the backbone, giving BBs their characteristic cylindrical topology. Second, as a consequence of the steric clash, BBs do not overlap, causing the unique viscoelastic properties observed in BBs and encourages ordering[59].

The backbone's flexibility is determined by the distance between neighboring side chains. High grafting densities lead to stiff BBs while low grafting densities result in more flexible BBs. When side chain length is significantly shorter than backbone length and densely grafted, BBs portray a marked conformational anisotropy. The semi-flexible cylindrical conformation is adopted on length-scales than far exceed side chain lengths. The conformation is described by contour-length (L), brush diameter (D) and Kuhn length (λ_K). The persistence length of the backbone is dependent on the side chain length and grafting density, i.e. the number of pendant side chains per backbone monomer atom. BBs may adopt a range of conformation depending on their state[117].

In dilute solutions in a good solvent they adopt a worm-like structure[118]. Degree of polymerizations of both backbones and side chains, as well as grafting density determine the exact conformation of the entire brush, although the precise interplay of these parameters remains subject to scholarly debate. As concentrations are increased above a certain threshold a concentration, molecular BBs may spontaneously orient to increase their order, as is well-established for various semi flexible cylindrical materials[119]. In semi-dilute concentrations or in melt, the macromolecules start to interpenetrate. However, in contrast to their linear analogues, BBs have significantly larger entanglement molecular weights. Interpenetration of polymers increases with increasing flexibility and increasing molecular weight[119]. At the

entanglement molecular weight, entanglement becomes significant enough to represent an additional barrier to flow and diffusion. At a molecular weight greater than the entanglement molecular weight, viscosity scales with $M_n^{3.4}$ rather than with M_n^1. Molecular BBs are much less flexible than their linear analogues, while also occupying much larger excluded volume (see Figure 1-9). The side chains lead to a *de-facto* dilution of the backbone chain. As a consequence, densely grafted brushes self-disentangle and show remarkably low entanglement plateaus and low viscosities, making them ideal for application as rheological modifiers[118,120–124].

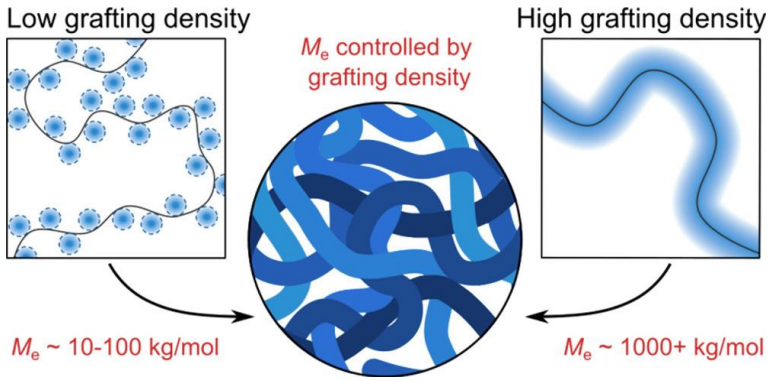

Figure 1-9: Comparison of comb and bottlebrush molecular architectures and chain conformations. Scaling of backbone length between grafts (L_g) and side chain diameter (D_{SC}), are shown for each case. (A) At low grafting densities the graft polymer has a comb conformation where the backbone and side chain are both unperturbed Gaussian coils (B) At high grafting densities, the grafts and backbone are extended. Reproduced with permission from[118]. Copyright © 2018, American Chemical Society

Molecular BBs may be visualized by atomic force microscopy[119]. A dilute solution of polymer brush deposited on an atomically flat surface allows to depict their morphologies, sizes and distributions. However, the conformations depicted by AFM do not reflect the conformations in solution. The various equilibrium conformations adopted by BBs on a surface or interface depends on the strength of interaction between side chains and surface material. Interaction with an interface breaks the cylindrical shape and leads to a partitioning of the side chains. Some of the side chains are directly adsorbed on the surface while the remaining side chains interact with the solvent or air. The ratio of adsorbed and desorbed side chains depends on their affinity to the substrate. When brushes are deposited on a surface that is attractive to the side chains, a majority of side chains interacts with the surface. To accommodate maximal adsorption on the surface, the side chains extend leading to a stretched out conformation of BBs. AFM micrograph then show extended ribbon-like structures. When the interactions between surface and side chains are not attractive, different conformations are adopted depending on the quality of the surrounding solvent. In poor solvents (or air), side chains attract one another and form curved or globular structures[119].

In a good solvent, the side chains may stabilize another cylindrical structure. These structures can then directly be observed *via* AFM (see Figure 1-10). Long-scale ordering may be observed, too when the anisotropic brushes orient according to flow rates and directions. A particularly interesting phenomenon was observed by the MATYJASZEWSKI[125] group who adsorbed BBs on a substrate that interacted strongly with the side chains. Maximization of side chain contact with the substrate led to stretching of the backbone to the point where the tensile force sufficed to cleave carbon-carbon bonds of the backbone. Over the period of 42 h, enough bonds had ruptured to dramatically shorten the brushes to change the observed morphology from rod-shaped to globular. The average length of the brushes were tracked and fitted to a first order reaction rate.

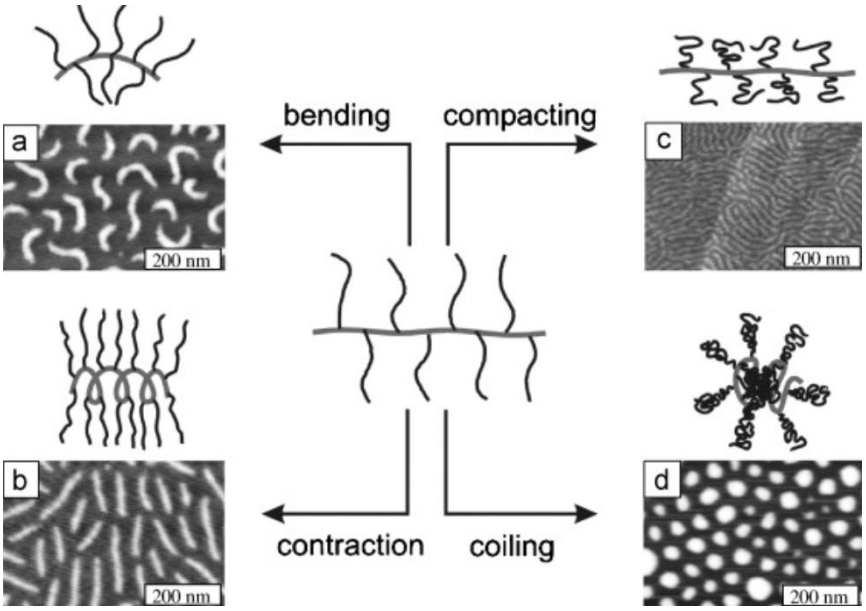

Figure 1-10: AFM micrographs showing four of the possible conformations adopted by molecular bottlebrushes after deposition on surfaces. (a) spontaneous curvature (b) ribbons, (c) cylindrical (repulsion between desorbed side chains), and (d) globular (attraction between desorbed chains). Reproduced with persmission from[119]. Copyright © 2008 Elsevier Ltd.

All BBs are by necessity copolymers of two different monomers: the backbone monomer(s) and the side chain monomer(s)[126]. However, as the backbone constitutes only a small volume fraction of the overall molecule, it is convention to refer to BBs with only one type of homogeneously grafted side chains and one homogeneous backbone as linear homopolymer brushes. The ability to incorporate multiple diverse monomers for both the backbone as well as the side chains leads to a large structural and compositional variation in possible BB architectures. Figure 1-11 provides an overview over some of the structural variations reported. As the material properties of BBs are sensitively dependent on their architecture, the large library of accessible brush structures has led to a rapid growth of (possible) applications. Controlling the backbone composition allows to synthesize branched

or cyclic BBs[127]. Importantly, crosslinking between polymer brushes allows to access a range of super-soft elastomers. Like the mechanically related hydrogels, covalent crosslinking allows for structural stability while retaining local mobility. While hydrogels rely on the diffusion of and solvation by small molecules that are liable to leaching or evaporation, polymer brush networks are solvated by their side chains. The mobility of their side chains allows the structure to retain responsiveness to exterior forces while their covalent attachment to the network imparts them with structural stability. As a consequence, polymer brush networks do not collapse nor do they leach out solvents. Such systems have been reported to show low modulus (~100 Pa) and high strain at break (~1,000%)[128,129]. Exploiting the high mobility of poly ethylene glycol (PEG) chains, PEG-grafted, cross-linked polymer brush electrolytes are heralded as safer alternatives to liquid lithium ion battery electrolytes[130]. XUE et al.[131] further imparted self-healing capacities to such PEG-grafted battery materials by introducing ureidopyrimidinone containing physical crosslinks.

Figure 1-11: Structural variations of molecular BBs. Reproduced with permission from[126] Copyright © 2019, American Chemical Society

Brush-coil BBs are a type of block copolymer consisting of a brush segment

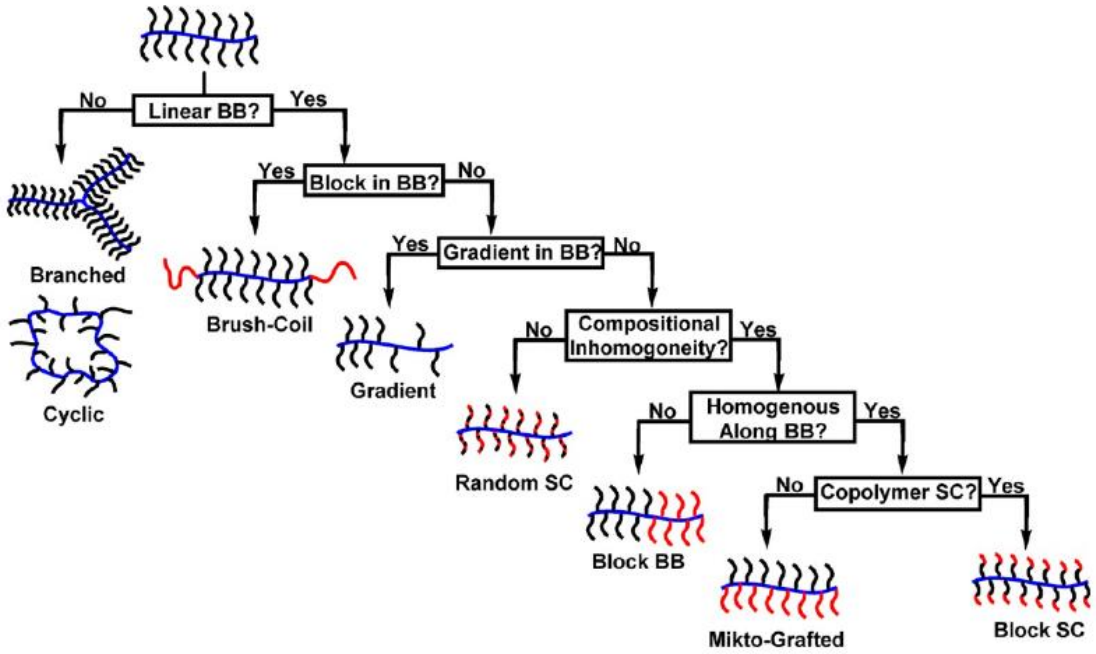

sandwiched between two linear polymers. Such macromolecular architectures allow to impart one macromolecule with flexible, random-coil segments together with the semi-flexible regimes of BBs. A naturally occurring coil-brush-coil polymer is the lubricating protein lubricin. Lubricin belongs to the group of proteoglycans: heavily glycosylated proteins that are responsible for a large range of functions within the body. Their brush-like structure imparts them with viscoelastic properties that enable them to act as water-sponges and lubricants in cartilage, or help in clearing lung pathways[119]. Lubricin contains a brush-like

segment sandwiched in between two coil segments and conducts boundary lubrication between joint surfaces. Similarly, triblock brush-coil BBs with poly(2-methacryloyloxyethyl phosphorylcholine) (PMPC) brushes sandwiched in between two quaternized poly(dimethyl aminoethyl methacrylate) (q-PDMAEMA) chains were synthesized to mimic the lubricating properties of lubricin. The q-PDMAEMA segments interacted strongly with the surface of glass slides, to create a loop conformation. The PMPC-grafted brush segment led to weak and long-range repulsive interaction forces with a second glass slide, reporting low frictional coefficients.[132]

Controlling the backbone incorporation of grafting sites allows to synthesize brushes with grafting density gradients. Likewise, BBs can have multiple types of side chain monomers. As with their linear analogues, copolymerization in side chains may yield statistical or block side chain brushes. Statistic brush copolymers can show highly fascinating material properties if the two polymers are incompatible. For example, frustrated packing in poly(octadecyl methacrylate) statistic copolymer with poly(ethylene glycol methacrylate) (PODMA-co-PEGMA) brushes[133] lead to an intramolecular compositional interface. Block BBs have two (or more) segments of different homopolymeric sidechains, separated along the backbone. Such structures allow to introduce amphiphilicity within brushes, leading to disparate polymer domains within the same polymer structure. For example fluorophilic and hydrophilic section within the same brush have been reported[134] together with their supramolecular arrangements.

Molecular BBs have also been investigated as promising candidates as drug carriers. Several factors speak for their employment as polymer-drug conjugates. Their uniform and nanoscopic size mirror metabolic proteins, encouraging cell uptake and by benefit of their branched architecture prolong circulation timespan. These factors are of vital importance for passive tumor targeting. In addition, the broad synthetic platform allows to tune sizes, compositions and functionalities. By functionalizing the side chains with pharmaceutically active agents, the drug loading capacity is greater than in other polymer-drug conjugates.[135,136] Grubbs for example used ROMP of a macromonomer consisting of a hydrophilic PEG chain and doxorubicin or camptothecin anti-cancer drugs. The hydrophilic grafts act as unimolecular micelles that are highly efficient of shielding hydrophobic drugs and backbones. Drug release was accomplished *via* UV irradition[137]. Similarly, the CHENG group reported the synthesis of well-defined bottlebrush statistical copolymers functionalized with anticancer drugs and solubilized with PEG side chains. They accomplished pH-sensitive drug release. [138]

1.3 Motivation and Aim of This Work

The physical properties of polymer brushes - and therefore their possible applications - are sensitively dependent on the composition and two-dimensional arrangement of their constituent polymer segments[126]. Their synthesis must therefore be both robust, reliable and precise. However, the commonly employed synthetic strategies to yield mixed binary brushes or molecular bottlebrushes suffer from a range of undesirable effects. Some of the issues encountered in brush synthesis are inherent in synthesizing block copolymers such as the synthetic challenge of yielding discrete blocks rather than gradients. Additional obstacles are architecture specific, introduced by the necessity to control the spatial resolution of tethering points.

Usually the two block constituting mixed binary brushes or backbone and sidechains in molecular bottlebrushes are synthesized one after the other[5956]. This stepwise approach is necessary as block copolymerization relying on the same mechanism is precluded by the need to spatially resolve the two blocks and their grafting points. As a result, the two blocks may either be synthesized (i) sequentially or (ii) independently from one another, followed by a coupling step. Both these solutions come with their specific caveats.

When employing the sequential polymerization approach, chemists may either combine two different initiation mechanisms or else use protection-deprotection strategies. In the first case, care must be taken to avoid contamination of incompatible catalysts, monomers, or solvents from the first polymerization into the reaction mixture of the second polymerization step. As a result, this approach usually requires careful purification of the first chain before polymerization of the second chain. In addition to requiring large volumes of solvent, achieving high degrees of purity is often difficult and catalysts or monomers remain in the polymeric product[59]. These residuals encourage side reactions in the second polymerization step. When furthermore, the second monomer is of different polarity to the first, a solvent switch may be necessary, while potentially introducing solubility issues.

The protection-deprotection approach can be employed when both monomers polymerize *via* the same polymerization mechanism. By this method, the chemist can selectively polymerize one monomer, quench the polymerization, deprotect the second initiator and achieve discrete, spatially resolved blocks. Synthetic polymer chemists routinely use this approach to successfully synthesize block copolymers[14]. However in the context of grafted architectures, this approach can be difficult to control with accuracy. The high density of grafting points inherent in brush architectures together with the kinetic constraints

imposed by conducting polymer analogous reactions translate to less than quantitative conversions of the deprotections. Isolation, transfer and re-dissolution of intermittent polymeric products encourage side reactions that may lead to a loss in end group functionality, making any targeted post-polymerization functionalization modification difficult. Finally, when synthesizing graft copolymers in a stepwise fashion, there will necessarily be a large mismatch between the low steric hindrance of the first polymerization and the much more encumbered second polymerization that often leads to incomplete grafting or low grafting densities of the second polymerization. Undesired homopolymeric impurities often remain in the polymerization mixture that are difficult to extract and rely on solvent-intense techniques like cycles of precipitation, dialysis and liquid chromatography.

Coupling two independently synthesized polymers with complementary functionalities suffers from the same limitations as outlined above, with the added constraint of much greater steric barriers. While in the two above approaches, only small molecules — reagents or monomers — have to diffuse to the increasingly crowded brush, the coupling approach necessitates two macromolecules to diffuse towards an ever-denser brush. This effect is exacerbated when two immiscible blocks are to be tethered. As a result, poor grafting densities are usually observed.

Aim of this work is to overcome or circumvent these issues by employing orthogonal polymerizations that are mutually tolerant of the two sets of catalysts, monomers, solvents and reaction conditions. With such mutually tolerant but monomer-selective polymerization techniques, it is envisioned that two polymerizations can be conducted in the same vessel at the same time as a tandem polymerization. The term *tandem* is inconsistently used in literature to describe any interdependent chemical transformation conducted in one reaction vessel. Tandem reactions include cascades of orthogonal reactions catalyzed by different mechanisms in a one-pot approach. Similarly, WECK et al[139]. described their non-orthogonal reaction cascades in nanoreactors as tandem catalyzed. Sometimes, the term is extended to the synthesis of spatially resolved polymer nanocomposites from two monomers in one reaction vessel[140]. A synthetic strategy that involves only one catalyst and monomer to produce nanocomposites is usually referred to as *twin polymerization*[141]. Even sequential transformation where a second catalyst is added to the same reaction mixture after completion of the first step is sometimes loosely referred to as a tandem transformation. FREUDENSPRUNG et al.[39] coined the term *simultaneous tandem block polymerization* for describing systems where two independent, orthogonal polymerization techniques are employed to produce diblock or triblock copolymers from a feed of two monomers in one single polymerization step. Likewise in the following, the expression *simultaneous tandem grafting* will be employed.

The simultaneous tandem approach is expected to leverage the superior diffusivity of monomers over polymer chains. Control over the resulting architecture will be established through monomer and initiator design. A particular focus is directed towards incorporating monomers with disparate functional groups and polarities. At the same time, discreet segments of the two blocks are desired, while care must be taken to avoid gradient incorporation of the two monomers. Besides the intrinsic value of decreasing the labor load of the synthetic process, such a simultaneous approach should decrease the occurrence of unwanted side reactions. Furthermore, this work seeks to achieve a careful balance of the two independent polymerization kinetics and thus circumvent unfavorable steric hindrance regimes, as well as gain insight into potential interactions between polymerizations.

2 SIMULTANEOUS BOTTLEBRUSH POLYMERIZATION

2.1 State of Literature

This chapter discusses the implementation of a tandem grafting approach to synthesize molecular bottlebrushes in only one reaction step. A particular focus was placed on achieving high grafting densities. To contrast the simultaneous approach presented herein, a brief overview over present synthetic strategies and their shortcomings is presented.

2.1.1 Sequential Synthesis of Molecular Bottlebrush Polymers

The allure of molecular bottlebrushes with their broad range of applications and their role as model compounds for natural systems has inspired a broad body of work devising synthetic strategies to reliably yield BBs with the desired characteristics. Generally speaking, all reported polymerization pathways can be summarized into three overarching themes: *grafting to*, *grafting from*, and *grafting through*[126].

Conceptually, the grafting through process is a polymerization of *macromonomers* (MMs). The side chains of the targeted molecular bottlebrush are synthesized first and equipped with a polymerizable chain end. In a second step, these moieties are polymerized, yielding the desired BB polymers. The grafting through method reliably produces high grafting densities, as each backbone monomer is necessarily functionalized with a side chain. Lower than 100% grafting densities can also be targeted as desired. If the MM solution is

diluted with additional monomer of equal reactivity to the macromonomer, the grafting density can be lowered to yield pseudo-graft copolymers[126].

The most common approach is to functionalize the macromonomer with an olefin chain end to allow for anionic or radical polymerization[142]. The advantage of this approach is that very high grafting densities can be achieved. If every backbone monomer is functionalized with one side chain, neighboring side chains are only separated by one carbon-carbon bond. While living anionic polymerization is generally capable of producing polymers with low dispersities under excellent control, anionic polymerization of macromolecules introduces several issues. The concentration of polymerizable functionalities is intrinsically low in macromonomers due to the presence of the side chains. Large steric bulk of the side chains further impede the polymerization and conversion was found to be dependent on side chain length[119]. While the side chains dilute monomer concentrations on one hand, they also cause gelation at relatively low conversions. Additionally, the high purity requirements of anionic polymerization are often difficult to achieve for macromonomers. As a result, anionic grafting through is frequently characterized by low conversions with a large homopolymeric population remaining in the product[143].

(Conventional) radical polymerization of macromonomers is much more tolerant of impurities and a range of reaction conditions. However the broad dispersities associated with radical polymerization make this approach unattractive for many applications. RDRP approaches and specifically ATRP are much more commonly employed for macromonomer polymerization[142]. To avoid bimolecular termination reactions, these polymerizations are conducted with rates of deactivation exceeding rates of activation. As a result, polymerization rates are very low. This effect is exacerbated by the low concentrations of polymerizable end groups. The low ceiling temperatures of macromonomer radical polymerization limit the applicability of this technique further. The steric challenges and low gelation points discussed for anionic grafting through also apply for radical polymerizations[143].

Introducing strained cyclic olefins as end groups for the side chains allows to employ ROMP as a viable alternative for grafting through. Most commonly, side chains are functionalized with norbornenyl groups due to their high reactivity towards ROMP. Norbornenyl groups alleviate the steric hindrance of side chains[144]. In contrast to vinyl polymerization of macromonomers, where each chain is separated by two carbons, norbornenyl derived backbones produce side chain distances of six carbons. Using highly active GRUBBS or HOVEYDA-GRUBBS catalysts, rapid polymerizations with full conversions and low dispersities are routinely reported[145,146]. Using norbornenyl derivatives as initiators for side chain ROP allows to synthesize end-functionalized side chains in one step. Using the

same approach with ATRP-derived side chains is less successful as there is competition between norbornenyl incorporation into the side chains. Nonetheless, all grafting through polymerizations suffer from the issue of incomplete chain-end functionalization. If the reactions introducing vinyl or norbornenyl groups are not quantitative, the polymerization mixture contains both macromonomer as well as homopolymeric impurities that cannot be grafted. As a result, solvent intensive purifications such as dialysis or liquid chromatography are required to separate homopolymers from BBs. CZELUSNIAK et al.[145] conducted systematic research in the synthesis, characterization and degradation of polylactide functionalized polyoxanorbornanes using the grafting through technique. The group used stannous octoate ($Sn[Oct]_2$) as catalyst and oxanorbornanes as initiators to produce Polylactide functionalized macromonomers. They noted the increased ROMP activity of 2nd Generation Grubbs catalysts over the first generation equivalents. The 3rd Generation Grubbs catalyst was found to produce more narrowly distributed bottlebrushes. All their polymerizations produced bimodal distributions due to macromonomers remaining in the reaction mixture.

For the second method - g*rafting from* -, the polymeric backbone is synthesized first and equipped with pendant initiating sites. This macroinitiator is then used as a template in a second polymerization step, where side chains are grown at the initiating sites[147]. The advantages of this approach lies in the possibility to reliably synthesize long backbones with low molecular weight distributions. By denaturing proteins, followed by site specific functionalization with initiating functions, unimodal length distributions of the backbone can be achieved[148]. Additionally, grafting from has lower steric barriers as the small monomers can easily diffuse to the active sites in contrast with the high steric demands of polymerizing macromonomers. Any unpolymerized monomer can subsequently be removed from the polymerization mixture by precipitation. A drawback to this technique lies in greater side chain dispersities and lower grafting densities[143]. Initiators may either be introduced by post polymerization modification of functional groups of the monomer or by employing monomers with initiating functionalities, so called *inimers.* Both approaches have advantages as well as disadvantages. Introducing the functionalities *post* polymerization suffers from the same issues as all *polymer analogous reactions*. In brief, polymer modifications generally have lower yields than their small molecule analogs. The success of polymer analogous reactions depends on the diffusional mobility of the reactants, intermediates, and products in the reaction mixture[149]. Moreover, the primary, secondary and tertiary structure of the polymer chain (in solution) dictates the steric hindrance of inbound reagents onto the reaction sites. As a result, achieving 100% conversion to initiating sites is unrealistic and the maximal grafting density cannot be reached. The inimer approach on the other hand ensures that all backbone monomers do indeed carry initiating sites. However this method is

contingent on employing polymerization techniques that are tolerant of the functionality at hand. Usually this necessitates that backbone polymerization and side chain polymerization be orthogonal techniques.

Polymerization of the side chains can proceed through a large range of polymerization techniques. Radical polymerization is most commonly employed with reversibly deactivating agents as the close proximity of propagating radicals in neighboring chains encourages bimolecular termination resulting in looped side chains[142]. ATRP is commonly employed, partially owed to the fact that ATRP initiators are easily introduced in the backbone. Additionally, the technique is tolerant to various functional monomers. Core-shell BBs can easily be prepared by sequential addition of different monomers[150]. However, despite the low radical concentrations, active ATRP chain ends can still undergo termination reactions[143]. The occurrence of bimolecular radical coupling is particularly detrimental if it takes place between two different brushes. Even a very low incidence of such crosslinking can lead to rapid gelation and notably impacts product properties.[117] Moreover, in ATRP grafting from, not every initiating site does indeed start the growth of a side chain. Direct comparisons between brush initiator efficiency and linear initiator efficiency in ATRP systems were made and found to be consistently lower due to the site congestion.[151] Side chain polymerization *via* anionic polymerization tends to be a more reliable approach. The propagating anions do not participate in mutual coupling reactions and lower side chain PDIs are reported[152]. However, as with anionic grafting through, the technique is contingent on high purities in monomers and macroinitiator.

The final technique - *grafting to* - relies on the separate synthesis of side chains and backbone with complementary functional groups[126]. The separate synthesis of side chains and backbone in this approach allows to produce narrow dispersities in both sets of polymers. As a result, bottlebrushes with narrow molecular weight distributions could be expected. However, the synthetic success of this technique is conditional to the fidelity of the coupling reactions as well as the steric barriers. Fast and high conversion reactions such as “click” chemistry is frequently used in context of grafting to[136]. An elegant alternative includes using living anionic side chain ends in nucleophilic substitution on poly (chloromethyl styrene) backbones. Notwithstanding the high conversions of such reactions, the grafting densities using this technique are usually low. In the high steric bulk of the brush, equal reactivity assumptions between small molecule and polymer analogs break down. The dissolved side chains in their coil conformation represent a formidable hindrance to allow the two functional groups to react. Moreover the concentration of reacting groups is very low for longer side chains. With increasing conversion, the bulk of the brush grows ever larger,

shielding inbound side chains from the reaction sites. As a consequence, brushes with low grafting densities are produced with large amounts of homopolymeric impurities[117].

2.1.2 One-pot Syntheses

Various groups have reported one-pot synthetic strategies for the synthesis of molecular bottlebrushes. However, so far no truly *simultaneous* synthesis could be reported.

MATSON et al.[153] employed diazabicycloundecene (DBU) for ROP of cyclic lactones. The group synthesized an oxanorbornene inimer capable of initiating ROP, while the strained norbornenyl group readily undergoes ROMP in the presence of Grubbs-III. Side chain polymerization was conducted first, quenched and after addition of ROMP catalyst, narrowly distributed bottlebrush polymers could be isolated. However, FOGG[154] et al. already showed that amines and other BRONSTED bases are highly efficient in the decomposition of phosphine-free metathesis catalysts. Therefore, the DBU catalyst was found to deactivate the Grubbs-III catalyst, necessitating that the side chains be polymerized first, followed by a quenching step. The catalytic system therefore does not allow a one-step simultaneous process.

Previous work by CHARVET and NOVAK[155] exploited the ability of the First Generation GRUBBS catalyst (Grubbs-I) to initiate ROMP of strained olefins while simultaneously shuttling halides as ATRP catalyst. The group synthesized a strained cyclic olefin with ATRP initiator functionality. The Grubbs-I catalyst then polymerized the inimer, while also polymerizing methyl methacrylate (MMA) side chains. However in their syntheses, the group found that ROMP was complete within 30 min while ATRP did not achieve full conversion after 48 h. Moreover, it was found that certain reaction conditions encouraged competition of the unsaturated backbone with MMA for ATRP. As a result, GPC analyses revealed molecular weight distributions ranging from 1.67 to 2.62 or bimodal distributions. The targeted DP of the backbone was 20 while side chains of 5 and 40 monomers were synthesized. Low yields were reported for side chain DPs of 40, while DPs of 5 led to better conversions. The elegant approach of using only one catalyst for both polymerizations led to some interesting insight, despite falling short of a truly orthogonal polymerization.

Similarly, ZHU et al.[156] used a phosphoamidate ROMP inimer and dimethyl aminoethyl methactrylate (DMAEMA) with Grubbs-I and the Third Generation GRUBBS catalyst (Grubbs-III) to synthesize dense brushes. The group directly contrasted the one-pot approach with grafting from and grafting through of the same monomers. All three pathways produced polydispersities between 1.52 and 1.75. However, only the grafting through method led to yields greater than 30%. Likewise, poor control over DPs led to molecular weights divergent from theory. No kinetic profiles were established between the two polymerizations.

Likewise, various other groups have successfully combined two orthogonal polymerization strategies in one-pot syntheses, among which WOOLEY et al[157]. and GRUBBS[158] and coworkers deserve particular mention. Often the term “tandem” is used in these contexts to describe the dual role of backbone inimers. However, most of this work is conducted in a step-wise manner. Truly orthogonal and *simultaneous* copolymerization towards bottlebrushes had never been reported. Part of the work presented in this chapter has been published elsewhere[159] and is adapted with permission from[159] Copyright 2021 American Chemical Society.

2.2 Concept

The unique mechanical properties that underpin the many uses of molecular bottlebrushes are a result of high grafting densities coupled with low dispersities[117]. For the successful synthesis of molecular brushes, the chemist must control chemical composition, backbone degree of polymerization, side chain length and grafting density. With the three techniques presented above it is challenging to control many parameters at once. The common pitfall for the established polymerization techniques lies in steric hindrance: grafting through is sterically encumbered through the polymerization of macromonomers, grafting to is sterically hindered when side chains diffuse to the backbone and grafting from is sterically hindered in the growth regimes. Efforts to improve synthetic pathways should therefore focus on devising strategies to mitigate the diffusion barriers, while retaining the inimer motif to ensure maximal grafting densities.

The following work was inspired by the observation that small molecules diffuse much more readily towards active chain ends than macromonomers, side chains or backbones. If, therefore polymerizations could be conducted in such a way as to ensure that both backbone monomers and side chain monomers can freely diffuse towards their respective growing chain ends with the same reaction rates, both polymerizations could take place with minimal steric hindrance. This concept is represented graphically in Figure 2-1.

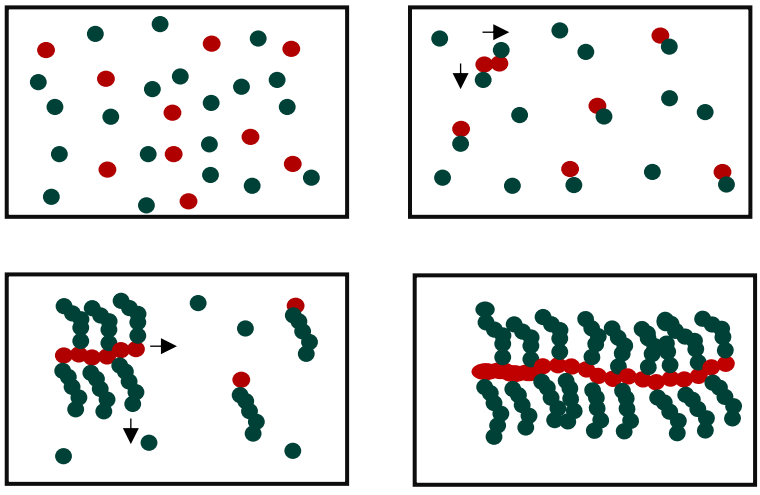

Figure 2-1: graphic representation of simultaneous backbone and sidechain polymerization

The polymerization mixture (top left) is a dissolved mixture of the two monomers: backbone inimer and side chain monomers. The dual polymerization is initiated by addition of the respective catalysts/initiators. During the early polymerization stages (top right), the

inimers are unhindered to initiate side chain polymerization so that a quantitative initiation rate can be achieved. At the same time, backbone polymerization can take place without steric hindrance of the side chains as at this stage, the side chains are still short. If the polymerization conditions and catalyst systems can be adjusted to ensure comparable reaction rates, the backbone polymerization can proceed with little steric hindrance for the majority of the polymerization timeframe. Likewise, the side chain growth occurs predominantly in unhindered regimes, as in early reaction times, most side chains grow in solution (bottom left). In later reaction times when most inimers are incorporated into the backbone, side chain polymerization takes place off the backbone. However as side chains grow longer, the active chain ends enjoy greater mobility due the radially increased degrees of freedom. Depending on the precise reactivity ratios between the two polymerizations, it can be envisioned that bottlebrushes with narrow dispersities and high grafting ratios can be synthesized with minimal steric hindrance (bottom right). The resulting technique would be a novel synthetic strategy, combining aspects of *grafting-from* and *grafting-through.*

For such a vision to be feasible, the backbone polymerization must occur independently from the side chain polymerizations. No inimer should be incorporated into the side chains so as to avoid multi-branched structures. Conversely, no side chain monomer should dilute the backbone grafting density. To avoid statistic incorporation of monomers, the two polymerizations must proceed *via* two mutually exclusive mechanisms. Additionally, the two processes should be independently tunable so as to ensure truly simultaneous reactions. As a consequence of these premises, two different polymerization mechanisms must be chosen. Previous attempts to afford simultaneously polymerized molecular bottlebrushes (*vide supra*) informed the choice of polymerization techniques. Of the many polymerization techniques, examples of *grafting-through* in literature is limited to ROMP and ATRP. However as ATRP suffers from low ceiling temperatures and inherently slow polymerization rates, it was decided to choose ROMP as backbone polymerization technique. The excellent substrate tolerance of ROMP allows to polymerize a range of inimer substrates. The side chain polymerization must initiate reliably and offer synthetic opportunities to match the kinetic rates with those of ROMP. Due to the large range of catalysts and monomers and therefore large range of polymerization rates, it was decided to polymerize the side chains through ROP.

2.3 Studies of Orthogonality

In order to assess the feasibility of simultaneous grafting, the orthogonality of the chosen catalytic systems needs to be established. As outlined above, the system must be such that

(i) The two catalysts do not degrade each other (catalyst tolerance)
(ii) The propagating mechanism is specific to the respective monomers (specificity)
(iii) Monomers and catalysts do not undergo side reactions (catalyst-monomer interaction)
(iv) The two monomers do not interfere with each other (monomer-monomer interaction)
(v) One solvent system can dissolve all reagents (solvent choice)
(vi) The reaction temperature is amenable to both polymerizations (temperature)

Additionally, the specific demands based on the target architecture demand that the two systems

(vii) Be covalently attached (inimer choice)
(viii) Occur truly simultaneously to minimize unfavorable steric regimes, i.e. have similar reaction timeframes (kinetics)
(ix) Achieve full conversion to avoid macromonomeric impurities (high conversion)

Every requirement above must be addressed in order to afford a well-controlled simultaneous system.

2.3.1 Catalyst-Catalyst Interactions

For the orthogonal combination of ROP and ROMP, it is particularly important that the catalysts be mutually tolerant. It was already established that basic reagents deactivated Grubbs-type catalysts *vide supra*. As a consequence, many organocatalysts commonly employed for ROP are unsuitable for these purposes. Basic organocatalysts for the ROP of cyclic lactones are usually nucleophilic tertiary amines or phosphines. They include for example 4-dimethylaminopyridine (DMAP), 1,8-diazabicyclo[5.4.0]undec-7-ene (DBU); 7-methyl-1,5,7-triazabicyclo[4.4.0]dec-5-ene (MTBD), 1,5,7-triazabicyclo[4.4.0]dec-5-ene (TBD) or phosphazene bases[160]. Moreover, common metathesis catalysts are late transition metal complexes whose catalysis performance is sensitively dependent on the electronic structure of the frontier orbitals[161]. As a consequence, reducing catalysts used in ROP like stannous

octoate are unsuitable for the purpose outlined herein. In contrast, FREUDENSPRUNG et al.[39,162] recently showed that the NHC 1,3-dimesitylimidazolin-2-ylidene (SIMes) can be employed to effect ROP of cyclic lactones together in a one-pot, one-step process with the Second Generation GRUBBS catalyst (Grubbs-II) for ROMP of strained cyclic olefins to yield di- and tri-block copolymers. Notably, FREUDENSPRUNG showed that the two polymerizations both proceeded exceedingly fast, achieving full conversion within 15 min. This catalytic system therefore showed great potential to fulfill the requirements outlined above and was adopted as a potential catalytic tandem system for the synthesis of molecular bottlebrushes.

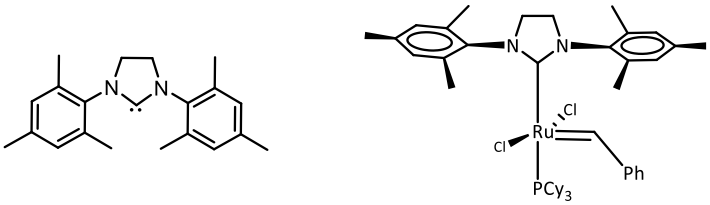

Chart 2-1: The two mutually compatible catalysts employed by FREUDENSPRUNG: NHC 1,3-dimesitylimidazolin-2-ylidene (SIMes) and Second Generations Grubbs catalyst (Grubbs-II).

FREUDENSPRUNG and coworkers further undertook ^{1}H NMR experiments to prove that the two catalysts are mutually tolerant. In brief, the two catalysts were also dissolved together, allowed to react for 90 min and changes in catalyst structure were tracked *via* ^{1}H NMR. However, the choice of CD_2Cl_2 as solvent did not allow to make conclusive statements concerning their structural integrity, as chlorinated solvents are known to react with and therefore deactivate NHCs.[163,164]The experiment outlined by FREUDENSPRUNG[162] was therefore repeated in deuterated toluene (toluene-d_8) to observe the active SIMes catalyst interacting with Grubbs-II. The solvent was thoroughly degassed and dried over molecular sieves before dissolving the NHC. Nevertheless, the freshly purchased SIMes catalyst showed some degradation products in the ^{1}H NMR spectra (see Figure 2-2 bottom). Particularly the signal at 7.92 ppm present in both pure SIMes as well as in the Grubbs-II and SIMes solution can be allocated to the imidazolium product from protonation of SIMes. The degradation product may be the result of trace acidic impurities in either catalyst or deuterated solvent[165]. The relative concentration of 15% of the impurity was taken into consideration for effective catalyst concentrations in subsequent experiments. The signal at 5.65 ppm further highlights the sensitivity of SIMes catalyst to trace amounts of residual water in the reaction medium. When mixing the SIMes and Grubbs-II catalyst and allowing for two hours reaction time at room temperature under inert atmosphere, the impurity signal at 5.65 ppm could not be detected. Apart from this impurity's absence, the ^{1}H NMR spectrum of the catalyst mixture does not show any significant changes from the pure catalyst solutions. Particularly the

alkylidene proton of the Grubbs-II catalyst at 19.58 ppm reveals the electronic structure at the active catalyst center. As this proton's chemical shift is unaltered, it can be concluded that the Grubbs-II catalyst remains intact. FREUDENSPRUNG[162] observed a significant shift of an unassigned proton signal from 4.42 ppm to 4.44 ppm. This signal was not observed in the experiments described herein and was instead attributed to an interaction with the chlorinated solvent. The ^{1}H NMR experiments therefore supported the mutual tolerance of the two catalysts and it was decided that the combination of SIMes and Grubbs-II was an excellent starting point for the implementation of simultaneous tandem grafting.

2.3.2 Specificity of Polymerization Mechanisms

For the synthesis of well-defined molecular bottlebrush polymers in one step, the two

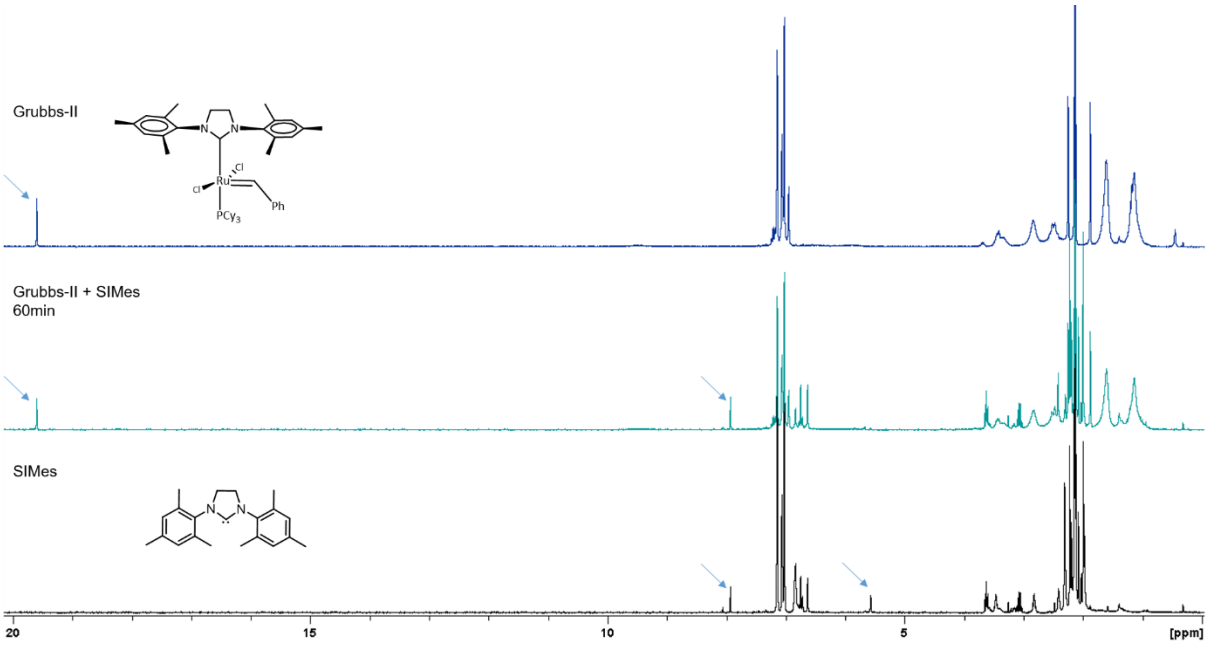

Figure 2-2: ^{1}H NMR spectrum of SIMes (bottom), Grubbs-II (top) and their mixture after 2 h incubation under inert atmosphere (middle). All spectra recorded at RT with a 250 MHz spectrometer in toluene-d_8.

polymerizations must be *specific* to the respective monomers, rather than *selective*. If the two polymerizations proceeded according to only one mechanism but with varying selectivity, a gradient polymer would be produced. True specificity can only be ensured if the mechanistic pathways of the two polymerizations are limited to one monomer each. For this reason, the underlying mechanistic motifs of NHC-mediated ROP and metalalkylidene-mediated ROMP should be considered.

As the name indicates, *ring opening metathesis polymerizations* are metathesis transformations[49]grubbs. Metathesis of strained cyclic olefins result in the spontaneous polymerization into linear, unsaturated polymers. During initiation, a cyclic olefin

coordinates to the metalalkylidine catalyst, followed by [2+2] cycloaddition to yield a metallacyclobutane intermediate. Through cycloreversion of the intermediate, a new metalalkylidine is produced, releasing the ring strain of the monomer. This release of ring strain is the thermodynamic driving force of polymerization. If the monomer concentration is sufficiently high, analogous steps produce a growing polymer chain. The polymerization ceases when all monomer is consumed, an equilibrium is reached or the reaction is quenched[166].

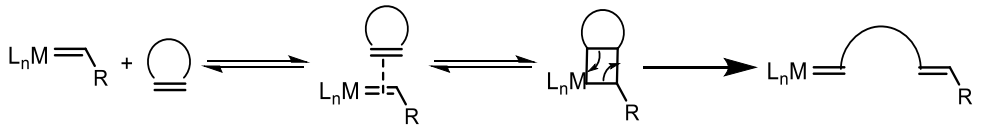

Scheme 2-1: Equilibrium reaction steps in the mechanism of ROMP, where L_nM represents the ligated late transition metal. The final step in the mechanistic cycle that results in the ring-opened new metal alkylidene is irreversible due to the loss of ring strain.

ROP effected by NHCs on the other hand proceed through a zwitterionic or hydrogen-bonding nucleophilic pathway in the absence or presence of alcohol respectively[42]. With an alcoholic initiator, NHCs produce linear polymers with one chain end derived from the initiator and the other end derived by the quenching reaction. In the absence of initiator however, NHCs have been shown to produce macrocyclic polyesters. Without alcohol, polymerization proceeds *via* a zwitterionic pathway[42]. In brief, the nucleophilic carbene attacks the carbonyl group of the lactone and forms a zwitterionic tetrahedral intermediate. The tetrahedral intermediate ring opens to form a zwitterionic oligomer. Ring closure of the oligomer liberates the catalyst and a macrocycle (see Scheme 2-2 a)). In the presence of an alcohol however, the polymerization may proceed either *via* a zwitterionic monomer-activated pathway or *via* a hydrogen-bonding mechanism. The polymerization of ε-caprolactone by the NHC 1,3,4,5-tetramethylimidazol-2-ylidene [42]has been shown to follow a hydrogen-bonding mechanism. The carbene acts as a base by hydrogen bonding to the alcohol, therefore activating it for nucleophilic attack. The alcohol-initiated nucleophilic pathway has been shown to be faster than the zwitterionic macrocycle forming route[42]

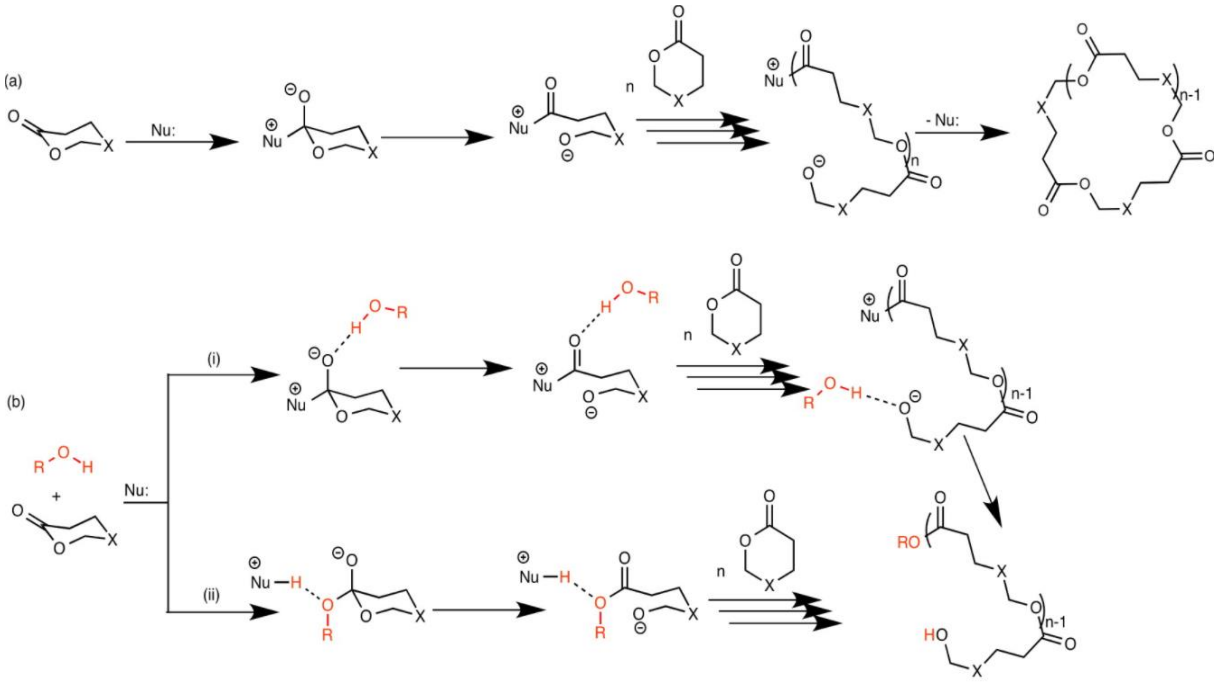

Scheme 2-2: Base-Catalyzed (a) Zwitterionic Ring-Opening Polymerization (ZROP) of Lactones and (b(i)) Nucleophilic and (b(ii)) Hydrogen-Bonding Mechanisms for the Ring-Opening Polymerization of Lactones in the Presence of Alcohol Initiator. Reproduced with permission from[42]. Copyright © 2015 American Chemical Society.

Therefore, the two propagation mechanisms are specific for the respective monomer functionalities: ROMP is a metathesis reaction requiring a strained olefin and NHC-catalyzed ROP is a successive transesterification reaction requiring a strained cyclic ester. So as long as the strained olefin does not contain an ester functionality and the strained lactone does not contain unsaturated carbon-carbon bonds, the two polymerization mechanisms proceed exclusively by propagation of the respective monomers. In addition to these theoretical concepts, FREUDENSPRUNG[39] has shown that the simultaneous ROP by SIMes of L-lactide and glycolide with ROMP by Grubbs-II of norbornene and cyclooctene resulted in the formation of two discreet block of the respective monomers. IR, ^{1}H NMR, DSC and TGA measurements were used to confirm their discreet structure[162]. However, in order to assess orthogonality, all functionalities of the participating monomers must be taken into consideration. It has been reported that NHCs can indeed polymerize monomers with olefin functionality *via* polyaddition. In particular, the small NHC 1,3-ditert-butylimidazolin-2-ylidene was found to polymerize linear and cyclic acrylates *via* conjugate-addition[167]. However, the polymerization requires (i) a sterically accessible NHC (ii) conjugation of the double bond to a carbonyl group. Indeed, it was shown that in a series of multivinyl functionalized γ-butyryl monomers, the polymerization occurs selectively at the conjugated α-methylene double bond while leaving other vinyl groups intact[168]. These considerations were given due attention in the catalyst selection and monomer design.

2.3.3 Covalent Attachment: Monomer Selection

In order to control the macromolecular architecture, covalent attachment between the side chains and backbone must be enforced. One elegant option to achieve this covalent attachment is to employ a monomer with initiating functionality for the backbone chain. While the initiating functionality should reliably initiate the side chain polymerization, it should not interfere with the ROMP polymerization of the backbone. As discussed above, monomers capable of polymerization *via* ROMP are strained cyclic olefins. By functionalizing the monomer with a hydroxyl group, ROP of the side chain can be initiated.

Among the large pool of monomers commercially available to undergo ROMP, 2-norbornene and its derivatives are an attractive option. The bicyclic structure imparts particularly large ring strain on the monomer. As a consequence, norbornene-derived monomers are highly active in ROMP [46,169–171]. High monomer reactivity is particularly important when synthesizing densely grafted polymers[166]. Particularly when polymerizing functionalized monomers, monocyclic monomers have been found to be generally less reactive, with the recent work by TANAKA et al. providing an exception to prove the rule[170]. An additional advantage of norbornenyl monomers is their ease of functionalization. Norbornene and its derivatives are readily synthesized *via* DIELS-ALDER reactions between cyclopentadiene and a dienophile[172].

The simplest monomer design combining the two motifs would be the norbornene monomer functionalized with a hydroxyl group at any position of the bicyclic system. The reactivity of ROMP-monomers is regio-sensitive to the introduced functionalities, a functionalization at the 2-position (respective to the bridge-head) produces the most reactive monomers[14]. Likewise, ROP initiation has been found to be more efficient by primary alcohols over secondary or tertiary alcohols.[163] This concept is combined in the monomer 5-norbronene-2-methanol (NBM) (see

). The spatial arrangement of the methanol group with respect to the bridging carbon allows for two isomers: *endo*- and *exo*- methanol (referring to the orientation of the

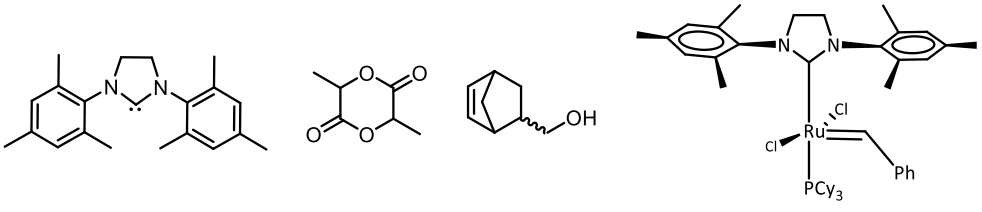

SIMes **L-lactide** **NBM** **Grubbs-II**

dienophile during DIELS-ALDER addition). A mixture of these isomers is available commercially.

Chart 2-2: Monomers and catalysts used for simultaneous tandem grafting.

As FREUDENSPRUNG has shown the successful combination of norbornene with L-lactide, it was expected that the structurally related norbornene-methanol could be applied together with L-lactide, using the same catalysts, reaction conditions and solvents to afford the corresponding bottlebrush polymer. Additionally, polylactide functionalized graft polymers are interesting target molecules as their biocompatibility and biodegradability allow *in-vivo* applications. Their many potential applications make polylactide brushes a much researched set of polymers. So it was decided that the monomers employed for the tandem grafting experiments should be NBM and L-lactide.

2.3.4 Monomer-Monomer Interactions

After establishing the monomer combination of L-lactide and NBM it was investigated

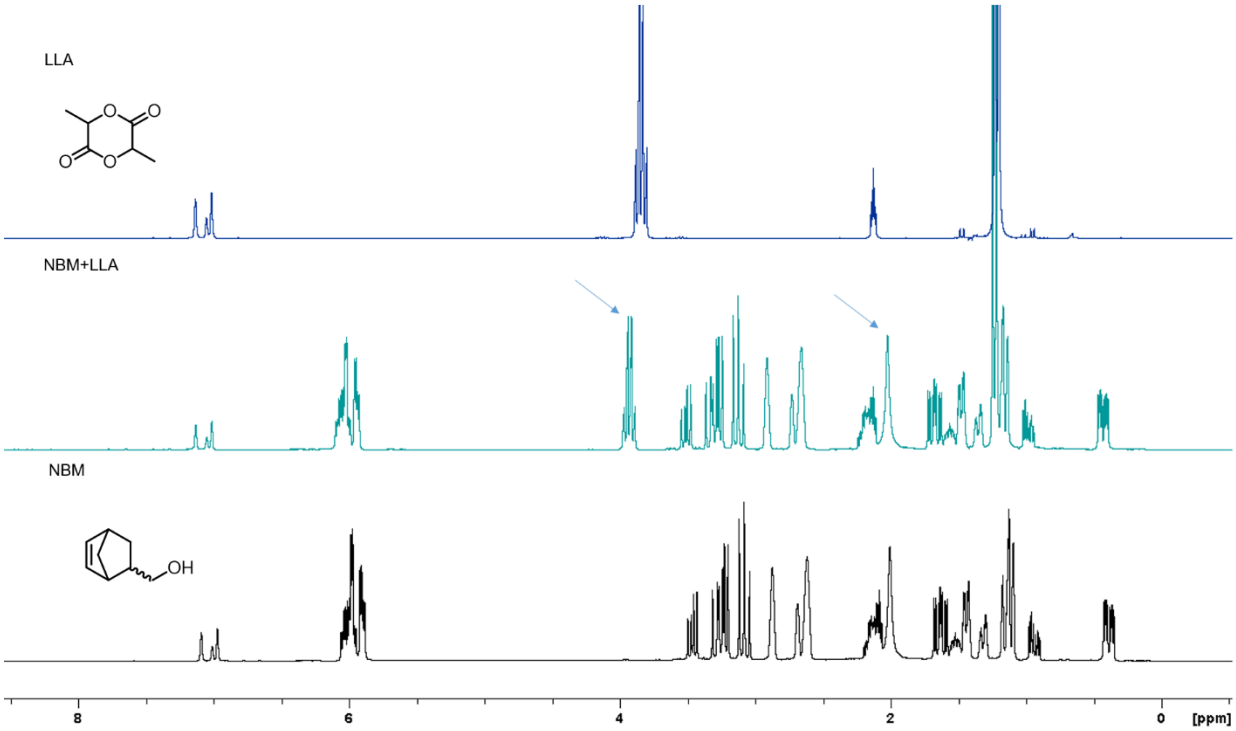

Figure 2-3: ^{1}H NMR spectrum of NBM (bottom), LLA (top) and their mixture after 2 h incubation under inert atmosphere (middle). All spectra recorded at 250 MHz in toluene-d_8.

whether the two monomers are compatible with one another. The two monomers should not undergo reactions, including polymerizations in the absence of catalysts. To assess their compatibility, the two monomers were dissolved together in toluene-d_8 and allowed to react for two hours in a glove box. Then, ^{1}H NMR spectra were recorded of the mixture. The ^{1}H NMR spectra of the incubated solution (see Figure 2-3) revealed two noteworthy shifts when compared to pure solutions of monomer. The methine proton of LLA monomer shifted

downfield from 3.84 ppm to 3.93 ppm, while the hydroxy-proton of NBM is shifted upfield from 2.00 ppm to 2.02 ppm. These minor shifts are due to the interactions of the mildly nucleophilic hydroxy-group with the carbonyl center in LLA. The interactions are strong enough to alter the chemical environments of these two proton centers but not sufficient to cause ring opening, as evidenced by the absence of secondary alcohol peaks. The NBM bridge system and olefin signals remain unchanged. The two monomers were therefore concluded to be compatible for the purposes of this project.

2.3.5 Test Homopolymerizations

The two monomers were then polymerized by their respective catalysts to gauge wither the combination affords efficient initiation and polymerization. Reaction conditions were adopted from FREUDENSPRUNG[39] and the test homopolymerizations were conducted in dry THF at room temperature. Table 2-1 summarizes the molecular weights of the resulting homopolymers. Molecular weights established through GPC matched closely to those expected theoretically when assuming 100% conversion. In contrast to previous findings[162], prolonging LLA polymerization over 15 min to 90 min resulted in decreased dispersities from 1.39 to 1.24, with concomitant increase in molecular weights from 8 400 g.mol^{-1} to 10 800 g.mol^{-1}. Grubbs-II initiated and polymerized NBM reliably, as evidenced from relatively narrow dispersities (1.34 after 60 min and 1.33 after 90 min) and a close match between theoretical molecular weight (12 500 g.mol^{-1}) and experimental molecular weight (11.500 g.mol^{-1}). The reliable initiation and the control over molecular weight were previously established as two key requirements for this project. These test reactions therefore show promise for the orthogonal combination of the two polymerizations. ^{1}H NMR spectra were recorded to compare the homopolymer with tandem polymerizations. The spectra of **1** and **2** revealed the covalent attachment of NBM initiator with the PLLA chains.

Table 2-1: Homopolymerizations of LLA and NBM with SIMes and Grubbs-II respectively.

Entry	Monomer	Temp. [°C]	Mn_{theo}[a] [g·mol^{-1}]	Time [min]	Mn[b] [g·mol^{-1}]	Mw[b] [g·mol^{-1}]	PDI[b]
1[c]	LLA	RT	14 400	15	8 400	11 700	1.39
2[c]				90	10 800	13 500	1.24
3[d]	NBM	RT	12 500	60	8 100	10 800	1.34
4[d]				90	11 500	15 200	1.33

[a]assuming 100% conversion. [b]determined via GPC in THF versus polystyrene standards. [c]NBM:SIMes:LLA ratio 1:1:100 in dry THF. [d]Grubbs-II:NBM ratio 1:100 in dry THF.

The GPC traces (seeFigure 2-4) show a certain low molecular weight trailing for the ROMP homopolymerizations **3** and **4**.

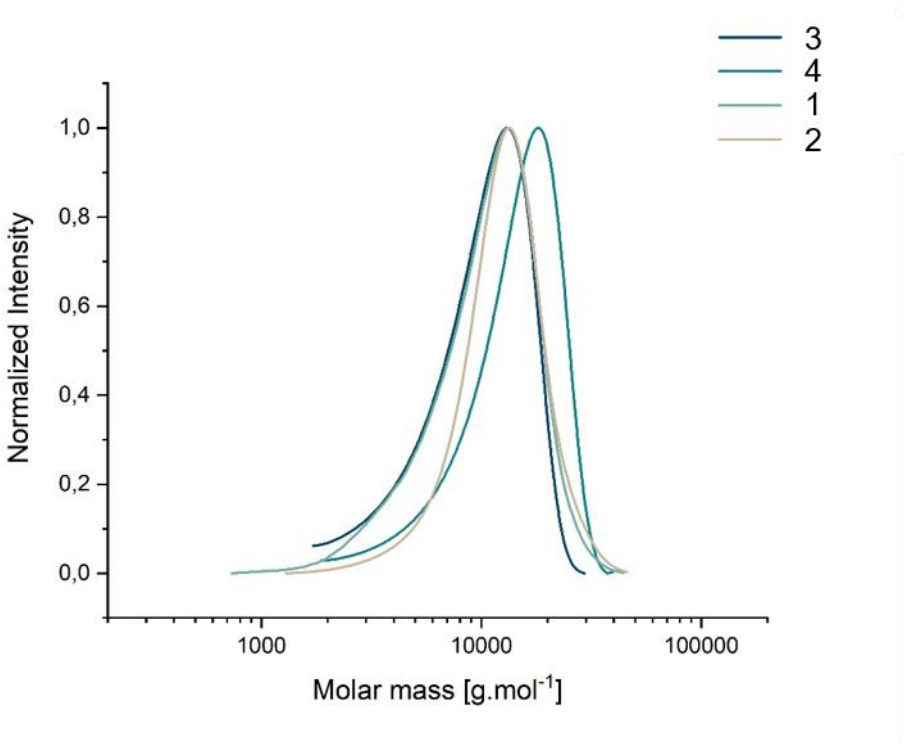

Figure 2-4: GPC traces of Test homopolymerizations **1-4** in THF *versus* PSt standards.

2.3.6 Catalyst-Monomer Interactions

For true orthogonality of the two polymerizations, it does not suffice that the two polymerizations proceed by distinct pathways. Moreover, it is essential that the two processes do not encourage mutual side reactions. In the tandem system of L-lactide polymerized by SIMes, and NBM polymerized by Grubbs-II, such unwanted side reactions can include transformations of NBM effected by SIMes or degradation of Grubbs-II by L-lactide and *vice versa.* To assess the strength of these potential interactions, the two catalysts were mixed with the respectively presumed orthogonal monomer and were allowed to react for several hours under inert atmosphere. The mixtures were then analyzed *via* ^{1}H NMR and compared to the pure substrate.

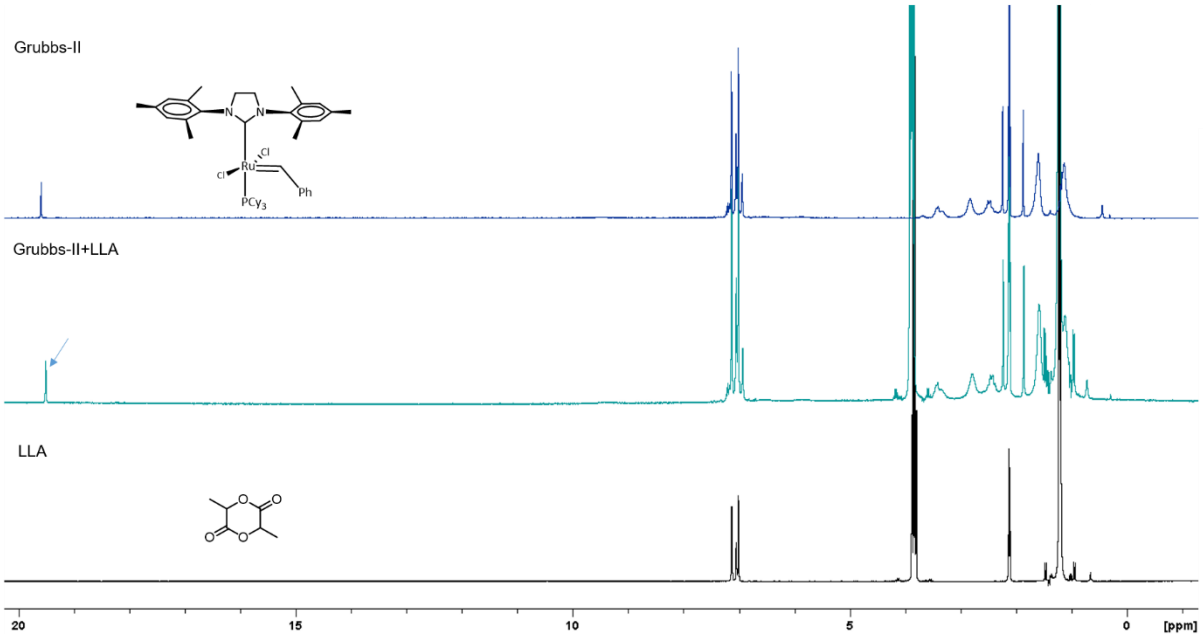

Figure 2-5: ^{1}H NMR spectrum of LLA (bottom), Grubbs-II (top) and their mixture after 2 h incubation under inert atmosphere (middle). All spectra recorded at 250 MHz in toluene-d_8.

The ^{1}H NMR spectrum of the Grubbs-II and LLA incubated solution in toluene-d_8 shows no significant shifts with the exception of a minor upfield shift of the alkylidene proton (seeFigure 2-5). The pure Grubbs-II catalyst spectrum (also in toluene-d_8) showed the alkylidene proton shift at 19.59 ppm. The spectrum recorded after incubation with LLA showed that proton to be shifted upfield to 19.51 ppm. This shift, though small, may be significant as it indicates a change in the electronical structure at the active catalyst site. Such changes could in turn lead to altered polymerization kinetics when employing Grubbs-II together with LLA in a tandem system. However as the other signals of the catalyst and the LLA monomer remain unchanged, it appears that the small alkylidene shift does not represent a catalyst degradation. Indeed, this shift of 0.08 ppm is within the order of magnitude associated with dissolving Grubbs-II in different solvents. For example. the alkylidene proton of Grubbs-II was reported to appear at 19.16 ppm when dissolved in CD_2Cl_2[53]. This is not to say that the catalyst shows no changes in polymerization kinetics when employed together with LLA. It is well known that Grubbs-type catalysts' reactivity are sensitively dependent on solvent choice.[173] Still, FREUDENSPRUNG showed that the catalyst performs ROMP even in the presence of LLA[39] (although no investigations into kinetic profiles were made). It was therefore decided to proceed with this combination, even with the minor changes.

In the combination of SIMes and NBM, it was feared that the carbene might interact with the olefin which would render the monomer inactive with respect to ROMP. FREUDENSPRUNG[162] observed a broadening of PDI in the tandem process compared to stepwise

synthesis. Potential interactions were therefore investigated. The spectra in Figure 2-6 show limited interactions between SIMes catalyst and norbornenyl monomer NBM. The signal at 7.92 ppm that was previously stipulated to represent an inactivated form of the catalyst, decreased upon reacting with NBM monomer. It therefore appears that the "inactive" catalyst does interact with the monomer in some way. The nucleophilic interaction between carbene and alcohol leads to the disappearance of the alcohol proton together with the appearance of signals at 2.56 ppm and 1.93 ppm. Likewise, the adjacent protons to the alcohol are shifted. These effects can all be explained by the hydrogen-bonding interactions of the NHC. The association between alcohol and carbene plays a substantial role in the mechanism of NHC-catalyzed ROP in the presence of alcoholic initiator (*vide supra*). Through hydrogen bonding between alcohol and NHC, the alcohol is activated towards nucleophilic attack at the carbonyl. It was therefore expected to observe the shifts detailed above. Importantly, the olefinic proton signals between 6.13-5.91 ppm do not undergo changes in position or peak patterns. And it was concluded that the SIMes catalyst does not undergo addition to the double bond. Likewise, the characteristic bridge-protons at 1.25-1.12 ppm remain unchanged. It can therefore be deduced that the ring system remains intact in the presence of SIMes.

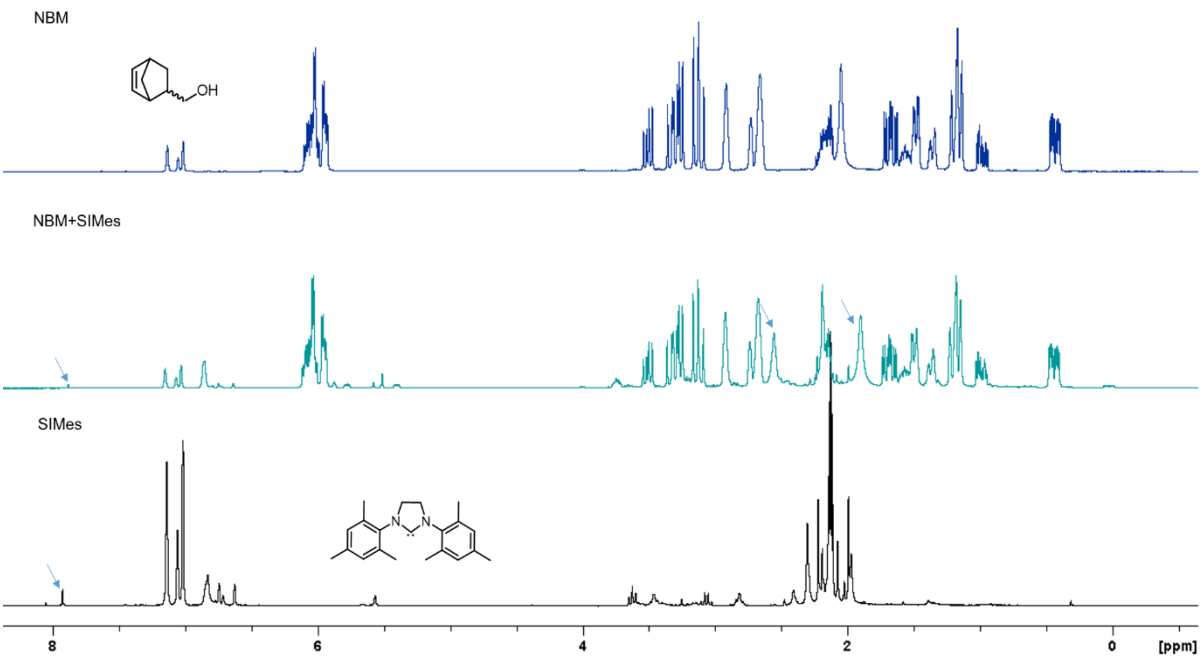

Figure 2-6: ^{1}H NMR spectrum of SIMes (bottom), NBM (top) and their mixture after 2 h incubation under inert atmosphere (middle). All spectra recorded at 250 MHz in toluene-d_8.

Following these conceptual studies, the tandem system defined by the combination of LLA and NBM polymerized by SIMes and Grubbs-II fulfills most of the requirements set on an orthogonal system. The propagating mechanism was shown to be specific to the respective monomers, no side reactions were observed between the two catalysts and monomers, all reagents could be dissolved in THF and conducted at RT to high conversions and covalent attachment between NBM and PLLA was observed. The system therefore shows promise for successful tandem polymerizations.

2.4 Tandem Polymerizations

2.4.1 Tandem Grafting with Grubbs-II and SIMes

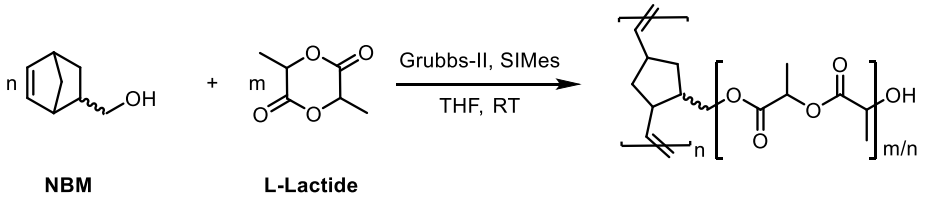

Scheme 2-3: Simultaneous tandem grafting of LLA and NBM effected by NHC SIMes and metathesis catalyst Grubbs-II

Following the conceptual studies above, the tandem system was tried in practice. Starting with a targeted side chain DP of 100 LLA units and a backbone DP of 100 NBM units, all monomers and catalysts were dissolved in dry THF. The LLA monomer concentration was fixed at 0.1 M. The red-violet tint originating from the Grubbs-II catalyst rapidly changed to orange, indicating catalyst activation. After 60 min, the reaction was quenched through the addition of one drop of trifluoro acetic acid (TFA) and ethyl vinyl ether (EVE). The precipitated polymers were analyzed *via* GPC. Table 2-2summarizes the results of these first attempts at tandem grafting. Theoretical molecular weights of the polymers were calculated according to Equation 2-1 and Equation 2-2.

$$Mn_{theo}(graft) = M_{NBM} + M_{LLA} \times Eq_{LLA}$$

Equation 2-1

where Mn_{theo}(graft) refers to the expected molecular weight of the side chain, M_{LLa} is the molar mass of LLA monomer, Eq_{LLA} the equivalents of LLA with respect to NBM monomer and M_{NBM} the molar mass of NBM monomer. The calculation assumes that all chains were initiated by NBM monomers and LLA monomer reached 100% conversion.

$$Mn_{theo}(brush) = Eq_{NBM} \times (M_{NBM} + M_{LLA} \times Eq_{LLA})$$

Equation 2-2

where Mn_{theo}(graft) refers to the expected molecular weight of the side chain, M_{LLa} is the molar mass of LLA monomer, Eq_{LLA} the equivalents of LLA with respect to NBM monomer and M_{NBM} the molar mass of NBM monomer and Eq_{NBM} is the equivalents of NBM employed with

respect to Grubbs-II catalyst. The calculation assumes that all chains were initiated by NBM monomers and LLA monomer reached 100% conversion.

Table 2-2: Simultaneous tandem grafting of NBM and LLA with SIMes and Grubbs-II at RT.

Entry	Eq. LLA[a]	Eq. NBM[b]	Mn_{theo} [c](graft) /g.mol-1	Mn_{theo} [d](brush) /g.mol-1	Mn_{exp} [e] /g.mol-1	PDI[e]
5	100	100	14 500	1 450 000	3 500	1.31
6	100	50	14 500	725 000	6 700	1.35
7	100	20	14 500	290 000	3 500	1.33

Polymerizations conducted in THF at a concentration of 0.1M with respect to LLA. Quenching after 60 min. [a] equivalents of LLA with respect to NBM monomer. [b] equivalents of NBM with respect to Grubbs-II initiator. [c] theoretical molecular weight of side chains assuming 100% conversion of LLA monomer deriving exclusively from NBM initiated chains. [d] theoretical molecular weight assuming 100% conversion of NBM monomer and 100% conversion of LLA monomer. [e] determined *via* GPC against PSt standards.

Entry **5** shows that the isolated polymer diverges dramatically from the theoretical weights that would be expected at full conversion. The isolated polymer M_n of 3 500 g.mol^{-1} falls far short of even the side chain theoretical molecular weight of 1 450 000 g.mol^{-1}. The corresponding GPC trace was asymmetric with a large shoulder or bimodal distribution towards early elution times. The bimodal distribution is included in the PDI of 1.31. This trend was also observed for entries **6** and **7** with targeted backbone DP's of 50 and 20 respectively. Such large mismatches indicate very poor control over the polymerization. NMR analyses (see Figure 2-8 for representative spectrum) indicated that the isolated polymer is PLLA, while the NBM ring remained closed, i.e. ROP proceeded, while ROMP did not occur. Furthermore, the much lower than expected molecular weights (even compared to the expected side chains lengths) indicate that either ROP suffered from poor conversion (due to premature catalyst death) or chain transfer reactions (like transesterification side reactions). To rule out catalyst death due to residual amounts of water in the commercially dried THF, all following polymerizations were conducted in freshly distilled THF. The bimodal distributions observed for entries **6** and **8** represent two polymer populations. A coexistence of NBM-derived homopolymer PLLA chains and NBM-dimers with PLLA chains might explain the observed distribution. The ROMP process might therefore occur at very low conversions, undetectable by NMR.

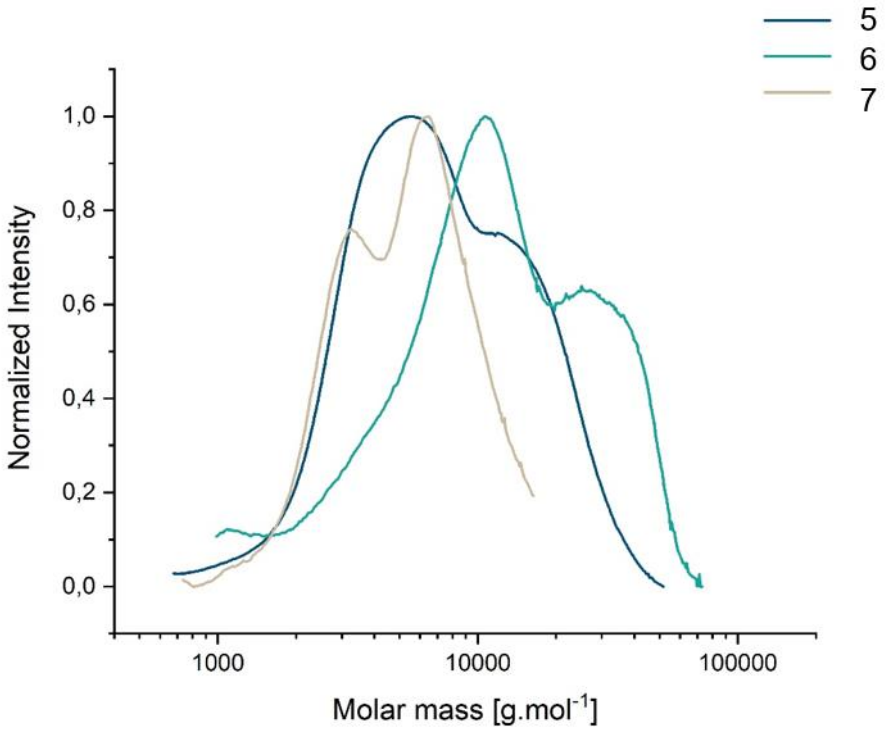

Figure 2-7: GPC traces of polymers isolated from simultaneous tandem grafting of NBM and LLA with SIMes and Grubbs-II at RT. Elution medium THF *versus* PSt standards.

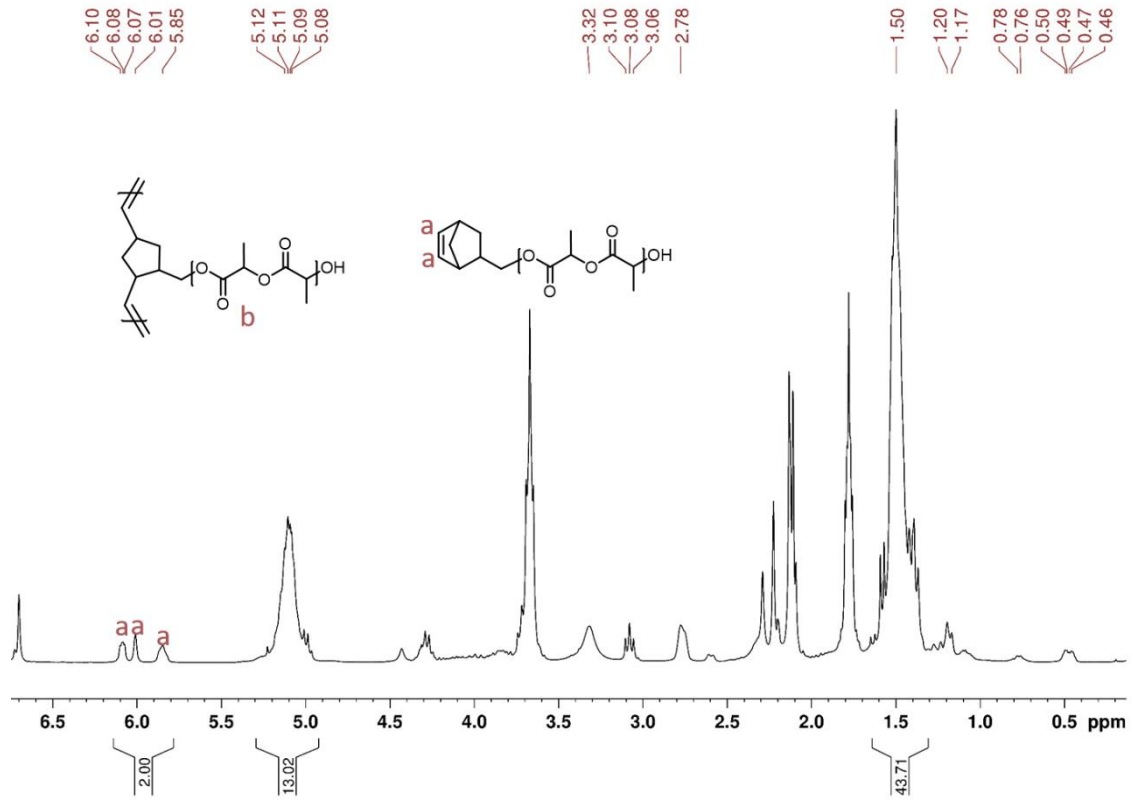

Figure 2-8: Representative ^{1}H NMR spectrum of **7** recorded in $CDCl_3$ with a 300 MHz spectrometer. Characteristic olefin signals associated with closed ring structure highlighted (a).

2.4.2 Impact of Steric Crowding

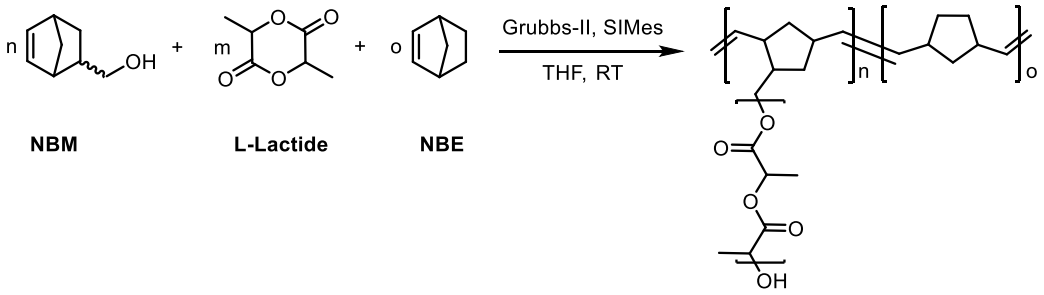

Scheme 2-4: Tandem polymerizations including spacer monomer NBE.

As the ROMP process was hindered, it was stipulated that the growing side chains might represent a large steric bulk even at early reaction times. The steric bulk would then impede the Grubbs-II catalyst from polymerizing the NBM inimer. To assess this hypothesis and mitigate the steric hindrance, a lower DP of side chain grafts was targeted. Entry **9** had a targeted side chain DP of 20 and a backbone DP of 100. The number average molecular weight was somewhat larger than the expected molecular weight (4500 $g.^{mol-1}$ vs 3000 $g.mol^{-1}$). This difference is explained when considering the weight distributions. The peak shape is clearly bimodal with a large lighter fraction and a smaller heavier fraction. The PDI of 1.51 reflects the distribution over the two populations. Still, the expected heavy bottlebrush polymers could not be observed either *via* GPC or ^{1}H NMR. Therefore, the shorter sidechain lengths failed to bring about the desired improvements in ROMP.

Table 2-3: Simultaneous tandem grafting of shorter side chains with spacers.

Entry	Eq. NBE spacer[a]	Eq. NBM[b]	Mn_{theo} [c](graft) /g.mol-1	Mn_{theo} [d](brush) /g.mol-1	Mn_{exp} [e] /g.mol-1	PDI[e]
9	0	100	3 000	300 000	4 600	1.51
10	0.5	100	3 000	300 000	11 000	1.65
11	1	100	3 000	300 100	10 900	1.53
12	2	100	3 000	300 200	9 400	1.57

Polymerizations conducted in THF at a concentration of 0.1M with respect to LLA. Quenching after 60 min. [a] equivalents of NBE with respect to NBM monomer. [b] equivalents of NBM with respect to Grubbs-II initiator. [c] theoretical molecular weight of side chains assuming 100% conversion of LLA monomer deriving exclusively from NBM initiated chains. [d] theoretical molecular weight assuming 100% conversion of NBM monomer and 100% conversion of LLA monomer. [e] determined *via* GPC against PSt standards.

As a second option to lower the suspected steric bulk, polymerizations were then conducted with the inclusion of "spacer" monomers. These spacers are un-functionalized norbornene (NBE) monomers, incapable of initiating ROP. By inclusion of these spacers, the distance between adjacent side chains is increased. Polymerization of entry **10** was conducted with a polymerization mixture including 0.5 equivalents of unfunctionalized NBE (with

respect to NBM monomer). In contrast to the earlier experiments, the isolated polymer had a molecular weight (11000 g.mol^{-1}) exceeding that expected of a single side chain (3000 g.mol^{-1}), but falling far short of the expected bottlebrush molecular weight. The GPC trace of this product was asymmetric and lacked the bimodal distribution observed in the previous polymerizations. Entry **11** was conducted with a 1:1 ratio of NBE to NBM and entry **12** had a 2:1 NBE:NBM monomer feed. The polymerizations with larger NBE ratios surprisingly showed lower average molecular weights, but retained the asymmetric peak shape observed for **10**. The asymmetric, yet monomodal peak shape may be explained by a preferential homopolymerization of NBE ROMP over a statistical incorporation of NBM and NBE monomers. Such behavior is well-documented for ROMP of norbornene derivatives[174]. The observed peak shape could therefore correspond to a mixture of PNBE, PLLA and potentially NBM-*g*-PLLA oligomers.

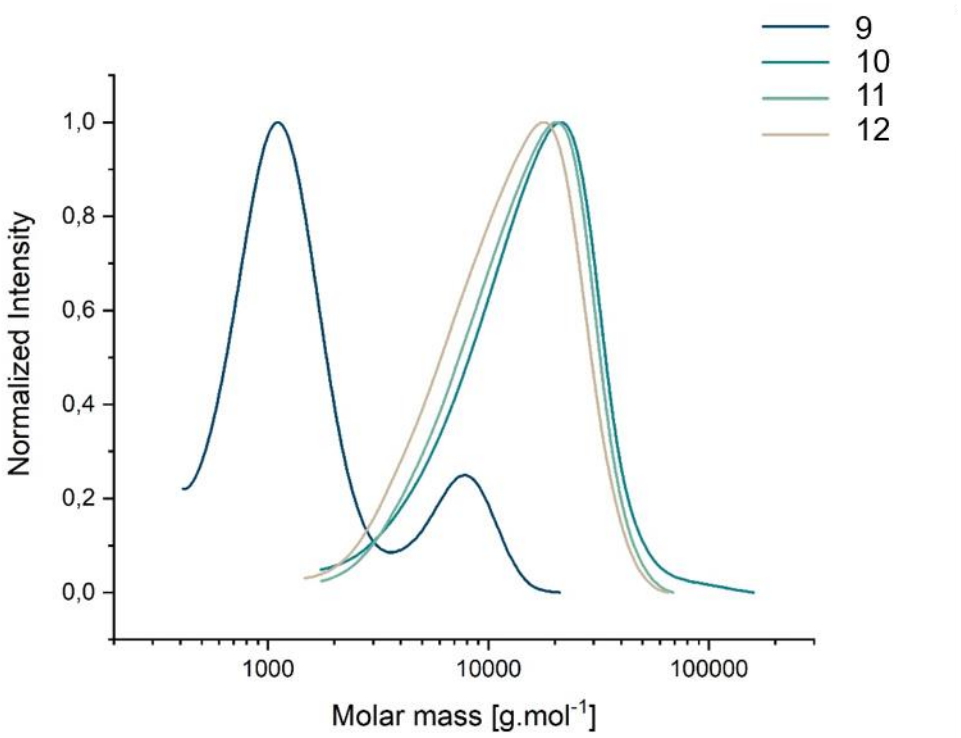

Figure 2-9: GPC traces in THF *versus* PSt standards of polymers synthesized through simultaneous tandem grafting with spacers.

2.4.3 Impact of Metathesis Catalyst

As neither the shorter side chains nor the use of spacers led to significant improvements in the ROMP conversion. It was theorized that the ROP of LLA might occur at a much faster rate than the ROMP of NBM. As a consequence, the side chains would grow rapidly, leading to high steric bulk even at low NBM conversions. This "simultaneous" system would therefore show much more grafting-through character. With grafting-through characteristics, the system would likely suffer from the same issues such as incomplete backbone polymerization and high steric challenges (see above). Likewise, the short polymerization times would see all LLA monomer consumed, while NBM reached only low conversion. To counter this effect, it was attempted to increase the rate of ROMP by altering reaction conditions and metathesis catalysts.

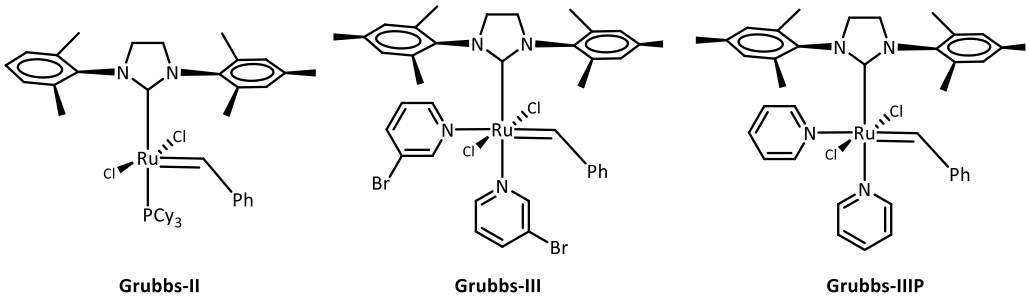

Chart 2-3: overview over metathesis catalysts employed to increase the rate of ROMP. The Second Generation Grubbs catalyst (Grubbs-II), The Third Generation Grubbs catalyst (Grubbs-III), and its pyridine analogue (Grubbs-IIIP).

Among the large range of metathesis catalysts, the superior functional group tolerance of Grubbs-type over Schrock-type catalysts, inspired the decision to limit experiments to Grubbs-type catalysts. Additionally, the Hoveyda-Grubbs catalysts, despite their superior moisture, oxygen and thermal stability, have far slower rates of initiation than their non-chelated analogues[175,176]. The First Generation Grubbs catalyst (Grubbs-I) was not considered for the tandem system at hand, as the SIMes catalyst would rapidly displace one equivalent of phosphine ligand and thus effect the transformation from Grubbs-I to Grubbs-II. This ligand exchange was employed by GRUBBS et al.[177] when first synthesizing Grubbs-II. Instead, owing to its excellent stability tolerance of functional groups and fast initiation rates[50], the Third Generation Grubbs catalyst (Grubbs-III) was employed. Indeed it has been shown that the initiation rate of Grubbs-III is at least six orders of magnitude faster than that of Grubbs-II[176]. Grubbs-III has also been shown to be more effective in the polymerization of macromonomers than its Second Generation predecessor[178]. Additionally, a pyridine analogue to Grubbs-III, the catalyst Grubbs-IIIP was synthesized according to a method

reported by GRUBBS and coworkers[179]. The pyridine ligands of metathesis catalyst Grubbs-IIIP are particularly labile, allowing for fast initiation.

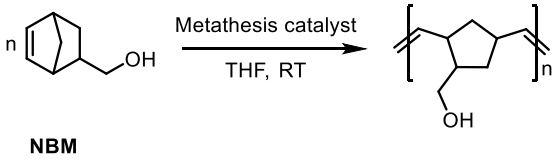

NBM

Scheme 2-5: Homopolymerizations of NBM monomer by metathesis catalysts Grubbs-II, Grubbs-III and Grubbs-IIIP.

Table 2-4: Homopolymerizations of NBM with different metathesis catalysts.

Entry	Catalyst	Temp. [°C]	Time [min]	Mn $_{theo}$ [g·mol-1]	Mn $_{exp}$[a] [g·mol-1]	Conversion[b]	PDI[c]
3	Grubbs-II	RT	60	12 400	8 100	98%	1.34
4			90		11 500	97%	1.33
13	Grubbs-II	60	60	12 400	6 000	95%	2.13
14			90		11 300	98 %	1.44
15	Grubbs-III	RT	60	24 800	19 400	100%	1.37
16			90		19 500	100%	1.38
17	Grubbs-IIIP	RT	60	12 400	13 900	85%	1.06
18			90		16 300	100%	1.07

Homopolymerizations of 100 eq. NBM with respect to initiator conducted in dry THF at 0.01 M monomer concentration). [a] determined *via* GPC in THF *vs.* PSt standards. [b] determined *via* ^{1}H NMR.

First, homopolymerizations of NBM monomer were conducted using the catalysts Grubbs-IIIP, Grubbs-II and Grubbs-III. The results are summarized in Table 2-4. Conducting ROMP of NBM at elevated temperatures led to a broadening of dispersities. While room temperature polymerization yielded polymers with dispersities of 1.33 and 1.34, the elevated temperatures led to polymers with a PDI of 1.44-2.13. This broadening of molecular weight distributions is well-documented for ROMP and occurs due to increases in side reactions[180]. While polymerization was incomplete even after 60 min and 90 min at RT, for both room temperature and elevated temperature polymerizations with Grubbs-II. In both temperature regimes, the experimentally established molecular weights remained lower than the targeted weights. At room temperature, the 8 100 g.mol^{-1} determined after 60 min and the elevated temperature polymerization product with 6 000 g.mol^{-1} were below the expected 12 400 g.mol^{-1}. However at longer polymerization times, the 11 500 g.mol^{-1} and 11 300 g.mol^{-1} for room temperature and elevated temperature polymerization respectively were only marginally lower than the theoretical molecular weight.

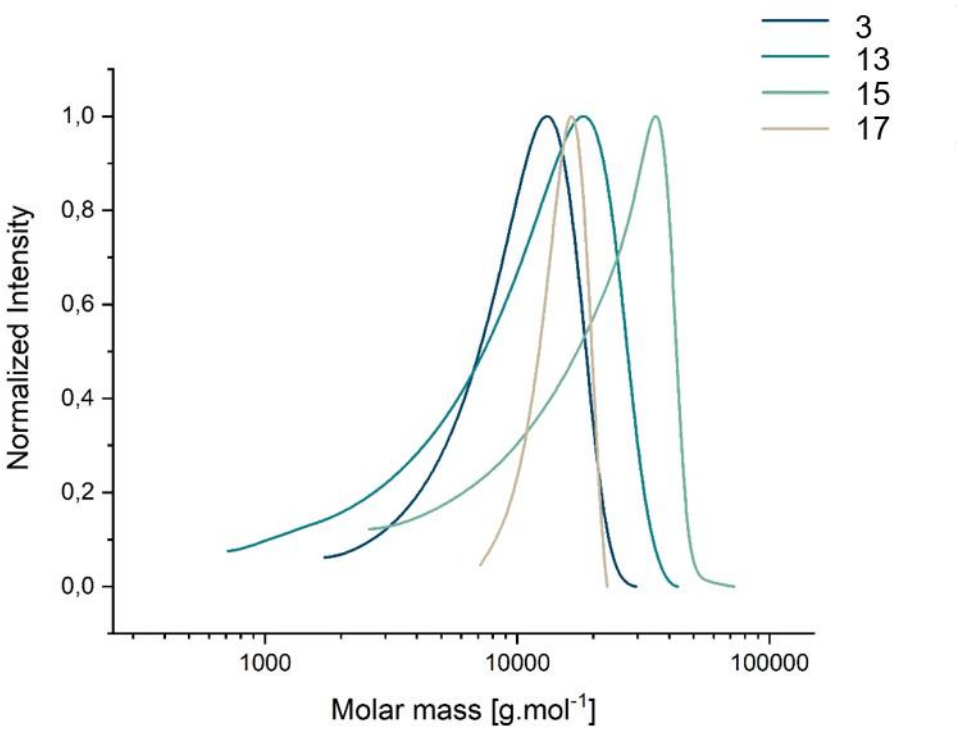

Figure 2-10: GPC traces of homopolymerizations of NBM with different metathesis catalysts, in THF *versus* PSt standards.

The fast initiating Grubbs-III catalyst reached full conversion within 60 min, indicating faster polymerization rates than for the Grubbs-II catalyst. The dispersities of 1.37 and 1.38 after 60 min and 90 min respectively are still elevated in comparison to the low dispersities frequently reported in literature. Experimentally established molecular weights after 60 min and 90 min were 19 400 g.mol^{-1} and 19 500 g.mol^{-1} respectively and lower than the expected 24 800 g.mol^{-1}. The Grubbs-III derivative Grubbs-IIIP reached 100% conversion within 90 min with much lower dispersities (1.06 and 1.07) than achieved with the other catalysts (1.37 and 1.38 for Grubbs-II and 1.33-2.13 for Grubbs-II). The theoretical molecular weight also matched those found *via* GPC. At 100% conversion, GPC established a M_n of 16 300 g.mol^{-1} with a theoretically expected molecular weight of 12 400 g.mol^{-1}. The differences in dispersities are reflected by the shapes of the GPC traces (see Figure 2-10). The most narrowly distributed polymer **17** has a symmetrical peak shape. The polymerizations by Grubbs-II and Grubbs-III all show low molecular weight tailing.

Table 2-5: Simultaneous tandem grafting of NBM and LLA by SIMes and metathesis catalysts Grubbs-IIIP and Grubbs-III

Entry	Catalyst	Time[a] /min	Eq. LLA[b]	$M_{n\ theo}$ [c](graft) /g.mol^{-1}	$M_{n\ theo}$ [d](brush) /g.mol^{-1}	$M_{n\ exp}$ [e] /g.mol^{-1}	PDI[e]
19	Grubbs-IIIP	15	50	7 300	730 000	10 500	1.35
20		60	50	7 300	730 000	12 700	1.23
21	Grubbs-III	60	20	3 000	300 000	4 800	1.60
22		15	45	6 600	660 000	4 500	1.22

Polymerizations conducted in THF at a concentration of 0.1M with respect to LLA. Targeted backbone DP 100 units of NBM. [a] reaction time before quenching with EVE and TFA. [b] equivalents of LLA with respect to NBM. [c] theoretical molecular weight of side chains assuming 100% conversion of LLA monomer deriving exclusively from NBM initiated chains. [d] theoretical molecular weight assuming 100% conversion of NBM monomer and 100% conversion of LLA monomer. [e] determined *via* GPC against PSt standards.

The two catalysts were then employed for the tandem system. The results of these tandem reactions are presented in Table 2-5. The simultaneous polymerizations involving metathesis catalyst Grubbs-IIIP led to a polymeric product with a monomodal GPC trace (see Figure 2-11). The experimentally established weights were greater than expected for a single graft chain (10 500 g.mol^{-1} and 12 700 g.mol^{-1} compared to the theoretical weight of 7 300 g.mol^{-1}) but far lighter than would be expected for a bottlebrush structure (730 000 g.mol^{-1}). PDIs were between 1.23 and 1.35. The ^{1}H NMR spectrum showed no PNBM specific signal. However for bottlebrush structures, lacking backbone signals have been reported due to very long relaxation times of the backbone protons.[181]

In contrast, the Grubbs-III polymerized products showed the distinctive bimodal trace observed previously for the Grubbs-II catalyst. Entry **21** with 20 equivalents of LLA showed a much greater polydispersity at 1.60 than the 45 eq. LLA product, **22** with a PDI of 1.22. The isolated polymers were much lighter than the expected bottlebrushes. Entries **21** and **22** had similar molecular weights with 4 800 g.mol^{-1} and 4 500 g.mol^{-1} respectively, while a theoretical molecular wight for bottlebrushes would be expected at 300 000 g.mol^{-1} and 660 000 g.mol^{-1}. Overall, the change of catalysts did not result in the desired improvements of full backbone conversion and high molecular weights.

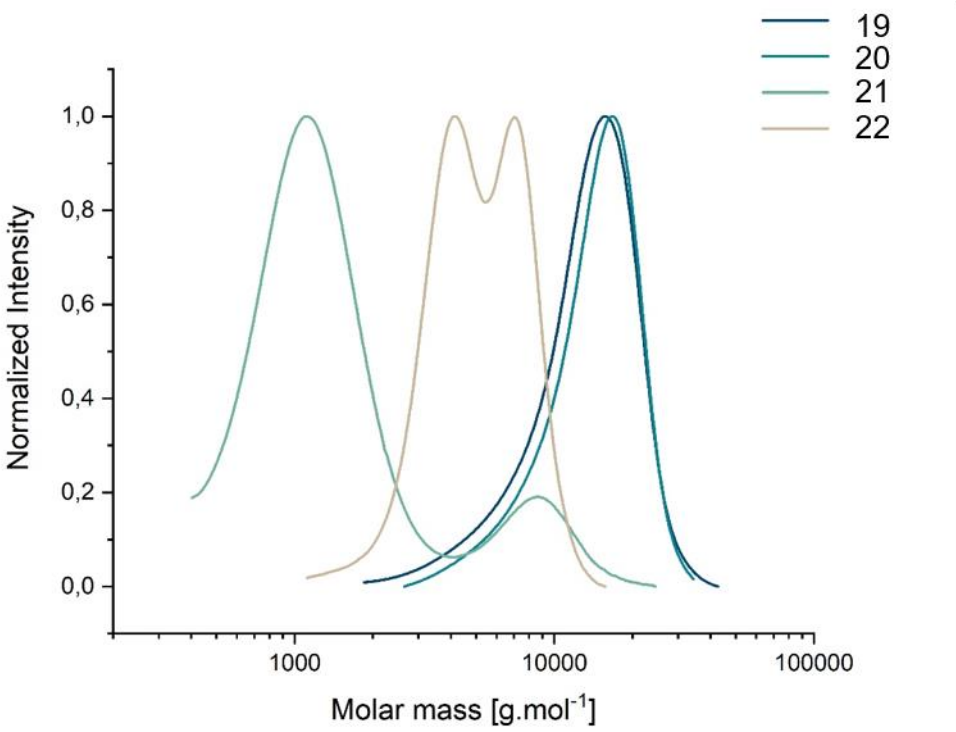

Figure 2-11: GPC traces of polymers produced by simultaneous tandem grafting using different metathesis catalysts. Elution medium THF *versus* PSt standards.

2.4.4 Impact of Inimer

Despite the promising findings by FREUDENSPRUNG et al.[162] and the theoretical insight provided by GUIRONNET et al.[166], the above results clearly show that the orthogonal combination of ROMP and ROP for the synthesis of molecular bottlebrushes is anything but trivial. Neither the inclusion of spacers nor changes in metathesis catalysts or targeted DPs resulted in satisfactory ROMP performance. The preliminary NMR experiments should have ruled out any mutual interference between the monomers and catalysts. Therefore, the difficulties observed herein must be due to interferences intrinsic to the *simultaneous* nature of the polymerization, i.e. the interferences must derive from species present in the actively polymerizing mixture. As the ROP seems to proceed without interferences, the tandem issues can be pin-pointed to interferences of active ROP intermediates with the ROMP catalyst. The active ROP reaction mixture is distinct from the preliminary NMR studies and the work of FREUDENSPRUNG by the presence of a) carbonyl-containing macromonomers and b) the reaction intermediaries arising from SIMes interaction with (i) the cyclic lactone or (ii) the norbornenyl-monomer.

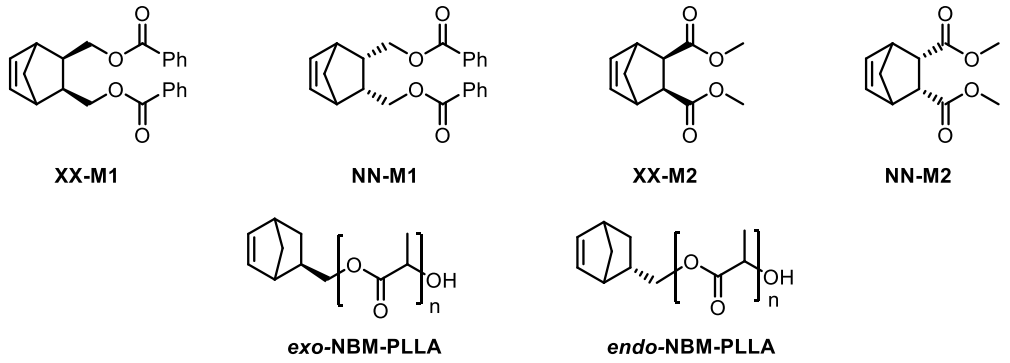

Chart 2-4: Substrates studied by Guironnet et al.[166] via DFT modeling to assess the potential for complexation with Ru-center. XX-M1 and its stereo-isomer NN-M1 are unlikely to complex to Grubs-type catalysts and have fast polymerization rates. Compound XX-M2 does not complex, while NN-M2 does. The growing inimer-chains are structurally related to the model compounds XX-M1 and NN-M1 and should therefore not complex.

Despite their otherwise excellent functional group tolerance, Grubbs-type catalysts, are sensitive to strong LEWIS bases[153]. Moreover, even substrates bearing mild LEWIS bases like carbonyl groups can be problematic and show slow reaction rates, depending on their substitution pattern and capability to chelate with the active Ru center[166,182]. Slow polymerization rates could therefore stem from the growing polyester chains pendant off the backbone monomer. Substrates that are capable of forming five- or six-membered rings with the ruthenium center (similar to the HOVEYDA-GRUBBS catalysts see Chart 1-3) are particularly unfavorable[166]. The ability of this macromonomer carbonyl to chelate depends on its three-dimensional orientation during polymerization resting states. These are dependent on the regio-isomerism of the backbone monomer. Norbornenyl-derived monomers (such as NBM) exist as two regio-isomers: *exo*- or *endo*-functionalized. The former is well-known to react more rapidly than the latter for a range of monomers[50,166]. MATSON et al.[183] conducted thorough investigations to assess the impact of backbone monomer structure on grafting-through polymerization rates of polyester macromonomers. The group used density functional theory (DFT) calculations of exclusively *exo*-norbornenyl substrates to act as models for macromonomers and contrasted observed polymerization rates with their ability to chelate through carbonyl groups in their resting states. The results indicated that macromonomers derived from *exo*-NBM should polymerize rapidly. Additionally GUIRONNET and coworkers [166] recently refined the insight provided by MATSON by studying the energy landscapes of intermediates in the polymerization mechanism of similar substrates for both *exo*- and *endo*-isomers. Their DFT calculations and kinetic modelling showed that for the model substrates XX-M1 and NN-M1 (see Chart 2-4), the ability to chelate is low and does not depend on stereo-isomerism. As a consequence, for NBM-derived macromonomers, both *exo*- as well as *endo*- isomers should rapidly polymerize.

Additionally, reports of Grubbs-type catalysts readily polymerizing macromonomers[184] of various lengths to yield dense BBs further discredit hypothesis a).

As for hypthesis b), the mechanistic studies of NHC-catalyzed ROP of cyclic lactones has clearly been shown to proceed *via* a hydrogen-bonding mechanism rather than a nucleophilic pathway in the presence of primary alcohols. It can therefore be concluded that the interaction of SIMes with the inimer is the most likely source of the unsuccessful ROMP. However, the hydrogen-bonding mechanism might indeed cause issues in the ROMP of NBM. The SIMes catalyst activates the primary alcohol towards nucleophilic attack of carbonyl groups. In particular, the *endo*- isomer could form a stable six-membered ring, as demonstrated by GUIRONNET et al.[166] In the commercial monomer employed so far, the *exo*- *vs. endo*- content is relatively low with a ratio of 1:2 respectively. The SIMes-induced activation of *endo*-NBM could thus be the cause of the Grubbs-catalyst deactivation observed in the experiments above.

To investigate this effect, it was decided to conduct tandem polymerizations with *exo*-enriched NBM (*exo*-NBM). For this purpose, *exo*-enriched NBM monomer was synthesized according to a route described by KANAO et al.[172]. ^{1}H NMR analyses confirmed that the stereo-selective hydrolysis led to an improvement of the *exo:endo* ratio from 1:2 in the commercial source to 3.5:1 (see Figure 2-12).

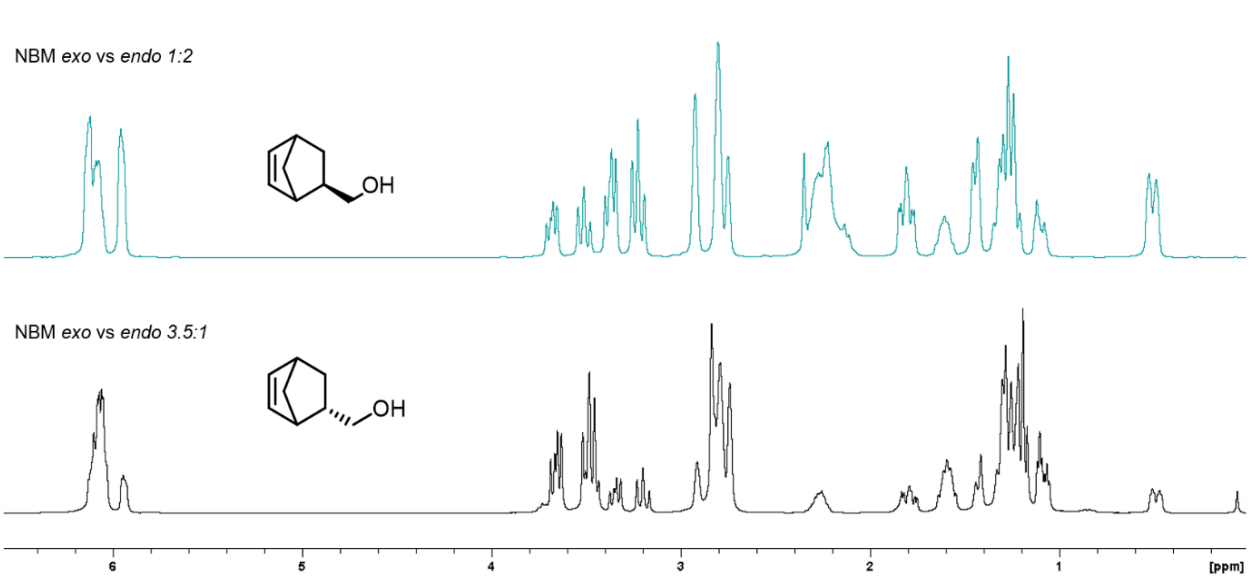

Figure 2-12: Comparison of ^{1}H NMR spectra of commercial NBM monomer with a distribution *exo:endo* ratio of 1:2 (top) and the synthesized monomer *exo*-NBM with a *exo:endo* ratio of 3.5:1 (bottom). Recorded in $CDCl_3$ at 300 MHz.

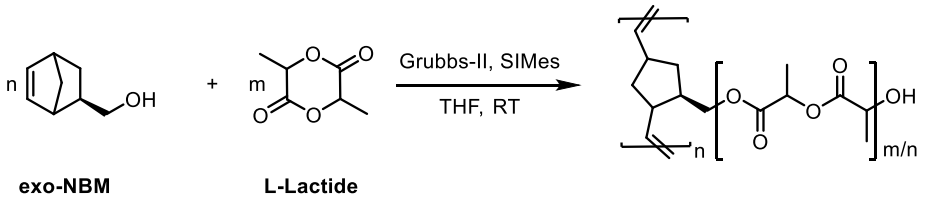

Scheme 2-6: Simultaneous tandem grafting of *exo*-enriched monomer *exo*-NBM and LLA.

Table 2-6: Simultaneous tandem grafting with *exo*-enriched NBM, monomer *exo*-NBM

Entry	Eq. LLA[a]	Eq. NBM[b]	time /min	Mn $_{theo}$ [c](graft) /g.mol^{-1}	Mn $_{theo}$ [d](brush) /g.mol^{-1}	Mn $_{exp}$ [e] /g.mol^{-1}	PDI[e]
23	50	20	15	7 300	146 000	3 500	2.24
24			45			8 000	4.57
25	80	10	15	11 700	117 000	12 500	2.06
26			45			14 600	2.94
27	100	200	15	14 500	2 900 000	13 500	1.30
28			45			10 500	1.37
29	200	5	15	29 000	145 000	14 800	1.25
30			45			16 400	1.80

Employing a higher content of *exo*-NBM, led to a marked change in the GPC traces of isolated polymers. With all targeted backbone and sidechain DPs, bimodal or trimodal distributions were observed (see Figure 2-13). In addition, the lighter fraction of the bimodal GPC traces closely matched the expected molecular weights of the targeted side chains (see Table 2-6). The large contrast in molecular weights between lighter fraction and heavier fraction allowed to individually integrate the two peaks. These results are shown in Table 2-7. For e.g.: entry **27**, the expected side chain molecular weight was 14 500 g.mol^{-1} which compared particularly well with the molecular weight of the lighter polymer fraction with 13 500 g.mol^{-1}. Polydispersities for the lighter fractions (assumes side chains) ranged from 1.25 to 1.37. The heavier fractions showed a number average molecular weight around 10-40 times heavier than the lighter fractions. For **27**, the lighter fraction had a M_n of 13 500 g.mol^{-1} while the heavier fraction had an M_n of 110 300 g.mol^{-1} and a PDI of 1.17. The lighter polymer fraction of entry **28** was 10 500 g.mol^{-1}, while the heavier fraction had a M_n of 462 400 g.mol^{-1}. If the lighter fraction represents PLLA homopolymer derived from initiation by NBM, the heavier fraction could then be a ROMP product of the NBM-PLLA macromonomers. In that case, the degree of polymerization for the backbone of polymer **28** would be ~44. Such a reading is supported by considering the ^{1}H NMR spectra of the products. ^{1}H NMR analyses showed the characteristic shifts expected from poly(NBM) protons. So even

with a large portion of homopolymeric side chains remaining in the polymerization mixture, significant improvements in ROMP conversion could be made. Therefore, the use of *exo*-enriched monomer helped mitigate the unfavorable catalyst interferences. However, full conversion could not be achieved. It was stipulated that the residual *endo*-monomers might still interfere with the Grubbs-catalyst. With the large excess of inimer concentration over catalyst concentration, this effect remains pertinent even with the enriched monomer.

Table 2-7: Separately integrated molecular weight distributions of polymer products using monomer *exo*-NBM

Entry	Mn_{theo} [c] (graft) /g.mol^{-1}	Mn_{exp} [e] (graft) /g.mol^{-1}	PDI[e] (graft)	Mn_{theo} [d] (brush) /g.mol^{-1}	Mn_{exp} [e] (brush) /g.mol^{-1}	PDI[e] (brush)
27	14 500	13 500	1.30	2 900 000	110 300	1.17
28	14 500	10 500	1.37	2 900 000	462 400	1.24
29	29 000	14 800	1.25	145 000	107 000	1.21

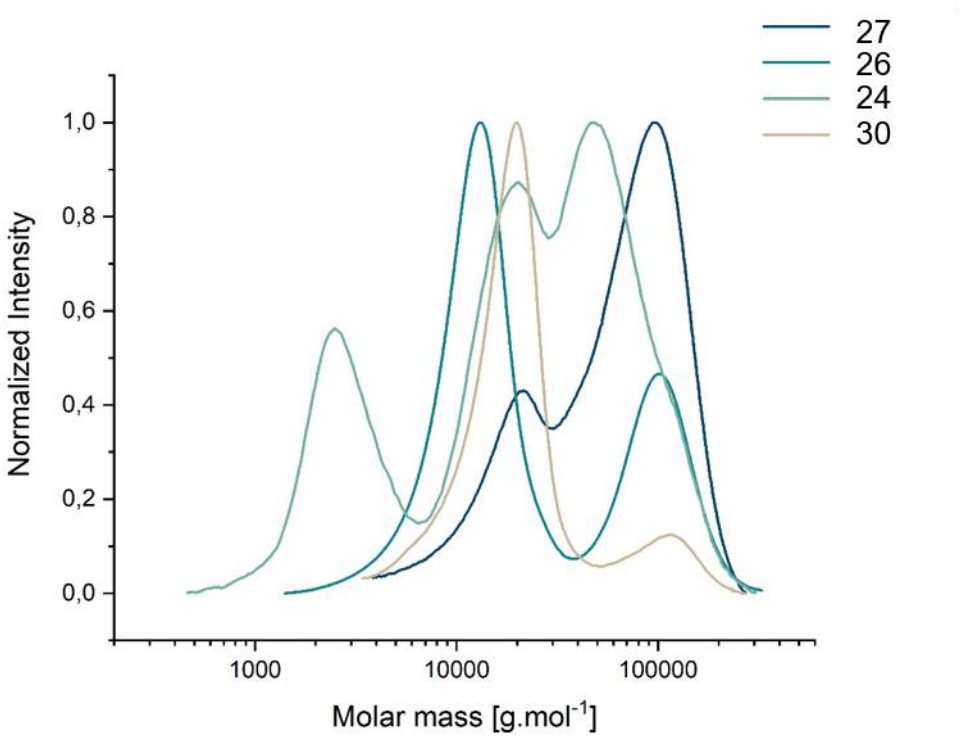

Figure 2-13: Simultaneous tandem grafting of *exo*-enriched NBM led to multimodal distributions. GPC traces in THF *versus* PSt standards.

2.4.5 Monomer Design

For successful tandem grafting, the rates and conversion of ROMP must be improved to match the rates of ROP or else the rate of ROP slowed down. The polymerizations with *exo*-enriched backbone monomer did not lead to full conversion but the improvements in conversion allow to flag the nucleophilic interactions of SIMes-activated monomer with Grubbs-catalyst as the likely origin of the issues encountered so far. This points towards the possibility to establish a successful tandem system by help of monomer modification. Clearly backbone monomer reactivity should be as high as possible to achieve higher conversions. Additionally, the *endo*- interactions stipulated above should be suppressed completely, either by employing isomerically pure *exo*-monomers or by controlling accessibility of activated alcohols towards the active ruthenium center, or a combination thereof.

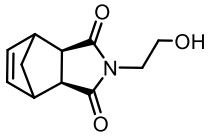

N-(hydroxyl ethyl)-
cis-5-norbornene-exo-
2,3-dicarboximide

HONDC

Chart 2-5: Backbone monomer N-(hydroxyl ethyl)-cis-5-norbornene-*exo*-2,3-dicarboximide (HONDC)

Chart 2-5 shows the backbone monomer designed to fulfill the requirements listed above. Several considerations motivated the introduction of the succinimide functionality. On one hand, it was previously shown that tricyclic norbornene dicarboxamides are highly active in ROMP due to their high ring strain. Polymerizations yield high molecular weight polymers with relatively low dispersities, even when employed in grafting-through polymerizations[46]. Furthermore, stereo-isomeric isolation is facile with this monomer, as the succinimide ring can exclusively form from *cis*-isomers. Simple recrystallization allows to isolate undesired isomers, leading to isomerically pure monomer feed. High monomer purity is crucial for BB synthesis[144]. The ability to isolate pure *exo*-monomer is a further important factor to avoid steric bulk, as well as for the reactivity desired herein. The structurally related, *endo*-oxanorbornenes have been shown to undergo single addition to a metathesis initiator, while *exo*-oxanorbornenes rapidly polymerize.[185]

The succinimide motif was chosen over a maleimide motif to account for the latter's affinity towards MICHAEL addition. Maleimide and its derivatives have been found to polymerize *via* conjugate addition in the presence of NHC's[143]. As such interactions would be disadvantageous for the application at hand, a succinimide motif was chosen. Finally, the hydroxyl group was introduced with a variable spacer. By help of this spacer, the hydroxyl

functionality is farther removed from the active site of polymerization during the stationary point after [2+2] cycloaddition. Chelation of activated alcohol and ruthenium in the stationary point would require formation of an entropically unfavorable nine-membered ring. As a consequence, it is expected that even with NHC activation, interference with the ruthenium center is minimized. A potential disadvantage of the monomer design is the possible interaction of the two carbonyl group with the ruthenium center. However, DFT calculations showed that at 298 K, the enthropic penalty for chelation greatly mitigates the enthalpic contribution, leading to an overall GIBBS free energy change of +0.1 kcal.mol^{-1} when chelated to Grubbs-type catalysts[182,183]. Therefore, chelation through the carbonyl - although possible - is unfavorable for the monomer design shown above.

Subsequently, the monomer was synthesized according to a procedure reported by REN et al.[186] from ethanolamine and *cis*-5-norbornene-*exo*-2,3-dicarboxylic anhydride. The synthesis was both straight forward and produced good yields (80%). Monomer identity and isomer purity were confirmed by NMR techniques, elemental analysis and mass spectrometry. Figure 2-14 shows the assigned ^{1}H NMR spectrum. The axial symmetry of monomer HONDC and its isomeric purity account for the single olefin peak (a) observed at 5.77 ppm. The hydroxyl proton (e) at 1.59 ppm shows the triplet fine structure expected from coupling with the neighboring protons (g) at 3.44 ppm. The bridging protons (c) are restricted

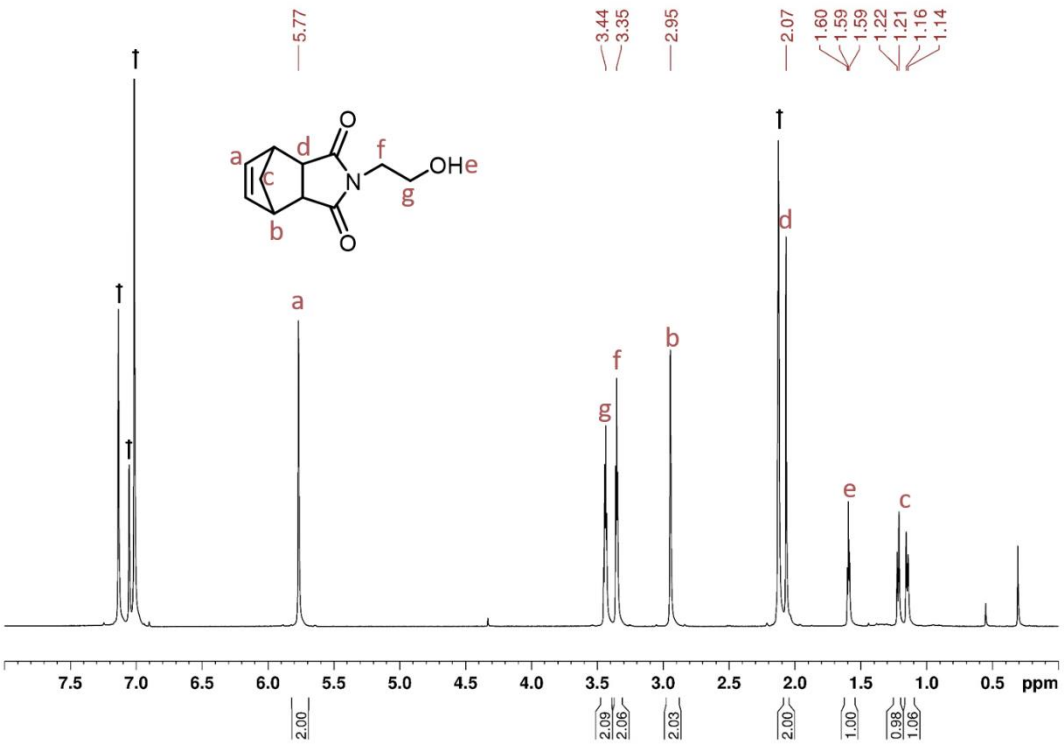

Figure 2-14: ^{1}H NMR spectrum of norbornenyl monomer HONDC recorded with a 700 MHz spectrometer in in toluene-d_8.

in their mobility and therefore show two different doublets at 1.21 ppm and at 1.15 ppm. Impurities from vacuum grease produced a signal at 0.20 ppm.

Table 2-8: Test reactions using the backbone monomer HONDC.

	LLA	HONDC	Mn_{theo} graft	Mn_{theo} BB	Mn_{exp}	PDI_{exp}
	Eq.	eq.	$g.mol^{-1}$	$g.mol^{-1}$	$g.mol^{-1}$	
31	N/A	100	N/A	20 700	15 800	1.16
32	10	100	1 600	160 000	8 200	2.24
33	30	N/A	4 300	N/A	6 000	1.44

Homopolymerizations of backbone monomer HONDC (see entry **31** of Table 2-8) were conducted in THF with Grubbs-III catalyst as previous investigations on similar substrates showed faster kinetics and narrower molecular weight distributions over other metathesis catalysts[153]. The polymerization yielded full conversion within minutes to produce a poorly soluble solid. The polymer dissolved in DMF with hexafluoroisopropanol (HFIP) due to strong hydrogen bonding. GPC analysis in DMF characterized a polymer with M_n of 15 800 $g.mol^{-1}$ and a dispersity of 1.16. ^{1}H NMR analyses confirmed that the monomer underwent ROMP as

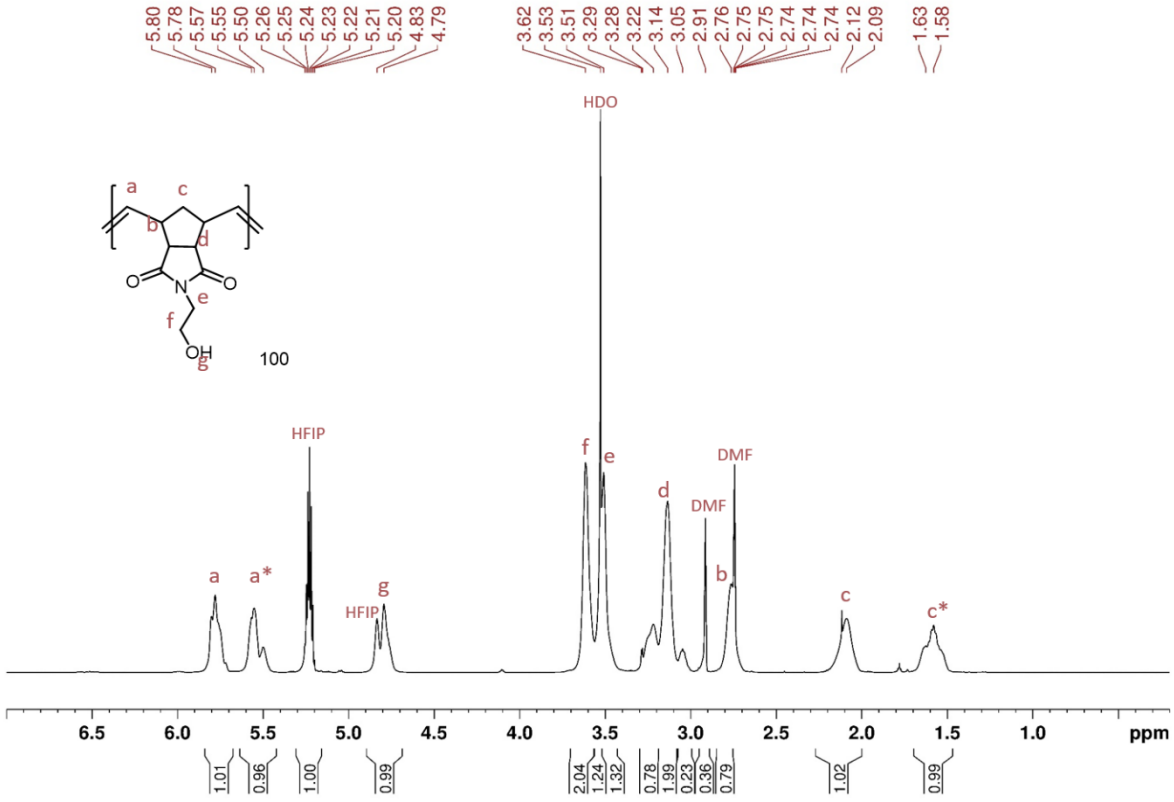

Figure 2-15: Representative ^{1}H NMR spectrum of homopolymer **31** in DMF-d_7 and HFIP (0.1% V/V) recorded on a 700 MHz Spectrometer.

expected, resulting in an unsaturated polymer with a *ca.* 1:1 ratio of *trans:cis* orientation. Likewise, Homo-ROP was conducted with LLA and HONDC as initiatior (see **33** of Table 2-8). GPC analysis revealed a M_n of 6000 g.mol^{-1} which is slightly heavier than the expected M_n of 4300 g.mol^{-1}.

With the new HONDC backbone monomer, simultaneous tandem grafting was attempted, using L-lactide in THF and the two catalysts SIMes and Grubbs-III (see entry **32** of Table 2-8). The expected improvements in conversion of the backbone polymerizations could not be observed. The isolated polymer had a M_n of only 8 200 g.mol^{-1} and a broad PDI of 2.24. The new backbone monomer failed to bring about the expected improvements in ROMP performance. It was previously established that metathesis reactions are sensitively dependent on the solvent in which they are conducted. WAGENER and coworkers[187] investigated the impact of solvent choice on alternating ADMet performance. While polymerizations conducted in dichloromethane resulted in high molecular weight polymers, THF was found to hinder the polymerization. The ability of THF to coordinate towards Grubbs-type catalysts was found to lead to lower conversions. Unfortunately, dichloromethane is an unsuitable solvent for the application at hand (*vide supra*) but the WAGENER group also established toluene to be an excellent solvent choice for challenging metathesis reactions[187]. While toluene dissolves both SIMes and Grubbs-type catalysts readily, neither L-lactide nor backbone monomer HONDC are readily soluble in room temperature toluene.

2.4.6 Impact of NHC catalyst

As has previously been discussed, the rates of polymerization in side chain ROP and backbone ROMP need to match in order to present a truly simultaneous process. In order to achieve that, ROMP parameters can be tuned to afford faster ROMP or the ROP paramters can be tuned to slow down the side chain polymerization. Having investigated the parameters temperature, backbone monomer, side chain length, grafting density, ROMP catalyst and temperature to increase ROMP rates, without achieving the desired results, it was therefore decided to slow down the rate of ROP to match the inefficient ROMP. Slower rates of ROP can be achieved either by lowering the L-lactide concentration or by altering either monomer or catalyst. Lower concentrations of L-lactide would by necessity imply even lower concentrations of backbone monomer. However as ROMP is highly sensitive to initial monomer concentrations[49], such an approach would not be beneficial. Alternatively, an L-lactide solution could be added at intervals over the course of the polymerization. However, it is unclear whether such an approach could still be considered a simultaneous

polymerization. Finally, the option of tuning the polymerization rate by employing a slower-polymerizing catalyst was explored. Among the multitude of NHCs capable of polymerizing L-lactide, a suitable candidate had to be established.

Certain limitations exist concerning the combined employment of NHC and metathesis catalysts. When FOGG et al.[188] explored the synthesis of Grubbs-type catalysts featuring NHC ligands with lower steric bulk, they observed ultra-fast catalyst decomposition. It was found that truncated NHCs are particularly efficient as quenching agents for Grubbs-I type catalysts. Even at -80 °C, full conversion of Grubbs-I derivative to a new complex incapable of participating in ROMP was achieved within minutes. Likewise, the second generation derivative was rapidly decomposed. Particularly in a grafting scenario where the concentration of metathesis catalyst is particularly low with respect to ROP catalyst, such combinations must be avoided. Therefore NHCs with low steric bulk cannot be combined with metathesis catalysts for this application.

Scheme 2-7: Reversible adduct formation of inimer HONDC with NHC catalyst DTT to yield the latent pre-catalyst (HONDC-adduct).

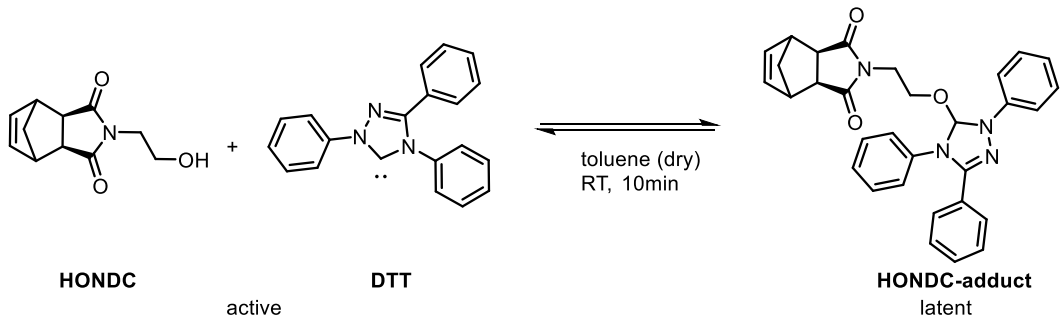

Coulembier et al. [163] have established the latent, thermally activated 1,3,4-triphenyl-4,5-dihydro-1H-1,2-triazol-5-ylidene carbene (DTT, see) as an attractive ROP catalyst with slower rates of propagation than SIMes. The three phenyl groups were expected to represent sufficient steric bulk to avoid the rapid decomposition pathway described above. Enticingly, the triazole forms a reversible adduct with alcohols. At elevated temperatures, the adduct dissociates and initiates polymerization (see). This association-dissociation equilibrium has three significant advantages for the application at hand. First, the adduct has been found to be less sensitive to oxygen and moisture than SIMes. Second, the adduct acts as a temporary protective group towards the hydroxyl functionality, avoiding potential chelation with the ROMP catalyst. And third, due to the phenyl groups of the NHC, the HONDC-DTT adduct readily dissolves in toluene.

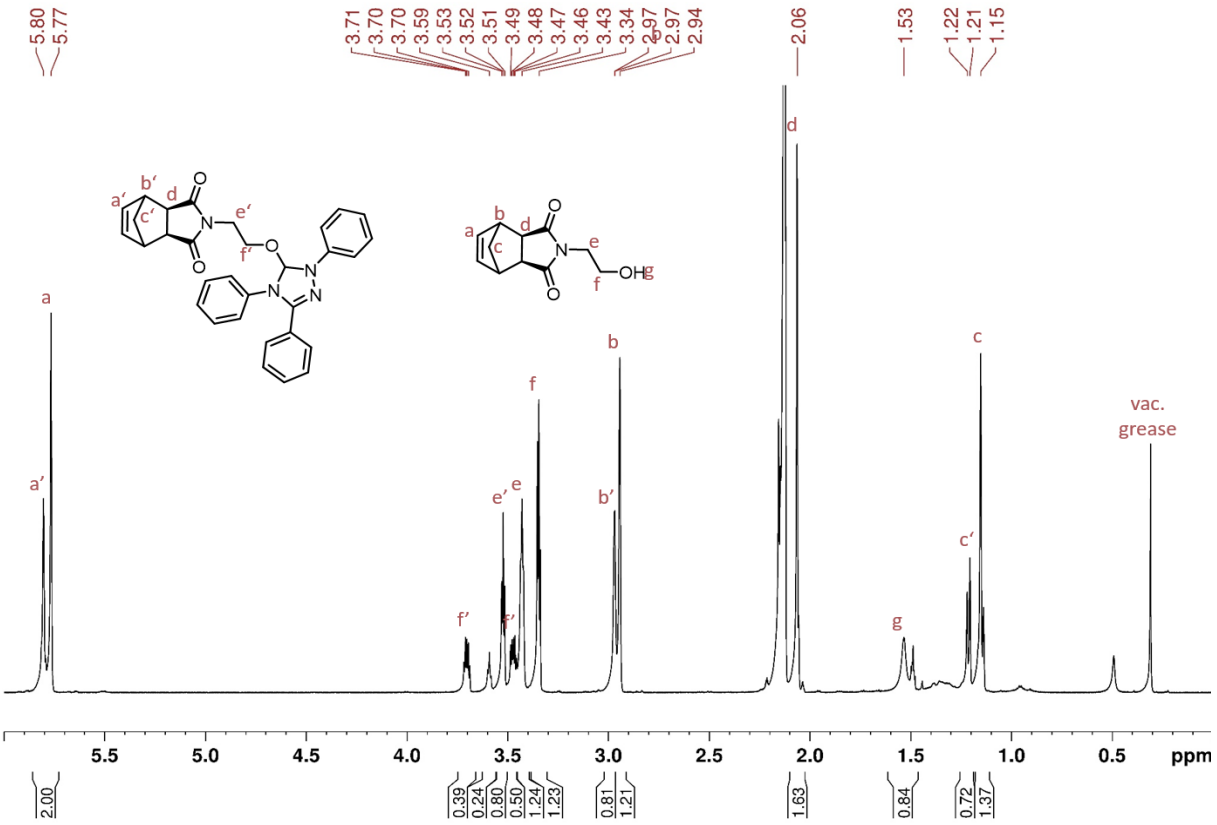

Figure 2-16: ^{1}H NMR spectrum (700 MHz, toluene-d_8) of monomer-DTT adduct HONDC at RT.

When combining triazol DTT (1 eq.) and inimer HONDC (1 eq.) in toluene, first a suspension was formed. Upon stirring for 10 min, all solids were dissolved and a pale yellow solution formed. Even at concentrations up to 0.2 M, the backbone monomer could be fully dissolved in toluene. ^{1}H NMR, ^{13}C NMR, HMBC, HSQC and NOESY experiments were conducted in deuterated toluene to elucidate the adduct structure. The ^{1}H NMR spectrum in shows the equilibrium population of adduct HONDC-adduct and free inimer. The adduct methylene signals are shifted significantly downfield. Particularly signal **f** at 3.34 ppm is split and shifted to **f'** at 3.46 ppm and 3.71 ppm. The vicinal protons are shifted to a lesser extend from **e** at 3.43 ppm to **e'** at 3.53 ppm. Interestingly, even the alkene protons are minimally shifted downfield from **a** at 5.77 ppm to **a'** at 5.80 ppm. Nonetheless, the integrity of ring structure and double bond is not impacted by the adduct formation.

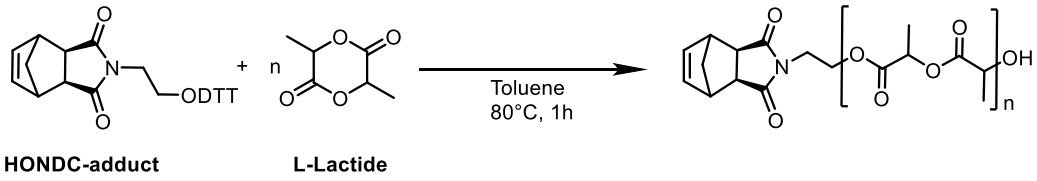

Scheme 2-8: Ring Opening Polymerization of L-lactide initiated by HONDC and DTT.

Homopolymerizations of L-lactide were conducted, employing HONDC as initiator and the NHC DTT as catalyst according to Scheme 2-8. The homopolymerization of L-lactide by pre-formed adduct produces narrowly dispersed, norbornene functionalized polylactide when polymerized at 80 °C for 60 min (see Table 2-9). Dispersities ranged between 1.20 for entry **34** and 1.30 for entry **35**. ^{1}H NMR spectra of the reaction solution showed the near quantitative conversion of monomer after 1 h. Conversions of LLA monomer (conv $_{LLA}$) were calculated according to Equation 2-3, where the numerator is the integral of PLLA methine proton and denominator is the sum of integrals of methine proton of closed LLA monomer and polymer.

Table 2-9: Macromonomers synthesized via DTT mediated ROP of L-lactide.

Entry	$[LLA]_0/[HONDC]_0$	Conv.	Mn $_{theo}$ /g.mol^{-1}	Mn $_{exp}$ ^{1}H NMR /g.mol^{-1}	^{a}Mn $_{exp}$ GPC /g.mol^{-1}	^{a}PDI
34	5	98%	900	900	1300	1.20
36	10	99%	1600	1800	2200	1.21
37	20	97%	3100	3400	3800	1.23
35	30	98%	4500	4400	7500	1.30

Initiated by inimer HONDC conducted in toluene at 80°C for 1h at an initiator concentration of 0.04 M ^{a}Determined *via* GPC using PSt as standards and THF as eluent.

$$conv_{NMR}\,(LLA) = \frac{\int(5.12\ ppm)}{\int(5.12\ ppm) + \int(3.83\ ppm)}$$

Equation 2-3

Likewise, degrees of polymerization of LLA with respect to initator HONDC (DP_{LLA}, see Equation 2-4) were calculated through the relative integrals of the olefin signal in the HONDC

initiator and polymeric methine peaks. Experimental M_n were established by GPC as well as ^{1}H NMR, according to Equation 2-5.

$$DP_{NMR}\ (LLA) = \frac{\int(5.12\ ppm)}{\int(5.12\ ppm) + \int(5.90\ ppm)}$$

Equation 2-4

$$Mn_{NMR}(LLA) = M_{\backslash cmpd\{HONDC\}} + M_{LLA} \times Eq\ (LLA) \times conv_{NMR}(LLA)$$

Equation 2-5

The expected molecular weights from initiator to monomer ratios matched closely the molecular weights established *via* ^{1}H NMR (see Equation 2-5), while GPC molecular weights are somewhat higher than expected. With a HONDC:LLA ratio of 1:5, the expected M_n of **34** was 900 g.mol^{-1}, which was also the experimental M_n established *via* NMR. The GPC M_n on the other hand was higher at 1 300 g.mol^{-1}. Likewise, for the longer polymer **35**, the expected M_n was 4 500 g.mol^{-1} and the molecular weight established by NMR was 4 400 g.mol^{-1}, while GPC analysis indicated a polymer with M_n of 7 500 g.mol^{-1}. This difference can be explained by the

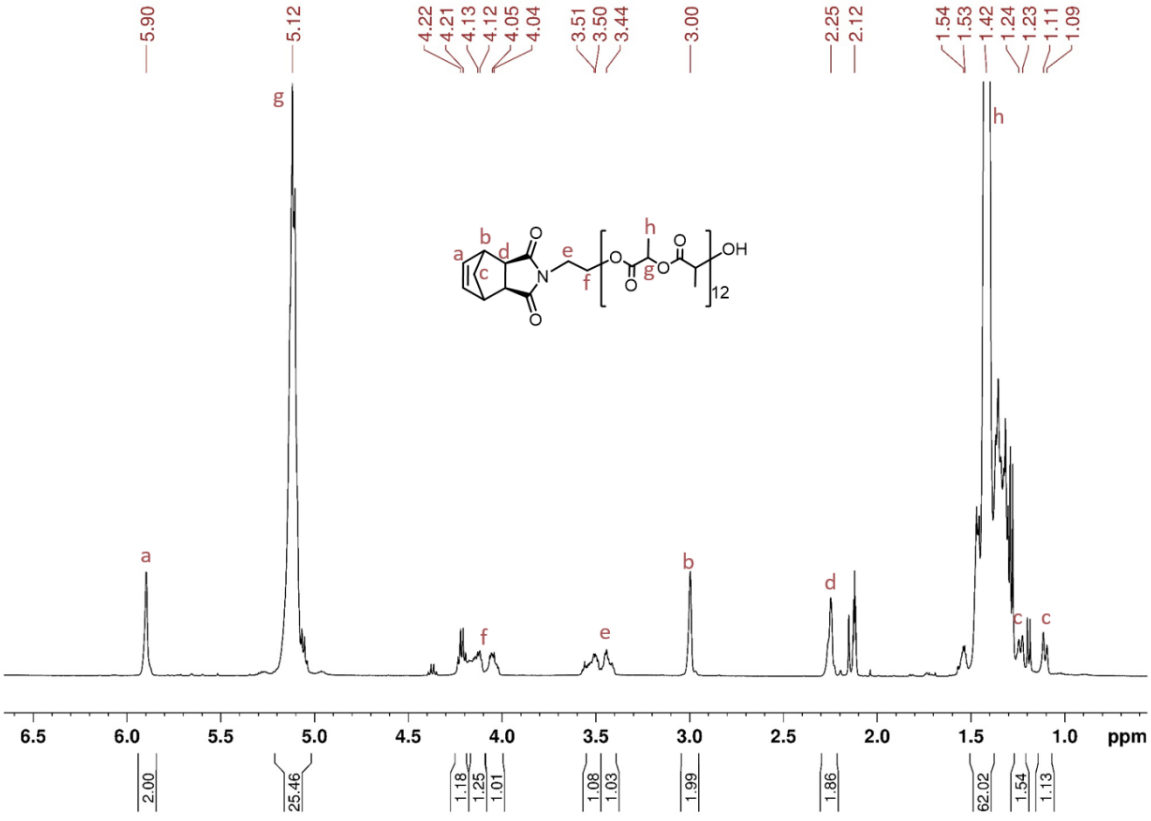

Figure 2-17: Representative ^{1}H NMR spectrum of PLLA initiated by monomer HONDC recorded in toluene-d$_8$ at a 700 MHz spectrometer.

mismatch between elution behavior of reference material (PSt) and sample of interest (PLLA). The associated GPC traces were unimodal at targeted DP's of five to 30 units of L-lactide (see Table 2-9) Figure 2-17 shows a representative ^{1}H NMR spectrum of inimer HONDC-initiated ROP of LLA. The bridging proton signals (**c** at 1.10 ppm and 1.23 ppm), as well as the two methine protons (**b** and **d** at 3.00 ppm and 2.25 ppm respectively) show that the ring structure remained closed, while the alkene peak (**a** at 5.90) proves that the catalyst did not react with the double bond. Meanwhile, PLLA-associated methine (**g** at 5.12 ppm) and methyl peaks (**h** at 1.42) prove the successful polymerization of LLA. DOSY ^{1}H NMR shows the covalent attachment of poly(L-lactide) chains and the HONDC initiator (see Figure 2-18).

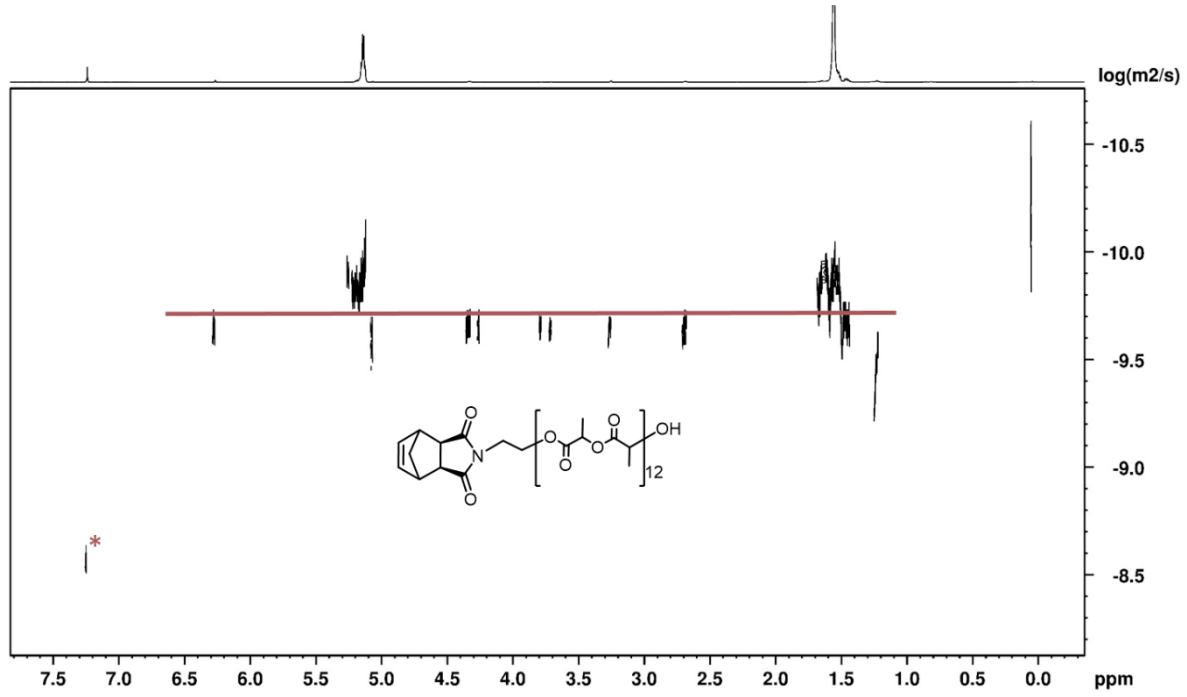

Figure 2-18: DOSY ^{1}H NMR of inimer HONDC-initiated PLLA, polymerized by the NHC DTT. Spectrum recorded in $CDCl_3$ at a 700 MHz spectrometer.

To exclude that the olefinic bond takes part in the reaction and hence prove the orthogonality of the two polymerizations, the reaction progress was followed by *in-situ* ^{1}H NMR in toluene d-8 at 85 °C. [redacted] recorded the spectra at a 500 MHz spectrometer. The collected spectra were overlaid digitally and aligned (see Figure 2-19). The peak at 5.89 ppm is the signal of the olefinic proton in the norbornene monomer. The insert in Figure 2-19 shows the rapid disappearance of the high field shoulder associated with the triazol adduct. Notice that in contrast to the spectra of inimer HONDC recorded at room temperature, the kinetic *in-situ* spectra were recorded at 360 K, resulting in temperature-dependent shifts of several protons. After full dissociation of triazol and inimer, the olefin peak remains unchanged, indicating that the olefin is stable to the reaction conditions of the

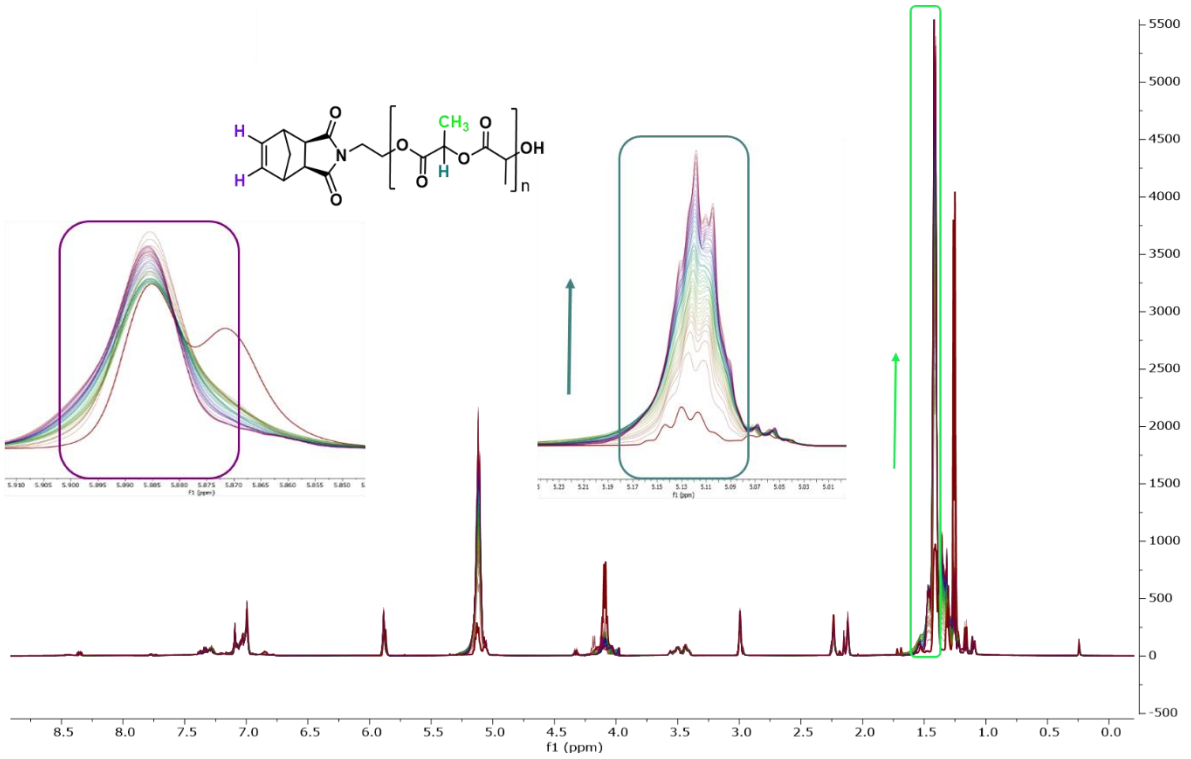

Figure 2-19: *In-situ* ^{1}H NMR spectra of DTT mediated ROP of L-lactide in toluene-d_8 at 85 °C recorded at a 500 MHz spectrometer. Inserts show the alkene signal of initiator at 5.90 ppm (left) and PLLA methine signals increasing at 5.12 ppm (right).

ROP. As the polymerization progresses, the polymeric methine peak at 5.12 ppm gains intensity, whereas the peak at 4.15 ppm associated with the methine signal of the monomer decreases. The methyl group of the monomer at 1.26 ppm decreases rapidly in intensity, whereas the methyl peak of the polymeric product at 1.42 ppm increases rapidly at first and then more slowly as the reaction proceeds. In summary, the in-situ ^{1}H NMR experiments proved that DTT polymerizes L-lactide without interfering with the integrity of the norbornene functional group.

2.4.7 Grafting Through

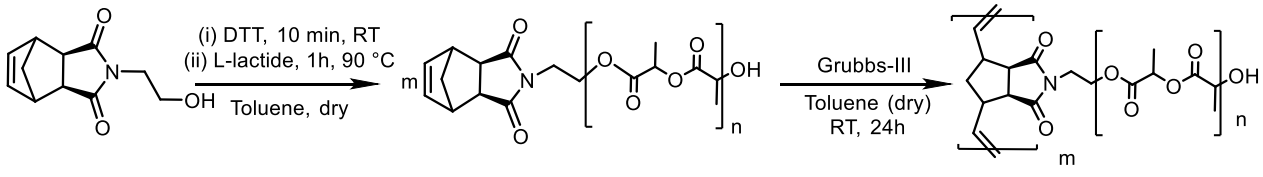

Scheme 2-9: Reaction scheme of one-pot, two-steps bottlebrush synthesis

After establishing that DTT catalyzes the polymerization of L-lactide without interfering with the olefin of the norbornene functional group, it was investigated whether the ROMP catalyst interferes with the DTT catalyst. For this purpose, HONDC initiated and DTT catalyzed ROP of L-lactide was conducted in a first step and in a second step, without

quenching, ROMP catalyst was added. Conceptually the two-step process represents a case of *grafting through* polymerization with the synthesis of macromonomers in a first step, and the subsequent ROMP to afford BBs (see Scheme 2-9).

Table 2-10. Equivalents and molecular weights of ttepwise bottlebrush synthesis (grafting through approach)

Entry	MM /g.mol^{-1}	Eq. MM	$M_{n\ theo}$ /g.mol^{-1}	Conversion [a] /%	$M_{n\ exp}$[a] ^{1}H NMR /g.mol^{-1}	$M_{n\ exp}$[b] GPC /g.mol^{-1}	PDI [b]
38	1 300	25	32 500	100%	22 800	28 200	1.20
39	1 300	50	65 000	100%	45 700	50 900	1.28
40	1 300	100	130 000	99%	90 400	95 900	1.26
41	2 200	25	55 000	100%	40 900	43 500	1.24
42	2 200	50	110 000	100%	81 700	64 500	1.31
43	2 200	100	220 000	100%	163 400	116 700	1.27
44	3 400	25	85 000	100%	75 100	56 000[c]	1.21 [c]
45	3 400	50	170 000	100%	150 200	103 100 [c]	1.23 [c]
46	3 400	100	340 000	98%	294 300	162 900 [c]	1.27 [c]

Conducted in toluene at RT for 24h at an initial concentration of 0.04 M. [a]Determined by ^{1}H NMR [b]Determined *via* GPC using PSt standards and DMF as eluent. [c]small amount of late-eluting polymer population.

Following DTT mediated ROP of L-lactide (see Table 2) in toluene at 80 °C, the reaction mixture was cooled to room temperature and various amounts of Grubbs-III were added for the ROMP of the macromonomers. Macromolecules with five, ten or 20 units of L-lactide

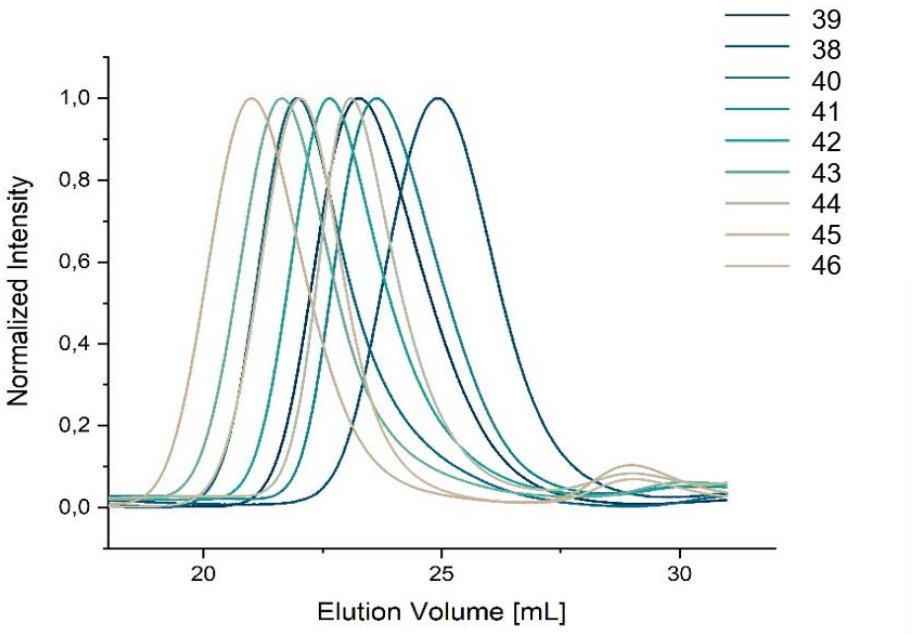

Figure 2-20. GPC traces of one-pot, two-step polymerizations detailed in Table 2-10. BBs **38**–**46** show a small amount of late-eluting polymer.

were synthesized and immediately subjected to ROMP with a targeted backbone DP of 25, 50 and 100 each. Bottlebrushes could be synthesized with excellent yield and quantitative conversion of macromonomer. GPC traces were narrowly distributed with dispersities between 1.20 and 1.31 (see Table 2-10). Some trailing was observed towards later elution times, as is expected with molecular bottlebrushes[189] (see Figure 2-20). It was previously established that the trailing is not necessarily due to lower weight macromolecules but a phenomenon originating in the characteristic interactions between molecular brushes and the stationary phase[189]. The molecular weight distribution may hence be even narrower than characterized. This clearly shows a good control over the ROMP process in particular. The experimental molecular weights were lower than the theoretical weights expected from (nearly) full conversion. For entry **38** for example, the theoretical M_n was 32 500 g.mol^{-1}, while GPC indicated an experimental M_n of 28 200 g.mol^{-1}. ^{1}H NMR analysis allowed to calculated an experimental molecular weight of 22 800 g.mol^{-1}. Likewise, polymerization **44** was expected to yield a polymer with M_n of 85 000 g.mol^{-1}, while the experimentally established M_n were at 75 000 g.mol^{-1} and 56 000 g.mol^{-1} for ^{1}H NMR and GPC respectively. The presence of a small, later eluting peak observed for polymerizations **44**, **45** and **46** (see Figure 2-20) may be the cause of such a mismatch. The lower molecular weight chains could be unfunctionalized PLLA chains that are incapable of participating in ROMP and therefore lower the molecular weights.

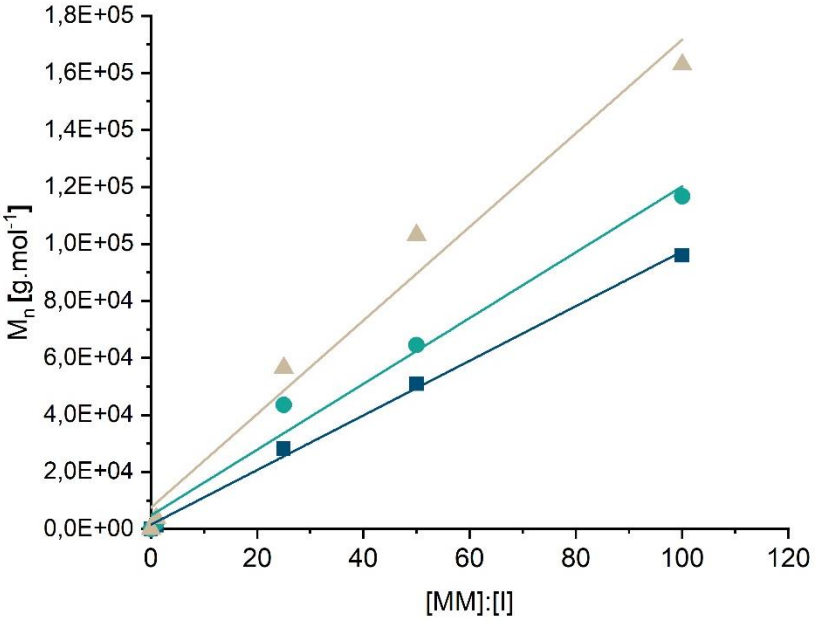

Figure 2-21: Linear relationship between Targeted DP of MMs (i.e. ratio of MM to initiator employed) and molecular weights of BBs. Squares for MMs with 5 units of LLA, circles for 10 units of LLA and triangles for 20 units of LLA. Lines indicate linear fits.

For all DP's tested, the polymerizations were well-controlled. There was a linear relationship between targeted DP and molecular weight of the resulting bottlebrushes (see Figure 2-21).

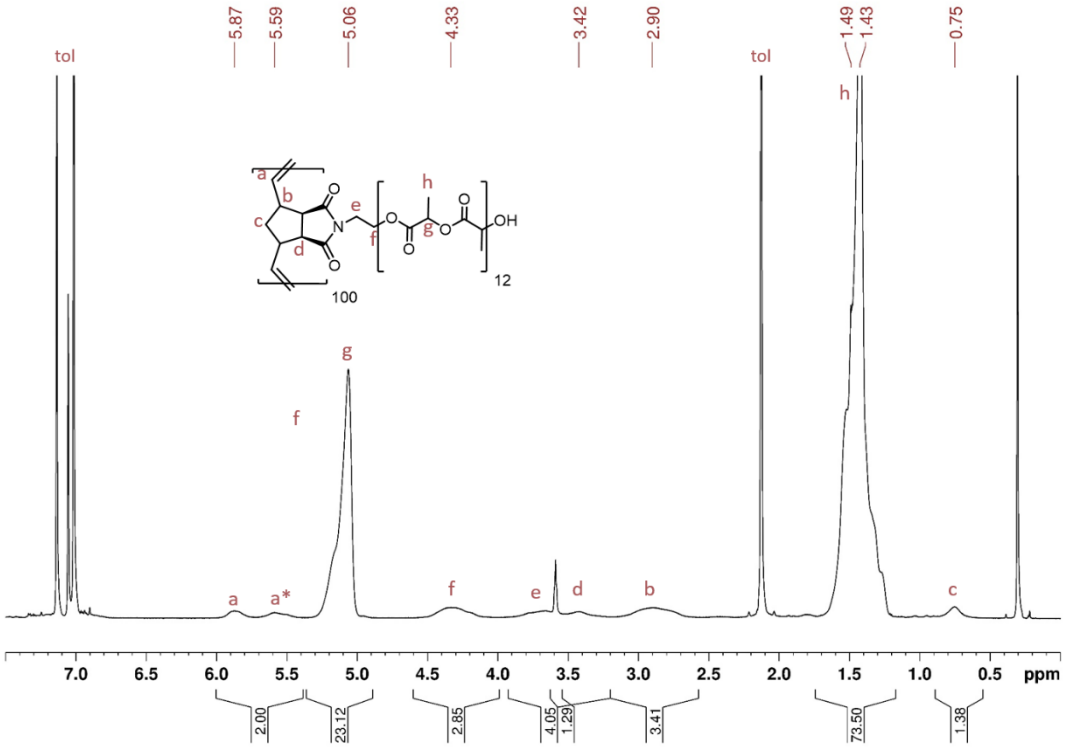

Figure 2-22: Representative ^{1}H NMR spectrum of bottlebrush synthesized from L-lactide and backbone monomer HONDC, recorded in toluene-d_8 on a 700 MHz spectrometer.

NMR experiments were conducted to establish whether the polymeric products are covalently attached. Figure 2-22 shows the assigned ^{1}H NMR spectrum of a PLLA grafted bottlebrush. In contrast to the sharp inimer-signals of the macromonomers (see Figure 2-17), the backbone proton signals are much broader. Notably, the unsaturation of the inimer HONDC persists in the bottlebrush. Significant shifts were observed for signals **b** (at 2.90 ppm), **c** (at 0.75 ppm) and **d** (at 3.42 ppm) as expected due to the open ring structure of the norbornene backbone. At first, the signal at 5.87 ppm was mistakenly attributed to an incomplete ROMP process and interpreted as inimer signal. However, 2D NMR experiments revealed that despite the similar chemical shift, the signal **a** at 5.87 ppm and **a*** at 5.59 ppm refer to the *trans* and *cis* joints in the polymer backbone, respectively. The approximate 50:50 *trans:cis* ratio is expected in Grubbs-catalyst polymerized ROMP polymers due to the facile carbene roation[190]. In deuterated chloroform, the difference of inimer methine signal and polymer methine signal is much more pronounced. The closed ring's alkene proton occurs at 6.29 ppm, while the polymer signals occur at 5.69 ppm (*trans*) and 5.46 (*cis*) in $CDCl_3$, while in deuterated DMF (DMF-d_7), occurred at 6.08 ppm and 5.79 ppm respectively. $CDCl_3$ and DMF are better solvents for the PLLA-grafted BBs. Conversion data was therefore collected in deuterated chloroform by integration of the alkene signals. Molecular weights of

bottlebrushes were determined according to Equation 2-6. DOSY ^{1}H NMR showed that all polymeric signals occur at the same diffusion coefficient and hence indicate a covalent attachment of the individual segments. No macromonomers could be detected, for brushes **39-43** indicating a complete reaction, as expected from the GPC traces. As for BBs **44-46**, it was expected to observe a second population of polymer at a greater diffusion coefficient to account for the late eluting polymers observed *via* GPC. However, this population could not be resolved *via* DOSY ^{1}H NMR.

$$Mn_{NMR}(BB) = Mn_{NMR}(LLA) \times conv_{NMR}(\backslash cmpd\{HONDC\}) \times Eq\ (\backslash cmpd\{HONDC\})$$

Equation 2-6

Although the bottlebrushes above were synthesized in a two-step process, unlike previous publications, the second step does not depend on the addition of a quenching agent of the ROP catalyst. As the DTT catalyst's equilibrium between active and dormant state is shifted towards inactivity at lower temperatures, conducting the ROMP step at room temperature is sufficient to deactivate the ROP catalyst. The presence of the inactive catalyst does not seem to interfere with the ROMP process. These model experiments proved that DTT does not interfere in the ROMP process, and that Grubbs-III polymerizes the sterically challenging macromonomers reliably, fulfilling most requirements for a tandem process. Finally, it remained to see whether the active DTT and the elevated temperatures required for DTT mediated ROP still allow for well-controlled ROMP.

2.4.8 Tandem Grafting with DTT and Grubbs-III

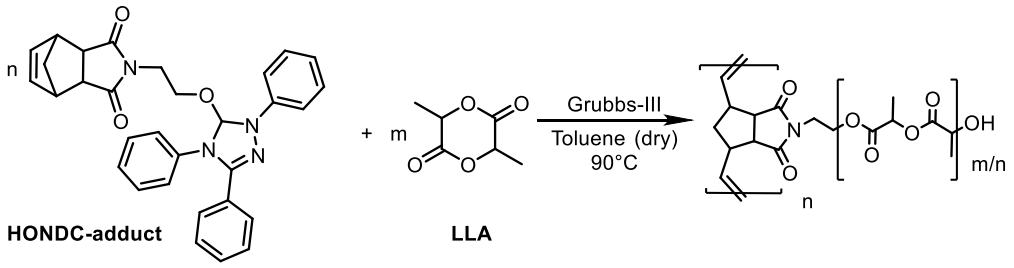

Scheme 2-10: Reaction scheme of tandem bottlebrush polymerization. One-pot, one-step reaction.

Following all the previous studies, it was established that at room temperature, the presence of DTT does not interfere with the Ruthenium catalyst, and the ROP does not interfere with the integrity of the olefin. A tandem approach combining the Grubbs Third Generation initiated ROMP of inimer HONDC and DTT catalyzed ROP of L-lactide was then investigated. The one- pot, one-step process was conducted at 80 °C in dry toluene, combining all reagents simultaneously in a SCHLENK tube (see Scheme 2-10). The tandem polymerization produced short bottlebrushes with excellent control. For bottlebrushes with targeted sidechain degrees of polymerization between five to 20 units of L-lactide, and backbone DP's of 25 to 50 units of inimer HONDC, quantitative conversions were achieved in under 1h reaction time (see Table 2-11).

Table 2-11: Tandem polymerizations of short bottlebrushes with various side chain lengths.

Entry	Equivalents		time /min	Conversion [a] /%	
	$[LLA]_0$/ $[HONDC]_0$	$[HONDC]_0$/ $[Grubbs\text{-}III]_0$		LLA	HONDC
47	5	25	60	95%	100%
48	9	25	60	94%	100%
49	5	50	20	99%	95%
50	10	40	60	94%	97%
51	10	50	60	99%	96%
52	20	40	60	95%	99%

Conducted in toluene at 80°C for $[HONDC]_0$ 0.04 M. [a] Determined by ^1H NMR

GPC data shows that the tandem process systematically produces narrowly distributed polymers with PDIs from 1.07 to 1.15 (see Table 2-12). Importantly, the polymeric product remained in solution during the polymerization. Hence the narrow molecular weight distributions do not arise from precipitation polymerization. The resulting polymer's average molecular weight, as determined via ^1H NMR, matches closely to the theoretical molecular weight. For example the expected M_n of entry **47** was 22 500 g.mol^{-1} and ^1H NMR and GPC M_n were established with 22 300 g.mol^{-1} and 22 300 g.mol^{-1}respectively.

Table 2-12: Theoretical and experimental number average molecular weights of short bottlebrushes.

Brush	M_n /g.mol^{-1}				PDI[a]
	Side chains theo	BB theo	^{1}H NMR exp	GPC[a] exp	GPC exp
47	900	22 500	22 300	24 200	1.12
48	1 500	37 500	35 700	34 600	1.15
49	900	45 000	43 700	38 700	1.15
50	1 600	64 000	60 600	59 900	1.07
51	1 600	80 000	78 400	73 600	1.15
52	3 100	124 000	116 600	85 300	1.08

[a] Determined by GPC using PS as standards and DMF as eluent.

The experimental molecular weight as determined via GPC is lower for entries **48-52** than both ^{1}H NMR and theoretic molecular weights. These findings are in line with the three dimensional conformation of molecular bottlebrushes as opposed to the linear polystyrene reference material for the GPC calibration curve[191]. Associated dispersities range from 1.07 to 1.15. Considering that the molecular weight distributions represent the distribution of two independent polymerization events, the polymers are indeed very narrowly distributed. They are indeed far more homogeneous than the stepwise process. GPC traces were either monomodal and narrowly distributed or else had a very small, clearly separated later-eluting fraction at the detection threshold of the RI detector (see exemplified for BB **51** in Figure 2-23).

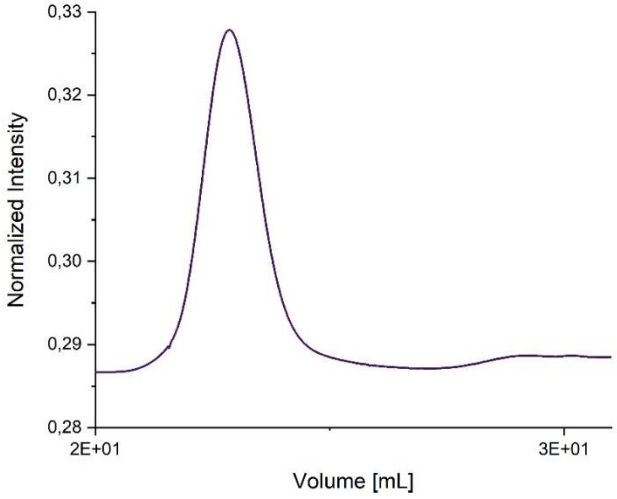

Figure 2-23: Representative GPC elution trace of **51** in DMF *versus* PSt standards, showing the narrowly distributed major fraction and a late-eluting minor fraction of a second population.

In comparison to the stepwise process, this later eluting polymeric fraction is much smaller in the tandem system. As stipulated before, these minor fractions could represent unreacted macromonomer or unfunctionalized PLLA, indicating that the tandem approach encourages quantitative backbone conversion or quantitative inititation respectively. In order to characterize the late-eluting polymer, DOSY experiments were conducted. DOSY ^{1}H NMR spectra (see Figure 2-24) show that all polymeric signals occur at the same diffusion

coefficient, indicating that the product is covalently linked. However, in contrast to the GPC results, a second, lower molecular weight population could not be detected via DOSY ^{1}H NMR. As a consequence, the small peak observed *via* GPC could not by characterized. This conspicuous absence of low molecular weight DOSY signals could have two origins: (i) DOSY sensitivity and (ii) inadequate deconvolution of signal processing. Regarding hypothesis (i), it is worth pointing out that the observed second peak is very low in intensity. With ^{1}H NMR being a relatively insensitive bulk characterization technique, the concentration of the lower weight polymers might be too low for detection. As for hypothesis (ii) it is worth noting that the single DOSY ^{1}H NMR diffusion coefficient may mask several polymer populations[192]. In a meticulous study involving mixtures of block copolymers and homopolymeric impurities, HILLER [193] has shown that when applying one-component exponential decays when processing DOSY spectra, homopolymeric impurities overlap with the block copolymer to yield an average diffusion coefficient. It is hence little surprising that the small amounts of homopolymer shown by GPC are not detected via NMR.

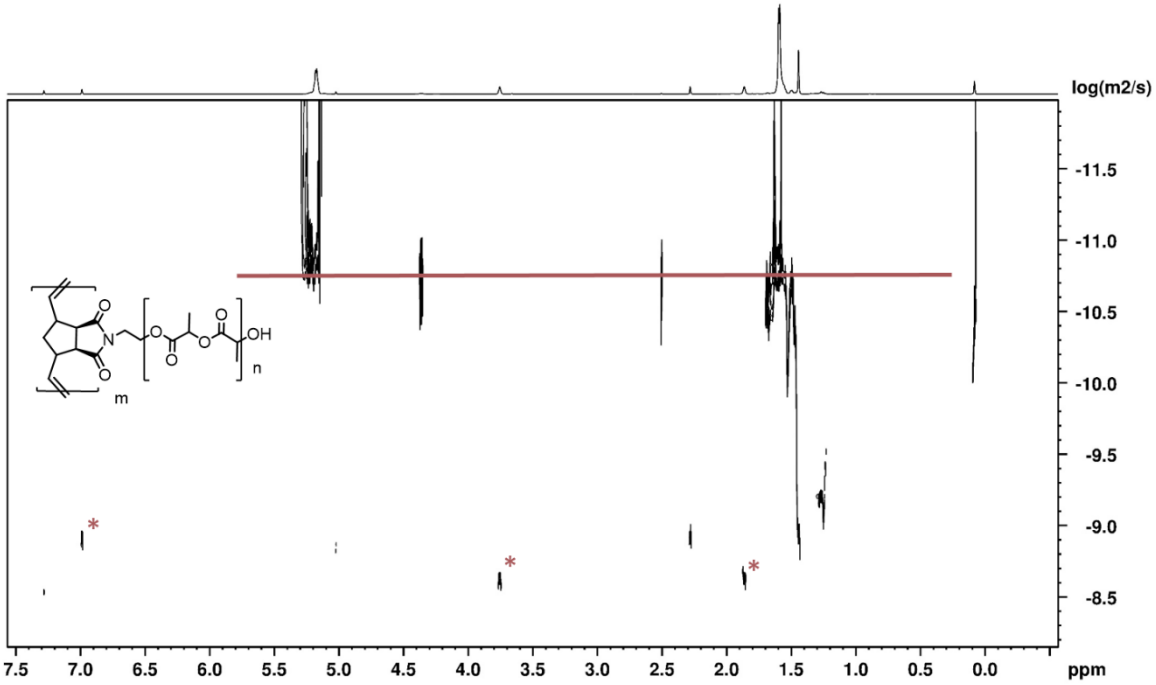

Figure 2-24: DOSY ^{1}H NMR showing the single diffusion coefficient associated with all polymer signals. Spectra recorded in toluene-d_8 at a 700 MHz spectrometer. Signals marked with asterisk are solvent-derived.

Figure 2-25 shows the narrowly distributed GPC traces of polymers **47-52**. A certain asymmetry could be observed due to trailing towards the late eluting side of the trace. This effect is well-established for bottlebrush polymers. Nakamura [191] showed that due to their confined geometry, molecular brushes have a smaller radius of gyration and hence elute later than their linear counterparts of equal weight. Determining the molecular weight of bottlebrushes through GPC calibrated on linear polymers hence leads to an underestimation

of their weight. Likewise, it was demonstrated that molecular weights can be underestimated by a factor of up to 10. [194] To account for such effects, the GPC results were contrasted to the ^{1}H NMR results.

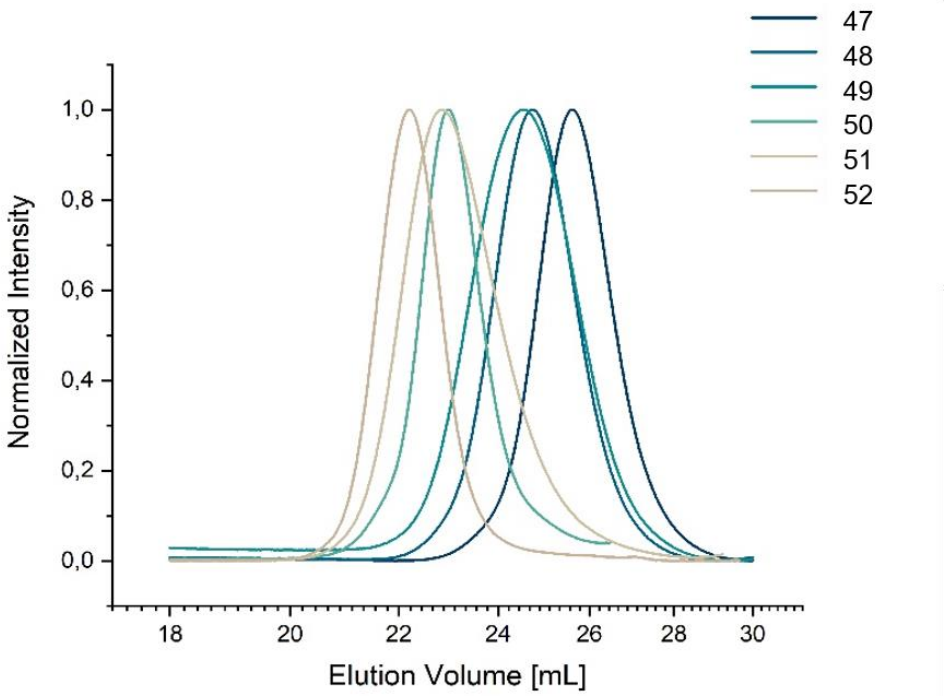

Figure 2-25: GPC traces of one-pot, on-step simultaneous polymerizations **47-52**, in DMF *versus* PSt standards, showing narrowly distributed polymeric products.

However, the ^{1}H NMR data may also be suffering from systematic bias. The molecular weight calculations based off ^{1}H NMR intensity integrations, as well as conversion data are all based on the assumption that the intensity of all protons depends solely on the concentration of the observed proton. However, in the case of molecular bottlebrushes, the decreased mobility of backbone monomers can lead to a decrease in backbone signal intensities. In ^{1}H NMR, the observed signals are net magnetizations that oscillate at the LARMOR frequency. The net magnetization is progressively dephased (dampened) due to inhomogeneities in the applied magnetic field as well as intrinsic transversal relaxation (T2) mechanisms. These processes are incorporated into the concept of T2* decay, a simple exponential decay with the time constant T2*[195]. MATYJASZEWSKI and coworkers[181] investigated the relaxation times of bottlebrushes in dependence of grafting density and chain length. The signals of backbone monomers had significantly lower transversal relaxation times (T2) than the more mobile side chains. T2 times are inversely proportional to the line width of signals in FOURIER-transformed NMR spectra. Short T2 times (i.e. rapid dephasing) leads to a broadening of signals. For very efficient dephasing, signals can decrease

in intensity or 'disappear' due to low signal-to-noise ratios[195]. Such effects could lead to the underestimation of backbone signal concentrations and therefore falsify kinetic calculations.

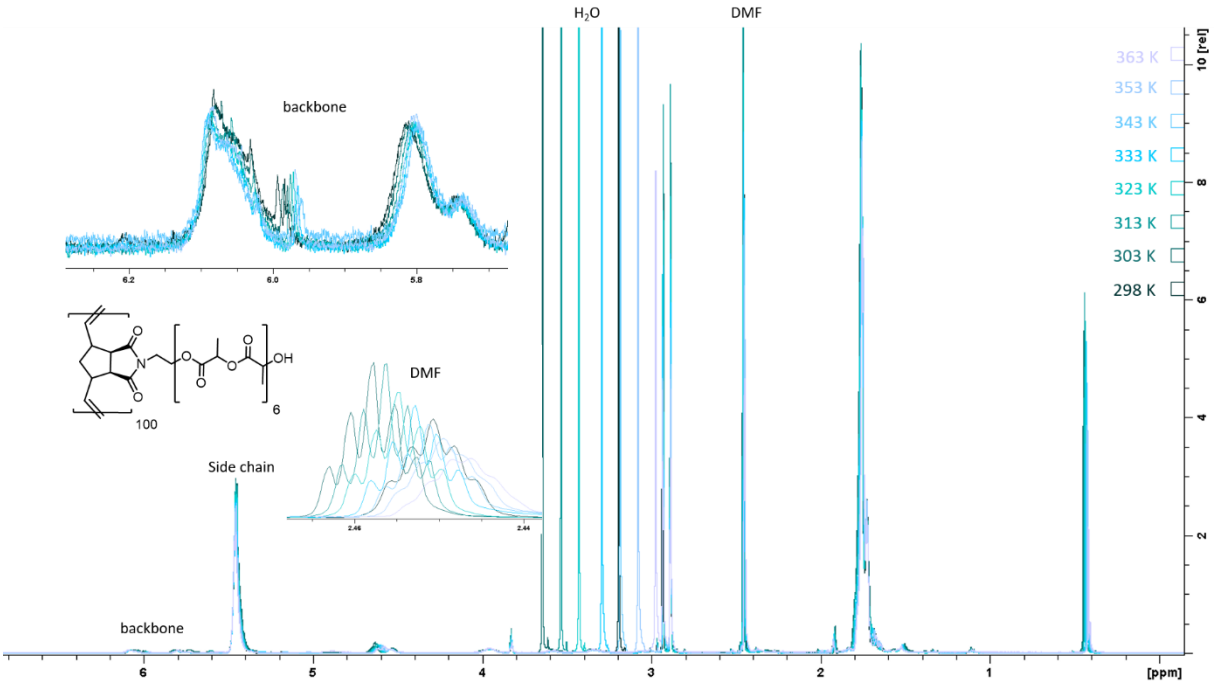

Figure 2-26: overlaid ^{1}H NMR spectra of bottlebrush polymer **53** measured at varying temperatures from 298 K to 363 K in DMF-d_7 at an 850 MHz spectrometer. Temperature-induced shift could be observed for DMF and H_2O, while peak shapes and positions of both backbone and side chains remained constant.

To assess whether the kinetic data gathered by ^{1}H NMR experiments suffers from such effects, a set of NMR spectra were recorded at different temperatures. As increasing temperatures correspond to an increase in molecular motion, relaxation becomes less efficient and T2 times increase[195]. Therefore, if some of the backbone signals were masked by low mobility, greater temperatures should lead to an increase in backbone signal intensity and a sharpening of signals. The side chain signals on the other hand with their greater mobility even at low temperatures should not change significantly. As a consequence, it would be expected that the ratio of side chain signal integrals to those of the backbone should decrease with increasing temperature. Figure 2-26 shows the digitally overlaid spectra of molecular bottlebrush **53** with a side chain DP of 6 LLA units at temperatures between 298 K and 363 K. The peak shape (line width) of the methine backbone proton (55.39 ppm to 5.96 ppm) does not does not shift nor sharpen with temperature. The temperature increase does affect residual DMF and water signals that shift as a function of temperature[196]. Figure 2-27 shows the integral intensities as a function of temperature as, well as the relative signal ratios as a function of temperature. Although large differences in relative integral ratios could be observed, the backbone signals do not increase in intensity with temperature. This behavior

indicates that even at room temperature, there is sufficient mobility in the backbone to show quantitative signal intensity. Therefore, relative integral intensities can be used for conversion and molecular weight calculations.

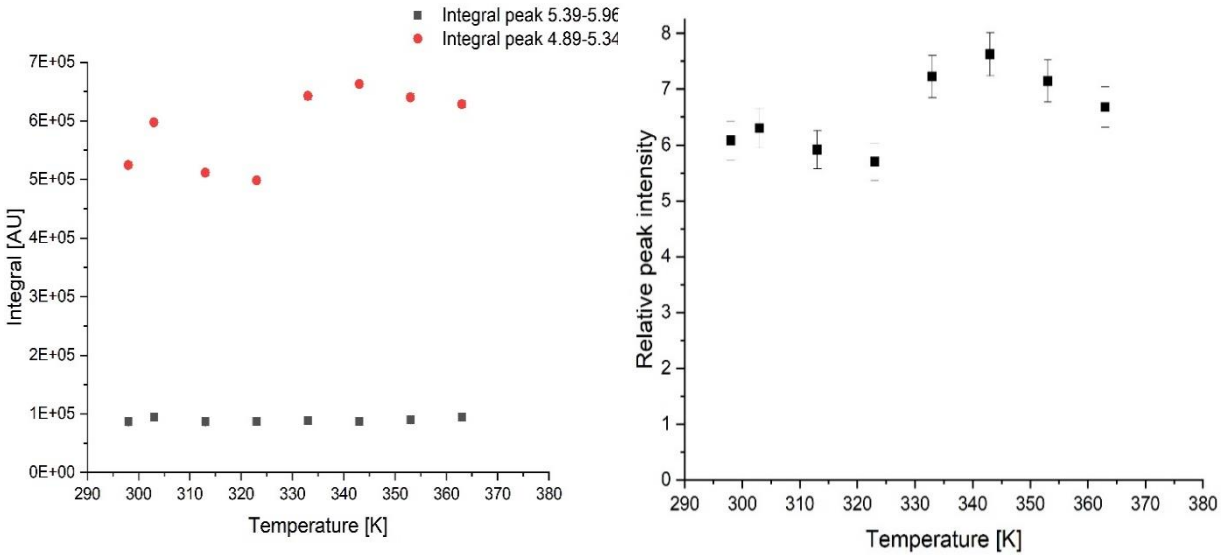

Figure 2-27: Left: integrals of backbone methine peak (5.39 ppm to 5.96 ppm, black squares) and side chain integral (4.89 ppm to 5.34 ppm, red circles) as a function of temperature. Right: relative peak intensity of side-chain to backbone integrals as a function of temperature.

Table 2-13: Tandem polymerizations of short bottlebrushes with different polymerization times

Entry	$[LLA]_0/[HONDC]_0$	$[HONDC]_0/[GrubbsIII]$	time /h	Conv LLA[a] /%	Conv HONDC[a] /%
54	5	25	0.5	100%	100%
55			1	95%	100%
56			3	95%	100%
57			20	100%	100%
58	9	25	0.5	94%	100%
59			1	94%	100%
60			3	94%	100%
61			20	100%	100%
62	10	40	1	94%	97%
63			2	95%	98%
64			39	96%	99%
65	20	40	1	95%	99%
66			2	96%	98%
67			17	97%	98%
68			23	96%	98%

Conducted in toluene at 80°C for $[HONDC]_0$ 0.04 M. [a] Determined by ^1H NMR

Following the successful tandem polymerizations, their relative rates of conversion were investigated. For this purpose, polymerizations were conducted and samples were removed for analysis *via* GPC and ^{1}H NMR (see Table 2-13 and Table 2-14). The different polymerization times show that high conversions are achieved rapidly. Importantly, ROMP conversions are high for all polymerizations even within 30 min reaction time. Dispersities are low for short reaction times with PDIs between 1.07 and 1.14. At short reaction times, the experimentally established molecular weights match closely the predicted weights. For example **54** had a theoretical M_n of 23 200 g.mol^{-1} while the molecular weights established by ^{1}H NMR and GPC were 23 200 g.mol^{-1} and 23 100 g.mol^{-1} respectively. With increasing targeted backbone degrees of polymerizations, the difference between predicted and experimental weights increases. In particular, entries **65** to **68** with a backbone DP of 40 show lower weights established by GPC than by ^{1}H NMR. While the molecular weights found by ^{1}H NMR matched closely with theoretical weights (117 000 g.mol^{-1} versus 116 600 g.mol^{-1}), the weights established by GPC was lower with 85 300 g.mol^{-1}. This effect might be expected for BBs due to their form factor. However, when allowing for longer polymerization times, dispersities increase and the difference between theoretical molecular weights and experimental molecular weights grow more pronounced (see Table 2-13 and Table 2-14). Especially when considering entries **65** to **68**, the average molecular masses seem to decrease with increasing polymerization time (from 89 000 g.mol^{-1} after 1h to 75 700 g.mol^{-1} after 24 h. This effect might be due to NHC induced side reactions, similar to the effects observed with SIMes catalyzed ROP.

Table 2-14: Molecular weights (experimental and theoretical) for polymerizations of short bottlebrushes (see Table 2-13)

Entry	Mn theo (graft) /g.mol-1	Mn theo (BB) /g.mol-1	Mn exp[a] ^{1}H NMR /g.mol-1	Mn exp[b] GPC /g.mol-1	PDI[c]
54	900	23 200	23 200	23 100	1.12
55			22 300	24 200	1.12
56			22 300	23 000	1.15
57			23 200	24 700	1.18
58	1500	37 600	35 700	32 100	1.14
59			35 700	34 600	1.15
60			35 700	34 800	1.15
61			37 600	35 800	1.18
62	1600	63 200	60 600	59 900	1.07
63			61 800	62 300	1.07
64			63 000	54 100	1.11
65	3100	117 000	116 600	85 300	1.08
66			116 600	89 100	1.09
67			117 700	74 700	1.16
68			116 600	75 700	1.17

[a] Determined by ^{1}H NMR [b] Determined by GPC using PS as standards and THF as eluent.

Table 2-15: Time-dependent conversions of polymerizations targeting longer backbone DPs.

Entry	$[LLA]_0$/ $[HONDC]_0$	$[HONDC]_0$ /$[Grubbs\text{-}III]_0$	time /h	Conv L-LA /%	Conv HONDC[a] /%
69	5	100	0.5	94%	70%
70			1	94%	70%
71			3	90%	68%
72	11	100	0.5	82%	63%
73			1	100%	63%
74			20	100%	63%
75			70	98%	59%
76	5	200	0.5	95%	38%
77			1	93%	40%
78	10	200	0.3	98%	42%
79			1	98%	41%
80			16	97%	41%
81			24	97%	38%
82	20	200	0.3	98%	41%
83			1	98%	45%
84			16	98%	45%
85			24	96%	36%

Tandem bottlebrush poymerizations with longer backbones. conducted in toluene at 80°C for $[HONDC]_0$ 0.04 M. [a] Determined by ^1H NMR

Further experiments were conducted to assess how well the tandem system performs when targeting longer backbone DPs. Polymerizations were conducted with a [inimer]:[Grubbs-III] ratio of 100:1 and 200:1 (see Table 2-15 and Table 2-16). At higher targeted DP's, conversion of HONDC decreases noticeably. Interestingly, the maximum DP yielded was between 70 and 80 repeat units for both sets of experiments, representing a conversions around 70% and 40% respectively. At lower targeted DP's, conversion is systematically quantitative or near quantitative. Entries **76-85** in Table 2-15 show that conversion of HONDC drops to 40% when an inimer HONDC to Grubbs initiator ratio of 200 equivalents is employed. In contrast to the entries with lower targeted DP's, the associated GPC traces show a distinct bimodal distribution. DOSY ^1H NMR show two distinct populations (see Figure 2-28). The heavier fraction are short bottlebrushes and the lighter fraction are HONDC-initiated poly L-lactide chains that have not undergone ROMP. These findings are supported by the presence of ^1H NMR signals corresponding to the metathesis ring opened HONDC associated with monomers in the backbone as well as signals of the closed structure covalently bonded to PLLA. Even when increasing reaction times from 1h to 40 h, conversion does not increase, indicating the deactivation of Grubbs catalyst. This finding is in keeping with the lower solution stability of Third Generation Grubbs catalysts at elevated temperatures compared to the earlier generations[197]. The high temperatures required for the successful DTT mediated ROP hence limit the versatility of this tandem approach.

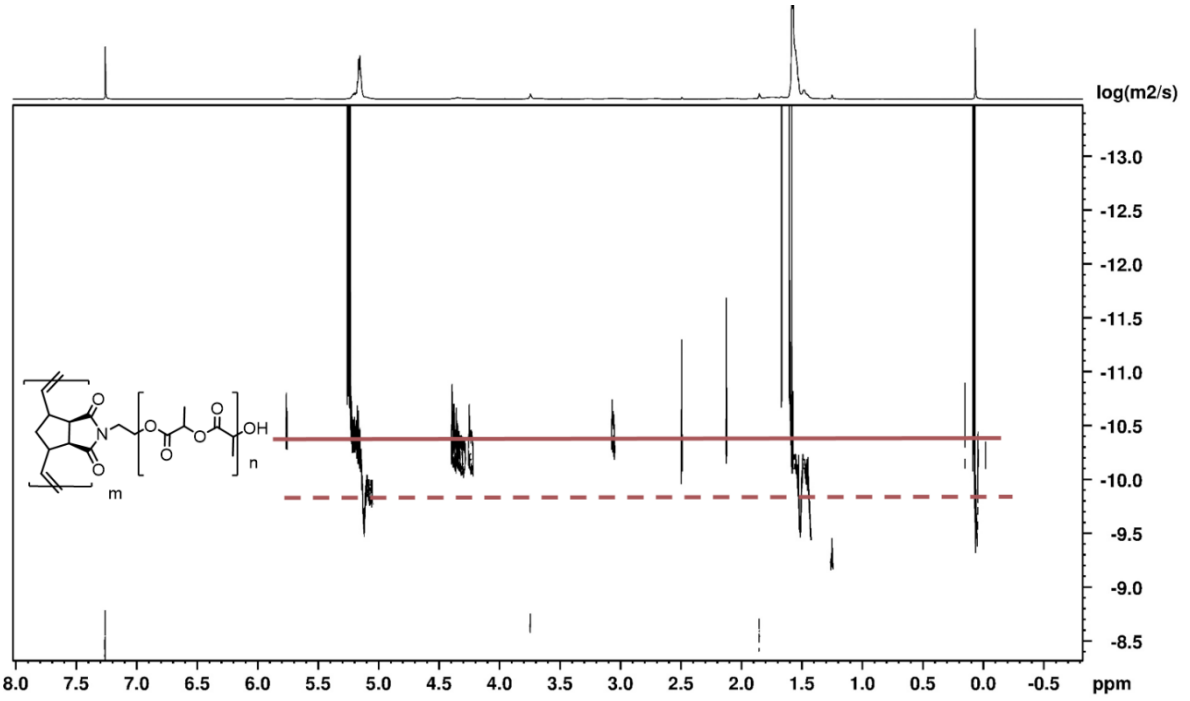

Figure 2-28: DOSY ^{1}H NMR of simultaneously polymerized bottlebrush **69** recorded in $CDCl_3$ at a 700 MHz spectrometer.

Table 2-16: Molecular weights (theoretical and experimental) of polymerizations targeting longer backbone DPs

Entry	Mn theo (side chain) /g.mol-1	Mntheo bottlebrush /g.mol-1	Mn exp ^{1}H NMR[a] /g.mol-1	Mn exp GPC[b] /g.mol-1	PDI[b]
69	900	92 800	61 900	56 300*	1.33*
70			61 900	58 400*	1.32*
71			58 200	55 900*	1.35*
72	1 800	179 300	95 000	89 200*	1.38*
73			112 900	95 400*	1.42*
74			112 900	91 200*	1.41*
75			103 900	93 600*	1.40*
76	900	185 600	67 800	84 900*	1.16*
77			70 200	86 500*	1.18*
78	1 600	329 700	136 100	85 200*	1.20*
79			132 800	102 700*	1.19*
80			131 600	95 900*	1.23*
81			122 000	94 100*	1.23*
82	3 100	618 000	248 600	101 300*	1.15*
83			272 900	127 500*	1.19*
84			272 900	133 600*	1.20*
85			214 200	131 200*	1.20*

Tandem bottlebrush poymerizations with longer backbones conducted in toluene at 90°C for $[HONDC]_0$ 0.04 M. [a] Determined by ^{1}H NMR [b] Determined by GPC using PS as standards and DMF as eluent. In case of multimodal distributions, refers to heavier fraction *Multimodal distribution.

The conversion of L-lactide ROP remains quantitative for 5, 10 and 20 equivalents with respect to backbone monomer. However, when considering entries **72**-**79**, experimental molecular weights are much lower than the calculated theoretical weight. Figure 2-29 shows the diversion between targeted molecular weights and targeted DP. Significantly, the difference increases with increasing side chain length. This discrepancy may either arise from the unique conformation of bottlebrushes impacting their elution behavior or else polymerization proceeds preferentially on unreacted side chains over side chains attached to the growing backbone polymer.

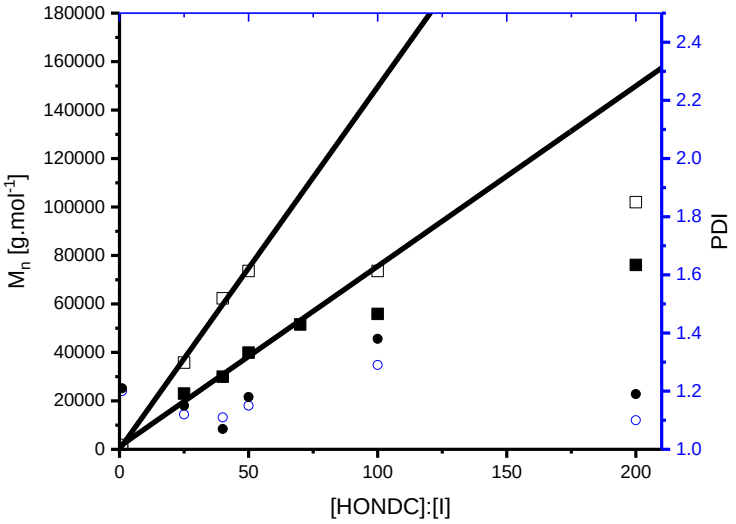

Figure 2-29: Linear correspondence of molecular weight of bottlebrush on monomer: initiator ratio employed for 10 equivalents of L-lactide (light squares) and 5 equivalents of L-lactide (dark squares. linear fits show strong linear dependence at low DP's. At higher DP's linear fit and experimental data diverges, indicating lack of control. Corresponding dispersities plotted on the same graph (circles).

On the other side, when considering the bimodal elution traces, the experimental molecular weight of the brush fraction is lower than expected, while the molecular weight of the unreacted homopolymer is heavier than expected. For the bimodal GPC trace of **84** for example, the two fractions were evaluated separately. ^{1}H NMR analysis of the reaction mixture predicted a theoretical molecular weight of 273 000 g.mol^{-1}, while the GPC determined an average molecular weight of 134 000 g.mol^{-1}. The lighter fraction, representing HONDC-initiated PLLA has an expected Mn of 3 100 g.mol^{-1} whereas the experimentally established weight is higher at 4 000 g.mol^{-1}. This indicates that L-lactide polymerization proceeds preferentially at the less sterically hindered free chains rather than at the crowded bottlebrush. If that be the case, incorporation of the growing side chains may result in a certain gradient effect reminiscent of the conical bottlebrush polymers that MATSON et al.[184]

have synthesized via sequential macromonomer addition. However, the simultaneous nature of this work makes it impossible to spatially resolve the side chain distribution along the backbone.

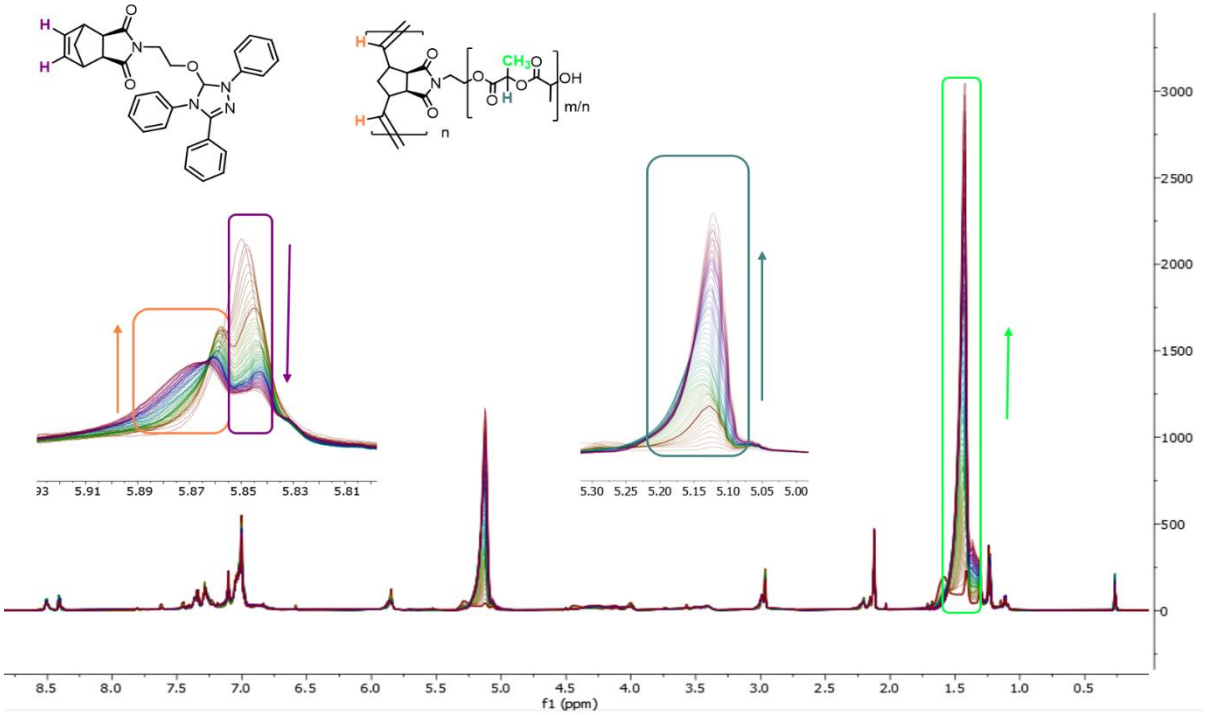

Figure 2-30: In-situ 1H NMR in toluene-d8 at 298K of tandem process. Olefin peak at 5.85 ppm of monomer HONDC decreases (window left) as polymeric HONDC olefin peak at 5.87 ppm increases. polymeric L-lactide methine peak at 5.07 ppm increases simultaneously (window right). Proving the simultaneous nature of the process. The spectra were recorded by Dr. Manfred Wagner.

As before *in-situ* ^{1}H NMR spectra were recorded by [redacted]. The polymerizations were conducted with an initial HONDC concentration of 0.06 M, a targeted side chain DP of 10 and a backbone DP of 100. The recorded spectra were digitally overlaid and globally aligned (see Figure 2-30). Red spectra show early stages in the polymerization and purple spectra represent late stages in the reaction. As in the ROP only kinetic study, the methine signal's intensity of the polymer increases steadily. Unlike the ROP only spectra, the Tandem process shows distinct changes throughout the reaction progress. The olefin peak at 5.85 ppm loses intensity as the reaction progresses, with the concomitant appearance of polymeric olefin peaks at 5.87 ppm and 5.59 ppm. These signals are characteristic for the successful ROMP of the HONDC backbone monomer. As the reaction was stopped after 24 h, the ROMP process has not reacted to completion as evidenced by the remaining intensity of

the signal at 5.85 ppm. These kinetic ^{1}H NMR prove that the polymerization does indeed take place simultaneously and the catalysts remain active during the entire timeframe surveyed.

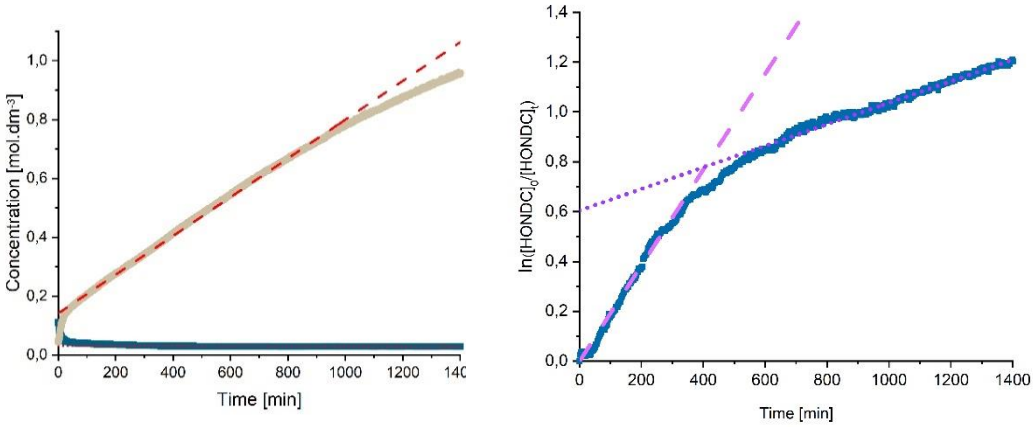

Figure 2-31: Kinetic plots of tandem polymerization. Left: concentration of L-Lactide monomer (black) with linear fit showing the rapid decrease in monomer during initial reaction stages followed by an equilibrium range due to monomer solubility and product concentration (red) showing rapid polymerization in the beginning and pseudo zero-order kinetics in later stages of the reaction. Right: half-logarithmic plot of conversion of HONDC monomer with reaction time with two distinct linear fits showing biphasic behavior.

The kinetic plots (Figure 2-31) show the L-lactide concentration (monitored via relative intensity of the peak at 4.08 ppm) in the tandem reaction mixture to decrease rapidly at first and then entering a stable plateau. These finding reflect the limited solubility of lactide in toluene at 80 °C. After an initiation period where dissolved L-lactide is consumed, an equilibrium establishes between dissolution rate and monomer being consumed through the proceeding polymerization. The constant concentration of monomer leads to pseudo zero-order kinetic behavior of the polymerization. Plotting product concentration as a function of time produces a straight line (see Figure 2-31). A linear fit shows good agreement after the initial polymerization period with a rate constant of k_{obs} = 1.1x10^{-5} mol.dm^{-3}.s^{-1}.

The concentration of HONDC monomer in the polymerization solution was monitored by the peak intensity at 5.85 ppm. Due to the partial overlap between monomer and polymer peaks, the data was deconvoluted using a data processing function in MESTRENOVA X64. To assess the reliability of the deconvolution software, a solution with known concentration of macromonomer and bottle brush polymer was prepared in toluene-d_8 and compared to the deconvoluted integrals. The deconvolution software was able to separate the two peaks efficiently. Additionally, the experiment was repeated in $CDCl_3$, as it was previously established that in a more polar solvent, the monomer and polymer signals are better separated.

Plotting the natural logarithm of HONDC conversion against reaction time produces a kinked line, characteristic for a biphasic exponential decay (see Figure 2-31). The biphasic nature of the system can be explained by the growing side chain length with progressing reaction extend, which limits the mobility of the reacting species. Two linear curves were fitted to the distinct reaction phases with the initial phase showing a rate constant of $k_1 = 3.2 \times 10^{-5}\ s^{-1}$ a later phase with rate constant $k_2 = 7.2 \times 10^{-6}\ s^{-1}$. These findings are in marked contrast to the first order kinetic behavior reported of ROMP homopolymerizations with Grubbs-III catalyst[51,188] and can be linked back to the interacting nature of the tandem system at hand. Nonetheless, this kinetic data shows that both polymerizations truly proceed simultaneously.

2.5 Bottlebrush Structure

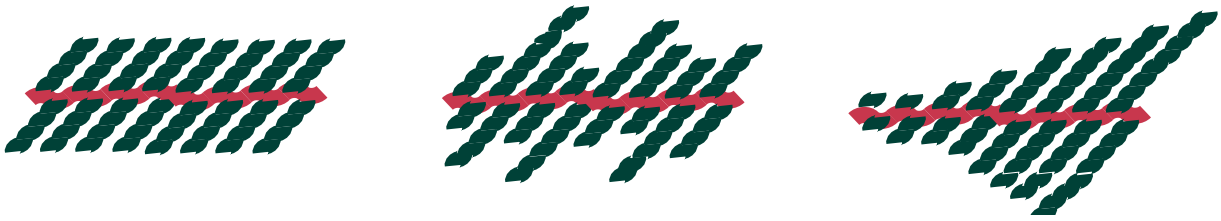

Figure 2-32: Schematic representation of potential intramolecular side chain distributions all resulting in the same number average molecular weight of molecular brush. Left: low dispersity of individual side chains, center: statistical incorporation of high dispersity side chains, maximizing side chain degree of freedom and right: preferential ROP in solution rather than at the growing backbone leads to conical shaped molecular brushes.

The markedly narrow molecular weight distribution of the short brush polymers synthesized via simultaneous tandem grafting was quite surprising, given that these copolymers are the product of two polymerizations. This low PDI and close match between theoretical molecular weight and experimental molecular weight may be taken as indicative of excellent control over both polymerization mechanisms. However, an alternative interpretation of the same results is conceivable when considering this particular molecular architecture. As with any block copolymer, the polydispersity index does not reflect the dispersity of the individual blocks but rather of the copolymer as a whole. This observation leads naturally to the question whether the narrow molecular weight distribution observed herein is the product of both narrow side chain distribution and narrow backbone distribution or whether the brush architecture masks a wider distribution. When considering molecular brush **50** for example, the observed molecular weight of ~60 000 g.mol^{-1} may either be a product of ~39 side chains, with each chain ~1 600 g.mol^{-1} and narrow polydispersity or else that of ~39 side chains with some side chains markedly heavier and some markedly lighter (see Figure 2-32 for a schematic representation). GPC and ^{1}H NMR experiments of molecular brushes allow only to make observations over the whole polymer's weight distributions, not that of the side chains.[198]

Additionally, when considering that the steric interactions of for ROP of L-lactide at the side chains that have already been incorporated *via* ROMP are much greater than those that are still freely in solution, it is conceivable that the free chains grow faster than the tethered chains. Such an effect might could in turn result in the formation of conical shaped molecular brushes with the terminal side chains much longer than the earlier incorporated

chains (see Figure 2-31). As the step-wise grown molecular brushes portray markedly different molecular weight distributions, analyzing ROP of L-lactide only would not help to answer this question as the characteristic interactions of the tandem system would be neglected. To test whether the low polydispersities arise from homogeneous and controlled polymerizations, from statistically distributed side chain lengths, or else from conically-shaped brushes, a two-fold approach was pursued: the shape of the molecular brushes was observed *via* atomic force microscopy (AFM), and depolymerization of the backbone was employed to determine the side chains' uniformity.

2.5.1 Atomic Force Microscopy

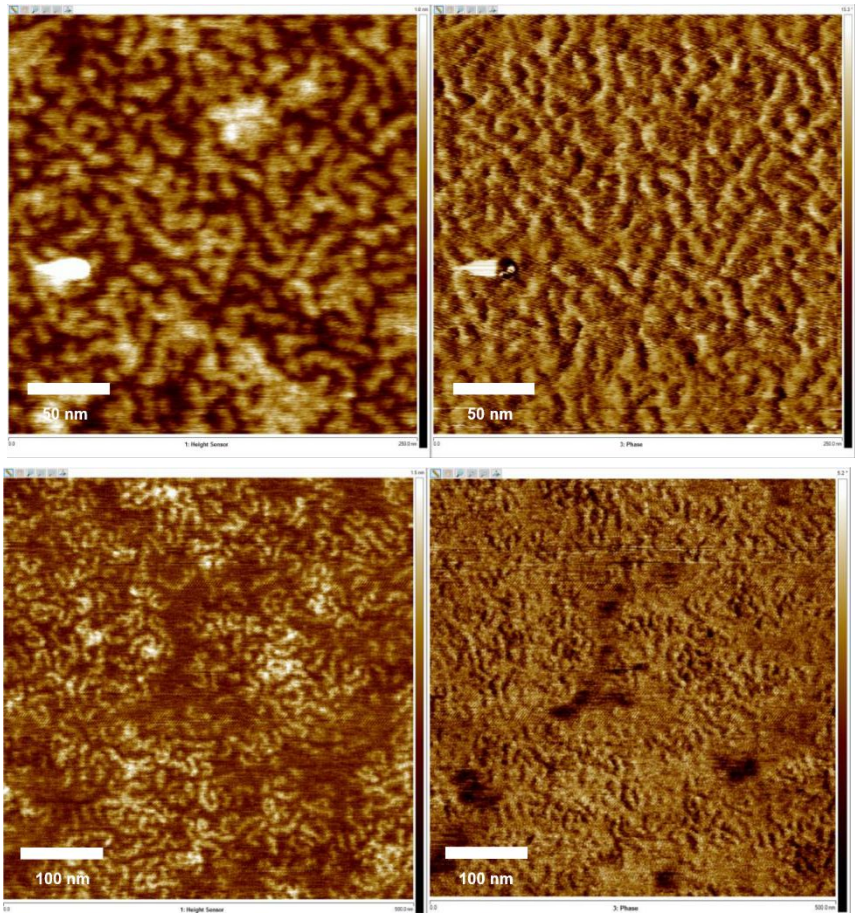

Figure 2-33: AFM micrographs of **86** on a freshly cleaved mica wafer. a) and c) topography, color legend 1.5 nm, b) phase, color legend 15.2 ° and d) phase, color legend 5.2 °.

In 2017, MATSON et al[184]. synthesized cone-shaped brushes by sequential addition of macromonomers with different DPs and proved AFM measurements to be capable of determining such form factors. Similarly, for this project AFM experiments were conducted to assess any potential form factors arising from a slower polymerization off the backbone than in solution. For this purpose, a dilute solution of **86** in THF was cast onto a freshly

cleaved mica surface. By this approach, a monolayer of molecular brushes was formed as the solvent evaporated. The AFM micrographs (see Figure 2-33) show the characteristic "worm-like" structure of molecular bottlebrushes. Light regions in the topographic micrographs represent higher structures and darker areas are lower structures. It is evident from the topography recordings that the brushes (although relatively uniform in general) show a certain variation in length. The observed length scales correspond to the extended backbone of molecular brushes, while the side chains may be observed indirectly through the height profiles. The length of extended brushes is in the order of magnitude of 50 nm while their height (i.e. the diameter) is around 1.5 nm and corresponds to the spatial arrangement of the L-lactide coils. Cone-shaped structure such as described above could not be detected, although such observations might be difficult to make at the length scales at hand. The curved conformation of the BBs are a result of the poor interaction of side chains with gold substrate. As a consequence, the PLLA coils minimize contact and adopt a curved conformation. [119]

2.5.2 Depolymerization of Backbone

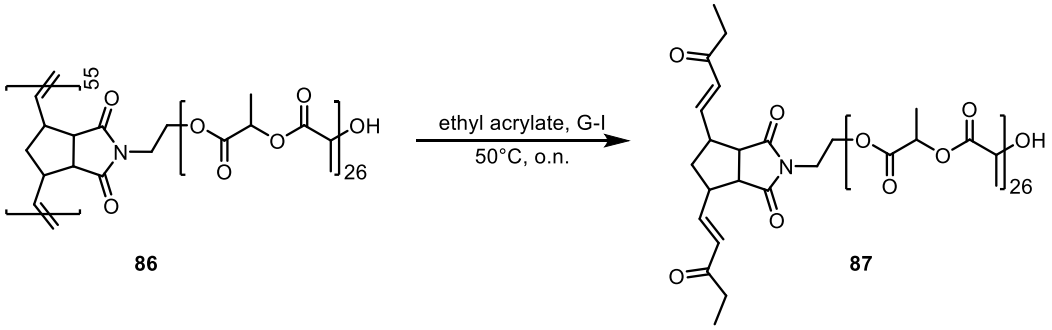

Scheme 2-11: Insertion depolymerization of **86** to investigate the side chain length distribution.

The orthogonal nature of the polymerizations employed herein also allow for targeted depolymerization. The unsaturated backbone can be depolymerized selectively while leaving the polyester side chains unaffected. This approach permits to investigate the origin of the low polydispersity index of the low backbone DP brushes, while also giving insight into the origin of the increased PDI of higher targeted DP's. If the side chains show a unimodal, narrow molecular weight distribution, the higher PDI must arise through losing control over the ROMP process only. WAGENER et al. have established that unsaturated polymers can be selectively depolymerized through catalyst Grubbs-I mediated metathesis with various acrylates[199]. As previously shown, Grubbs type catalysts do not interfere with (poly-) esters during polymerization and it may thus be safely assumed that the polyester side chains remain intact during depolymerization too. Employing acrylates for the depolymerization allows to work under atmospheric pressure unlike when polymerizing with ethylene gas.

Table 2-17: Molecular weights of molecular bottlebrush **86** and after depolymerization (**87**)

Entry	$DP_{side\ chain}$	$DP_{backbone}$	Mn_{theo}	Mn_{exp}	PDI[c]
86	26	55	220 000	224 000	1.42
87	26	1	4 000	6 000	1.15

A representative depolymerization was conducted with molecular brush **86** that portrays the characteristic high PDI of longer targeted backbones (55 repeat units of HONDC). A sample of **86** was dissolved in ethyl acrylate and after overnight depolymerization by Grubbs-I the side chains were isolated *via* preparative GPC. Figure 2-34 shows the molecular weight distributions before and after depolymerizations. The 224 000 $g.mol^{-1}$ molecular weight of molecular brush **86** with PDI of 1.42 was decreased to 6000 $g.mol^{-1}$ and a PDI of 1.15 in the isolated side chains **87**.

The isolated side chains were then submitted to MALDI-ToF MS to yield absolute mass

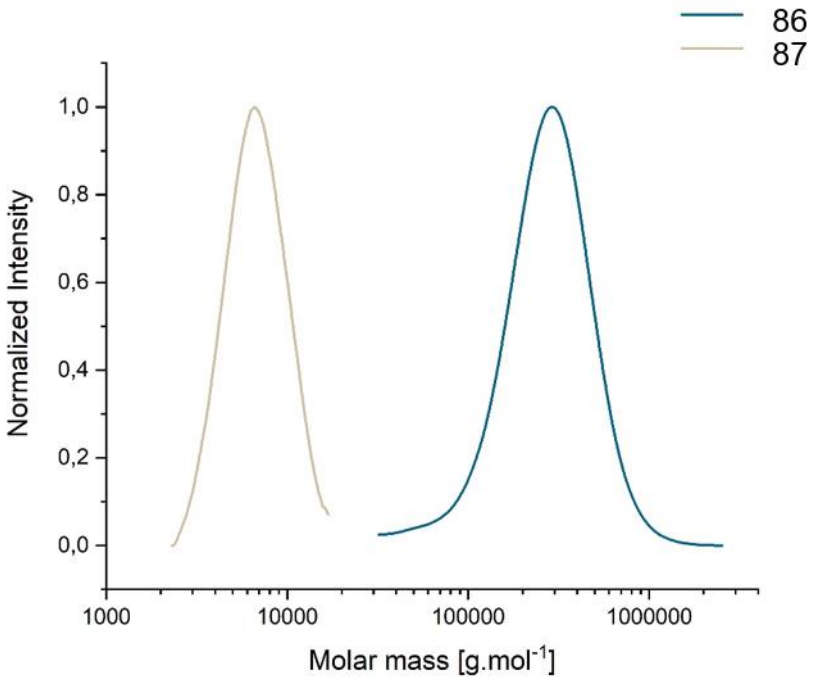

Figure 2-34: GPC traces of molecular bottlebrush **86** and its depolymerization product **87** Elution in THf *versus* polystyrene standards

information. Unlike the GPC results, MALDI-ToF MS showed a much more narrow distribution of the side chains at 1.05 (see Figure 2-35). Three main populations were identified when analyzing the isotopic fine structure, differing only in the mass of one ^{16}O and half of an L-lactide repeat unit only. The L-lactide repeat unit was confirmed by the 144.040 Da difference between individual peaks of the same population. Analysis of the fine structure did not lead to satisfying congruence between theoretic end-group and experiment.

The average degree of polymerization was calculated to be 26 repeat units of L-lactide, resulting in a number average molecular weight of 3 750 g.mol^{-1}. These results are in marked contrast to the molecular weights established *via* GPC but may be explained by the mismatch between polarities of the polystyrene reference material *versus* the PLLA sample. In comparing the two analytical tools, MALDI-ToF MS as an absolute method should take priority in interpretation. The very low dispersities of the individual side chains and the excellent match between the HONDC:LLA ratios as established by ^{1}H NMR with the established DP *via* MALDI-ToF MS indicates that the ROP of L-lactide is very well controlled and its polymer products homogeneous throughout the polymerization.

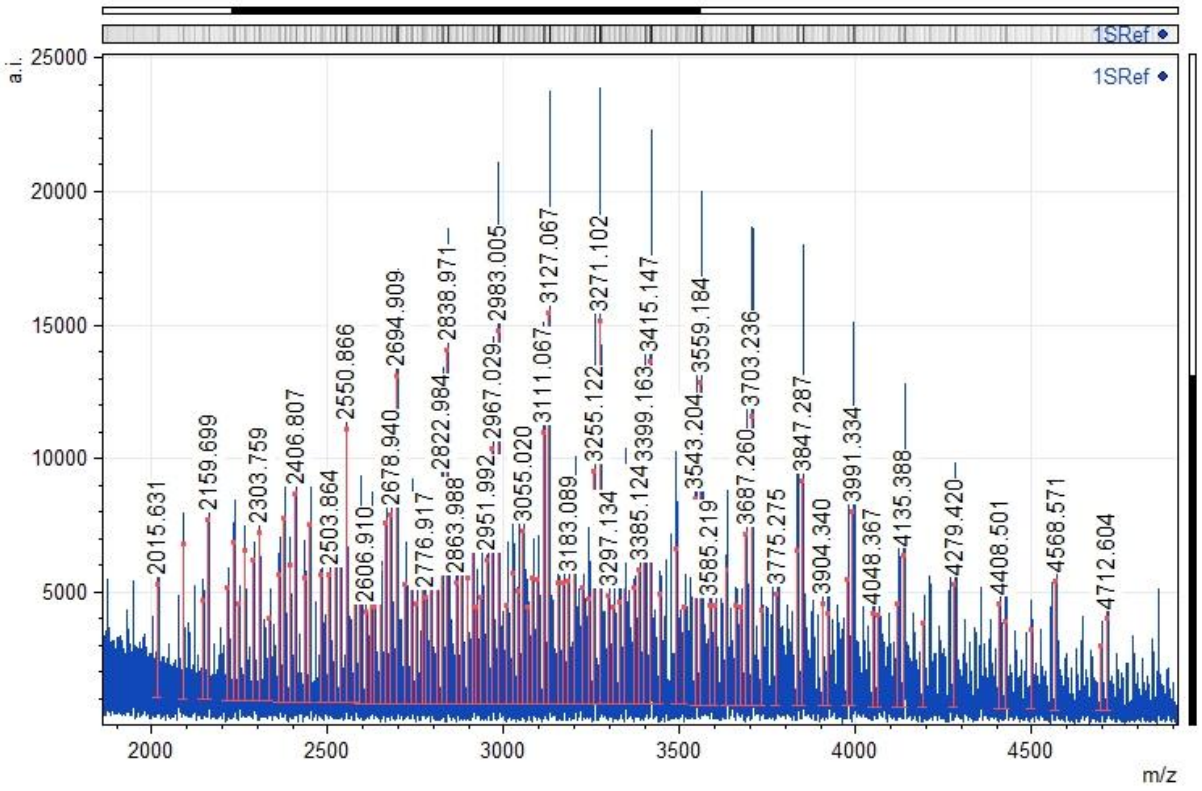

Figure 2-35: MALDI-ToF mass spectrum of depolymerized brush **87**.

2.6 Conclusion

The simultaneous bottlebrush project was motivated by a desire to simplify the synthesis of molecular bottlebrushes, while mitigating some of the caveats of established techniques. The orthogonal combination of ROMP with ROP was chosen as an advantageous path to allow for simultaneous polymerization of backbone and side chains in a single step.

Starting from a catalyst combination employed by FREUDENSPRUNG et al.[39], a promising catalyst-monomer combination was tested. The Grubbs-II catalyst was chosen to produce the poly(norbornene-methanol) backbone, while NHC SIMes catalyzes the poly(LLA) side chains. Orthogonality was assessed using ^{1}H NMR experiments and homopolymerizations. It was shown that the various combinations of orthogonal catalysts and monomers remained stable over the experiment timeframe. In contrast to the auspicious findings of these preliminary experiments, employing this set of monomers and catalysts did not result in the expected bottlebrush polymerization. It was established that the stereochemistry of backbone monomers plays a significant role for the polymerizability using Grubbs-type catalysts. As a consequence, monomers were designed to reduce steric interactions (*exo*-monomers) and lower the probability for forming inactive complexes with the metathesis catalyst. The norbornene-derived monomer HONDC combined great ring strain, *exo*- orientation and entropically favorable placement of hydroxy group.

In addition to compatibility and orthogonality, this project rested on the ambition to establish a tandem system with comparable reaction rates. Previous publications reported the simultaneous ATRP and ROMP to yield molecular bottlebrushes but saw full conversion of one monomer within minutes, while the second monomer polymerized in several hours. Likewise, for the purposes of this project, SIMes was found to polymerize LLA too fast to match the rate of ROMP by Grubbs-type catalysts Grubbs-II, Grubbs-III and pyridine analogue Grubbs-IIIP. The thermally activated NHC DTT finally allowed to match reaction rates. The DTT mediated ROP of L-lactide was proven to act orthogonal to the Third Generation Grubbs catalyst mediated ROMP of HONDC.

A two-step process was established involving the synthesis of a macromonomer and the subsequent ROMP thereof without quenching or work-up steps. Excellent yield and control was achieved with several side chain lengths as well as several backbone DP's. The DTT NHC proved both valuable in tuning reaction kinetics due to its temperature dependence, as well as solubilizing the monomer in an apolar solvent.

For the first time, a simultaneous tandem bottlebrush polymerization was conducted. In only one step, the Third Generation Grubbs catalyst mediated ROMP of HONDC produced a polymeric backbone. Simultaneously, the DTT mediated ROP of L-lactide was conducted in the same reaction vessel, which produced covalently tethered poly(L-lactide) chains off the HONDC polymeric backbone. The simultaneous nature of the process was highlighted through the *in-situ* ^{1}H NMR observation of the tandem procedure. The one-pot, one-step technique produced very well-defined, narrowly dispersed bottlebrushes under excellent control when low backbone DP's were targeted. The one-step approach produced much more narrowly distributed molecular brushes than the two-step process, even when using the same catalysts and monomers. Depolymerization of the backbone showed that both backbone and side chains are narrowly distributed. The low molecular weight distribution was attributed to the ability of tandem polymerizations to mitigate the steric demands usually associated with bottlebrush synthesis. However at longer targeted backbones, the high temperatures required for the tandem process hindered full conversion of the backbone monomer.

The tandem process extends the synthetic toolbox for yielding molecular bottlebrushes. The remarkable control over the reaction when targeting short brushes enable the synthesis of well-defined, highly precise products. Pursuing one-pot strategies not only lowers solvent consumption but provides a greatly simplified synthetic route.

3 SIMULTANEOUS SURFACE GRAFTING

3.1 State of Literature

The project described in this chapter aimed at synthesizing mixed binary brushes in only one polymerization step. Synthesizing densely grafted, covalently attached mixed polymer brushes requires both adequate control over the two polymerization steps, the grafting density as well as control over the individual chains' lateral distributions. Previously, these requirements are addressed *via* multistep syntheses that can be roughly divided into the "grafting to" and "grafting from" categories. An overview of these strategies is presented in Figure 3-1. Counting among the former, previously synthesized polymer chains can be deposited on a surface by functionalization with a reactive end group capable of bonding with the surface of interest. Either two different homopolymers bearing an anchoring group are deposited one after the other (see Figure 3-1 a) or else Y-shaped diblock copolymers are deposited on the surface in one step (see Figure 3-1 b). Using a sequential grafting-to approach, DUPONT-GILLAIN et al.[106] synthesized PEO/PAA brushes on gold surfaces to study protein adhesion, MINKO et al.[200] deposited poly dimethyl siloxane (PDMS)/P2VP brushes for chemical gate applications and PDMS/polyethylinimine[201] to study non-wettable hydrophilic brushes. Prominently, STELLACCI et al[202]. immersed nano-sized gold particles into a solution of hydrophobic and hydrophilic thiols to produce amphiphilic mixed brushes. The simplicity and versatility of this approach is counterbalanced by its poor control over the chains' lateral distribution. Although STELLACCI[202] established *via* (contested[203]) STM measurements that the

self-assembled structures led to a range of interesting surface separations, it remains that thermodynamic, rather than synthetic considerations dictate the self-assembly of the two polymers on the surface. A one-to-one lateral resolution can be enforced by employing previously synthesized diblock copolymers. As every surface reactive group is attached to both polymers, these two will by definition be neighboring. TSUKRUK et al[204]. have employed the above technique to synthesize mixed short chain polymer brushes and observed spontaneous micelle formation on the surface due to chain incompatibility. However the Y-shaped diblock grafting-to approach further exacerbates the predominant issue associated with grafting-to techniques: steric hindrance. Grafting-to requires either solution or melt conditions. As a consequence, polymer chains are in their random coil structure, potentially shielding the anchoring group and blocking other inbound polymers from attaching to the surface. Depending on the radius of gyration (and by extension molecular weight) of the inbound brushes, high grafting densities may not be achieved and the polymers often remain in a mushroom rather than a brush regime. Hence, if high grafting densities are a desired property, this technique is unsuitable.

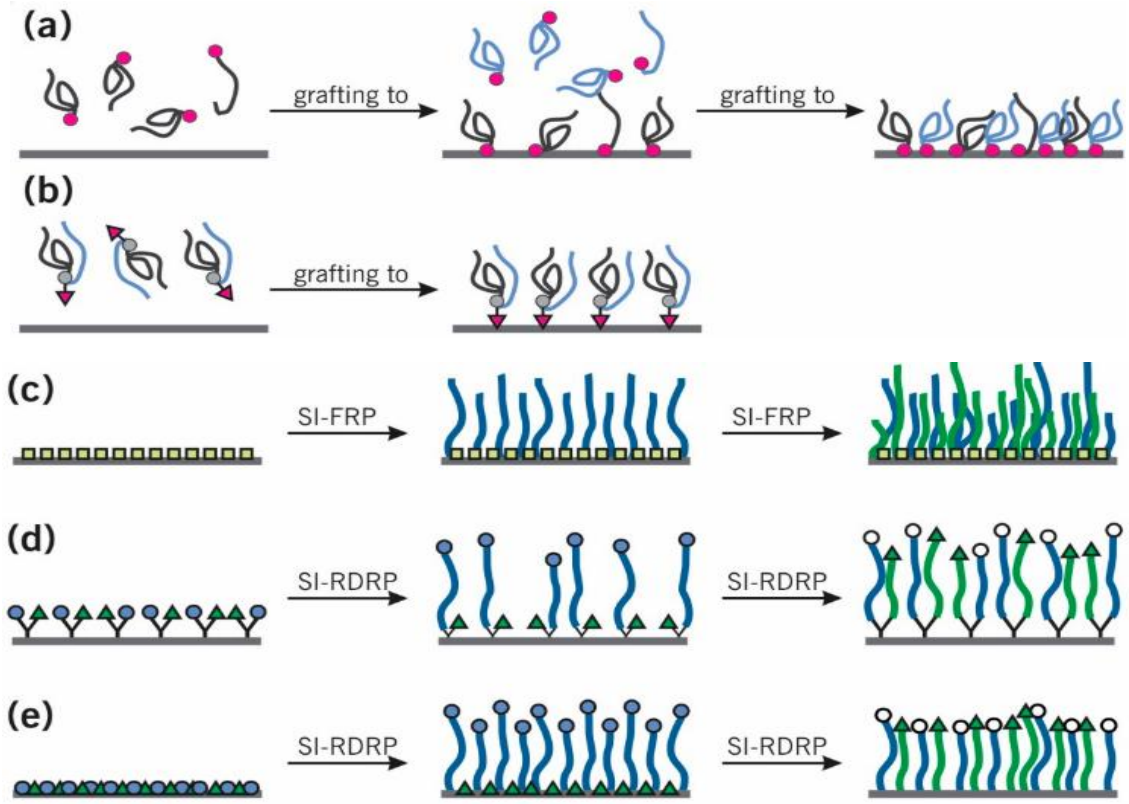

Figure 3-1: Schematic illustration of different synthetic routes. (a) Step-wise "grafting to" of individual homopolymers, (b) "grafting to" of Y-shaped diblock copolymers, (c) step-wise "grafting from" via surface-initiated free-radical polymerization (SI-FRP) using non-selective initiators, (d) "grafting from" via SI-RDRP using Y-shaped bifunctional initiators , and (e) "grafting from" via surface-initiated reversible-deactivation radical polymerization (SI-RDRP) using two disparate co-deposited initiators. Reproduced with permission from [99].

The grafting-from approaches can roughly divided into three groups of synthetic strategies. The synthetically most straightforward technique relies on the random surface-initiated (free radical) polymerization (see Figure 3-1c). The surface is first functionalized with a non-specific initiator (e.g. azo-initiators) that then initiates the free radical polymerization of the first monomer. As the thermal decomposition of azo-imitators is temperature dependent, the reaction conditions can be tuned so that only a portion of the initiators has been consumed by the end of the first polymerization. In a second step, the other monomer is polymerized by the remaining surface initiators. MINKO et al.[101,102,204] used this technique to graft thick incompatible brushes with the combination of PMMA/PSt, PSt/P2VP and PMA with the random copolymer Poly(styrene)-*stat*-poly(2,3,4,5,6-pentafluorostyrene) (PSF) and observed a responsive surface self-organization. Employing free radical polymerization has its own intrinsic issues: the immobilization of initiators on the surface dictates that the propagating chains are all in very close proximity to one another, increasing the probability of recombination. Employing controlled polymerization techniques may solve this particular issue but unselective initiators still suffer from poor control over lateral resolution. MINKO et al.[101] reported that using unselective initiators led to a "nucleation"-induced separation of the two homopolymers. The group observed that small fluctuations in the grafting points led to microphase separation and hence impacted the location of the phase separated domains.

To overcome the issue of unselectivity, one can employ two orthogonal polymerization techniques. Through deposition of two independent, selective initiators, the two brushes can be grown without competition for the same grafting site. The two initiators can either be (co-)deposited randomly (see Figure 3-1 e) or by exploiting three-armed (Y-shaped) initiators (see Figure 3-1 d). Employing a Y-shaped bifunctional initiator with anchoring moiety allows for much greater control over the location of the two immiscible polymers. In a first step, a monolayer is formed by reacting the bifunctional initiator with a complementary functional group on the surface of interest. The use of Y-shaped bifunctional initiators allows to introduce heterofunctional initiating moieties. By this approach, the two polymer chains can grow independently off the surface, while also ensuring that the two polymers are well-mixed. Indeed, an alternating surface coverage can be enforced[85]. This approach has been employed for the step wise RAFT and ATRP off mesoporous silica particles[115]. Through the combination of NMRP and ATRP, mixed brushes were synthesized at silica wafers[205].

If the aim is to produce a densely grafted surface, well within the brush regime, the step-wise polymerization is unsuitable. For all surface-initiated syntheses of binary brushes, one major issue remains: the steric hindrance of the represented by the radius of gyration of the first polymer blocks access to the initiating sites. The first polymerization step occurs (relatively) unimpeded: initiation takes place at the unhindered surface. If all chains grow at

comparable rates, monomers only have to diffuse to the polymerizing front of the brush. However when polymerizing the second set of chains, the monomer has to diffuse through the crowded chains of the first polymer to the surface. Although monomers are small, the high steric bulk inside the brush represents a great hindrance. The effect is only exacerbated when the second monomer has a polarity incompatible with the already existing chains. MINKO et al.[102] explored the effects of grafting sequence on the final polymer composition. When synthesizing PS/P2VP mixed polymer brushes, they found that grafting the second polymer was only possible if the less polar polymer was grafted first. The polar polymer interacted more strongly with the silica surface, impeding grafting of the second polymer. Increased steric hindrance is inherent in all step-wise polymerizations, irrespective of the polymerization technique or monomer identity.

The only way to avoid these steric effects is to ensure that both polymers grow at the same time and at comparable reaction rates — a simultaneous approach is required. Controlled and spatially defined polymerizations yielding two chemically distinct polymers necessitate the use of orthogonal techniques. The polymerizations must not interfere with one another while chemically distinguishing between the two monomers. Although such approaches have been successfully employed in the synthesis of block copolymers, their successful application for the synthesis of mixed binary brushes remains limited. BRITTAIN et al[206]. and ZHAO et al.[207] used the NMP/ROP system developped by SOGAH et al.[208] to graft respectively PSt/poly phenyl oxazoline and PSt/PCL chains "simultaneously", although no reports of the kinetic compatibility were made. The employment of NMP as orthogonal polymerization mechanism is attractive due to the ease of employment. On the other hand, NMP is notoriously difficult to control when monomers encourage side reactions[16]. NMP works best for the polymerization of styrene and its derivatives while with methacrylates is liable to suffer from disproportionation. As a result, the choice of monomers and hence the feasible polymeric architectures is further restricted.

HADJICHRISTIDIS et al.[209] have successfully employed ATRP/ROP grafting-from carbon nanotubes. The functionalization was achieved through [4+2] DIELS-ALDER reaction with the tube walls, followed by stepwise introduction of the two initiators. The stepwise nature of their synthesis led to a random distribution of initiating moieties across the nanotube. This approach does not allow to control the location of the initiating moieties, nor their density. To the best of our knowledge, a simultaneous synthesis has never been achieved while also controlling grafting density as well as enforcing maximal mixing on a molecular level. A system combining hydrophilic and hydrophobic polymers has never been reported.

3.2 Concept

As explained in the previous chapters, retaining control over the polymerization of two different monomers to form two discrete polymer blocks requires the employment of two distinct, mutually orthogonal polymerization techniques[39]. Employing two types of monomers with different properties but polymerized via the same pathway in a one-pot, one-step procedure would result in statistical copolymers. Ensuring an even distribution of hydrophilic and hydrophobic polymer brushes with nanometer-scale resolution is envisioned via control over the initiating sites. By choosing polymerization mechanisms that are initiated selectively by chemically different initiating functionalities, the placement of the initiators on a surface will thus determine the placement of the resulting polymer chains. To maximize the interface between hydrophobic and hydrophilic polymer chains, the two initiating sites are bonded together covalently at a one to one ratio, enforcing an alternating grafting. This is achieved by the help of a trifunctional center, where one arm initiates polymerization of a hydrophobic monomer, a second arm initiates polymerization of a hydrophilic monomer and the final arm serves to immobilize the initiators on the surface. After the formation of a monolayer of this trifunctional linker, the two monomers and necessary (co)catalysts are added in one step to start the simultaneous polymerization. The concept is pictorially represented in Figure 3-2.

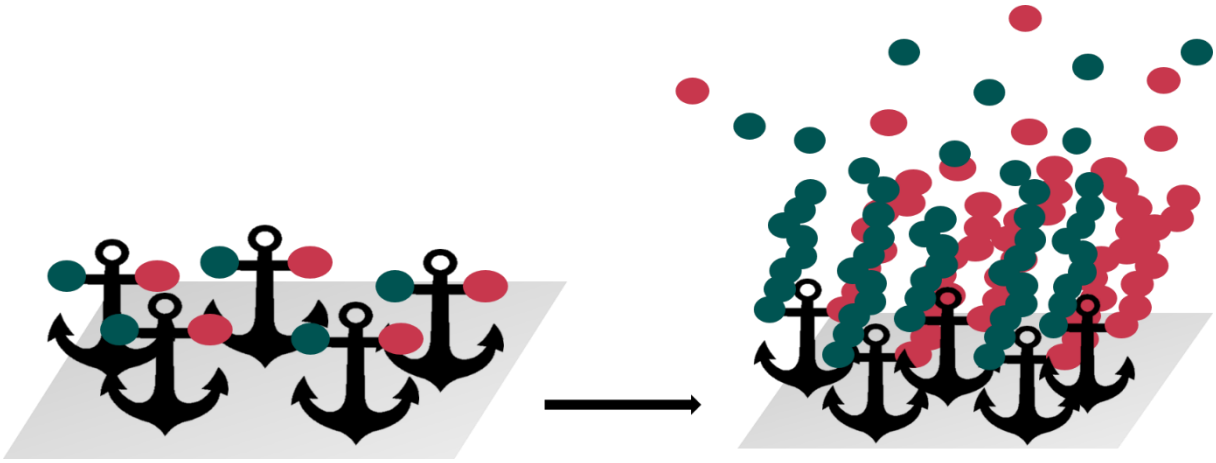

Figure 3-2: Schematic representation of simultaneous surface grafting concept. In a first step, a self-assembled monolayer (SAM) of the trifunctional, dual initiator is immobilized on a surface (left). In a second step, the two monomers are added to the reaction mixture and polymerized with the help of suitable catalysts (right).

The chemical identity of the initiating sites is dictated by the polymerization processes to be employed. ATRP appears to be a promising approach for the purpose of simultaneous surface grafting. The technique offers a relatively large range of reaction parameters that may be tuned and hence has been shown to successfully polymerize a large multitude of

monomer functionalities[210]. Synthetic access to the alkyl halides that commonly serve as ATRP initiators is relatively straightforward. These considerations dictate the chemical identity of the first initiating arm.

The second polymerization technique to be employed must be orthogonal to ATRP, i.e. must not proceed via a radical polymerization pathway. Anionic ROP of cyclic esters promises to be a viable candidate for this purpose due to the range of monomers and catalysts that may be employed, as well as the large ranges in polymerization kinetics that have been described[31,211,212]. ROP is most commonly initiated by primary alcohols, offering hence a motif for the second initiating arm.

It is of major importance that the two polymerizations occur with comparable rates so that the growing polymer front does not hinder access to the active chain ends. Additionally, the simultaneous polymerizations must allow to target different molecular weights. As was shown by simulations[98], a large mismatch in chain lengths (orders of magnitude) would lead to only one polymer dominating the interface (*vide supra*).

Depending on surface properties, various functionalities are conceivable for anchoring the initiators, including chemically bonded approaches as well as physisorption. While physisorption offers a synthetically more facile access, chemical bonding offers the advantages of greater robustness and greater specificity[104]. Physisorption is a dynamic, equilibrium controlled process. Although great stability has been demonstrated, particularly when exploiting multi-valent interactions, it is conceivable that in a high-temperature environment and subjected to various monomers, catalysts and solvents, the physisorbed linker may detach from the surface. The increased steric repulsion of the growing polymer chains on the other hand might then provide a barrier to re-attachment. Desorption of individual linkers would then lead to a decrease in grafting density, which is to be avoided, making the chemically bonded approach more attractive. The exact identity of the anchoring group depends on the substrate of choice. Gold surfaces, such as those explored by Stellacci[202], are often functionalized by the help of thiol groups. Silica and silicon surfaces are most commonly addressed by trialkoxisilanes, or trichlorosilanes. Iron oxide surfaces may be decorated by the help of phosphates etc. For the scope of this project, it was decided to explore the functionalization of silica or silicon surfaces. This decision was inspired by the relative price of the substrate as well as by the scope of comparable literature available of functionalized silica surfaces in a vast variety of geometries[213].

3.3 Synthesis of Bifunctional Initiator

For the envisioned concept, the key to attaining spatial resolution of the two polymers is the molecular design of the initiator. Generally speaking, initiator choices are dictated by the monomer that is to be polymerized and the polymerization mechanism. For a well-controlled system, the rate of activation should be at least as fast as the rate of propagation[214]. In a simplified picture, if the rate of initiation is much faster than the rate of propagation, most initiating sites will be activated within early polymerization times and monomers react statistically with all initiating sites. Conversely, if the rate of propagation is much faster than the rate of initiation, only few initiating sites will be activated and will consume large proportions of the available monomer before other initiating sites react. The selection of an efficient initiator is particularly important when employing ATRP to graft off surfaces. A dense distribution of ATRP-derived chains can only be achieved if each site initiates reliably. The initiator can be thought of as a dormant chain end and thus activity predictions for initiators rely on the same principles as predicting monomer reactivity: the better a radical is stabilized by adjacent functional groups, the higher the initiator activity[215]. Hence, tertiary alkyl halides are much more reactive than secondary or primary alkyl halides and neighboring ester groups result in better initiators than a phenolic residue[215]. Additionally, weaker C-X bonds make more efficient initiators and hence initiating efficiency increases in the order Cl<Br<I[215]. Generally speaking, choosing an initiator that is much more active than necessary is more desirable than an initiator that is not active enough for the system. A commonly applied rule of thumb dictates that the initiator be structurally related to the employed monomer[215]. ATRP of styrene for example is commonly initiated by 1-bromoethyl benzene and methacrylate polymerizations initiate well with alkyl 2-bromoisobutyrates.

A convenient synthetic access to highly active alpha-bromo ester initiators is provided through esterification of an alcohol or amine with the initiator precursor bromo-isobutyryl bromide. **88**

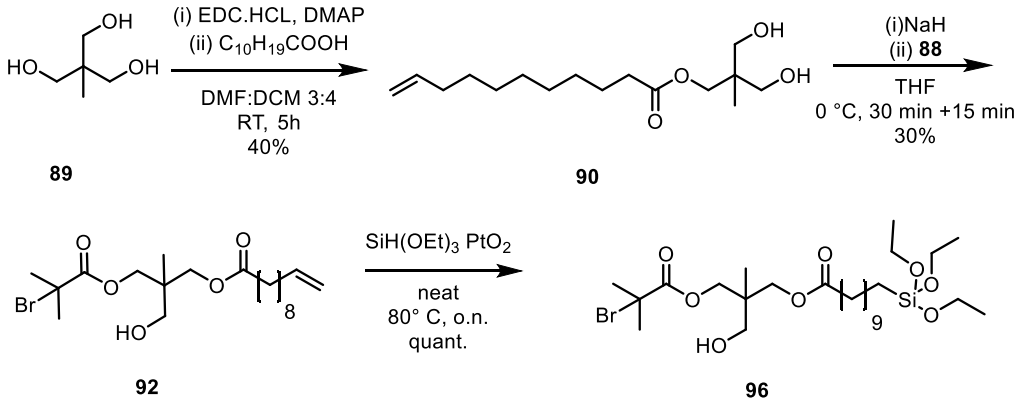

Scheme 3-1: Synthetic overview to yield trifunctional linker for planar silicon surfaces without protective groups. STEGLICH esterification of trimethylol ethane (**89**) by undecenolic acid in under-stoichiometric proportions followed by under-stoichiometric deprotonation and esterification by bromo isobutyryl bromide (**88**) and final platinum (IV) oxide mediated hydrosilylation.

In the first step, trimethyloyl ethane **89** was functionalized *via* STEGLICH esterification with 10-undecenoic acid. Several solvent systems were tried out and only the DMF:DCM 3:4 mixture was found to satisfactorily dissolve all educts and reagents. The lack of chemical specificity of this reaction involving three identical alcohols implies the formation of a statistical distribution of singly, doubly and triply esterified products, as well as unreacted starting material. To counteract this tendency and reduce the waste of valuable chemical resources, the inexpensive triol **89** was employed in three-fold excess to the coupling reagents. By this approach, the amount of doubly and triply functionalized side products was reduced. The water-soluble unreacted excess **89** could then be washed out in a simple extraction step. The target molecule 3-hydroxy-2-(hydroxymethyl)-2-methylpropyl undec-10-enoate **90** was isolated from the unwanted side products by column chromatography. The isolated yield was expectedly low with 40% with respect to the carboxylic acid. ^{1}H NMR (see Figure 3-3), MS and IR (see Figure 3-7 a)) were used to confirm the successful reaction.

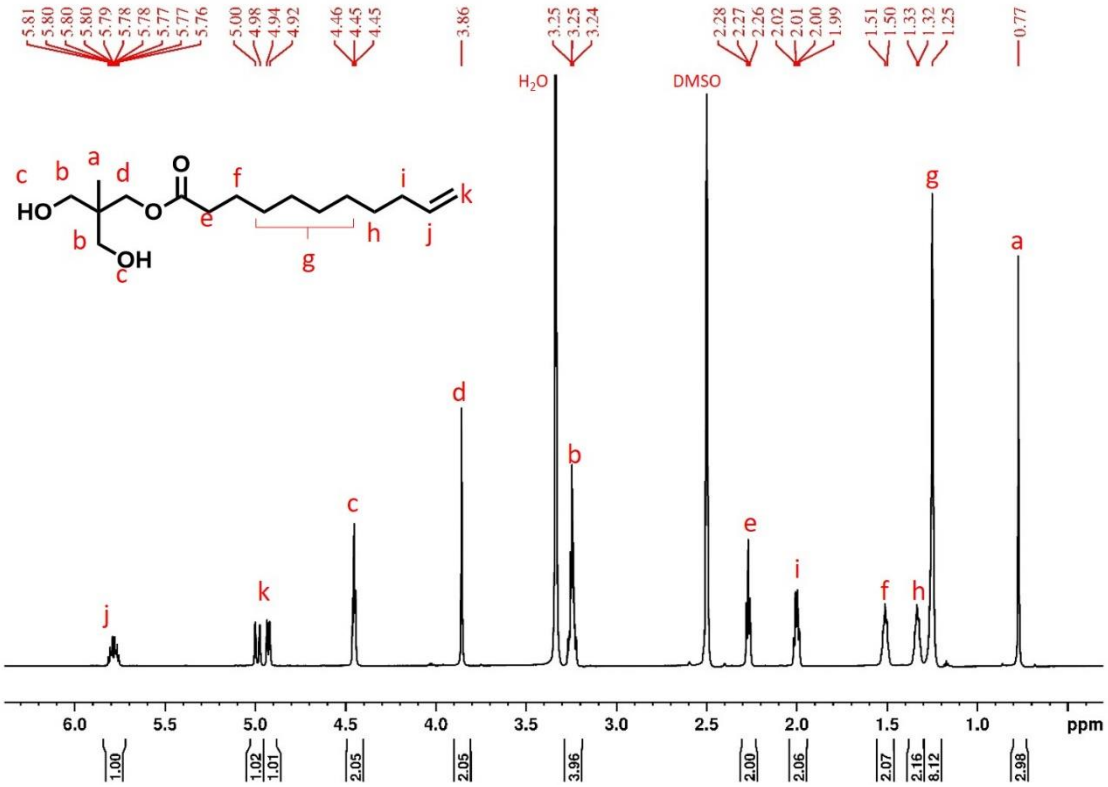

Figure 3-3: ^{1}H NMR spectrum of diol **90** isolated via column chromatography, recorded in DMSO-d_6 at a 700 MHz spectrometer.

The ^{1}H NMR of product **90** showed the characteristic olefin peaks with the multiplet at 5.87 — 5.66 (**j**) and the two doublets at 4.99 and 4.93 (**k**). The signal at 3.86 (**d**) shows the successful ester coupling through the significant downshift with respect to the four equivalent protons at 3.25 (**b**). Integration of the three methyl protons at 0.77 (**a**) show the expected 3:1 intensity with respect to the ß-vinylic proton (**j**).

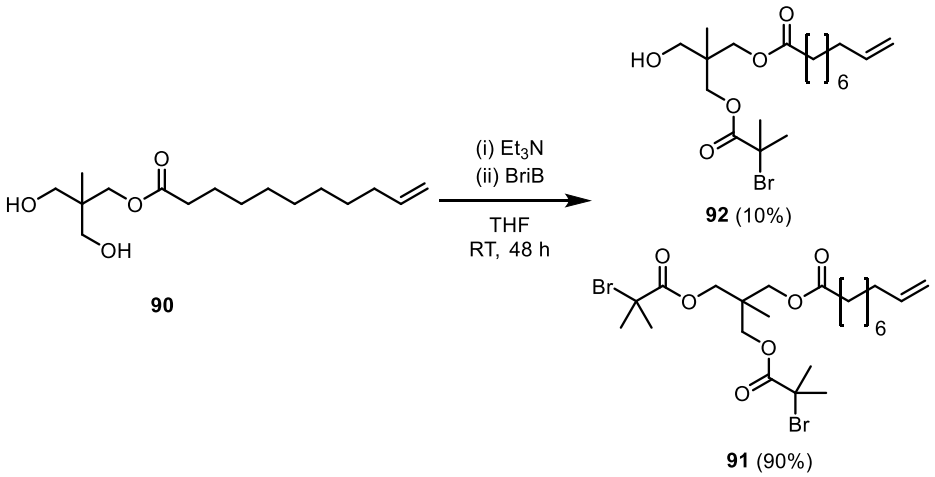

Scheme 3-2: Acylation of diol **90** by acylation with BriB and triethylamine in THF to yield the dual acylated product **91** preferentially over the single functionalized **92**.

In order to introduce the ATRP initiating group, one of the primary alcohols of the ester molecule **90** was acylated through reacting with the acyl halide α-bromo isobutyryl bromide **88**. As before, the two primary alcohols are equivalent to one another and a mixture of products is expected. The alcohol and trimethylamine were dissolved in THF and reacted with slowly added, neat acid bromide **88**. The acid bromide **88** was employed in just under-stoichiometric amounts so as to reduce the amount of doubly-functionalized product. After 48h, ^{1}H NMR spectra of the crude product proved the quantitative reaction of **88** with the diol **90**, while thin layer chromatography showed the disappearance of acid bromide **88**, with remaining diol **90** as expected given that **88** was employed as limiting reagent. However, after purification of the product by column chromatography and isolating the individual product fractions, it transpired that the crude product comprised two side products and unreacted starting diol **90**. The major product was the doubly functionalized ester **91** with 90% yield. A much smaller fraction was isolated and characterized as the desired compound **92** in only 10% yield. The reaction was repeated with 0.8 equivalents of acid bromide **88** with respect to diol **90**, to encourage a greater fraction of single functionalized product. Given that under-stoichiometric amounts of acyl halide were employed, it was concluded that the reaction conditions favored the dual functionalization *per se*. Two hypotheses were explored: either the addition of neat acyl bromide **88** into the reaction solution leads to a local concentration spike, followed by rapid reaction with more dilute diol or else the inter- or intramolecular interactions of diol **90** are strong enough as to make the diol less nucleophilic. To test the first hypothesis, the reaction was repeated with addition of 0.8 equivalents of **88** with respect to diol **90.** Contrary to the previous reaction, the acyl halide was added to a dilute solution of diol **90** in THF. The reaction again showed the preferential dual functionalization. The reaction progress was monitored via ^{1}H NMR and showed that the reaction of acid bromide

88 proceeded relatively slowly; after 2 hours of reaction time, conversion was only 8%. These findings speak against the hypothesis of local concentration differences that favor the dual functionalization, as such an effect could only be observed if the rate of diffusion is much lower than the rate of reaction. Observing that THF is a good solvent both for diol **90** as well as for acid bromide **88** and that the reaction rate is relatively slow, the hypothesis of diffusion controlled kinetics was rejected.

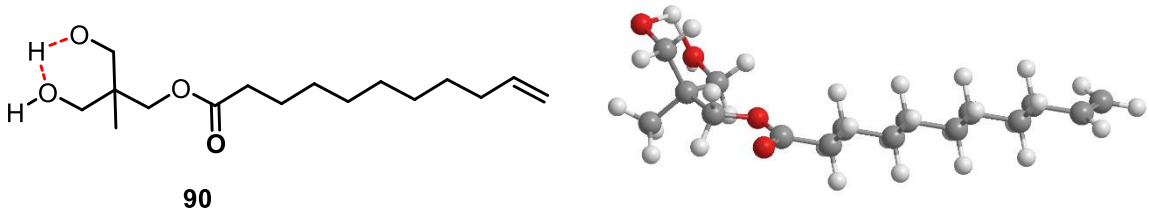

90

Figure 3-4: Three-dimensional model of diol **90** showing the intramolecular hydrogen bonding interactions, stipulated to discourage single acylation.

The presence of strong intra-molecular interactions have previously been demonstrated for 1,3-diols both in theory[216] as well as experimentally[217]. If the diol **90** exhibits strong intra-molecular hydrogen bonding, the oxygen lone pairs are less available for nucleophilic attack on the acyl halide**88**. Conversely, after undergoing one acylation reaction, the intramolecular interactions are interrupted and the remaining alcohol of **92** is activated with respect to the diol **90**. Formation of the dual acylated product **91** is hence favored and would explain the observed trends. This hypothesis was tested by changing the reaction medium to a more polar solvent. N,N-dimethyl formamide has a larger dipole moment than THF and with the addition of LiCl, it was hoped to break the hypothetical hydrogen bonding present in the diol. The reaction in DMF with LiCl yielded marginally higher yields of **92** than in THF. Still, these yields were deemed too low as to represent a worthwhile solution to the synthetic problem at hand.

Instead it was opted to encourage a single acylation by deprotonating the diol **90** with the help of under-stoichiometric amounts of NaH. It was stipulated that the dual deprotonation of the diol is thermodynamically unfavorable due to the presence of two negative charges within the same molecule. Additionally, deprotonation is a reversible process and hence an equilibrium may be reached so as to maximize the population of single alkoxides which are then trapped by the addition of acyl halide **88** to yield the targeted molecule **92**. This approach significantly increased the proportion of desired compound **92** to 80% in the crude product, and 65% overall yield after purification by column chromatography.

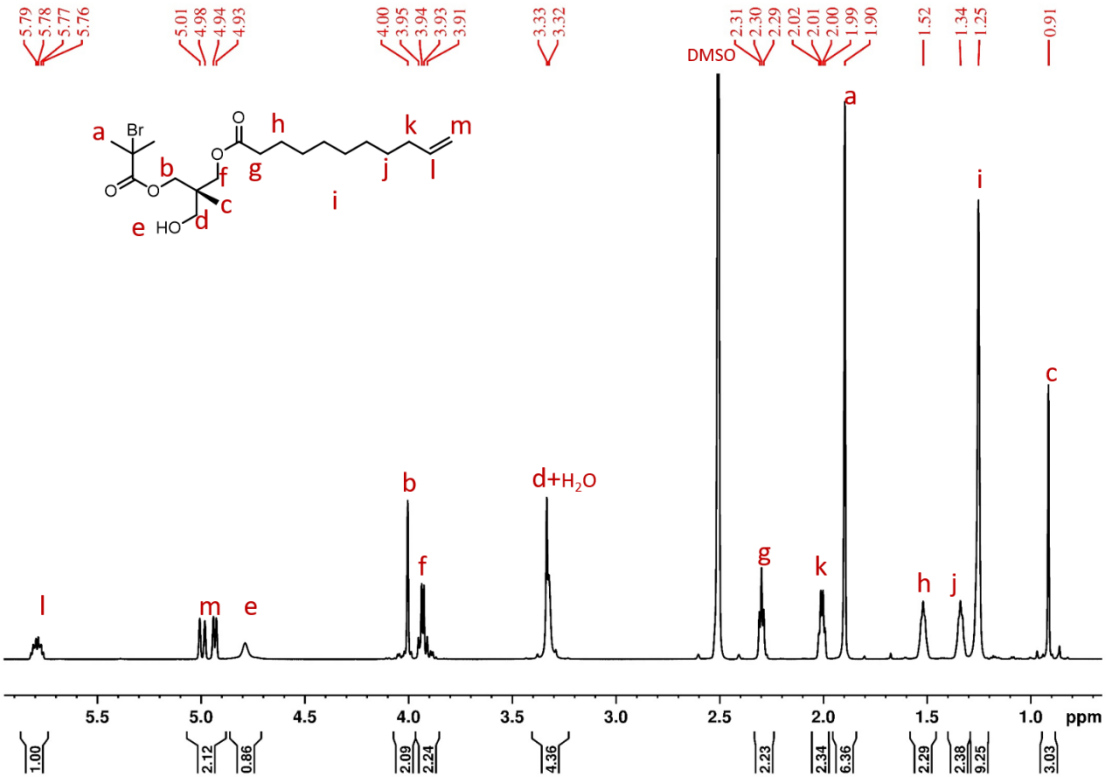

Figure 3-5: ^{1}H NMR of spectrum of bifunctional initiator **92** in DMSO-d_6 at a 700 MHz spectrometer.

^{1}H NMR spectrometry was used to confirm the chemical structures of isolated product **92**. Again, the vinylic proton (l) at 5.78 were used to compare the integral ratios between the three methyl protons (c) at 0.91 and the six methyl protons (a) at 1.90 and found the expected ratio of 1:3:6. The signal at 4.00 (b) reveals the successful synthesis of haloester **92** and the broad signal at 4.79 (e) confirms that only one equivalent of alcohol reacted.

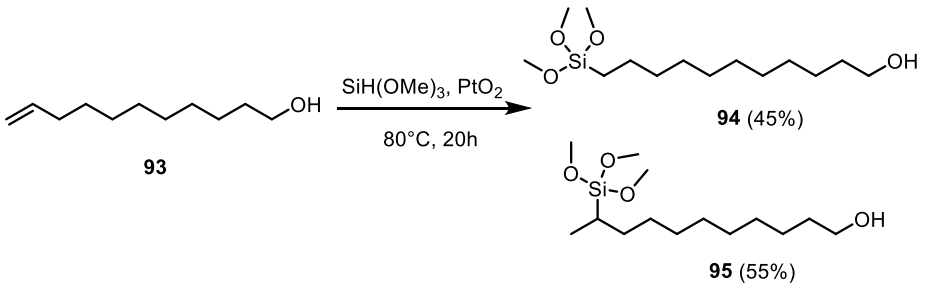

Scheme 3-3: Test reaction of hydrosilylation of 10-undecenol **93** with trimethoxysilane according to Mioskowski, yielding a mixture of terminal silane **94** and its regioisomer **95**

Hydrosilylation was conducted using platinum (IV) oxide according to a procedure published by MIOSKOWSKI et al. [218]. The procedure has been shown to be resilient and tolerant

of a wide range of functional groups, including primary amines and carboxylic acids. However, the group did not report on the efficiency for the reaction with vinyl compounds bearing alcohols. A model reaction was conducted to ensure the compatibility of this functional group with the hydrosilylation conditions. For this purpose, 10-undecenol **93** was reacted with trimethoxysilane using platinum (IV) oxide as catalyst. ^{1}H NMR spectra showed the complete disappearance of the olefin signals and the new appearance of two high field signals representing the products arising from silylation of the methine and the methylene carbon respectively.

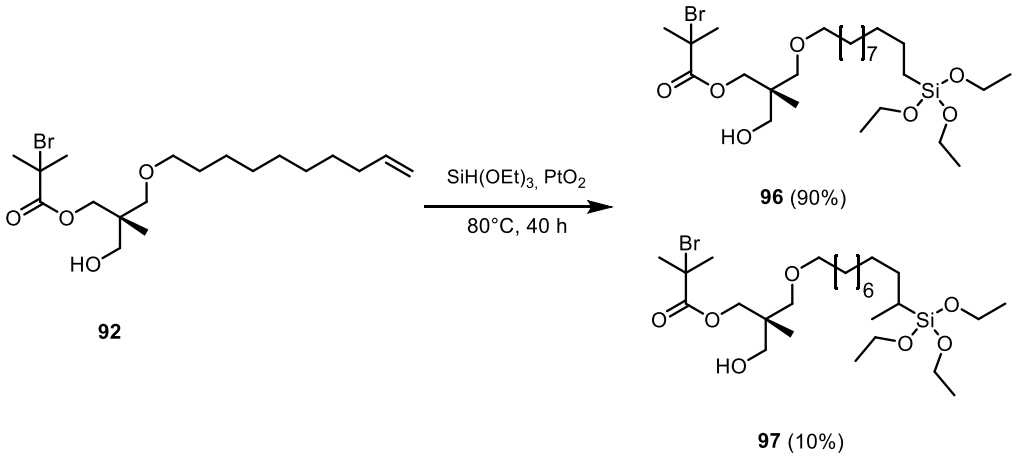

Scheme 3-4: Hydrosilylation reaction of **92** to produce the target compound **96** with a 10% occurrence of regioisomer **97.**

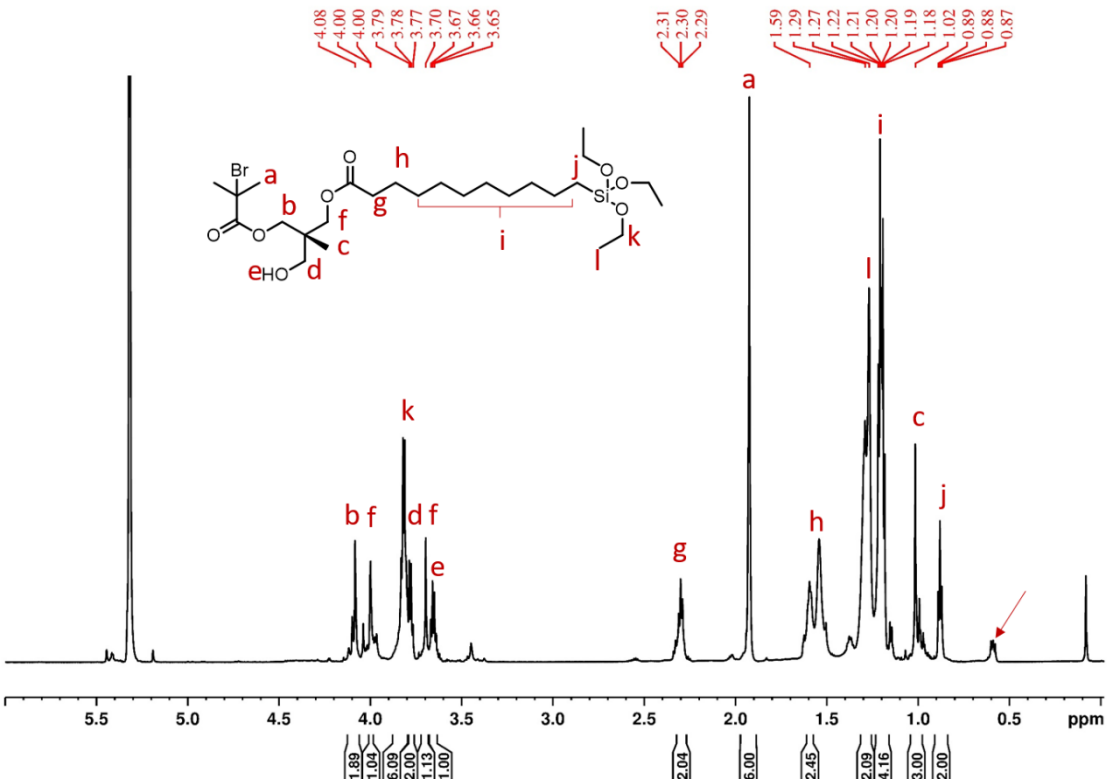

Figure 3-6: 1H NMR of bifunctional anchor **96** in DCM-d2 at a 700 MHz spectrometer.

After the successful test reaction, the hydrosilylation reaction was repeated with **92** to produce the target linker. Unlike the test reaction, the hydrosilylation was more selective towards terminal silylation with a selectivity of 90% **96** and 10% of regioisomer **97**. The silylation occurred quanitatively after 40 h reaction time. The linker was characterized via ^{1}H NMR, ^{13}C NMR, DOSY NMR, IR and MS.

Successful silylation was confirmed by ^{1}H NMR analysis (see Figure 3-6). The quantitative silylation was confirmed by the absence of vinylic protons in contrast to the earlier reaction steps. Noteworthy changes include the appearance of silyl ether signals (**k** and **l**) at 3.78 and 1.22 respectively and the shielded proton adjacent to the silyl ether (**j**) at 0.87 ppm. The calculated integrals match the expected signal intensity ratios of **a**:**c**:**j**:**k** of 6:3:2:6. The arrow in Figure 3-6 indicates the presence of minor product 2-silyl ether (**97**). Throughout the spectrum, signals of the minor isomer appear as impurities. Separate DOSY ^{1}H NMR experiments further confirmed the covalent attachment of all functional groups. All target molecule derived signals occur at the same diffusion coefficient. Mass spectrometric analysis confirmed the presence of a compound at 553.3 u. This mass reflects the expected mass of target molecule **96** of 598.25 lacking the mass of C_2H_5O as a consequence of fractionation at the silyl ether.

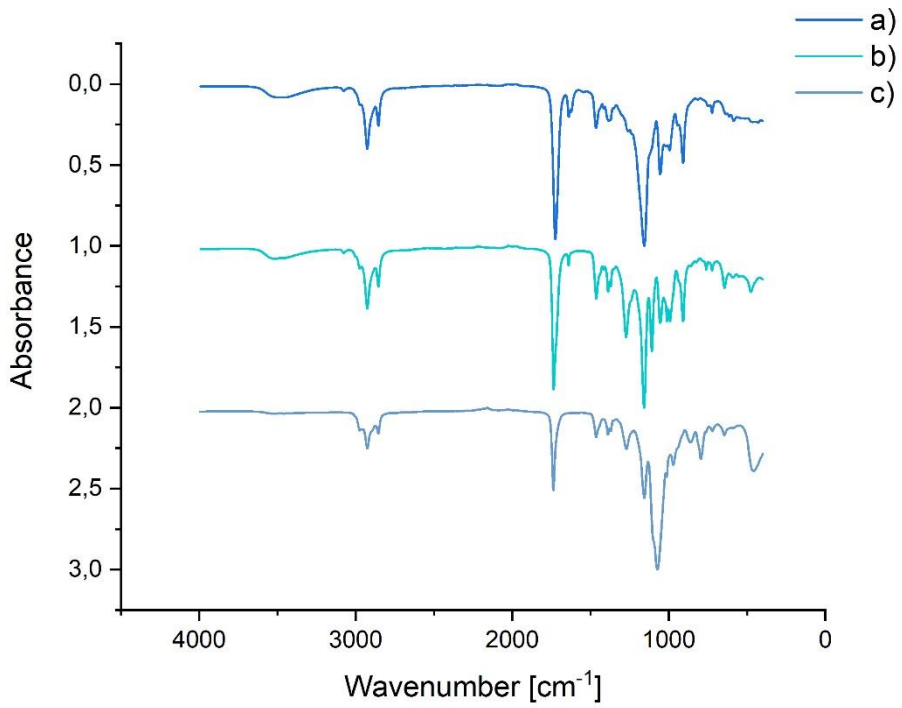

Figure 3-7: FTIR spectra of a) diol **90**, b) haloester **92** and c) linker **96**.

Fourier transform infrared spectroscopy was conducted on the intermediaries and the target molecule described above (see Figure 3-7) The characteristic signals are reported in Table 3-1 and confirm the ^{1}H NMR measurements. All three products show the broad O-H stretching vibrations between 3520-3475 cm^{-1} expected from the primary alcohol in all compounds. Unspecific alkane C-H stretches were observed for all compounds between 2850-2975 cm^{-1}. In contrast to diol **90**, products **92** and **96** showed the characteristic germinal dimethyl bending doublets at 1388 cm^{-1} and 1371/1368 cm^{-1}. As expected, diol **90** and haloester **92** show terminal olefin stretching at 1640 cm^{-1} and bending vibrations at 992 cm^{-1} and 908 cm^{-1} respectively. The hydrosylilated target molecule **96** in contrast does not show these olefin signals. All three compounds produce ester stretching vibrations between 1725 cm^{-1} and 1740 cm^{-1} and two signals at 1270 cm^{-1} and 1160 cm^{-1}. All these signals were expected and confirm the ^{1}H NMR results.

Table 3-1: Summary of characteristic vibrations measured by FTIR (ATR crystal) of compounds **90**, **92** and **96**

Compound	Wavenumber	Vibrational Mode
90	3479 br. med.	*ν (-O-H)*
	2924 and 2853, s, med.	*ν* (-CH, sp^3)
	1724, s, strong	*ν (-C=O Ester)*
	1158 s, strong,	*ν (-C=O Ester)*
	1052	*ν (-C-OH alcohol)*
	992 and 909	*δ* (-CH=CH_2)
92	3518 br. med.	*ν* (-O-H)
	2976, 2927 and 2855, s. med.	*ν* (-CH, sp^3)
	1731 s, strong,	*ν (-C=O Ester)*
	1640	*ν* (-CH=CH_2)
	1463 s, weak	*δ* (-C-H)
	1388 and 1371 s, med.	*δ* (-C-H *gem. dimethyl*)
	1272 s, med. and 1158 s, strong	*ν (-C-O-C Ester)*
	1055	*ν* (-C-OH)
	992 and 908	*δ* (-CH=CH_2)
96	3499, br. weak	*ν* (-O-H)
	2971, 2928 and 2854 s, med.	*ν* (-CH, *sp^3*)
	1739 s, strong,	*ν (-C=O Ester)*
	1465, s, med.	*ν* (-CH, *sp^3*)
	1388 and 1368, s, med.	δ (-C-H *gem. dimethyl*)
	1269, s, med. 1161, s, strong	ν (-C-O-C *Ester*)
	1076	*ν* (-C-OH)

3.4 Immobilization on Silicon Wafer

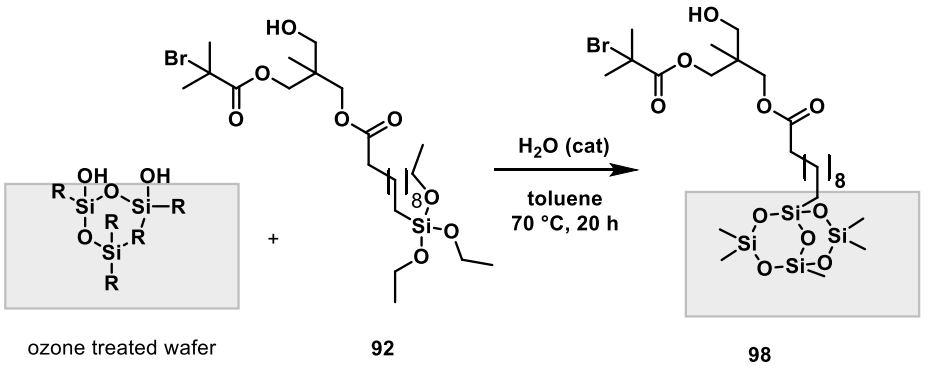

Scheme 3-5: Immobilization of linker **96** on an ozone pretreated silicon wafer to yield the linker modified wafers **98**.

Commercially available silicon (100) wafers have an ill-defined surface chemistry. In order to maximize the amount of linker binding onto the silicon surface and hence produce a full self-assembled monolayer, these wafers must be pretreated to produce a homogeneous surface, available for chemical targeting. For this purpose, the 5 mm x 5 mm wafer cutouts were first cleaned through consecutive washings in cyclohexane, methanol and acetone in an ultrasound bath to remove any soluble impurities on the surface. By treating the wafers in an ozone oven for 30 min, the surface was hydrophilized. Treatment of silicon surfaces with ozone plasma results in the oxidation of the surface reaching several nanometers into the wafer substrate[219]. This approach maximizes the number of accessible silanol groups on the surface. In the presence of trace amounts of water, these silanol groups react with the silyl ethers of linker **96** to yield the condensation product of linker modified silicon surfaces. The wafers were characterized via ToF-SIMS, XPS (see Figure 3-8) and contact angle measurements (see Figure 3-9).

XPS characterization showed a dominating signal associated with oxygen (O1s) on both the reference wafer **99**as well as the functionalized wafer **98**, as expected (arrows on Figure 3-8 A) and B)). The surface layer of the silicon wafers was fully oxidized by treatment in an ozone oven, reflected in the strong oxygen peak. A closer view at the characteristic binding energy of C1s between 280 and 290 eV (Figure 3-8 C) and D)) reveals the presence of carbon species both in the reference **99** and the functionalized wafer **98**. These findings are not surprising as most samples even in brief contact with atmosphere show a small (nanometer thick) layer of adventitious carbon[220]. During sample preparation, the both wafers were in contact with air and a clear signal of adventitious carbon is to be expected. However

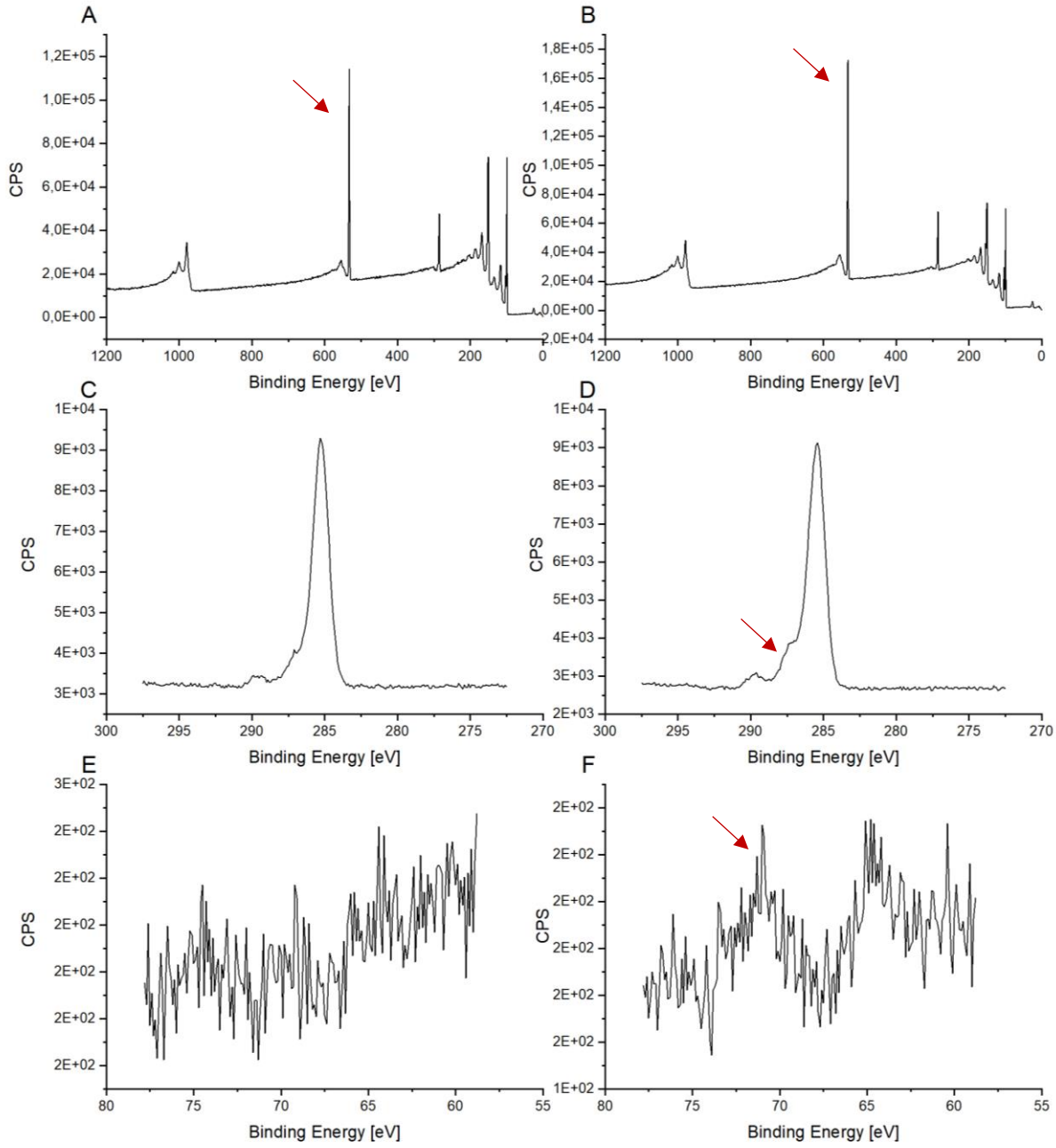

Figure 3-8: XPS plots of A) survey of clean reference wafer, B) survey of immobilized linker **98** C) high resolution C1s region of clean wafer D) C1s region of immobilized linker **98** with prominent carbonyl shoulder, E) Br1s region of reference wafer showing background noise only and F) Br3d region of linker wafer **98** showing weak signal of characteristic signal of bromine.

when observing the C1s peak of the functionalized wafer **98**, it is noticeable that in contrast to the reference **99**, a significant shoulder can be seen (see arrow in Figure 3-8 D)). This higher energetic shoulder indicates the presence of carbonyl carbons associated with the linker functionalities. The binding energies associated with bromine show a weak, yet significant characteristic signal for the initiating wafer **98** in contrast to the reference wafer **99** (compare arrows in Figure 3-8 F) to E)). These spectra strongly indicate the presence of linker species after treating a clean wafer with a solution of linker **96**.

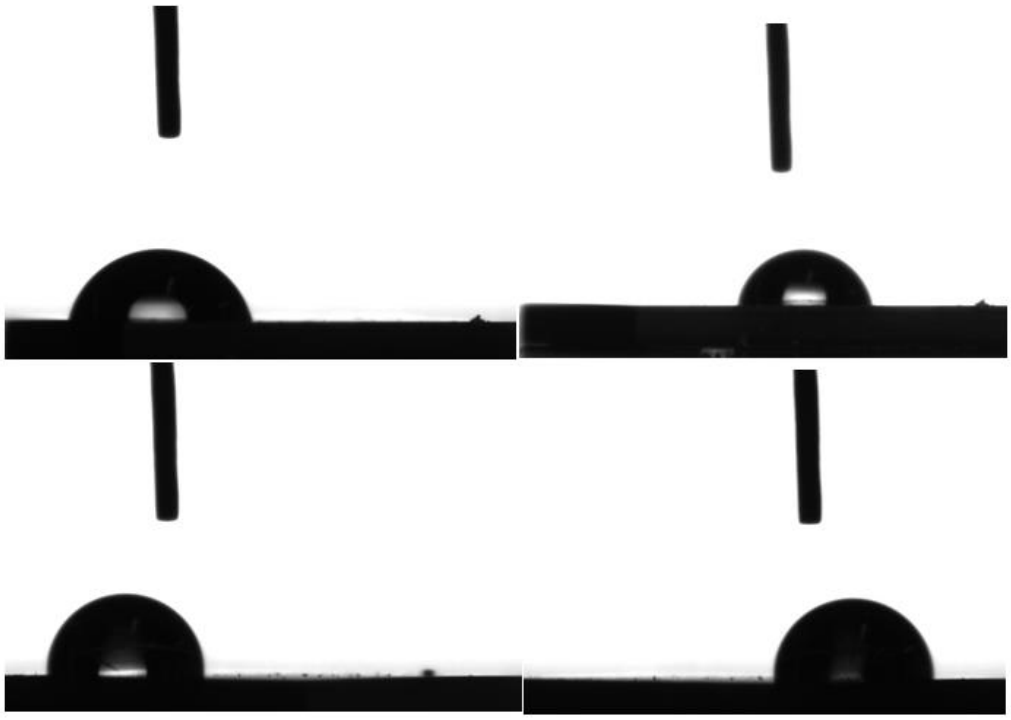

Figure 3-9: Contact angle measurement of water on reference wafer (top two images) revealed a contact angle of 79.9° ± 0.2°. The linker modified wafer **98** (bottom two images) had a contact angle of 92.7° ± 0.8°.

Contact angle measurements revealed a significant increase in contact angle following the immobilization of linker on pre-treated wafers. For the purpose of these measurements, the reference wafer chosen was a commercial silicon (100) wafer from the same batch as the functionalized wafer, washed with methanol and acetone in an ultrasound bath but was not submitted to ozone treatment. This is to reflect that wettability of ozone treated wafers depends on the time of ozone treatment, as well as the time elapsed after treating with ozone[221]. The cleaned wafer had a contact angle with water of 79.9° ± 0.2°. In contrast, the wafer functionalized with linker **98** had a much more hydrophobic surface, resulting in a contact angle of 92.7° ± 0.8°. These contact angle measurements will serve as basis for contrasting the grafted wafers.

3.5 Reaction Conditions for Simultaneous ATRP-ROP

In 2005, FONTAINE et al[222]. have shown that DBU can be used as a ligand for the ATRP of methacrylates and sytrene. Polymerization products of methyl methacrylate showed narrow molecular weight distributions (1.19) and good molecular weight control when using ethyl 2-bromoisobutyrate (2-EBiB) as initiator. Polymerization control was worse for methacrylic acid and styrene and in most cases, conversions remained relatively low (40% - 70%). A catalyst system that combines ATRP and ROP has been reported in 2015 by ZHANG et al. [223] ZHANG et al. have elegantly used DBU to act both as catalyst for the anionic ring opening of L-lactide as well as a ligand for CuBr to catalyze the ATRP of methyl methacrylate. Their one-pot approach yielded block copolymers with a polydispersity between 1.40 and 1.88. Although other synthetic strategies frequently yield block copolymers with much lower dispersities, this catalytic system looked promising for the implementation of simultaneous surface grafting and was adopted for the purposes of this work.

3.5.1 Polymerization mechanisms

Standard ATRP mechanism

ATRP is a firmly established and relatively robust type of controlled radical polymerization technique. The seminal work to establish ATRP was published by the MATYJASZEWSKI group in 1995 and has since found numerous applications in both industry and academia[224]. Well-controlled polymerizations have been reported for a range of vinyl monomers and targeted architectures. Monomers include the versatile groups of sytrenes, (meth)acrylates, (meth)acrylamides and acrylonitriles (see Scheme 3-6). ATRP was further employed yielding architectures ranging from homopolymers, block-copolymers[77,225–234], statistical copolymers[235–240], networks[241–244], grafted surfaces[245–249] or molecular bottlebrushes[142,150,250–255].

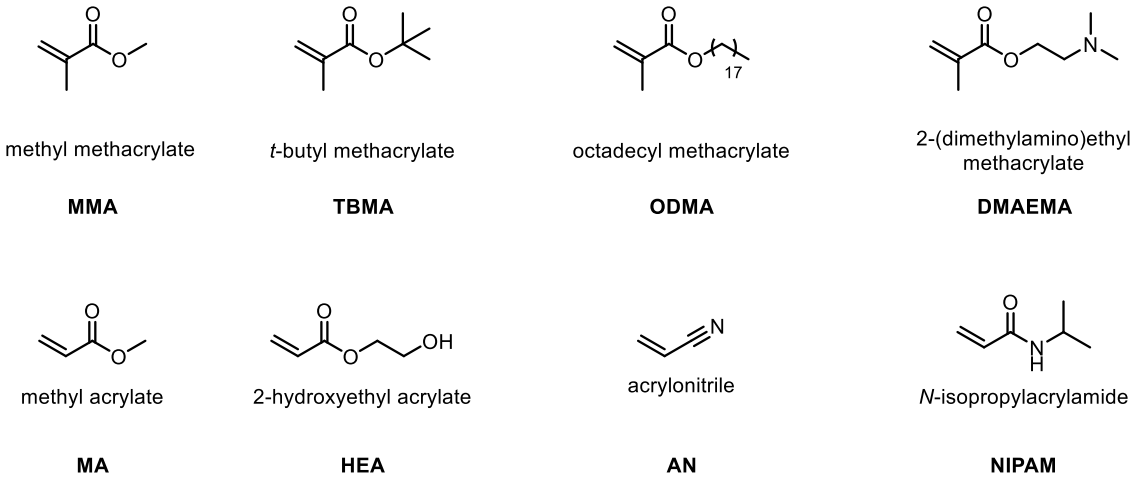

Scheme 3-6: Selection of monomers successfully polymerized via ATRP.

Control over the polymerization is achieved through a dynamic equilibrium between an active, propagating radical (initiator, monomer or propagating polymer) and a dormant species. Activation of a dormant chain end, controlled by rate constant k_a, occurs *via* homolytic cleavage of a carbon-halide bond (P-X) by a transition metal complex L/M_t^n to yield the radical $P^\bullet$ and the metal halide complex in its higher oxidation state L/XM_t^{n+1}. Deactivation with its associated rate constant k_d is the reversal of the activation process, where the higher oxidation state deactivator catalyst complex is reduced and the propagating radical is halide end-capped (see Scheme 3-7). The ratio between k_a and k_d determines the position of the polymerization equilibrium, K_{ATRP} and hence the rate of polymerization[256].

$$K_{ATRP} = \frac{k_a}{k_d}$$

Equation 3-1

Rate of deactivation and activation are both sensitively dependent on the choice of ligand and monomer. The overall equilibrium position depends on bond strengths of alkyl halide and Mt^{n+1}-X and thus their relative propensity towards homolysis[215].

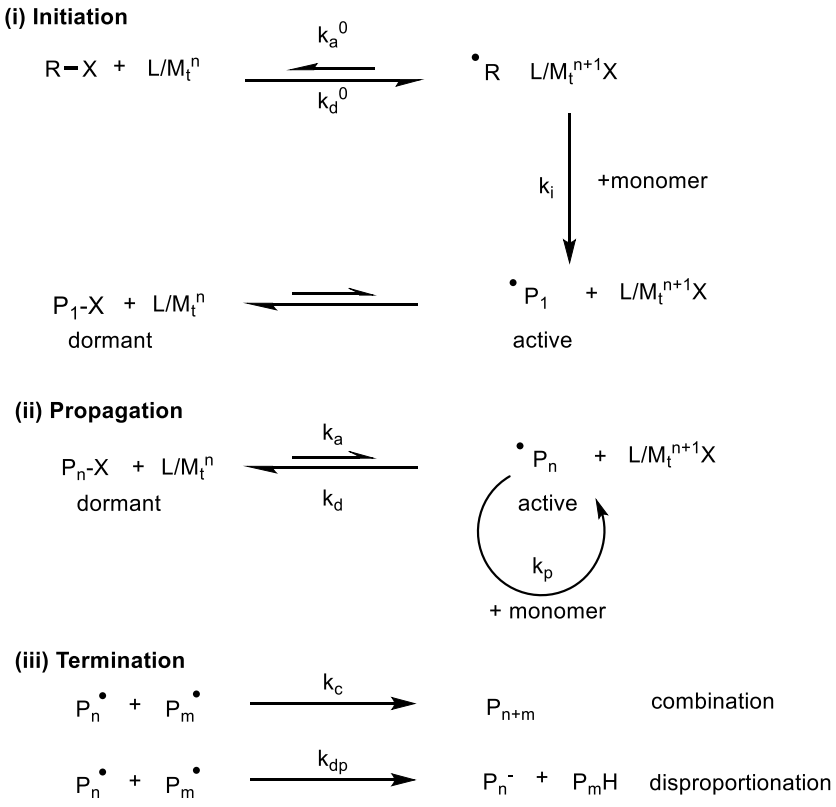

Scheme 3-7: Mechanism of ATRP.

The best control over the polymerization is achieved when a) the equilibrium is established rapidly and b) the equilibrium is positioned so as to favor a small concentration of active species only. These conditions can be fulfilled by choosing a catalyst that deactivates growing chains more rapidly than it activates dormant chains.

The ATRP equilibrium (K_{ATRP}) may be reached from either side: initiation of the polymerization can proceed *via* "normal ATRP" or *via* "reverse ATRP". Normal ATRP relies on the addition of catalyst in its activating, lower oxidation state. In the reverse approach, the catalyst complex is added in the deactivating, higher oxidation sate. During the initiation stage, the catalyst is reduced into its activating, lower oxidation state by the help of reducing agents or conventional radical initiators. As a results, various initiation techniques have been established with particularly noteworthy contributions from the MATYJIASZEWSKI group, including ARGET ATRP[229,257–261], AGET ATRP[243,262,263], photo-ATRP[264–266], SARA ATRP[142,267–270] and e-ATRP[267,270,271].

Ring Opening Polymerization with DBU

Diazabicycloundecene (DBU) as a catalyst for the ROP of cyclic esters was first reported in 2006 by LOHMEIJER et al.[272]. In the presence of a primary alcohol, the polymerization follows the activated-alcohol pathway with a ketene aminal as major intermediary[160] (see Scheme 3-8). Propagation occurs *via* a quasi-anionic mechanism with attack on the carbonyl carbon. As in the NHC mediated ROP discussed above, driving force for propagation is the alleviation of ring strain in the cyclic monomer. Without primary alcohol, the mechanistic picture becomes more complex, yielding cyclizations analogous to the NHC catalyzed ROP of cyclic esters[31]. The catalyst shows high activity even at ambient conditions and produces high molecular PLA with narrow molecular weight distributions[273].

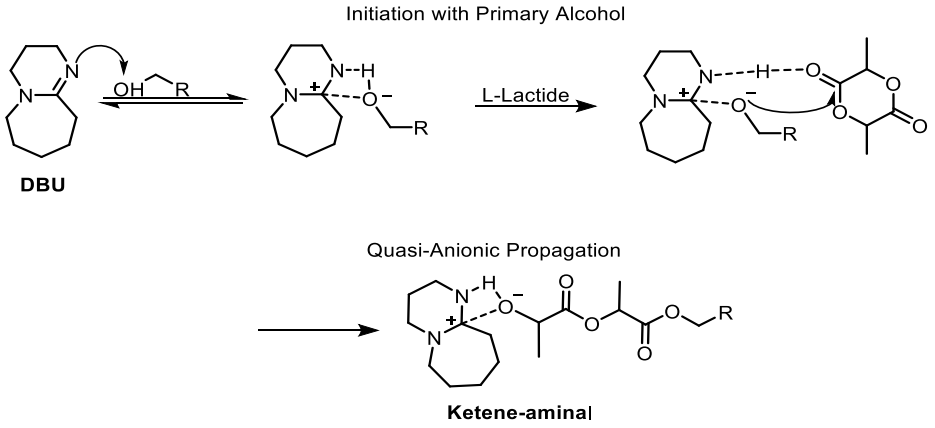

Scheme 3-8: Mechanism of DBU catalyzed ROP of L-lactide

3.5.2 Tandem DBU (co)Catalyzed ROP-ATRP

Table 3-2: Molecular weights and reaction conditions for test polymerizations

Entry	Monomer 1 LLA	Monomer 2 NIPAM	Time /h	Conversion 1 LLA	Conversion 2 NIPAM	M_n	PDI
100	-	100 eq	20	-	70%	2300	2.62
101	100 eq	-	20	100%	-	6000	2.38
102	97%	77%	20	100%	67%	5200	3.11

Polymerizations conducted in toluene at 85 °C for 20 h. M_n experimentally determined *via* GPC in THF against PMMA. Conversion calculated by ^{1}H NMR.

Unlike ZHANG et al. who polymerized two monomers with relatively similar polarities, grafting amphiphilic polymer brushes requires monomers with *dissimilar* polarities. For this purpose, the two monomers L-lactide (LLA) and N-isopropyl acrylamide (NIPAM) were selected. The choice of NIPAM as comonomer was inspired by its polymer's hydrophilic nature on one side and its thermoresponsive behavior on the other side. PNIPAM has a lower critical solution temperature (LCST) in aqueous solutions of 32-33 °C[274] and hence allows to control the hydrophilic-hydrophobic properties of surfaces grafted with PNIPAM.

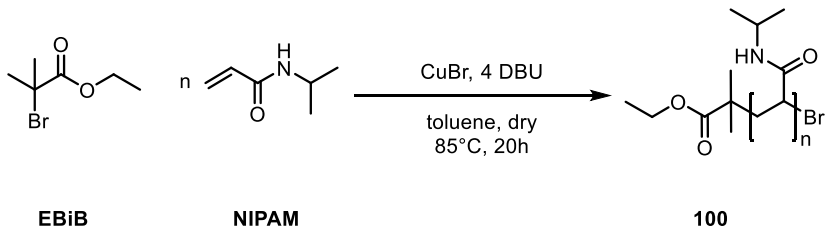

Scheme 3-9: Homopolymerization of NIPAM **100** with initiator EBiB and DBU-ligated CuBr

NIPAM homopolymerizations were first conducted and tuned so as to establish whether the catalytic system above reliably produces PNIPAM in a controlled fashion. NIPAM was polymerized with initiator and four equivalents of DBU as ligand for catalytic CuBr in toluene. The ligand to initiator ratio established by ZHANG[223] et al. reflects the ability of one copper center to complex with three DBU equivalents with an extra equivalent free for ROP of cyclic ester monomers. The reaction conditions outlined by ZHANG et al. resulted only in the formation of oligomers at low conversions before catalyst decomposition limited any further polymerization. The atypically poor reproducibility of these initial polymerization attempts indicated that the system is very sensitive to trace amounts of oxygen and water,

requiring rigorous drying and degassing procedures and the storage of all reagents under inert atmosphere.

Tuning the reaction conditions (toluene at 85 °C) allowed complete conversion of the monomer to produce a relatively broad distribution of PNIPAM (PDI 2.60, see Figure 1-2). The many ATRP catalyst systems that have frequently been reported to produce polymers with low dispersities[275—277] stand in marked contrast to the broad distributions yielded here. Narrow distributions achieved *via* ATRP occur only when the equilibrium between active and dormant chain ends is achieved rapidly and generally result in slow polymerization progress. Despite the broad distributions yielded herein, it was decided to continue working with this catalytic system, as the declared aim of grafting simultaneously off a surface does not require a narrow molecular weight distribution as much as a reliable initiation of the growing chains.

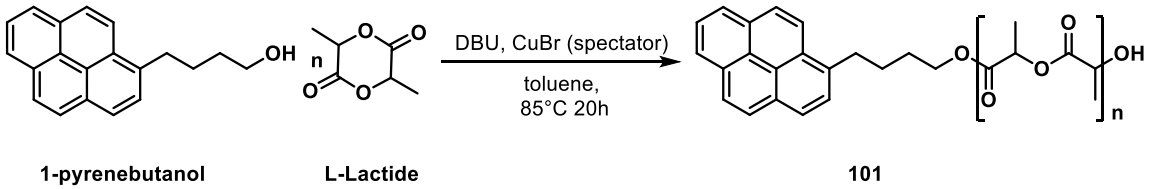

1-pyrenebutanol **L-Lactide** **101**

Scheme 3-10: Homopolymerization of L-lactide by DBU in the presence of spectator CuBr, initiated by 1-pyrenebutanol to yield PLLA homopolymer **101**.

Similarly to the test reactions above, homopolymerizations of L-lactide were conducted so as to establish ideal reaction conditions for both polymerization before moving towards the simultaneous approach. Polymerization of L-lactide was initiated by the UV-active 1-pyrenebutanol and catalyzed by DBU. CuBr was added as a spectator salt so as to gauge whether the catalyst interferes with the polymerization of L-lactide. Unlike the polymerization of NIPAM, after only 1 h, conversion was quantitative and produced a relatively broad distribution of PLLA with 2.38 (see entry **101** in Table 3-2: Molecular weights and reaction conditions for test polymerizations). Interestingly, prolonging the reaction timeframe led to a broadening of the molecular weight and a lowering of the number average molecular weight. These observations indicate that after consumption of the monomer, DBU encourages transesterifications.

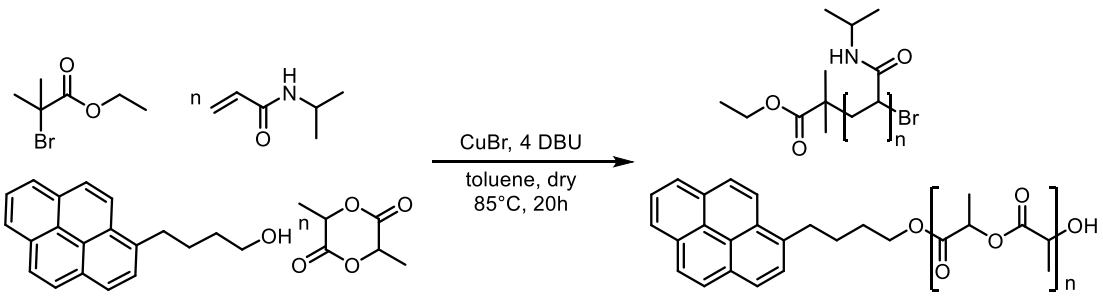

Scheme 3-11: Simultaneous, one-pot polymerization of LLA and NIPAM by the DBU-CuBr catalytic system to produce the polymeric mixture **102**.

The two independent polymerizations were then combined in a one-pot, one-step procedure to gauge the compatibility and mutual orthogonality. The polymerization of LLA and NIPAM in one reaction vessel at the same time was conducted in toluene at 85 °C. Conversion of the LLA polymerization was quantitative, while the maximal conversion for NIPAM polymerization stayed at 67%. (see entry **102** of Table 3-3) This lower conversion is in contrast to the homopolymerization of NIPAM, that yielded quantitative conversions. There seems to be minor interactions between the two polymerization techniques. GPC traces were bimodal with a dominating heavier fraction and a shoulder towards lower molecular weights. This type of bimodal distribution is expected for mixtures of polymeric products having two distinct molecular weight regimes. The ^{1}H NMR molecular weight calculations, already suggested that the two polymers were expected to have different molecular weights. The observed GPC shape is therefore expected. GPC traces do not provide information about the chemical composition of the individual populations. In addition, DOSY NMR

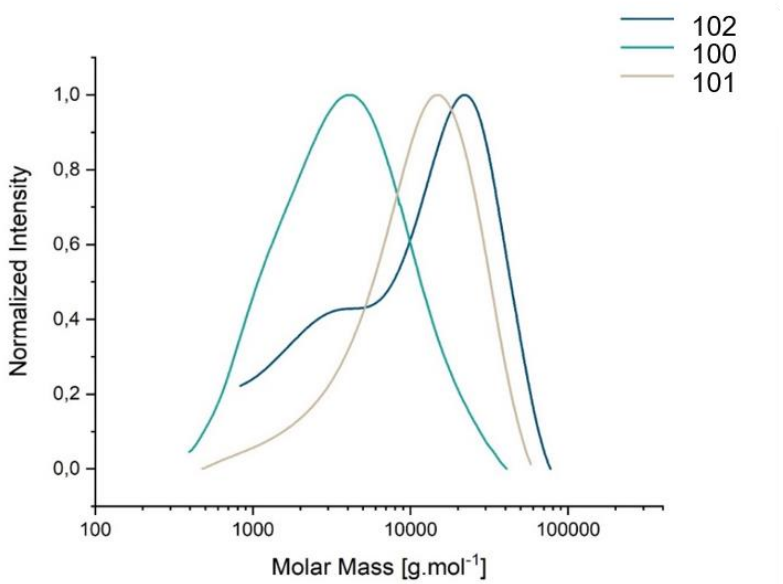

Figure 3-10: GPC trace of LLA test polymerization **101** (tan), NIPAM test polymerization **100** (turquois) and test tandem polymerization **102** (blue). THF was used as eluent and calibrated using a PMMA standard curve.

experiments were conducted to give information about the molecular structure as a function of hydrodynamic radius.

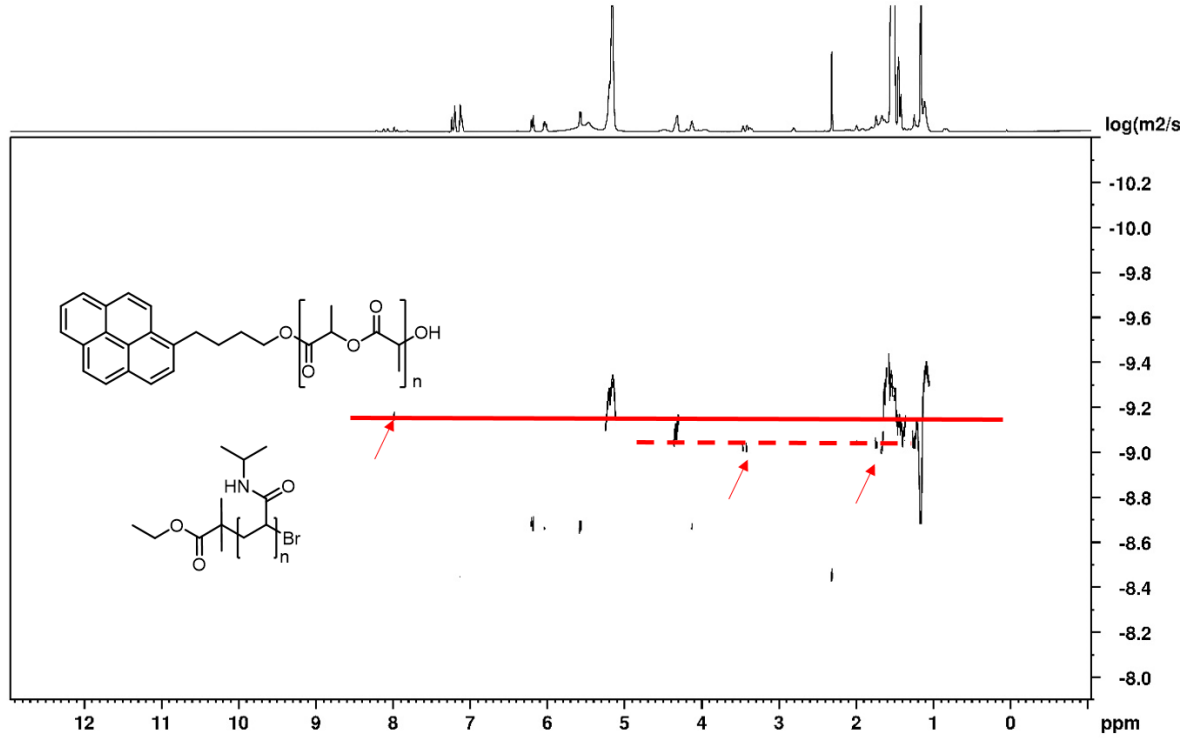

Figure 3-11: DOSY ^{1}H NMR of **102** showing the diffusion coefficients of the PLLA (solid line) and PNIPAM polymers (dashed line) respectively. Arrows indicate initiator signals.

The DOSY ^{1}H NMR spectrum (see Figure 3-11) shows two polymeric populations, only marginally separated by their respective diffusion coefficients. Species with larger hydrodynamic ratios appear higher on the spectrum, indicating that the PLLA block is larger than the PNIPAM polymer product, reflecting the greater degree of conversion achieved in the ROP than in ATRP of NIPAM. It is worth pointing out that the initiator derived signals (marked with an arrow) lie on the same diffusion coefficient as the polymer signals. The covalent attachment between initiator and polymer indicates that ROP of LLA and ATRP of NIPAM is indeed initiated by pyrenebutanol and EBiB respectively. This observation is of particular importance for the further steps in this project, as only initiator-derived polymers contribute to the grafting from a surface. In contrast, non-initiator derived polymer populations could occur by unwanted chain transfer reactions or by macrocycle formation, as is frequently observed in the ROP of L-lactide in the absence of alcohol initiators[31]. Such polymers have poorly defined end groups and would remain in solution rather than tethered to the surface.

Table 3-3: Reaction conditions for simultaneous ATRP-ROP catalyzed by DBU

Entry	Solvent	T /°C	Time /h	Conversion[a] LLA	Conversion[a] NIPAM
102[b]	Tol	85	20	100%	71%
103	Tol	85	24	99%	44%
104	Tol	90	18	97%	77%
105	Tol	75	20	99%	14%
106	MeCN	75	24	86%	58%
107[c]	Tol	90	23	100%	31%
108	DMF	90	20	75%	16%

Polymerizations were conducted with copper catalyst CuBr (1 equivalent) and DBU (co-) catalyst (4 equivalents) at 90 °C. Initial concentration of LLA monomer: 0.5 M. Equivalents with respect to initiator:CuBr:DBU:LLA:NIPAM.1:1:4:100:100: Precipitated in hexane. Initial LLA concentration 1M. [a]calculated *via* ^{1}H NMR; [b]ATRP initiator: EBIB, ROP initiator pyrenebutanol[c] CuBr ligand: PMDETA

For the next steps of gauging the applicability of the DBU system for this project, the two simultaneously occurring polymerizations were initiated by a covalently tethered heterobifunctional initiator in solution. The dual initiator 2-hydroxyethyl 2-bromoisobutyrate HBIB has a primary alcohol to initiate ROP of LLA and the isobutyryl bromide motif commonly employed as ATRP initiator (see Scheme 3-12).

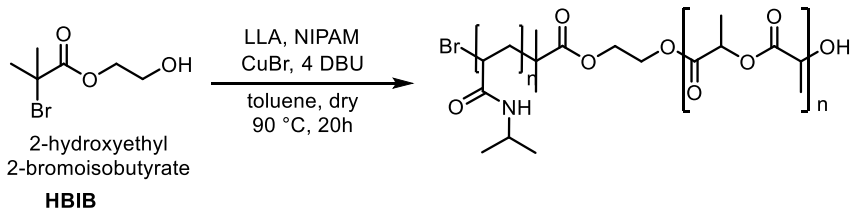

Scheme 3-12: Simultaneous tandem polymerization using hetero bifunctional initiator HBIB to yield P(LLA)-b-P(NIPAM) block copolymer **103**.

Employing dual initiator HBIB and DBU as ligand/catalyst led to nearly complete conversion of LLA within the first two hours, while NIPAM conversion remained incomplete (and low) even after 2 days of polymerization. Contrasting with the earlier, disconnected initiators, conversion of NIPAM was much reduced to 44% at the same reaction conditions (see entry **103**, Table 3-3). Incomplete conversions may be tolerated for the sake of this project but the much faster ROP over ATRP is undesirable. If one monomer polymerizes much faster than the other, steric hindrances increase for the slower polymerizing monomer to reach the propagating sites and the advantages of the simultaneous approach are lost. There are several

parameters through which balancing the rates of polymerization may be achieved: choice of monomer, solvents, temperature and catalyst all impact the polymerization kinetics.

Reaction temperature plays a crucial role for the successful implementation of simultaneous polymerizations. If the two polymerizations have different energetic requirements, adjusting the reaction temperature might allow to find a temperature regime where both polymerizations occur with comparable rates of propagation. Shifting the reaction temperature towards a regime that encourages one polymerization and is sub-ideal for the other polymerization technique might allow to control the reactivity ratios. To test the impact of the reaction temperature on conversion per time (i.e. the reaction rate), the polymerization temperatures were altered systematically. Raising the temperature from 85 °C to 90 °C doubled the rate of polymerization. In contrast to the findings of ZHANG et al. [223] who reported the highest activities for a temperature of 85 °C, the higher temperatures led to a marked improvement in NIPAM conversion (entry **104**). While at 85 °C, a conversion of only 44% was achieved, at 90 °C, 77% conversion of NIPAM was determined. Other temperatures (e.g. entry **105**) considerably lowered conversion to only 14%. Additionally, the GPC trace produced by polymers under these conditions showed marked trailing with a particularly high associated dispersity. M_n for entry **105** was found to be 16 800 g.mol^{-1} at a dispersity of 3.71. For all temperatures studied, LLA polymerization always proceeded quantitatively or near quantitatively within 2 h of reaction time. Further experiments were thus conducted at 90 °C.

As was demonstrated in chapter 2, the choice of solvent can be of central importance for matching reaction rates in tandem systems. In chapter 2, the choice of solvent allowed one polymerization to operate at optimal conditions, while limiting solubility (and hence concentration) of the faster polymerizing monomer. It was hoped that by altering the solvent, one could achieve a similar control over the ATRP-ROP combination. Both NIPAM and LLA are polar monomers but NIPAM solubility in toluene is relatively poor. By employing a better NIPAM solvent, ATRP reaction rates might be improved due to higher monomer concentration and greater polymer mobility. Most commonly, ATRP of NIPAM is conducted in protic solvents[278], such as *iso*-propanol or water. Unfortunately protic solvents are precluded due to the simultaneously occurring ROP but polar, a-protic solvents might still improve the polymerization. Additionally, a more polar solvent might help in the dissolution of the ATRP catalyst. The copper complex' solubility is highly dependent on the ligands' solvophilicity. DBU as a ligand is much more polar than other ATRP ligands commonly employed in toluene (e.g. 4,4'-di-5-nonyl-2,2'-bipyridine) and might therefore perform better in polar solvents. MATYJASZEWSKI et al. [210] have demonstrated that solvent choice strongly affects the rate of ATRP with kinetic differences being reported up to a factor of 80. The choice

of solvent affects the ATRP equilibrium through affecting the underlying equilibria positions in disproportionation, electron affinity of the halogen atom, alkyl halide bond homolysis and reduction/oxidation of metal catalyst, among others[210]. Additionally, it was reported that the solvent molecules compete with the ligand for complexation with the catalyst[279]. Commonly, the multidentate ligands employed in other ATRP systems show are stronger ligands than solvents like DMF and MeCN and this effect is negligible. However, as the DBU ligand employed herein is monodentate, the much higher concentration of solvent molecules over ligand concentration may shift the equilibrium significantly toward mixed solvent-ligand complexation. MeCN in particular has been shown to stabilize the lower oxidation state selectively over the higher oxidation state in copper-catalyzed ATRP. It was thus hoped that by employing MeCN, the reactivity of the catalyst can be modulated selectively and lead to longer reaction lifetimes.

The choice of solvent is somewhat limited by the need to avoid protic solvents as they my initiate ROP of LLA. Furthermore, not all solvents are stable to the catalysts and monomers employed. DMSO for example is not chemically inert in the presence of DBU[280]. The solvent was therefore varied from toluene to DMF and MeCN (see Table 3-3 reaction conditions **108** and **106** respectively). DMF as solvent resulted in the lowest conversions with only 16% w.r.t. NIPAM and incomplete ROP of L-lactide. ATRP in DMF stopped after only 2 h, allowing no further polymerization. MeCN as solvent (reaction **106**) resulted in higher NIPAM conversions despite lower reaction temperatures (due to the solvent's boiling point) but polymerization still stopped after 2 h. When considering the GPC traces of the precipitated polymers, the M_n of 10 300 g.mol^{-1} showed a marked shoulder towards longer elution times despite a relatively narrow molecular weight distribution of 1.37.

The (near) complete loss of catalytic activity within a few hours was a common trend for the simultaneously conducted ATRP of NIPAM. Suggestively, conversion stopped with concomitant color change of the reaction mixture. The DBU-CuBr complex is colorless or faintly green in dry toluene, turning moss green in the presence of NIPAM monomer and after a few minutes at elevated temperatures, turquois. As ATRP progresses, the colorful polymerization mixtures consistently turned brown within three to four hours. This color change was accompanied by precipitation of a dark brown substance at the SCHLENK flask walls. Such behavior is well-documented for poor ATRP systems and stems from oxidation of the copper catalyst by trace amounts of oxygen. The oxidized metal falls out of solution and no longer facilitates and controls the radical polymerization of acrylic monomers. Oxygen impurities may further react with active carbon radical chain ends, terminating the polymerization. The limited oxygen tolerance is one of the major pitfalls of conventional ATRP[275]. Despite the rigorous degassing procedures used for all polymerizations and

consistent application of SCHLENK techniques, sufficient amounts of oxygen seemed penetrate into the reaction vessel to impede further polymerization.

Alternatively, the catalyst degradation may be a result from poor ligand affinity. Well-controlled ATRP systems rely both on the relative and absolute catalytic activities as well as on the catalyst's stability within the reaction medium. Both the rates of activation and deactivation are sensitively dependent on ligand identity. Activity differences arising from ligand choice with up to nine orders of magnitudes have been reported[281]. The ability of a given ligand to donate electrons greatly influences the stability of the metal ion in its higher and lower oxidation states and its propensity to abstract or transfer (pseudo-)halogens. Hence, through the choice of ATRP ligand, redox potentials of the metal salts can be adjusted. Commonly, the most active ATRP ligands are nitrogen based, multidentate and represent low steric hindrance for interaction with chain ends. Ligands with four nitrogen atoms (e.g.: HMTETA see Scheme 3-13) available for complexation are more stable, as well as more active as those with three (like PMDETA, see Scheme 3-13) and three-nitrogen ligands are more so than those with two.

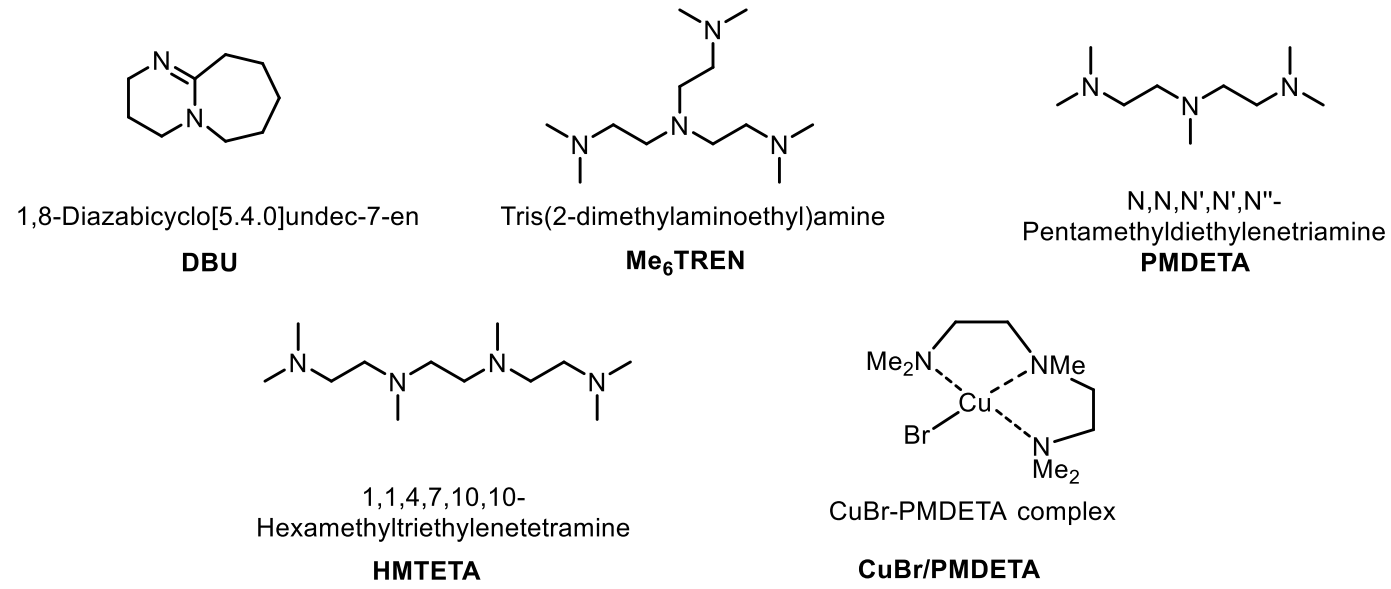

Scheme 3-13: Selection of ligands for copper halide ATRP catalysts.

Although the DBU ligand contains two nitrogen atoms, only one may bind with the copper ion at any time[282]. As a consequence, the entropically favored dissociation of ligand and copper ion cannot be counteracted by any chelating effects. The high temperatures required for polymerization might therefore suffice to cause catalyst dissociation. CuBr could then disproportionate to Cu^0 and $CuBr_2$. As both are insoluble in toluene, they would therefore precipitate, leading to the observed black precipitate on the reaction vessel walls. In the absence of reducing agent, this precipitation is irreversible and polymerization stops.

Additionally, it was found that the hybridization of the adjacent carbon atoms further impact the catalyst activity with alkyl amines showing the highest activity and then decreasing according to alkyl amine ≈ pyridine > alkyl imine >> aryl imine > aryl amine[281]. DBU as a ligand therefore performs poorly due to its monodentate structure, paired with it alkyl imine structure. When contrasting the ligand structure with the electronic structure of the monomer - NIPAM - it becomes evident that the ligand is in competition with the monomer for binding with the catalyst. The color change observed (from clear to green) during addition of monomer strongly suggests an interaction with the catalyst. This competition is compounded by the difference in concentration between NIPAM and DBU. For this combination of monomer and reaction conditions, the ligand DBU seems to be the key issue for the polymerization.

Expecting to achieve faster ATRP by employing a more active and more stable ATRP catalyst, PMDETA was employed as a ligand. PMDETA bears three nitrogen atoms able to chelate to the copper ion. Additionally, the methyl groups do not represent large steric hindrances. PMDETA ligated CuBr is a common catalyst choice for ATRP systems due to its high stability, high activity and commercial availability[283]. The PMDETA CuBr complex was formed by dissolving the ligand in toluene and suspending CuBr in the solution. DBU was still employed in the (co)polymerization as catalyst for the ROP of LLA (see entry **107** of table Table 3-3). Unfortunately, no marked improvement in either stability or conversion was

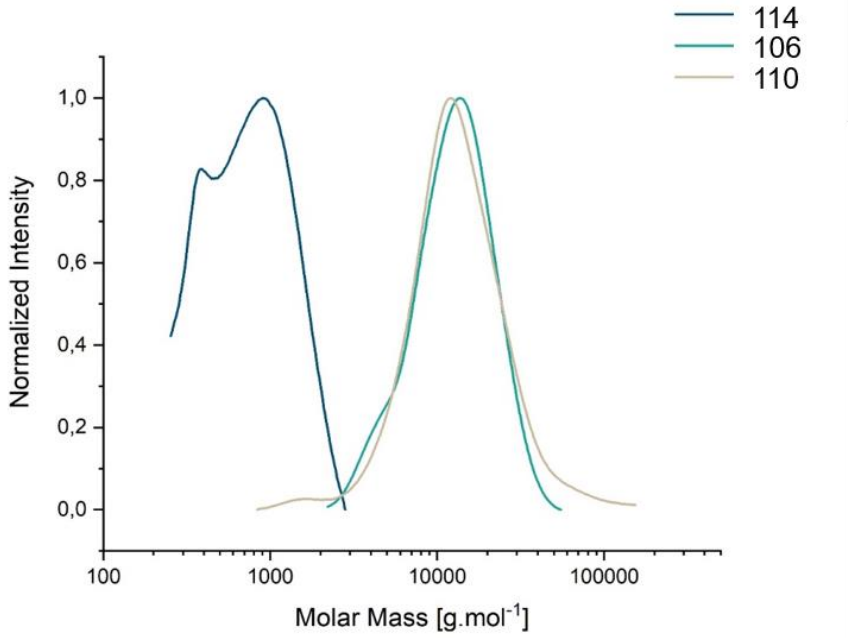

Figure 3-12: Representative GPC traces of simultaneous polymerizations. The eluent was THF for all measurements, using a PMMA calibration curve.

observed. Total conversion remained at 31% of NIPAM after catalyst decomposition occurred within 3 h. Within the first hour, meanwhile 91% of LLA monomer had polymerized.

Contrasting the sluggish polymerizations of NIPAM catalyzed with the DBU system with those of MMA reported by ZHANG et al.[223], indicated that the acrylamide monomer employed herein seems to cause the synthetic difficulties. As is well established for radical polymerizatios, methacrylic monomers are orders of magnitude more reactive towards polymerization than acryl amide monomers[215]. The propagating chain end's radical is stabilized by a tertiary carbon center in the case of methacrylic monomers, while the secondary radical in NIPAM is less stable. FONTAINE et al. have shown that DBU catalyzed ATRP is characterized by a slow electron transfer, as evidenced by slow redox processes measured by cyclic voltammetry. The slow redox process dictates a slow establishment of the ATRP equilibrium. A catalyst with poor activity is unsuitable for a polymerization of an unreactive monomer such as NIPAM[222]. Although MMA is not hydrophilic as NIPAM, PMMA's polarity is dissimilar enough to PLLA as to afford phase separation and self-organization within a selective solvent[223]. It was thus decided that further experiments were to be conducted with MMA as comonomer.

Table 3-4: Simultaneous polymerizations of LLA and MMA catalyzed by DBU

Entry	Equivalents		Solvent	Conditions	Reaction time	Conversions[a]	
	LLA	MMA		/°C	/h	LLA	MMA
109 [b]	100	100	Tol	90°C, dark	1 h	100%	14%
					20 h	100%	23%
110	100	200	Tol	RT, UV	2 h	100%	3%
					28 h	100%	5%
111	100	200	DMF	RT, UV	2 h	78%	0%
					20 h	75%	0%
112[c]	100	100	Tol	RT, UV	2 h	100%	0%
					20 h	100%	2%
113	100	100	THF	RT, UV	2 h	26%	0%
					20 h	33%	0%
114	100	100	Tol	95°C, dark	1 h	59%	0%
					6 h	85%	0%

Polymerizations were conducted with copper catalyst CuBr (1 equivalent) and DBU (co-) catalyst (4 equivalents). Equivalents with respect to initiator HBIB. Precipitated in hexane. Initial LLA concentration 1M. [a]calculated *via* ^{1}H NMR; [b]ATRP initiator: EBIB, ROP initiator pyrenebutanol[c] Initial concentration of LLA monomer:0.5 M.

Despite the higher reactivity of MMA compared to NIPAM, the ROP of LLA continued to proceed much faster than the ATRP of MMA. Full conversion of LLA was systematically

achieved within 1-2 h of polymerization, while only low conversions of MMA were achieved at long reaction times (20-28 h) (see entries **110** and **109** in

Table 3-4). These mismatching kinetics were discouraging for the purposes of this project. As before, it was stipulated that by altering the reaction temperature, the ATRP kinetics could be accelerated, while slowing down the ROP of LLA. Increasing the reaction temperature to 95 °C resulted in no ATRP taking place, while only slowing down ROP of LLA marginally (see entry **114** in

Table 3-4).

Hoping that lower temperatures might lead to a more favorable kinetic balance, it was then attempted to conduct simultaneous polymerizations at room temperature, initiated by UV irradiation. WANG et al[284]. have previously shown that the 360 nm UV absorption of CuBr can be exploited for the simultaneous photo-initiated ATRP of MMA with DBU catalyzed ROP of LLA. The group used 2,2,2-tribromoethanol as initiator and a 365 nm UV source and reported the formation of block copolymers at room temperature. Applying these conditions with the initiator HBIB led to full conversion of LLA within one hour reaction time and 5% MMA conversion after 28 h in toluene (see entry **110**). Altering the polymerization concentration (entry **112**) led to an even lower conversion for MMA while impacting the LLA polymerization very little.

Following the insight gained by MATYJASZEWSKI et al.[210], the solvents employed for these polymerizations were varied. Unfortunately, DMSO is not chemically inert under UV light in the presence of DBU[280], and could therefore not be employed for these polymerizations. Room temperature tandem polymerization were further attempted in DMF and THF (entries **111** and **113** respectively. In neither solvent did ATRP of MMA initiate at all, while conversion of LLA sank to 78% in 2 h for DMF and to 26% for THF. Clearly, the UV-initiated polymerizations performed even worse for the purposes of this project than the kinetically mismatched thermally activated ATRP-ROP system.

With (nearly) all DBU (co) catalyzed tandem polymerizations, GPC traces showed a marked shoulder, indicating several polymeric populations. This observation could be explained when referring back to the issue of DBU as a poor ligand. The ratio of DBU:initiator employed was set to 4:1 due to the catalyst complexing with three DBU ligands and an extra DBU equivalent to polymerize the cyclic ester, in accordance to ZHANG et. al[223]. If, however a large proportion of the ligand dissociates, an excess of DBU is free to react with cyclic monomers. As a consequence, complex mechanistic pathways may arise, as simulated by

SCHERCK et al. [31]. DBU can both initiate polymerizations in the absence of primary alcohols, as well as cause cyclization of growing polymer chains.

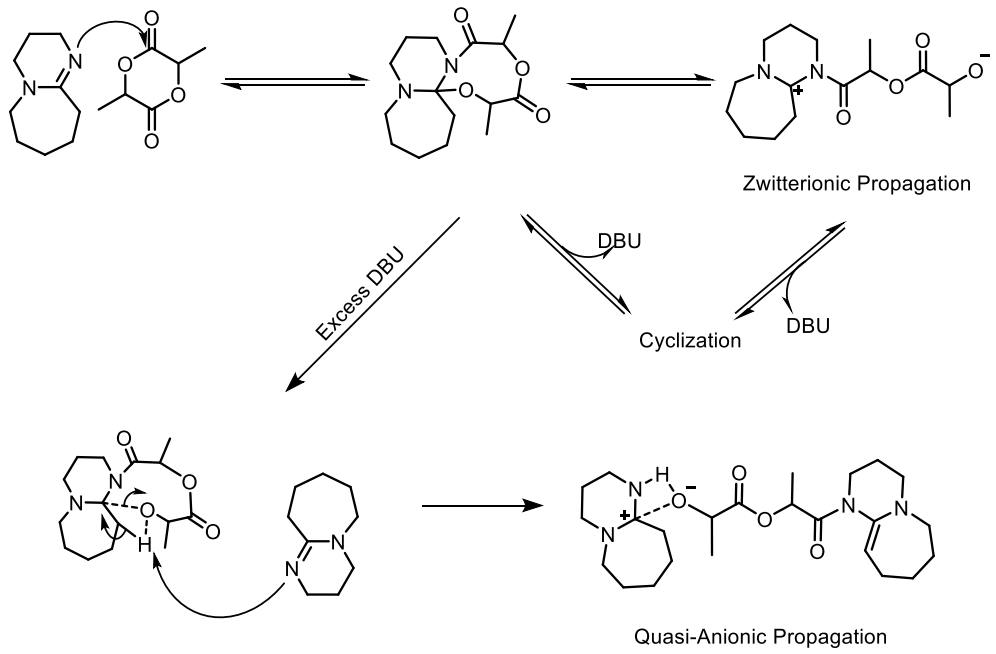

Scheme 3-14: Complex mechanistic pathways arise when DBU is employed in excess to ROH initiator.

Based on these dissatisfying results, it was determined that the kinetic mismatch between the DBU-catalyzed ROP and ATRP is too large to serve as a basis for this project.

3.5.3 Tandem $Sn(Oct)_2$ (co)catalyzed ROP and ATRP

When addressing polymerization rates, chemists have several options: altering reaction conditions, solvents, and monomers or change the reaction mechanism by employing other catalysts. The previous experiments using DBU as (co)-catalyst showed that the polymerization of cyclic ester was consistently (too) fast in comparison with the polymerization of LLA, while the polymerization of acrylic monomer *via* ATRP was slow, initiated unreliably, produced bimodal distributions (i.e. did not ensure covalent attachment) and resulted in catalyst death before completion of the polymerization. Wanting to preserve the general motif of ATRP-ROP combination due to the range of available monomers, a new set of reaction conditions and catalyst choices was explored to match the polymerization rates. Changing solvents and reaction conditions (temperatures and concentrations) did not lead to the desired results. Rather than altering monomers, it was decided to change the catalytic

system altogether to address the issues of catalyst instability and transesterification side reactions.

$Sn(Oct)_2$ catalyzed ROP of cyclic esters

The previous experiments suggested that the ROP was too fast compared to the ATRP and a ROP catalyst with lower turnover might be beneficial. The NHC catalysts employed in for simultaneous bottlebrush polymerization, might therefore be ill-suited for the purposes of this project. Additionally, the high affinity of NHC's towards transition metal complexes might interfere with the ATRP process. Similarly, as was exploited in the previous attempts, strong bases such as DBU or 1,5,7-Triazabicyclo[4.4.0]dec-5-en (TBD) have the tendency to form complexes with transition metals. Finally, metalorganic catalysts such as the industrially well-established tin (II) octoate[285], $Sn(Oct)_2$ (see Scheme 3-15) might be a viable choice. Stannous octoate owes its widespread use to it racemization-free polymerization of cyclic lactides with high yields and high molecular weights. Additionally, in combination with an alcohol co-initiator, control of molecular weights can be achieved with defined end-groups.

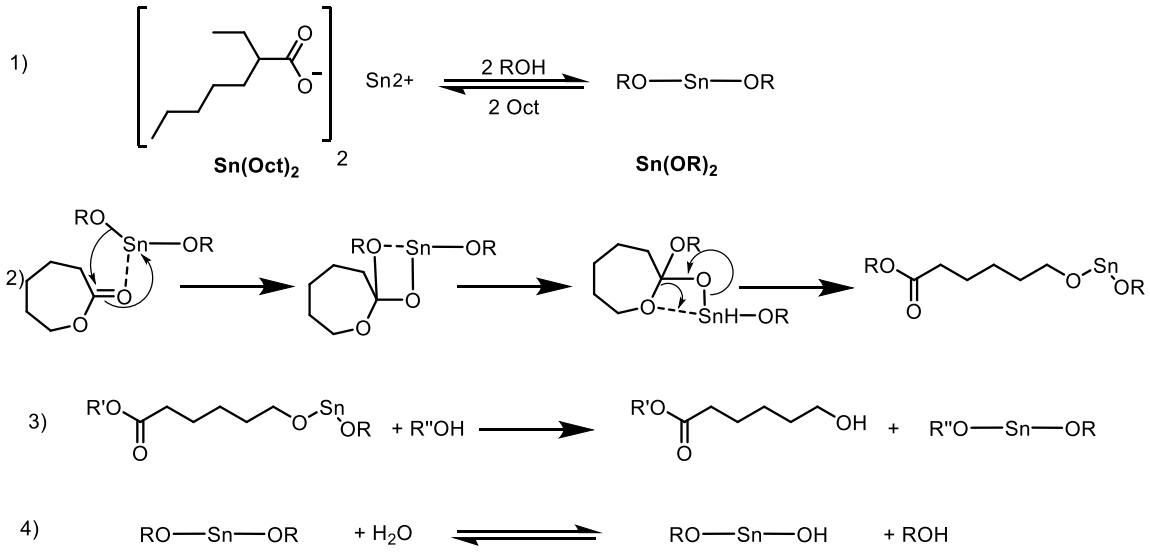

Scheme 3-15: Mechanism of stannous octoate $Sn(Oct)_2$ mediated ROP of CL. 1) Initiation, 2) chain extension 3) reversible termination and 4) side reaction in the presence of water.

The polymerization mediated by stannous octoate follows a general coordination-insertion ring opening polymerization mechanism. The catalyst $Sn(Oct)_2$ is added to a solution containing water or another hydroxy-functional initiator. Reaction between two equivalents of initiator and catalyst produces the true initiator, stannous alkoxide $Sn(OR)_2$, while liberating two equivalents of 2-ethylhexanoic acid (see Scheme 3-15, Step 1). The

stannous alkoxide species $Sn(OR)_2$ then proceeds to react with CL monomer (Step 2) by coordination-insertion at the ester bond. Further reaction with monomer constitute the propagation steps of the polymerization. KRICHELDORF et al[286]. Has shown that low dispersities may be achieved using this catalyst due to a rapid dynamic equilibrium of propagating stannous alkoxide and other hydroxy-functional molecules present in the reaction solution (see step 3). A particularly notable aspect of stannous octoate mediated ROP is the role of adventitious water (Step 4) as a (welcome) side reaction. KRICHELDORF has further demonstrated that complexation of water with the catalyst produces a much less active "dormant" species of catalyst, lowering the effective catalyst concentration. The reversible nature of addition of water allows to reactivate the catalyst when reacting with further alcohol present in solution. By this approach, (strongly depending on reaction temperatures), narrowly distributed PCL has been synthesized. The wide range of reaction temperatures as well as the option to tune reaction rates by addition of water or catalyst equivalents make this catalyst a promising option for the implementation of tandem reactions, as long as its interactions with the ATRP catalyst can be controlled.

$Sn(Oct)_2$ co-catalyzed ATRP

Since the first implementation of ATRP by the MATYJASZEWSKI group in 1994[287], the intense research on this type of CRP has led to the creation of a host of initiation techniques, (co-)catalyst complexes and monomer libraries. Various techniques have been established that rely on the reduction of copper complexes by an added co-catalyst or a radical generating initiator. Activator Generated by Electron Transfer-ATRP (AGET) ATRP is a technique whereby the copper complex is employed in its deactivating, higher oxidation state and by the addition of a suitable reducing agent, the copper catalyst is reduced to its activating form. For this approach, the reducing agent is employed in an amount that suffices to reduce the copper catalyst only once. Activator (Re-)Generated by Electron Transfer (ARGET) ATRP further exploits the reducing agent by consistently re-generating the activator and hence significantly decrease the degree of termination by catalyst death. In this approach, the higher oxidation state copper catalyst is employed in reduced quantities (ca. 10-50 ppm) and the excess of reducing agent leads to a continuing reduction of deactivating copper complex into its activating form. The mechanism of this technique is presented below. Other techniques, such as Initiators for Continuous Activator Regeneration (ICAR) ATRP, or Simultaneous Reverse & Normal (SR&NI) ATRP rely on the use of conventional radical sources in addition to copper catalysts. The continuous production of radicals in the polymerizing solution reduces the deactivating copper catalyst in a similar manner as in A(R)GET ATRP[258,259].

If the equilibrium position of K_{ATRP} is shifted towards the activator side, a larger proportion of chains are present in their active state. Hence, continuous regeneration of activator encourages a faster polymerization rate, albeit with the side effect of greater dispersities. For the purpose of this project, a faster rate of ATRP might allow to match the rapid ROP of cyclic ester. High dispersities, on the other hand may be tolerated to a certain degree. If, in addition, the lifetime of catalysts may be extended, the polymerization might proceed along a first order kinetic trajectory for a longer time.

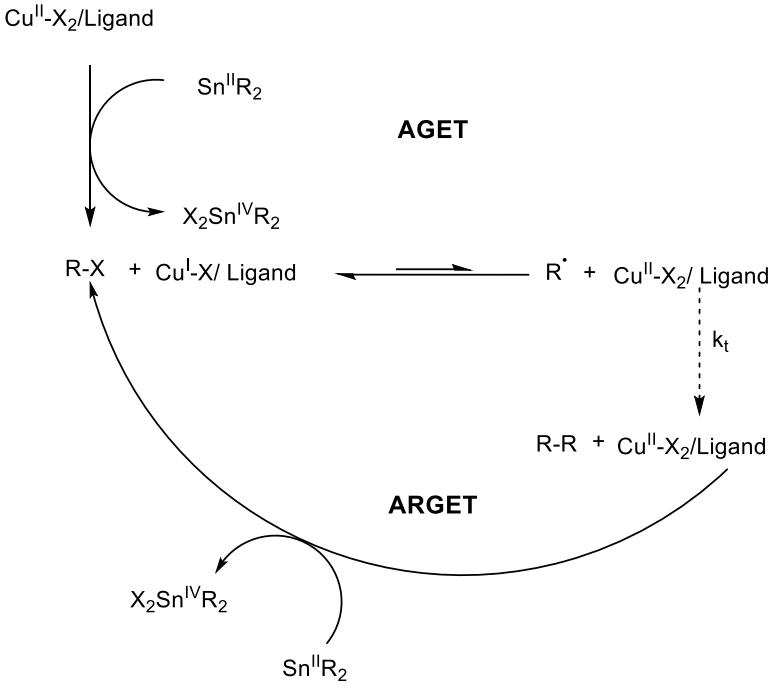

Scheme 3-16: Mechanism of Activator (Re) Generated by Electron Transfer ATRP - A(R)GET ATRP.

ATRP techniques that rely on conventional radical sources appears less favorable for the sake of surface grafting. Due to the addition of thermally decomposing radical sources, a certain number of chains would be derived from the radical initiators rather than off the surface. While washing off dissolved homopolymer is not an issue for this project, it is questionable whether the solution-initiated chains can diffuse to the crowded polymerization front. The tandem system would essentially combine a surface-initiated ROP with a *grafting-to* ATRP. Alternatively, azo-initiators could be anchored directly onto the surface with a different tandem linker. This option was dismissed due to the intrinsic sensitivity of azo-initiators to heat, which would limit synthetic options for the linker synthesis. In addition, the kinetics of ICAR ATRP depend on the rate of initiator decomposition, rather than on the position of the ATRP equilibrium.

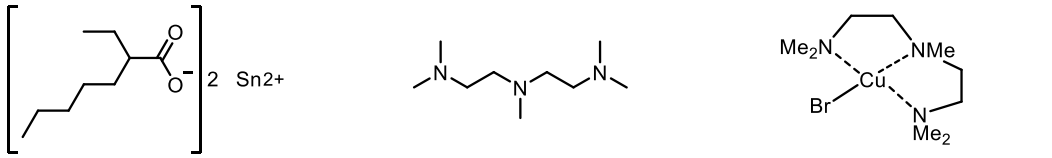

Stannous octoate
$Sn(Oct)_2$

N,N,N',N'',N''-Pentamethyldiethylenetriamine
PMDETA

CuBr-PMDETA complex
CuBr/PMDETA

Scheme 3-17: Catalyst system for simultaneous ROP and ATRP. Stannous octoate serves to catalyze ring opening as well as reduction of deactivator complex. CuBr/PMDETA complex activates initiators or dormant chain ends.

AGET and ARGET ATRP on the other hand, both employ copper catalysts in their higher oxidation state and initiation is achieved by first reducing the initiator to its activating lower oxidation number. The reducing agent itself is incapable of initiating radical polymerization. Therefore, a certain induction period exists, where no ATRP takes place, while the ROP of the cyclic ester monomer initiates rapidly. It was stipulated that by employing the copper catalyst in its lower oxidation state, ATRP would also initiate rapidly, while the presence of reducing agent still allows to take advantage of the regeneration of activator. It is worth noting that a system combining reducing agent and copper catalyst in lower oxidation state is not a case of either AGET or ARGET, although the reactivation is a common motif between these techniques. Various reducing agents have been reported for the purposes of A(R)GET ATRP, including tin(II) octoate[288] $Sn(Oct)_2$, ascorbic acid[262] and hydrazine[229]. Of these, the stannous catalyst $Sn(Oct)_2$ is particularly noteworthy as it is also a common choice for the ROP of cyclic esters (see above).

Tandem ATRP and ROP with $Sn(Oct)_2$

In contrast to the reports of DUMAS et al.[289], JAKUBOWSKI and MATYJASZEWSKI[225] have demonstrated that the two polymerization techniques can indeed be combined in a one-pot strategy to yield block copolymers. Although they did not succeed to copolymerize a hydrophilic with a hydrophobic monomer, the group demonstrated the simultaneous block-copolymerization of CL with ODMA. Hence, to combat the previously identified issues of catalyst death and poor initiation, it was opted to explore employing catalyst $Sn(Oct)_2$ as reducing agent and ROP catalyst for the system at hand.

In order to contrast the reactivity of this catalytic system with that of the DBU catalyzed system, the same monomer combination was employed. The cyclic ester LLA and the acrylic monomer MMA were combined in a tandem polymerization in toluene. For one equivalent of dual initiator HBIB, one equivalent of CuBr/PMDETA catalyst complex and two equivalents of stannous octoate were employed. Usually, $Sn(Oct)_2$ is employed at sub-

stoichiometric ratios due to the rapid equilibrium of the different stannous alkoxide species. However the dual role of the catalyst here, functioning also as a reducing agent leads to the catalyst being consumed throughout the ATRP process. Failure of the catalyst to initiate ROP when employed in stoichiometric or sub-stoichiometric amounts with respect to initiator, determined a 1:2 ratio of initiator to stannous catalyst. Reactions were conducted at monomer concentration of 1M in toluene or in bulk for liquid monomers at 90 °C.

Table 3-5: Conversions and reaction times of simultaneous tandem polymerizations using $Sn(Oct)_2$ and CuBr/PMDETA.

Entry	Time /h	Cyclic monomer equivalents	Conversion[a]	Acrylic monomer equivalents	Conversion[a]
115	20h	LLA	100%	MMA	26%
	4 d	100	100%	100	48%
116	2 h		66%		32%
	3 h	LLA	81%	MMA	37%
	6 h	100	87%	400	38%
117 [b]	1 h		5%		31%
	3 h	CL	86%	MMA	35%
	6 h	100	100%	200	38%
118	2 h		8%		8%
	3 h	LLA	9%	NIPAM	7%
	4 h	100	15%	100	14%
119 [d]	2 h		8%		37%
	3 h	CL	31%	MMA	39%
	4 h	100	63%	200	41%
120	2 h		6%		18%
	3 h	CL	10%	NIPAM	18%
	4 h	100	19%	100	19%

Polymerizations conducted with copper catalyst CuBr/PMDETA (1 equivalent) and stannous catalyst $Sn(Oct)_2$ (2 equivalents) at 90 °C monomers 1M in toluene, equivalents with respect to initiator. Precipitated in hexane. [a]calculated via ^1H NMR [b]in bulk

For entry **115** (see Table 3-5) 100 equivalents of each monomer were employed with respect to dual initiator HBIB. Polymerization of LLA proceeded to full conversion within 20 h, while MMA reached a conversion to 48% after four days of reaction time. After precipitation, the polymer's molecular weight was determined *via* GPC. The 8 200 $g.mol^{-1}$ found for this polymer is around half the theoretical weight calculated based on monomer conversion (see entry **115** in table Table 3-6). Some deviation might be explained by a mismatch between calibration standard (MMA) and monomers but the similar structure of MMA and LLA are unlikely to influence the elution behavior to this extend. Encouragingly though, the new catalytic system showed that the ATRP lifetime could be prolonged to several days of activity. The isolated polymer's monomer composition closely mirrored the theoretical composition based on the assumption that all converted monomer was incorporated into the polymer chain.

Using the same monomers, their respective equivalents were altered to mirror their relative reactivities (see entry **116** in Table 3-5). The lower conversion of MMA in the previous experiment led to a lower comonomer incorporation. Conversely, increasing MMA equivalents should therefore lead to a higher comonomer insertion. Samples were drawn periodically from the reaction mixture to assess conversion. Indeed, the fourfold excess of MMA resulted in a precipitated polymer with a much higher ratio of acrylic monomer incorporation. The polymerizations were quenched after 6 h to reflect the tendency of stannous catalysts to encourage transesterifications after prolonged reaction times[290]. Conversions accelerated to yield 38% MMA conversion within 6 h and 87% of LLA. However GPC results showed a much wider dispersity of 3.38 in the precipitated polymer (see **116** in Table 3-6. The very large dispersity might explain some of the deviation between theoretical and observed molecular weights. But as before, the theoretical molecular weight is *circa* twice the experimental molecular weight.

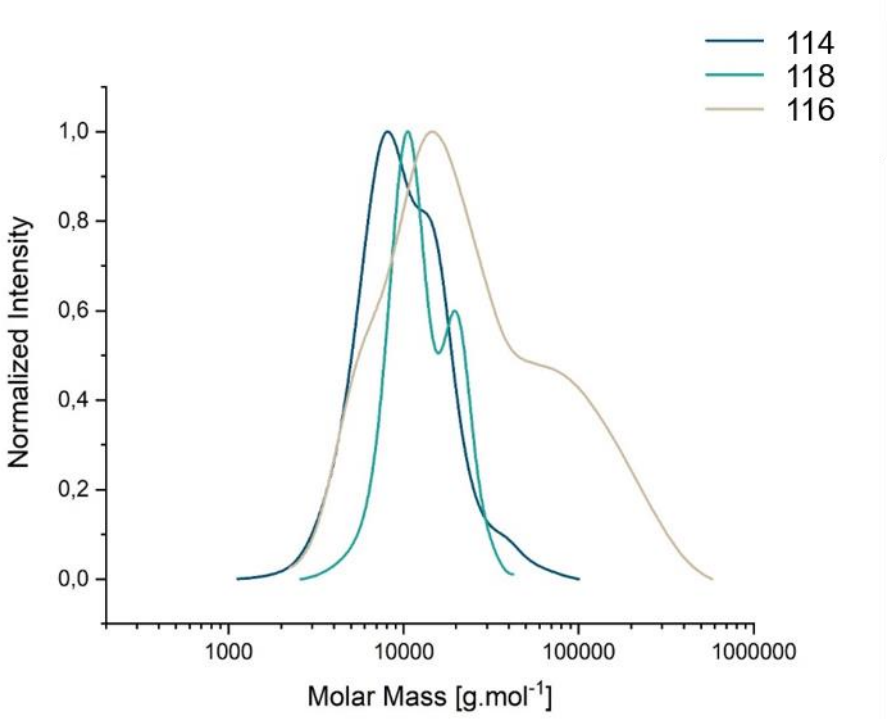

Figure 3-13: GPC traces of test tandem polymerizations **114, 118** and **116**. GPC eluent was THF and calibrated against PMMA standards.

Table 3-6: Experimental molecular weights and comonomer incorporation fraction of simultaneous tandem polymerizations using $Sn(Oct)_2$ and CuBr/PMDETA.

Entry	Time /h	$M_{n,exp}$ [a] g.mol^{-1}	$Đ_{GPC}$ [a] /g.mol^{-1}	$M_{n.theo}$ [b] /g.mol^{-1}	f [c]
115	P	8200	1.50		0.28
	20h	*n.d.*	*n.d.*	17000	
	4 d	*n.d.*	*n.d.*	19200	
116		14 500	3.38		0.75
	2 h	9 800	4.39	22300	
	3 h	10 600	3.81	26500	
	6 h	10 500	3.68	27800	
117 [d]	P	11 100	1.79		0.40
	1 h	5 700	2.50	6800	
	3 h	10 000	1.73	16800	
	6 h	8 800	1.94	19000	
118	P	*n.d.*	*n.d.*		0.24
	2 h	8 900	2.17	2100	
	3 h	900	1.09	2100	
	4 h	900	1.14	3700	
119 [d]	P	7 800	1.76		0.46
	2 h	835	1.14	8300	
	3 h	3 500	2.73	11300	
	4 h	4 100	2.22	15400	
120	P	10 800	1.79		0.45
	2 h	2 200	1.45	3400	
	3 h	4 100	1.35	2700	
	4 h	7500	1.35	4200	

Polymerizations conducted with copper catalyst CuBr/PMDETA (1 equivalent) and stannous catalyst $Sn(Oct)_2$ (2 equivalents) at 90 °C monomers 1M in toluene, equivalents with respect to initiator. Precipitated in hexane. [a] GPC in THF *versus* MMA standards;; [b] calculated *via* ^{1}H NMR [c] acrylic monomer fraction in isolated polymer; [d]in bulk. *N.d.* not determined.

With these reaction conditions, the tandem system was explored with a set of new monomers. ε-Caprolactone (CL) was first tested in a homopolymerizations. The PCL homopolymerization **121** yielded a polymer with M_n of 12 700 and PDI of 1.55. CL was then employed as cyclic ester monomer for ROP (see entry **117** and Figure 3-14 a)). Under the conditions outlined above, full conversion was achieved within 1 h when employed together with MMA in a 1:2 monomer ratio. The precipitated polymer mirrored the conversion of MMA and LLA with an acrylic comonomer incorporation of 0.4. The PDI was much narrower at 1.79 and the theoretical molecular weight matched the theoretical weight more closely.

The combination of LLA and NIPAM (see entry **118**) was found to proceed the slowest. GPC traces of the polymer after 1 h showed a molecular weight of 8 900 g.mol^{-1} while the reaction sample after 4 h reaction time indicated a polymer with molecular weights around 900 g.mol^{-1}. The low molecular weight does not reflect the true polymer weight. Instead, it

reflects the poor solubility of the (co)polymer in all GPC adequate solvents. The precipitated polymer could not be dissolved again. MMA and CL were copolymerized in bulk (see entry **119**). Employing a monomer ratio of MMA:CL of 2:1 led to a 0.41 acrylic monomer fraction. After four hours of reaction time, MMA conversion was 41% and LLA conversion 63%. The precipitated polymeric product had a dispersity of 1.76. Combining the two monomers with most disparate polarities (CL and NIPAM) resulted in poor NIPAM conversion that stopped around 19% and a slow conversion of CL that reached 19% after four hours (see entry **120**).In incorporation of NIPAM in the precipitated polymer was 0.45. The NIPAM and CL combination had most similar reaction rates - albeit slow. The molecular weight distribution was also relatively narrow at 1.70 (see Figure 3-14).

The poor solubility of NIPAM-derived copolymers synthesized above led to considering other hydrophilic monomers. The choice of comonomer is limited for this system as any hydrophilic monomer bearing primary alcohols or primary amines may initiate ROP of the cyclic ester comonomer. Furthermore, acrylamides bearing heterocycles such as gylcidyl methacrylate can undergo ring opening polymerization when employed in tin octoate co-catalyzed ARGET ATRP. Finally, the NIPAM polymerizations have shown that the lower reactivity of acrylates *versus* methacrylates impedes matching the polymerization kinetics. With these considerations in mind, the next choice for radically polymerizable comonomer fell on dimethyl aminoethyl methacrylate (DMAEMA). This monomer combines the advantages of methacrylate reactivity with pH-dependent amine hydrophilicity without

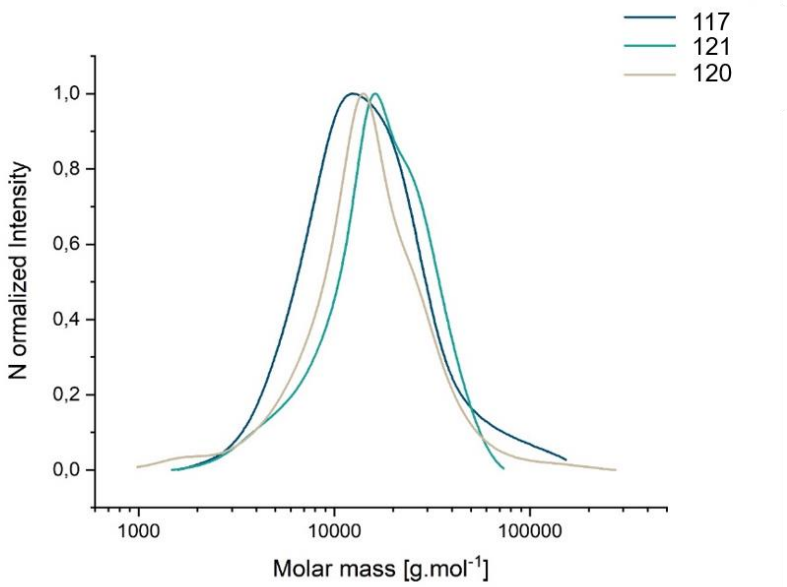

Figure 3-14: GPC traces of test tandem polymerizations yielding the P(CL)-b-P(MMA) copolymer **117** (in blue), PCL homopolymer **121** (in turquois) and PCL-b-PNIPAM homopolymer **120** (sand color). GPC eluent was THF and calibrated against PMMA standards.

being able to initiate or undergo ROP. Additionally, PDMAEMA portrays a LCST of 32-53 °C, depending on chain length, pH and salt concentration[291]. Hence, the following reactions were conducted with DMAEMA as co-monomer.

Table 3-7: Monomer equivalents and conversions of DMAEMA and CL polymerizations using simultaneous ATRP-ROP with stannous co-catalyst $Sn(Oct)_2$

	time	CL		DMAEMA	
	/h	equivalents	Conversion[a]	equivalents	Conversion[a]
122	1 h	100	42%	-	-
	20 h		98%		
123	1 h	-	-	100	44%
	20 h				64%
	26 h				74%
124	1 h	100	15%	100	52%
	3 h		72%		53%
	20 h		90%		72%
125[d]	1 h	100	22%	100	58%
	2 h		34%		58%
	3 h		54%		58%
126	2 h	200	21%	160	57%
	6 h		46%		61%
	20 h		85%		80%
127	2 h	100	37%	160	51%
	6 h		58%		56%
	20 h		74%		88%

Polymerizations conducted with copper catalyst CuBr/PMDETA (1 equivalent) and stannous catalyst $Sn(Oct)_2$ (2 equivalents) at 90 °C in bulk equivalents with respect to initiator. Precipitated in hexane. [a]calculated *via* ^{1}H NMR ; [b]GPC in THF *versus* MMA standards; [c] DMAEMA fraction in isolated polymer; [d]4 equivalents of $Sn(Oct)_2$.

Homo-polymerization of DMAEMA at 90 °C in bulk, with the previously established catalytic system using copper complex CuBr/PMDETA and stannous reducing agent $Sn(Oct)_2$ reached a conversion of 44% within one hour and 64% after 20 h (see entry **123** in Table 3-7). Precipitation into ice cold hexane yielded a polymer with M_n of 6000 g.mol^{-1}, and a PDI of 2.10, contrasting with a theoretic molecular weight of 9000 g.mol^{-1} (see entry **123** in Table 3-8) The dispersity determined *via* GPC is very large for an ATRP derived product, this broadening of molecular weight distributions were previously reported for a similar system and was interpreted as a consequence of the shifted K_{ATRP} equilibrium towards the activation side. However, the rate of conversion compares favorably to that of CL polymerized under the same conditions. The polymerization of CL reached 42% conversion after 1 h and 98% conversion after 20 h. The isolated PCL had a molecular weight distribution of 1.71 with molecular eight of 15 000 g.mol^{-1}, comparing to a theoretical molecular weight of 11 000 g.mol^{-1} (see entry **122** in Table 3-8). These first test reactions encouraged to proceed

with simultaneous tandem polymerizations. The choice of monomers and reaction conditions allowed to match the conversions within the first few hours of polymerization. Hence it was expected that based on the time of polymerization quenching, truly simultaneous tandem polymerization may be conducted.

Table 3-8: Experimental molecular weights and comonomer incorporation fraction of DMAEMA and CL polymerizations using simultaneous ATRP-ROP with stannous co-catalyst $Sn(Oct)_2$

	time /h	$M_{n,exp}$ [b]	$Đ_{GPC}$ [b]	$M_{n.theo}$ [a]	f [c]
122	Isolated	15 700	1.71		0
	1 h	5 500	1.10	4 800	
	20 h	10 700	2.11	11 200	
123	Isolated	6 000	2.10		1
	1 h	3 000	2.12	6 300	
	20 h	4 600	2.75	9 200	
	26 h	6 000	2.45	10 600	
124	Isolated	10 300	1.86		0.41
	1 h	2 700	1.72	9 200	
	3 h	6 800	1.39	15 800	
	20 h	6 700	1.60	20 600	
125[d]	Isolated	5 140	1.68		0.40
	1 h	2 000	1.87	10 800	
	2 h	2 600	1.69	12 200	
	3 h	4 100	1.41	14 500	
126	Isolated	11900	1.98		0.30
	2 h	9800	2.20	17900	
	6 h	11100	1.85	24500	
	20 h	9500	2.29	37700	
127	Isolated				0.50
	2 h	6000	1.43	15900	
	6 h	7700	1.44	19400	
	20 h	7300	1.59	28600	

Polymerizations conducted with copper catalyst CuBr/PMDETA (1 equivalent) and stannous catalyst $Sn(Oct)_2$ (2 equivalents) at 90 °C in bulk equivalents with respect to initiator. Precipitated in hexane. [a]calculated *via* ^{1}H NMR ; [b]GPC in THF *versus* MMA standards; [c] DMAEMA fraction in isolated polymer; [d]4 equivalents of $Sn(Oct)_2$

Using the same conditions as in the test reactions, CL and DMAEMA were employed in a simultaneous tandem polymerization in bulk. The dual initiator HBIB was employed together with the catalyst system described above. In contrast to the individual polymerizations, the DMAEMA conversion after 1 h reached 52% and plateaued at 72% after 20 h, while the CL conversion after 1 h was much lower at only 15% to reach full conversion after 24 h, see entry **124** in Table 3-8). In contrast to the DBU (co)catalyzed reactions, this monomer-catalyst system allowed to conduct simultaneous chain growth. Despite not achieving a perfect congruence of polymerization rates, the two chains grew at a comparable time frame.

However when contrasting the conversions within one hour between individual polymerizations and the tandem system, the increased conversion of DMAEMA and the decreased conversion of CL seems to indicate that the combination of the two polymerization processes leads to some degree of mutual interference. The ATRP shows only a slight increase in activity despite a two-fold dilution in DMAEMA concentration. The ROP on the other hand showed a marked decrease in polymerization rate during the first hour of polymerization. This effect may indicate that the combination of the two techniques results in increased side reactions. On the other hand, the change in reaction kinetics may also be explained by a lower percentage of stannous catalyst $Sn(Oct)_2$ available for polymerizing CL due to its consumption by copper catalyst reduction. To test the influence of stannous catalyst concentration on relative reaction rates for the two polymerizations, the polymerization was repeated with the same concentration of both monomers and copper catalyst but with an increased concentration of stannous catalyst (see entry **125** in Table 3-8). Increasing catalyst $Sn(Oct)_2$ to four equivalents with respect to initiator led to an increase in polymerization rate for both ATRP and ROP. The conversion of CL reached 22% within one hour, while at the same time, the ATRP consumed 58% of DMAEMA monomer. The increase in polymerization rate was more pronounced for ROP than for ATRP. This experiment suggests that the interaction between the two polymerizations is a kinetic effect due to available catalyst concentration.

ROP of cyclic esters are known to experience significant amounts of transesterification side reactions when employing organo-stannous catalysts[290]. As the transesterifications increase after with increasing monomer conversion and with reaction time, polymerizations were stopped when conversion of CL neared 100%. When monitoring CL conversion *via* ^{1}H NMR, (near) quantitative conversions were usually achieved within 24 h of reaction time. Within the same time frame, conversions of DMAEMA of up to 88% could be achieved. The precipitated products' ^{1}H NMR spectra revealed a comonomer distribution that matched the relative monomer equivalents and their conversions. By adjusting the initial monomer concentrations, the polymeric products reflected the expected monomer distributions. By this approach, polymers with DMAEMA:CL ratios between 1:2 and 1:1 were targeted, as well as isolated (see entries **126** and **127**). Dispersities of the polymers ranged between 1.41 and 2.20. Although much narrower molecular weight distributions have been reported for a range of copolymers, these values are relatively low considering the simultaneous nature of their polymerization.

It is worth pointing out that in all simultaneous copolymerizations of CL and DMAEMA, the NMR signals of polymer product indicated that both monomers indeed polymerize. This observation is in contrast to MATYIJESWESKI's work who found that,

simultaneous polymerization of these two monomers is not possible. They stipulated that DMAEMA complexes with the tin catalyst and therefore impedes ROP of CL[288]. By contrasting the reaction conditions employed herein and in the cited work, the employed stannous catalyst and its equivalent with respect to ATRP catalyst were found to vary. The 1:1 ratio of copper catalyst to stannous catalyst employed by MATYIJESWESKI et al. suggests rather that the reduction of $CuCl_2$ by catalyst $Sn(Oct)_2$ occurs preferentially over polymerization of CL monomer. As a result, stannous catalyst is continuously removed from the polymerization mixture with each reduction of copper catalyst and ROP cannot proceed. The excess $Sn(Oct)_2$ employed herein counters this effect.

^{1}H NMR spectra of precipitated polymers were recorded and confirmed that both monomers participated in polymerization (see Figure 3-15).

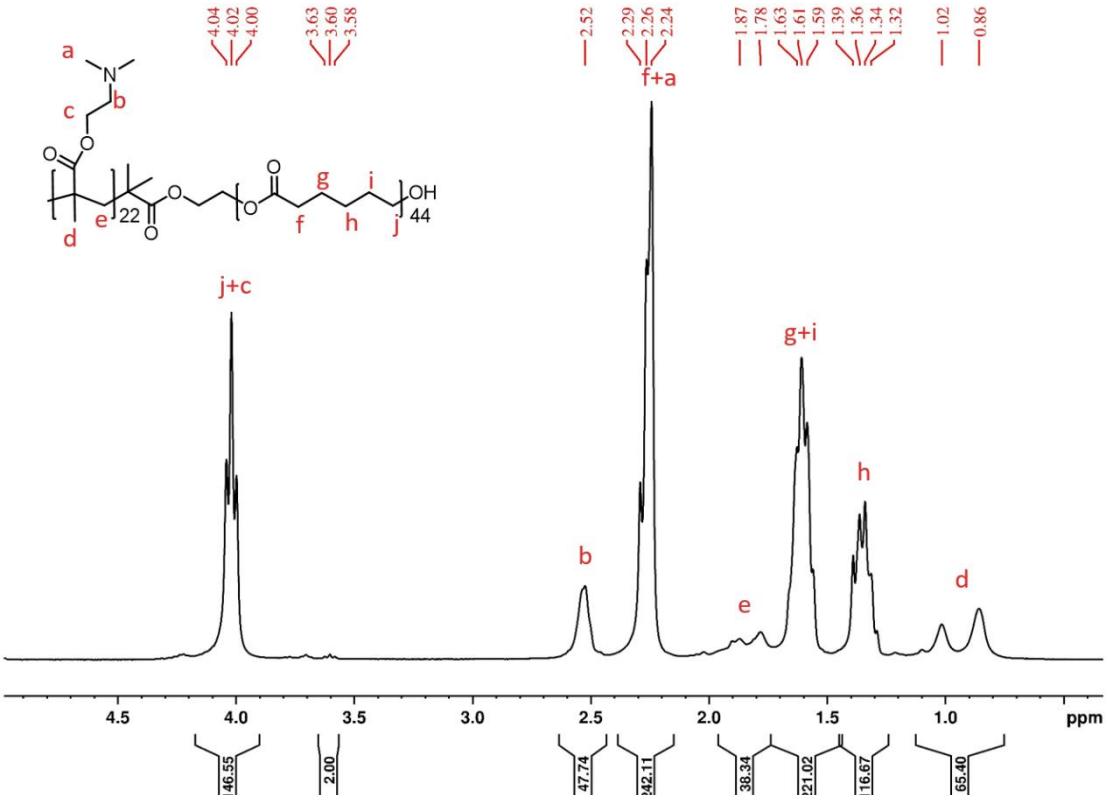

Figure 3-15: ^{1}H NMR spectrum diblock polymer **126** in $CDCl_3$.

With these promising results, it was decided to adopt the $Sn(Oct)_2$ and CuBr/PMDETA catalyzed simultaneous tandem polymerization of CL and DMAEMA for surface grafting.

3.6 Tandem Polymerization on Silicon Wafers

After functionalizing the wafers with heterobifunctional initiators, and establishing that the two polymerization techniques — $Sn(Oct)_2$ catalyzed ROP and ATRP — are mutually orthogonal, the polymerization system was then tested for simultaneous surface grafting.

Conducting polymerizations initiated off a surface confront the synthetic polymer chemist with an interesting issue: how to track reaction progress *in situ*? Usually, when tracking the kinetics of a polymerization, samples are drawn periodically, quenched and after (optional) removal of catalyst, both conversion (*via* NMR or IR) and molecular weight (*via* MS or GPC) of the growing polymer chains are determined. However, when trying to observe the polymer chains growing off a surface, this approach is complicated by the covalent attachment to said surface. This issue precludes liquid NMR as a method to determine conversion directly, as well as GPC to measure molecular weight. One way to overcome this limitation is by calculation conversion by integrating monomer signal with respect to an internal, inert reference material and measuring molecular weight by cleaving the brushes from the substrate. In the case of silica surfaces, this is commonly achieved by treatment with concentrated hydrofluoric acid. However, this approach is not only labor intense and potentially dangerous, it also suffers from the uncertainty of whether the individual chains are cleaved in completion or have been degraded by the harsh conditions of the cleaving process. To overcome this obstacle, the polymerizations were conducted with a short, sacrificial initiator present in the reaction mixture. Assuming that the kinetics of polymerizing chains in solution are comparable to those at the wafer interface, samples drawn periodically from the reaction mixture allow to make approximations for the polymerization progress. This approach is commonly chosen for the ease of drawing samples without the need to resort to harsh, destructive methods[213,292,293]. Evidently, the assumption that this approach rests on — namely the comparable kinetics of solution and interface polymerization — is the major weakness of this approach. The much higher steric demand at a surface and the lower degrees of freedom of tightly growing polymer chains intuitively speak against the assumption. On the other hand, a TROMMSDORF-like effect has been suggested[102,294]. Various publications have investigated the validity of this assumption by comparing the polymer properties grown in solution with a sacrificial linker with that of the polymers yielded when cleaving off the linker[213,292,293]. Although some controversy regarding specific systems remains, there is consensus that this assumption holds well enough to make good approximations about the polymerization kinetics. A fuller picture relies on contrasting

the insight gained by free-linker derived kinetics with information from XPS, film thickness, contact angle and ToF-SIMS.

The sacrificial initiator allows to further assess the initiation efficiency of the tandem system. Additionally, through sacrificial initiator, the molecular weight of the polymer can be controlled more accurately. With the surface initiating groups present in such low concentrations (with respect to the overall polymerization mixture), even small amounts of inhibitor would suffice to quench the reaction. The amount of initiator on the surface also depends on the exact area of the wafer employed. Employing sacrificial initiator allows to target molecular weights[294]. Poor or unequal initiation efficiency would be highly detrimental to the functionalization of surfaces. If, for example, initiation at the alcohol were much slower than that of ATRP, the growing PDMAEMA chains could impede growth at the neighboring ROP initiating sites. Or else, if initiating efficiency is generally poor, only a sparsely grafted surface could be synthesized. Similarly for the free sacrificial linker, if initiating efficiency is relatively poor, a large proportion of the resulting polymeric products would be expected to be homopolymers of either one or both monomers. Hence by assessing whether the simultaneous tandem system yields block copolymers, some information about the initiating efficiency can be derived.

Table 3-9: Monomer equivalents and molecular weights for simultaneous tandem polymerizations on silicon wafers.

Entry	CL	DMAEMA	M_n[a]	PDI[a]	f[b]
128	20	20	5 140	1.68	0.40
129	100	-	15 700	1.71	0
130	-	100	6 000	2.10	1
131[c]	100	-	14 400	2.00	0
132[c]	-	100	17 100	2.21	1
133	200	160	11 900	1.98	0.3
134	30	30	9 000	2.00	0.5
135	100	160	7 000	1.56	0.6
136[c]	200	200	10 700	1.66	0.4
137[c]	100	160	14 000	2.00	0.6

[a]Determined *via* GPC in THF *versus* PMMA standards. [b]fraction of PDMAEMA in polymer sample, determined *via* ^{1}H NMR. [c]using a functionalized glass slide.

The polymerizations of DMAEMA and CL were conducted with a CuBr/PMDETA catalyst : initiator HBIB : $Sn(Oct)_2$ ratio of 1:1:2 at 90 °C in bulk. Just before the polymerization was initiated, a functionalized wafer was added to the SCHLENK flask. In order to ensure stirring, a very small stir bean was added to the flask. Care was taken that the stir bar was not in direct contact with the wafer to avoid scratches on the surface. Various monomer ratios were targeted. When employing the DMAEMA and CL monomers in a 1:1 ratio, the DMAEMA fraction was between 0.4 and 0.5 of the precipitated polymer (see entries **128**, **134** and **136** of Table 3-9). Homopolymerizations yielded the expected pure homopolymer. When employing a lower ratio of DMAEMA,:CL the incorporated DMAEMA is lowered. For entry **133**, a DMAEMA:CL ratio of 1.6:2 was employed and the isolated polymer had a DMAEMA fraction of 0.3. When employing a DMAEMA:CL monomer ratio of 1.6:1, the isolated polymer had a DMAEMA monomer fraction of 0.6 (see **137**. Polymeric products had a PDI between 1.56 for entry **135** to 2.21 for entry **132**.

Interestingly, when using a functionalized microscope slide rather than a small silicon wafer, the isolated polymers had greater molecular weights. While employing 100 equivalents of DMAEMA in a homopolymerizations, the wafer polymerization yielded a polymer with M_n of 6 000 g.mol^{-1} (see entry **130**). The polymer isolated from the glass slide polymerization had a M_n of 17 100 g.mol^{-1} with the same equivalents (see entry **132**. Likewise, when contrasting entry **137** with **135**, the glass slide polymerization produced a polymer with 14 000 g.mol^{-1}, while the small wafer produced a polymer of only 7 000 g.mol^{-1}. The difference between the ROP only of **129** polymerized with a small wafer with entry **131** on a glass slide is less pronounced. This effect might be explained by different diffusions in the reaction vessel. When using the large glass slide, no stir bar was employed.

GPC traces of the polymers derived from sacrificial linker in the simultaneous surface grafting generally showed a unimodal distribution (see Figure 3-16). However, some asymmetries could be observed. Polymer **136** and **131** showed low molecular weight trailing and **134** showed some indication of a high molecular weight shoulder. A unimodal distribution of two polymerizations can arise either as a result of block copolymers eluting as a function of their molecular weight, or else due to the presence of two homopolymers with only one being soluble in the elution medium. GPC separates based on molecular weights of eluting polymers. It does not provide information about the chemical composition of the analytes. The ^{1}H NMR data shows the chemical composition of the precipitated polymer but does not differentiate between a mix of two polymers and block copolymers.

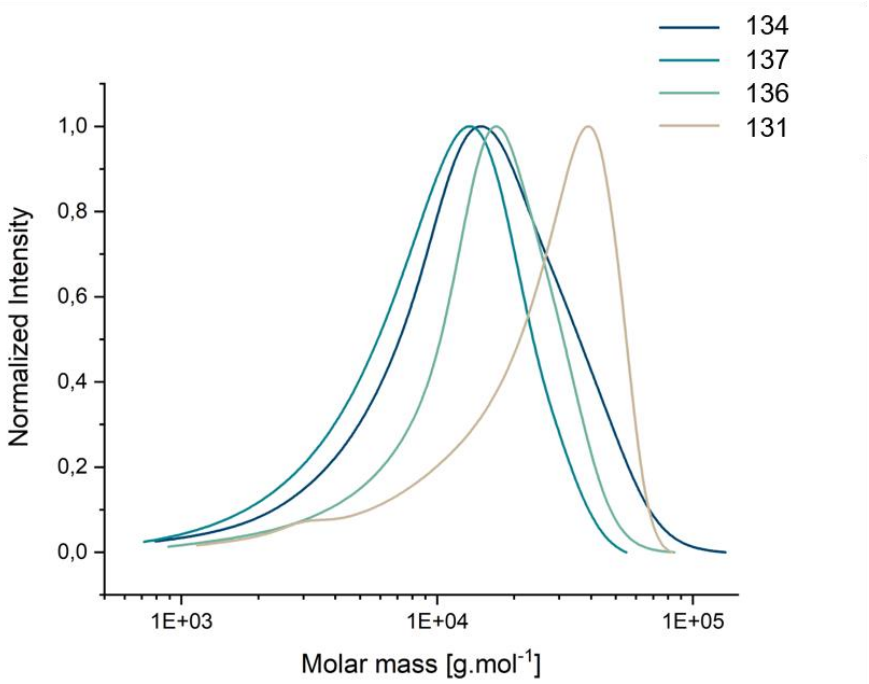

Figure 3-16: GPC traces of sacrificial initiator derived polymers of simultaneous surface polymerizations **137** and **134**. GPC versus MMA standards in THF.

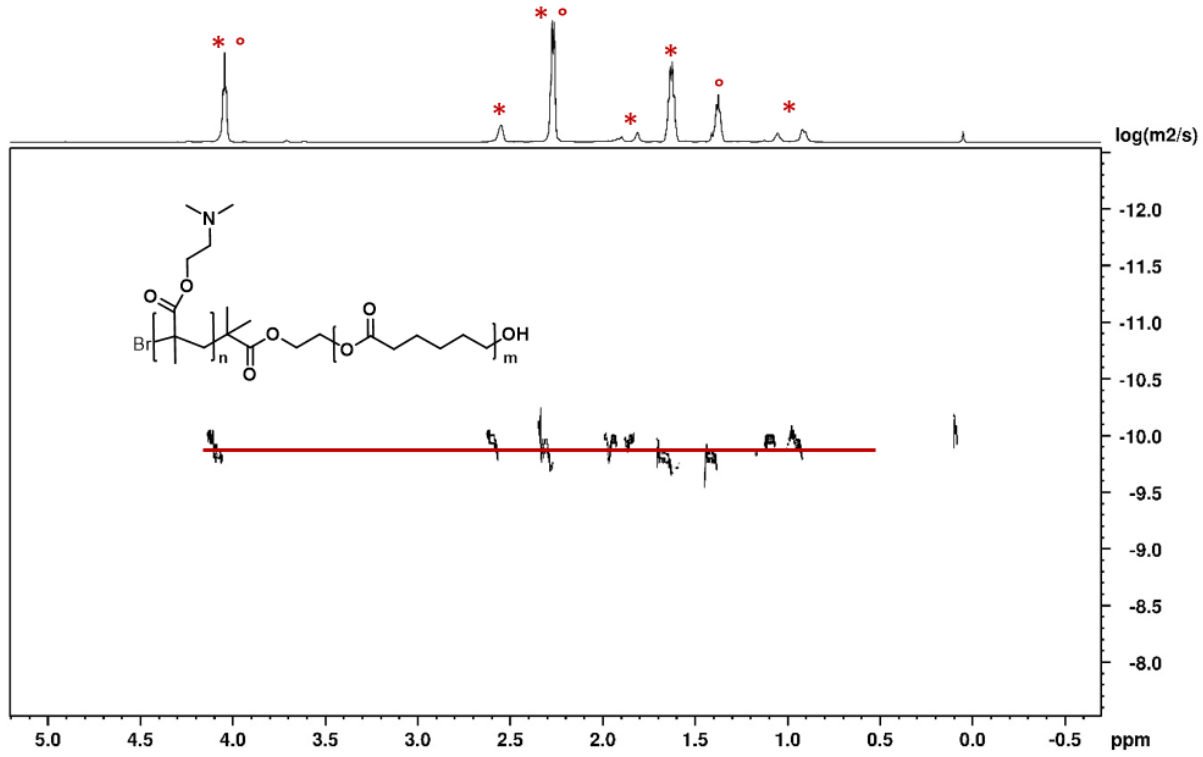

Figure 3-17: DOSY ^{1}H NMR of simultaneously polymerized PDMAEMA-PCL block copolymer **134** shows all polymer signals occurring at the same diffusion coefficient. Signals marked with asterisks refer to DMAEMA derived chemical shifts and circles were used to mark CL signals. Recorded in $CDCl_3$ at 700 MHz.

To overcome these limitations, ^{1}H DOSY NMR spectra were recorded. These NMR experiments show chemical shifts ordered by diffusion coefficients. A pure block copolymer

with narrow molecular weight distribution would be expected to show only one major diffusion coefficient for all chemical shifts. Indeed, Figure 3-17shows that all polymeric species have the same diffusion coefficient. Of course two separate polymer populations with similar molecular weights could also give rise to the observed effect. However, given the disparities in comonomer incorporation with DMAEMA making 30% of the total polymer signals, this explanation is highly unlikely. The DOSY experiment therefore proves that the above describes system initiates reliably to produce copolymers.

Thermogravimetric analysis (TGA) was conducted of the polymer synthesized using the above system. Figure 3-18 shows the gravimetric loss curves as a function of temperature at a heating rate of 10 $K.min^{-1}$. The PCL reference **121** shows one single decomposition step with an inflection at 330 °C as is expected from literature[295]. The PDMAEMA homopolymer portrays the characteristic two decomposition temperatures associated with scission of C-N bond in the first step and carbonyl degradation in the second step[296]. The two decomposition steps occur at 285 °C (45% weight loss) and 405 °C (37% weight loss) respectively. KASHIWAGI et al.[297] demonstrated that poly (methyl methacrylates) show a marked weight loss below 200 °C as a result of carbon-carbon scission from head-to-head monomer addition. Radical polymerization, as well as ATRP is selective for head-to-tail monomer addition[5]. The more labile head-to-head sites are therefore indicative of termination reactions by combination of

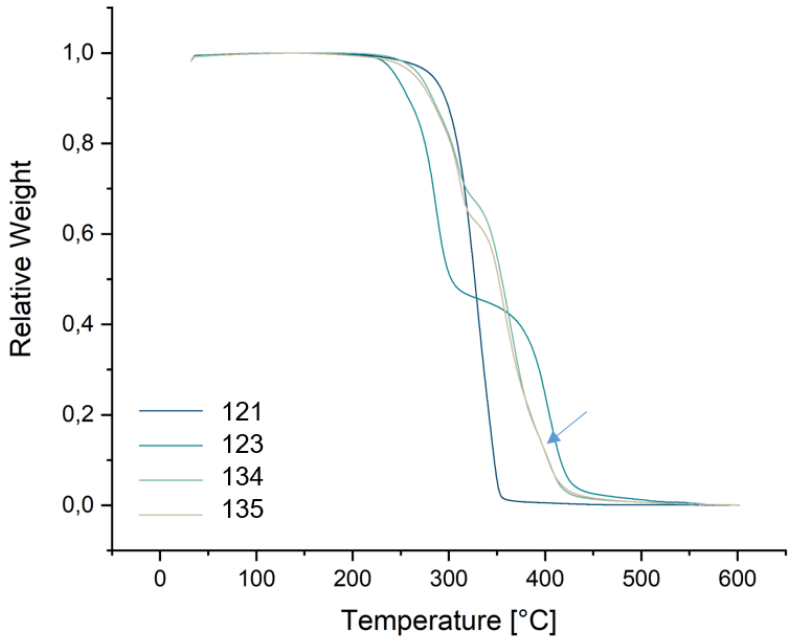

Figure 3-18: TGA curves of PDMAEMA reference **123**, PCL reference **121** and copolymers **135** and **134**. Arrow indicates shoulders.

active radicals. Absence of degradation at this temperature range therefore indicates that the polymerization shows very few termination events. The two copolymers **134** and **135** show two marked decomposition temperatures each with inflection points at 310 °C and 360 °C. The higher temperature decomposition peak has a shoulder around 400-410 °C in both cases (see blue arrow). However this shoulder is not very prominent. The higher PDMAEMA bearing sample **135** also shows a greater weight loss (32%) associated with the first PDMAEMA decomposition temperature than the lower PDMAEMA containing sample (28%). Again, no decomposition could be observed below 200 °C and is therefore indicative of a low incidence of combination events.

Dynamic Scanning Calorimetry (DSC) was used to gain insight into the macroscopic thermal properties of the polymers synthesized above. The glass transition temperature (T_g) of PDMAEMA reference **123** had a point of inflection at 8 °C. A melting point (T_m) was not observed in the temperature range studied and therefore indicates amorphous behavior. PCL reference **121** showed no T_g. This absence of glass transition is unexpected. Literature reports glass transitions of PCL at around -70 °C[298]. A marked T_m occurred at 54 °C, indicating the semi-crystalline nature of the reference material. The copolymer containing a DMAEMA fraction of 0.30 (**134**) had a T_m at 53 °C and a glass transition at -49 °C, indicating that the copolymer has a semi-crystalline structure. In contrast, the 1:1 PCL-PDMAEMA copolymer (**135**) showed a T_g at -46 °C, a T_m at 50 °C and underwent cold crystallization at -4 °C.

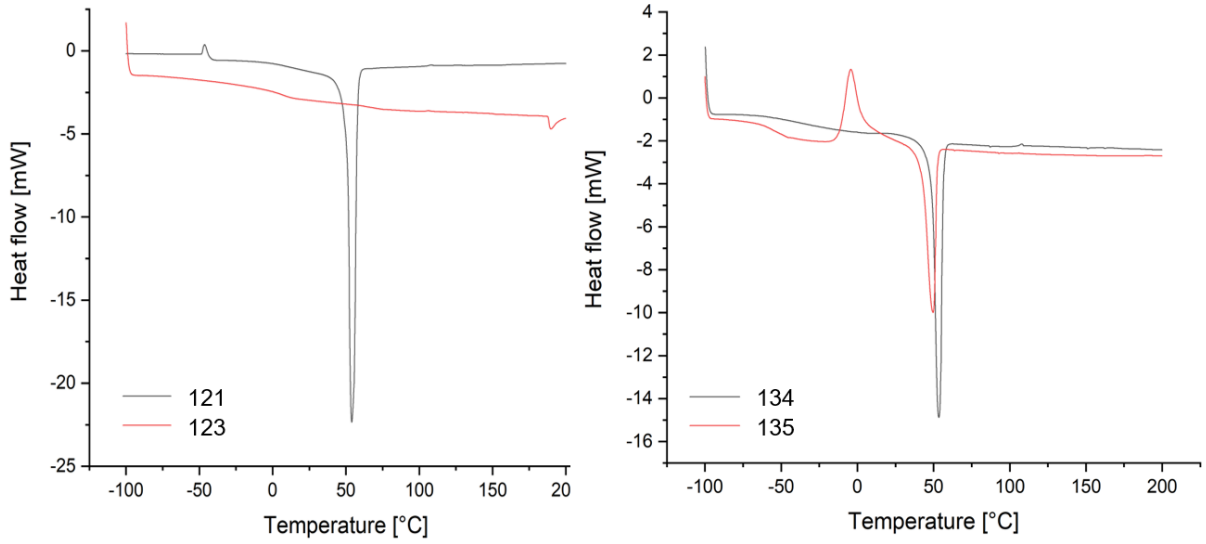

Figure 3-19: DSC curves of PDMAEMA reference **123**, PCL reference **121** and copolymers **134** and **135**.

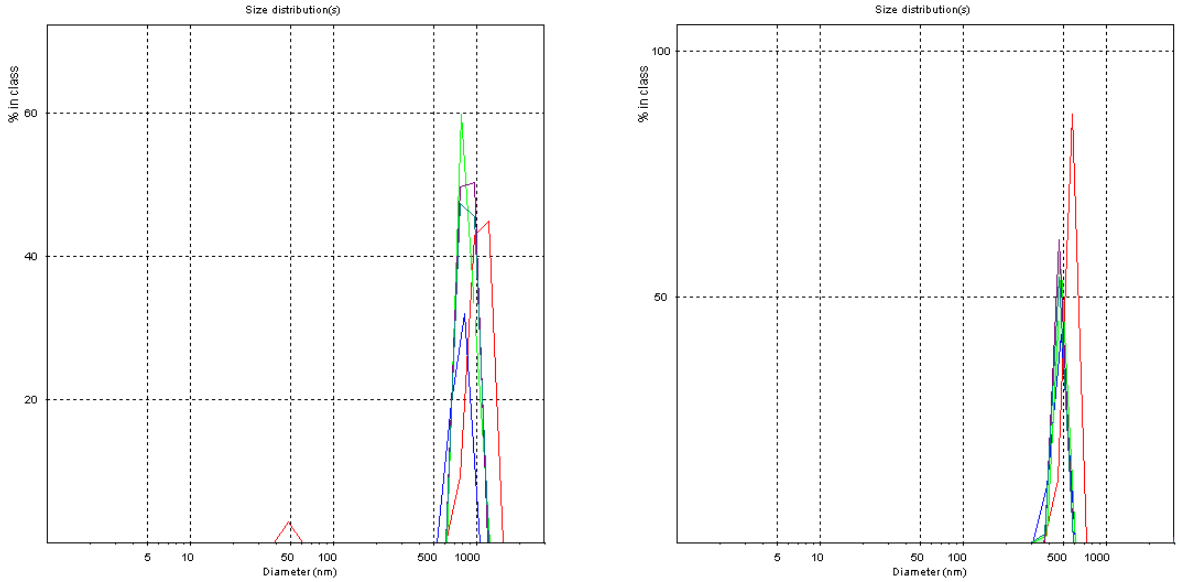

Figure 3-20: DLS of block copolymers **133** (left) and **135** (right) showing supramolecular assemblies.

Amphiphilic block copolymers have the tendency to form supramolecular structures when dissolved in a selective solvent. Solubility of the produced polymers can therefore be seen as an indirect assessment of covalent attachment between the two polymer blocks. Dissolving the PDMAEMA-PCL in water under stirring immediately produced a turbid solution. Dynamic light scattering (DLS) determines the diffusion coefficient of the supramolecular structures formed. *Via* the STOKES-EINSTEIN relationship, their hydrodynamic radius can be determined. Figure 3-20 shows the DLS plots of copolymers **133** and **135**. The block copolymer with lower PDMAEMA fraction **133** produced structures in water with 554 nm diameter with a PDI of 1.0. The higher PDMAEMA fraction in **135** led to smaller structures of 420 nm with a PDI of also 1.0.

3.7 Surface Characterization

3.7.1 Atomic Surface Composition — XPS

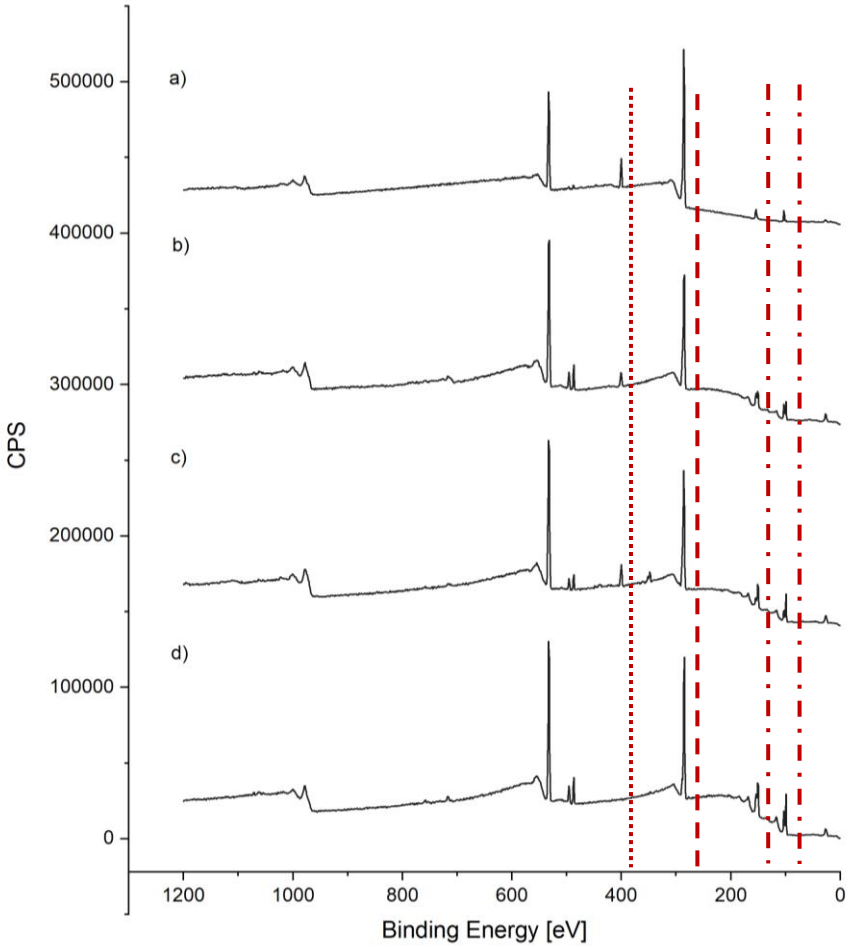

Figure 3-21: XPS survey of grafted wafers. a) binary brush **135**, b) binary brush **134**, c) PDMAMEA homopolymer brush **130** and d) PCL homopolymer brush **129**: Dotted line indicates the N1s peaks (to the left), dashed line shows C1s signal (to the left) and dotes/dashed line shows Si2s and Si2p signals (to the left).

To assess whether the surface was functionalized successfully, its atomic composition was determined *via* XPS. XPS is both surface sensitive as well as non-destructive and allows to make semi-quantitative determinations of atomic surface composition. The plain silicon wafer has an oxidized surface and only silicon and oxygen derived signals are expected, with the customary carbon signals derived from adsorption and surface reactions by handling under atmosphere. The linker-functionalized wafer **98** showed weak bromine signals, and strong carbon and oxygen signals (see Figure 3-21). With these references, a change in signal intensity ratios can be used to qualify whether the polymerizations led to the growth of polymer chains. DMAEMA monomers further contain nitrogen atoms and it is expected that

only those wafers grafted with PDMAEMA contain (strong) nitrogen signals. So for all grafted wafers, the carbon, nitrogen, oxygen and bromine signals are regions of interest.

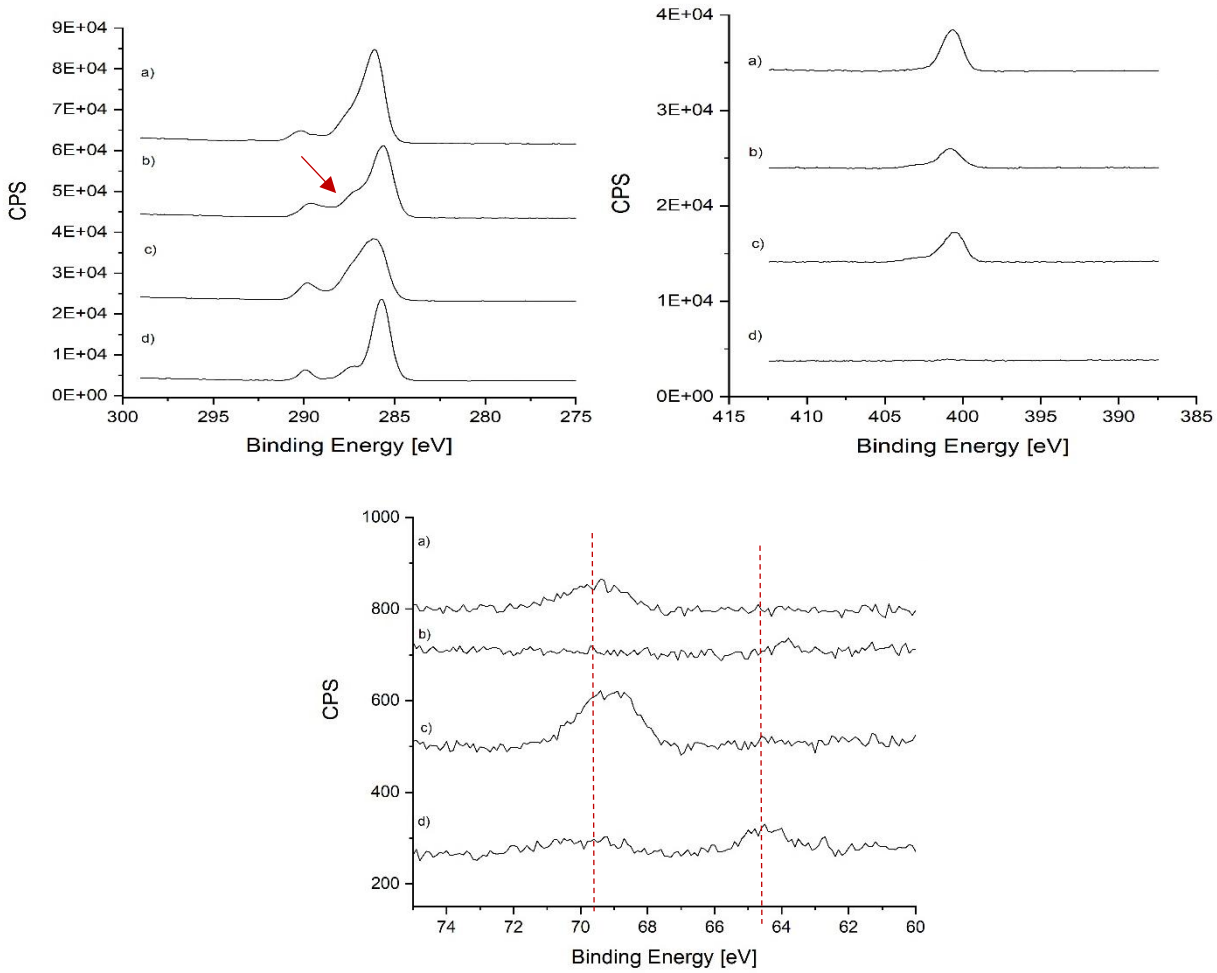

Figure 3-22: XPS spectra of grafted wafers. a) copolymer **135**, b) copolymer **134**, c) PDMAEMA homopolymer **130**, d) PCL homopolymer **129.** Top left: C1s region, top right: N1s region and bottom: Br 3d region.

The survey of a representative selection is presented in Figure 3-21 with the two homopolymer reference brushes **130** and **129** (for PDMAEMA and PCL respectively, see Figure 3-22 (c) and d)) and two binary PDMAEMA-PCL brushes (for binary brushes **135** and **134** see Figure 3-22 a) and b)). Regions of interest in the spectrum were identified as the N1s, C1s and Br3d regions — these are shown in Figure 3-22. All grafted wafers show characteristic carbon peaks around 286 eV. This signal was identified as deriving from sp3 bonded C-C. Both PCL and PDMAEMA contain such groups. Additionally, a smaller peak at 290 eV was identified deriving from sp2 bonded O-C=O carbons. Again, both PDMAEMA and PCL contain ester groups and the presence, as well as relative intensity of this peak is expected. Additionally, the C-H derived peak at 286 eV shows a pronounced high binding energy

shoulder of varied intensity. The shoulder derives either from sp3 bonded C-O carbons or else from sp3 C=N carbons. The PCL reference wafer **129** shows the lowest and most discrete shoulder, while the PDMAEMA reference wafer **130** shows the most intense shoulder. Both PDMAEMA and PCL contain sp3 C-O carbon groups. Only PDMAEMA further features nitrogen bonded carbon. The relative intensities between C-C and C-N sp3 bonded carbons therefore reflect the trend of PDMAEMA incorporation, with the most intense shoulder in the pure PDMAEMA sample **130**, a lower intensity in sample **135**, an even lower intensity for the lower PDMAMA fraction sample **134** and the lowest for PCL homopolymer reference **129**.

The spectrum showing the Br3d region (around 69 eV) had a low signal to noise ratio. Only a low Br signal was expected as the concentration of Br in relation to the brushes is low. It was further expected to see similar intensities for all PDMAEMA-containing samples while the PCL reference was expected to show a lower intensity, as it is expected that successful grafting of PCL would bury the haloester functionality derived from the linker under the PCL layers. As XPS is a surface sensitive technique, signal intensities are lowered with increasing depths. Indeed, the Br peak of the PDMAEMA wafer **130** was the most intense, while much lower for the PCL reference **129**. The asymmetric shape derives from the $Br3d_{3/2}$ and $d_{5/2}$ spin-orbit coupling. Surprisingly, the mixed brush **134** showed no Br signal, while **135** had a Br signal less intense than the PDMAEMA reference **130**.

The XPS spectral region around 400 eV shows the presence or absence of nitrogen on the sample. Neither CL nor the linker contain nitrogen atoms. As a consequence, no N1s signal would be expected. Indeed, the respective spectrum showed no such peak. All other, PDMAEMA containing brushes (wafers **130, 134** and **135**) all showed an intense N1s peak at 400 eV, as expected. Their relative intensities match the intensity of the C-N shoulder observed in the carbon spectrum.

3.7.2 ToF-SIMS

The functionalized surfaces were characterized *via Time of Flight — Secondary Ion Mass Spectrometry* (ToF-SIMS). For this technique, *regions of interest* (ROI) on sample surfaces are sputtered with primary ions (usually noble gas, gallium or bismuth ions) that trigger a collision cascade in the molecules on the surface. Polymeric samples respond through a collective molecular motion regime. As kinetic energy is dissipated with each collision, typically only fragments originating from the topmost multilayers have sufficient energy to overcome the binding energy of the sample. Ejected fragments may be electrons, atoms, ions, clusters of ions/atoms and molecules. These fragments can be positively or negative charged, radicals or neutral. Only the charged species (less than 1%) are accelerated towards a mass spectrometer's detector and separated as function of their time of flight. The distribution of mass-to-charge ratios thus gives highly sensitive (ppm to ppb) information about elemental, isotopic and molecular composition of the surface.[299]

With all ToF-SIMS techniques, it is worth keeping in mind that the high variation in ionization probabilities of different substrates necessitates well-calibrated reference systems in order to yield quantitative results[299]. Barring such standards, the insight gained from ToF-SIMS measurements must be seen as qualitative only. Furthermore, the high sensitivity of ToF-SIMS means that even small, fortuitous impurities can yield noticeable signals. This issue is compounded with the before-mentioned difficulty in quantification due to differences in ion yields. Nevertheless, ToF-SIMS analysis can be employed to provide valuable information about the identity and homogeneity of the wafers functionalized *via* simultaneous surface grafting. The abundance of signals mandates a selection of characteristic signals. The choice can follow a *manual* selection, where characteristic peaks are matched to specific ions that are considered representative of the samples at hand, or else *via* statistical methods.

The analytical approach chosen for the system at hand involved ToF-SIMS measurements of sample wafer **128** after simultaneous tandem polymerization and subsequent cleaning steps. To identify the origins and identities of the secondary ions, five reference wafers were measured: one cast with a solution of the catalyst complex CuBr/PMDETA, one with tin catalyst $Sn(Oct)_2$, one functionalized only with the linker (wafer **98**), one grafted exclusively with PDMAEMA (wafer **130**) and one grafted exclusively with PCL (wafer **129**). The reference measurements and the sample measurement were recorded in both positive and negative ion channels. From the resulting signals, characteristic mass-to-charge-ratios were selected manually and assigned to specific fragments, using the mass fine structure, typical isotopic patterns and chemical probability, wherever possible. The sample measurement of wafer **128** was subsequently contrasted to the reference signals. Additionally, multivariate data analysis (PCA, NMF) was performed to identify and separate signals arising

from different compounds. Depth profile measurements were then conducted on sample wafer **128** to assess the vertical distributions of previously identified signals and hence judge the vertical homogeneity of the grafted samples. Finally, ToF-SIMS imaging mode was employed to assess the horizontal homogeneity of the simultaneously grafted wafer **128**.

Manual Selection of Signals and Interpretation

An overview of the surface spectra gathered from the two polymer references (wafers **129** and **130**), the linker modified wafer (**98**) and the simultaneously grafted sample (**128**) is provided in the appendix (see Figure 7-2 for positive channel and for the negative channel). From these spectra, individual signals were selected and their likely empirical formula established by considering the isotopic fine structure of the mass-charge signals detected *via* ToF-SIMS. Contrasting these identified signals between the individual reference spectra and the sample spectra allows to infer the origin of the compounds. An overview of these manually selected signals is provided in Table 3-10 and Table 3-11 for negative and positive channels respectively.

Table 3-10: Selection of noteworthy negative ion channel ToF-SIMS signals, their likely empirical structure and origin. Counts are compared between the sample and reference wafers for each signal.

Area Norm. By Total Ion Intensity Statistics								
	Origin	Mass (u)	CuBr/PMDETA	SnOct2	Linker	PCL	PDMAEMA	Mixed Brush
Cu-		62.9448	7.75E-04	1.33E-06	1.51E-05	8.16E-06	2.90E-05	1.19E-04
CuBr-	Cu cat	141.865	7.40E-04	3.32E-05	1.06E-04	6.39E-05	5.00E-05	3.07E-04
304.68 u		304.695	4.55E-03	5.67E-05	1.59E-05	1.21E-03	5.23E-05	1.91E-04
C_8H_15O_2-		143.149	1.53E-02	2.03E-01	6.50E-04	3.78E-04	1.23E-04	2.59E-04
C_16H_29O_4Sn-	Sn cat	405.109	3.70E-05	2.66E-03	2.47E-06	6.40E-06	3.03E-05	3.07E-05
453.31 u		453.301	5.93E-05	7.31E-04	2.63E-06	6.61E-06	1.55E-05	2.55E-05
Br-	Linker	78.9418	4.62E-03	4.96E-06	1.36E-01	8.45E-02	2.94E-03	3.30E-02
SiO_2-		59.9657	1.18E-04	2.10E-03	1.95E-02	4.38E-03	2.25E-03	1.45E-04
Si_2O_5H-	substrate	136.939	8.80E-05	1.75E-04	1.27E-02	4.59E-03	4.57E-04	4.38E-04
Si_3O_7H-		196.899	2.27E-04	1.04E-04	5.11E-03	2.10E-03	2.32E-04	7.83E-04
C_6H_9O_2-		113.078	2.14E-04	4.46E-03	1.31E-04	1.21E-02	4.85E-04	6.34E-04
C_6H_9O_3-	PCL	129.096	1.64E-04	1.03E-03	4.59E-05	1.07E-02	1.26E-04	4.70E-04
C_2H_2O_2-		58.0087	2.50E-05	1.34E-04	1.80E-03	1.62E-02	5.67E-04	1.12E-03
C_3H_3O_2-		71.0196	1.02E-03	1.64E-02	1.92E-03	2.97E-02	3.02E-03	1.32E-02
CHO_2-	PCL/PDMAEMA	45.0005	1.68E-04	1.90E-03	1.92E-03	1.06E-02	6.12E-03	4.14E-03
CN-		26.0128	3.01E-03	2.97E-04	7.19E-03	7.71E-03	8.38E-02	2.29E-02
C_2H_3O-	PDMAEMA	43.0207	3.94E-05	4.68E-04	1.63E-03	1.08E-02	1.86E-02	7.36E-03
C_4H_5O_2-		85.0367	3.07E-04	7.04E-03	6.83E-03	7.47E-03	1.18E-01	4.62E-03
163.07 u	PDMS	163.063	1.71E-04	2.67E-03	2.16E-04	5.50E-04	4.79E-03	2.17E-04
SiC_3H_9O-		89.0531	2.04E-04	4.45E-03	3.95E-04	1.57E-03	2.26E-02	1.82E-03
NO3/C4N?		61.9799	8.56E-06	5.66E-05	6.61E-04	3.10E-03	1.61E-03	7.80E-03
S-		31.9749	7.11E-06	4.70E-07	3.10E-04	8.99E-05	5.25E-05	1.80E-04
SO_2-	unclear	63.9731	6.93E-06	6.62E-06	1.89E-03	1.39E-03	1.44E-03	3.18E-03
SO_3-		79.9583	6.44E-05	1.63E-05	1.00E-02	1.93E-03	3.59E-03	1.86E-02
SO_4H-		96.9627	6.62E-05	2.40E-05	4.94E-03	1.08E-03	2.57E-02	1.19E-01
CNO-		41.9941	2.64E-04	3.36E-04	3.32E-03	9.37E-03	5.82E-03	9.64E-03
Total Counts			5.78E+07	1.69E+07	6.48E+06	1.10E+07	2.40E+07	2.87E+07

Table 3-11: Selection of noteworthy positive ion channel ToF-SIMS signals, their likely empirical structure and origin. Counts are compared between the sample and reference wafers for each signal.

Area Norm. By Total Ion Intensity Statistics								
	Origin	Mass (u)	CuBr/PMDETA	SnOct2	Linker	PCL	PDMAEMA	Mixed Brush
C_16H_40N_6Cu+	Cu cat	379.234	5.83E-02	2.25E-05	2.85E-05	8.66E-06	8.93E-06	8.28E-06
C_9H_23N_3CuBr+	Cu cat	315.052	4.71E-03	3.69E-05	3.52E-05	4.08E-05	7.90E-05	6.81E-05
C_5H_10N+	Cu cat	84.0778	5.42E-03	1.52E-05	7.76E-04	3.66E-04	3.71E-03	1.44E-03
Cu+	Cu cat	62.9281	2.54E-03	4.41E-06	2.81E-05	1.58E-05	3.73E-05	2.96E-04
C_5H_8N+	Cu cat	82.0635	3.48E-03	1.04E-05	8.38E-04	3.84E-04	1.63E-03	1.04E-03
Si_2C_5H_15O+	PDMS	147.085	1.93E-03	6.18E-02	1.04E-02	5.36E-03	1.39E-03	6.73E-04
SiC_3H_9+	PDMS	73.085	1.30E-02	1.74E-01	3.35E-02	3.08E-02	1.92E-02	1.24E-02
SiC_2H_7+	PDMS	59.0333	2.23E-04	6.78E-03	1.90E-03	9.96E-04	4.90E-04	2.47E-04
Si_3C_5H_15O_3+	PDMS	207.057	1.02E-03	1.50E-02	2.33E-03	1.25E-03	3.57E-04	1.90E-04
Si_3C_7H_21O_2+	PDMS	221.125	1.52E-03	8.95E-03	2.21E-03	9.51E-04	2.25E-04	1.21E-04
Si_4C_7H_21O_4+	PDMS	281.091	5.11E-04	8.06E-03	1.46E-03	7.63E-04	1.22E-04	7.61E-05
Si+	substrate/PD	27.9744	1.22E-04	3.26E-03	2.94E-02	2.15E-03	2.00E-04	4.14E-05
530.46 u	Linker?	530.474	4.30E-06	4.68E-05	3.22E-04	1.43E-06	9.99E-07	1.39E-06
368.43 u	Linker?	368.429	2.10E-05	1.99E-05	7.73E-05	3.17E-06	1.59E-05	3.64E-05
NH_4+	unclear	18.0353	6.59E-05	0.00E+00	5.89E-04	1.38E-04	3.31E-04	5.02E-04
CH_3+	unspecific	15.0228	7.62E-04	2.81E-04	6.54E-03	1.74E-03	2.92E-03	3.05E-03
SiOH+	substrate	44.9782	4.40E-05	4.18E-04	1.84E-02	1.84E-03	1.48E-04	8.48E-05
SiO_3H_3+	substrate	78.9986	5.07E-05	1.79E-05	9.04E-03	7.55E-04	2.91E-04	4.04E-04
SiO_2H_3+	substrate	62.9923	2.76E-05	4.35E-05	5.40E-03	1.15E-03	1.70E-04	1.67E-04
C_3H_3O+	PCL	55.0186	3.26E-04	8.77E-04	8.23E-03	6.28E-02	1.61E-03	1.78E-02
97.07 u	PCL	97.0706	4.81E-03	2.00E-04	6.96E-04	1.22E-02	5.48E-04	1.08E-03
C_6H_11O_2+	PCL	115.085	5.24E-04	9.84E-05	2.66E-04	3.50E-02	4.98E-04	2.42E-03
153.03 u	PCL	153.038	7.17E-05	2.14E-05	1.38E-04	8.73E-04	1.94E-04	1.46E-04
197.09 u	PCL/PDMAE	197.093	2.43E-05	2.46E-05	5.73E-04	1.51E-03	2.08E-03	1.06E-04
135.07 u	PCL/PDMAE	135.078	7.81E-05	5.58E-04	3.39E-03	4.08E-03	7.01E-03	3.90E-04
C_4H_10NO+	PDMAEMA	88.0799	2.98E-04	2.70E-05	3.68E-04	1.63E-04	8.18E-03	8.61E-03
C_2H_4N+	PDMAEMA	42.0343	9.12E-03	2.18E-05	9.82E-03	1.69E-03	2.97E-02	2.02E-02
C_8H_14NO_2+	PDMAEMA	156.117	7.13E-04	1.41E-05	8.84E-05	1.02E-04	3.61E-02	7.34E-03
158.13 u	PDMAEMA	158.132	1.12E-04	2.06E-05	2.55E-04	2.61E-04	2.27E-02	1.97E-02
C_3H_4O+	unclear	56.0255	4.31E-04	3.37E-05	1.24E-03	4.51E-03	1.55E-03	1.17E-02
C_3H_6N+	unclear	56.0491	5.84E-03	1.48E-04	7.40E-03	4.81E-03	1.06E-02	1.26E-02
C_4H_5O+	unclear	69.039	4.04E-04	5.14E-04	4.88E-03	8.51E-03	2.66E-02	2.78E-02
217.08 u	unclear	217.076	4.34E-05	1.00E-04	9.21E-05	2.74E-05	4.21E-05	1.64E-03
271.09 u	unclear	271.093	8.69E-05	4.56E-05	5.15E-05	7.70E-05	1.03E-04	3.14E-04
289.08 u	unclear	289.084	4.90E-05	5.23E-05	3.58E-05	1.45E-05	1.87E-05	3.88E-04
Na+	unspecific	22.9895	5.33E-05	1.46E-02	1.84E-02	3.51E-02	2.46E-03	1.42E-03
K+	unspecific	38.9637	1.29E-05	6.67E-04	1.20E-02	2.20E-02	4.87E-03	1.28E-03
C_3H_5+	unspecific	41.0403	5.86E-03	1.74E-03	7.34E-02	8.54E-02	1.96E-02	3.47E-02
C_4H_7+	unspecific	55.0551	5.20E-03	2.96E-03	3.13E-02	5.73E-02	3.33E-03	1.05E-02
Total Counts			3.93E+07	2.27E+07	6.54E+06	1.33E+07	2.31E+07	2.84E+07

By this approach, the positive ion channel showed several identified signals that can be traced back to the copper catalyst CuBr/PMDETA. The copper catalyst reference sample contained signals matching the empirical formula of the full catalyst complex ($C_9H_{23}N_3CuBr^+$), as well as fragments ($C_5H_{10}N^+$, $C_5H_8N^+$, Cu^- and Cu^+) and other products thereof (e.g. $C_{16}H_{40}N_6Cu^+$). These signals were most intense in the copper catalyst reference sample as expected. The signals assigned to $C_5H_{10}N^+$ and $C_5H_8N^+$ also showed significant intensity in reference **130** and in binary sample **128**. The appearance of these signals is expected, as CuBr/PMDETA was employed in the functionalization of both wafers. The presence of Cu^+ in binary brush sample **128** further indicates that after the polymerization, some catalyst remains in the sample despite several washing steps. The remainder of trace amounts of copper is a common issues in ATRP-derived materials and remains a hindrance to the application of such materials in certain medical fields[300,301].

For the Sn catalyst reference, notable signals from the Sn catalyst $Sn(Oct)_2$ were detected in the negative ion polarity. Signals could be matched to the organic anion of the catalyst complex ($C_8H_{15}O^-$) as well as to the full catalyst complex ($C_{16}H_{29}O_4Sn^-$). These signals seem to be exclusive to the Sn cat sample and could not be detected in at significant intensities

in any other reference material nor in the simultaneously grafted wafer **128**. This observation seems to indicate that the removal of the stannous catalyst is efficient. Additionally, intense polydimethylsiloxane (PDMS) signals were found in the positive channel of the Sn catalyst $Sn(Oct)_2$ reference sample. Generally speaking, PDMS signals are a very common contaminant on ToF-SIMS samples, owing in part to the widespread use of PDMS-based materials in laboratory settings as well as to the "exquisite sensitivity" of ToF-SIMS to traces of PDMS impurities[302,303]. It is likely that the contamination comes from the INJEKT BRAUN™ needles used for transfer of the catalyst for stock solution preparation. These needles are lined with silicone oil which may react with tin octoate[304] and can thus be leached out, and subsequently concentrated on the surface while the solvent evaporated. Sn-related signals themselves could not be observed.

Spectra of the linker sample **98** showed no specific signals, although some signals could be associated with it. However, these signals were mostly non-specific hydrocarbon and substrate related signals (e.g.: the 468.43 u signal and the CH_3^+ signals). Br^- was found to be most intense on the linker sample **98**. Lower intensities were detected also on the PCL sample **129**and the simultaneously grafted sample **128**. Interestingly, Br^- levels were much lower for the sample grafted solely with PDMAEMA.

The wafers bearing both linker and subsequently grafted PCL (wafer **129** showed both specific (e.g.: $C_6H_{11}O_2^+$ and $C_6H_9O_2^-$) and non-specific (e.g.: Na, hydrocarbon) signals. The specific $C_6H_{11}O_2^+$ signal is of particular interest as it matches the empirical formula of one PCL repeat unit. This signal is conspicuously low/absent in the catalyst, linker and PDMAEMA reference samples. On the tandem grafted wafer however, $C_6H_{11}O_2^+$ signal intensity was observed, indicating strongly the presence of PCL on the tandem grafted wafer. When observing the low intensity however, several explanations can be offered. Either the total PCL concentration on the wafer is low in comparison with other species present, indicating an ineffiecient surface-initiated ROP in comparison to the SI-ATRP. Alternatively, PCL is present in comparabable quantities but suffers from low ion yield, as discussed above. Or else, the PCL brushes are shorter than the PDMAEMA brushes (or collapsed), meaning that the brushes are absent from the top-most surface and hence yield fewer signals. Further analytical tools (multivariate analysis and depth profiles) were employed to elucidate these options *(vide infra)*.

When observing the spectra gathered from the PDMAEMA reference sample **130**, several nitrogen containing hydrocarbon species could be identified. These signals were interpreted as characteristic for PDMAEMA. The simultaneously grafted wafer **128** also showed a high intensity in these PDMAEMA specific signal, while the other reference

materials had very low signal intensities only. The $C_2H_4N^+$ signal, that was also found to be intense on reference **130** makes an exception and can also be found with significant intensity on the copper catalyst CuBr/PMDETA reference and the linker reference **98**. These references do not contain PDMAEMA and therefore the signal is correlated but not specific to this polymer. Further signals were seen to be most intense in the PDMAEMA reference but also intense in the PCL and linker reference spectra (e.g. 197.09 u and 135.07 u). No empirical formula could be established for these signals. The empirical formula of DMAEMA monomer is $C_7H_{13}NO_2$. The strong $C_8H_{14}NO_2^+$ signal observed in the PDMAEMA reference can be rationalized as a fragment consisting of one PDMAEMA repeat unit with an additional carbon from a second DMAEMA monomer. The signal is conspicuously low for all other reference sample and is thus characteristic for PDMAEMA. If this interpretation holds, the presence (albeit lower) of this fragment is a strong indicator for successful SI-ATRP during simultaneous tandem grafting.

In addition to the aforementioned signals, which were found in some or all of the reference spectra, the simultaneously grafted wafer **128** also showed several signals that were observed in lower intensities for the reference spectra. The $C_3H_4O^+$ and $C_3H_6N^+$ signals for example bear the highest intensity in the simultaneously grafted wafer. Several SO_xH_y signals were found to show very high intensities for the simultaneously grafted sample **128**. Other signals (mostly unassigned) seem to be only present on wafer **128** too. It is unclear where these contaminations come from. It was first considered that the sulfate and sulfite impurities may have been left behind in the washing steps but the use of deionized water should have precluded such contaminations.

Multivariate Analysis of ToF-SIMS Data

In addition to the manual selection of noteworthy signals, a multivariate analysis was performed on the spectra of the simultaneously grafted wafer and its reference materials. ToF-SIMS spectra are usually highly complex, involving several hundreds of signals that are influenced by composition, chemistry and orientation of the surface. Additionally, as evidenced from the manual selection and comparison of peaks, several chemical species produce the same fragments (e.g. non-characteristic hydrocarbons) that only vary in their relative abundance and composition. ToF-SIMS data that investigates the difference in surface composition is therefore multivariate by definition. Employing a statistical approach to analyzing the spectra helps to detect trends in the distribution of constituent surface species that may have been undetected following the manual approach. This way, principle

differences between surfaces can be reliably established and the presence of engineered differences can be verified[305].

Two approaches for *multivariate analysis* (MVA) were pursued: *principle component analysis* (PCA) and *non-negative matrix factorization* (NMF)[305]. The geometrical principle underlying PCA is an axis rotation. In a first step, the mass spectral data is converted into a matrix where the rows are spectra and the columns are individual mass channels. In the next step, the maximal directions of variance within a sample are identified that then serve as the basis of a new set of axes, called *principal components* (PC). The matrix is rotated to be aligned with the new PC axes. It hence serves as a method to investigate the overall variance within the data sets and concisely portrays the differences and origins of differences between two samples. After MVA transformation, three new matrices are created containing the scores, loading and residuals of the samples. Scores and loadings must be interpreted together as scores solely show the relationship between the spectra based on a projection of the original data points onto a PC axis, while the loadings show which peaks cause the separation. The residuals do not contain useful information for the interpretation of the spectra as they are random noise[305,306].

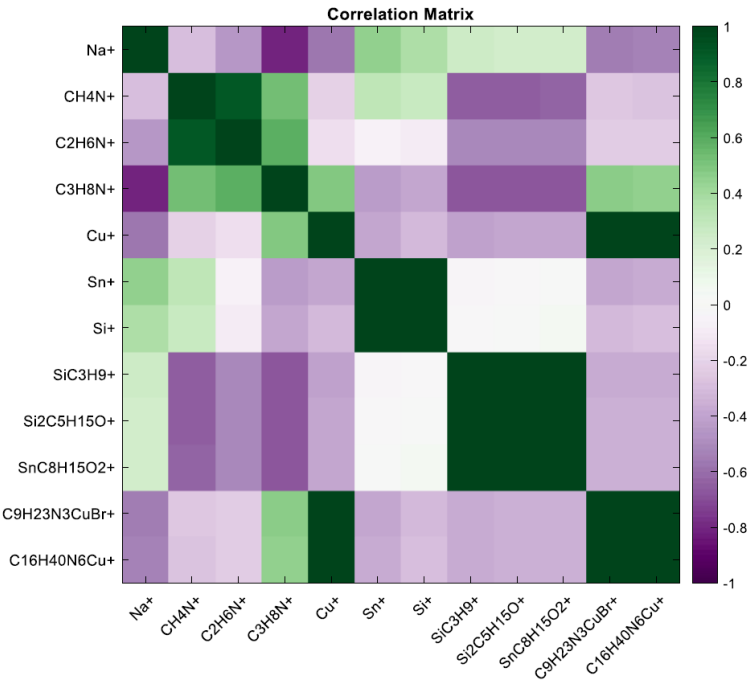

Figure 3-23: Correlation matrix between selected signals in the positive ion channel for MVA with positive (dark green) or negative (purple) correlation or uncorrelated (white).

The positive ion correlation matrix (see Figure 3-23) produced by comparing the sample and reference spectra using statistical methods shows which signals have a positive

or negative correlation or are uncorrelated. They serve as the basis for the principle component analysis. Noteworthy positive correlations exist between $SiC_3H_9^+$, $Si_2C_5H_{15}O^+$ and $SnC_8H_{15}O_2^+$ fragments. This effect has been identified and discussed for the manually selected signals too. Interestingly, the Si^+ and Sn^+ signals are highly correlated with each other but have no correlation to the previous signal cluster. Strong negative correlations are observed between Na^+ on one hand and $C_3H_8N^+$ and Cu^+ on the other hand.

Using the correlations established above, the multivariate analysis yielded several PC axes. When observing the total variance explained by the principle components, PC1-4 make out >95% of total variance, PC 5 still contains 3.04%, whereas PC6 only contains 0.23%. Further analyses were therefore performed for PC1-5.

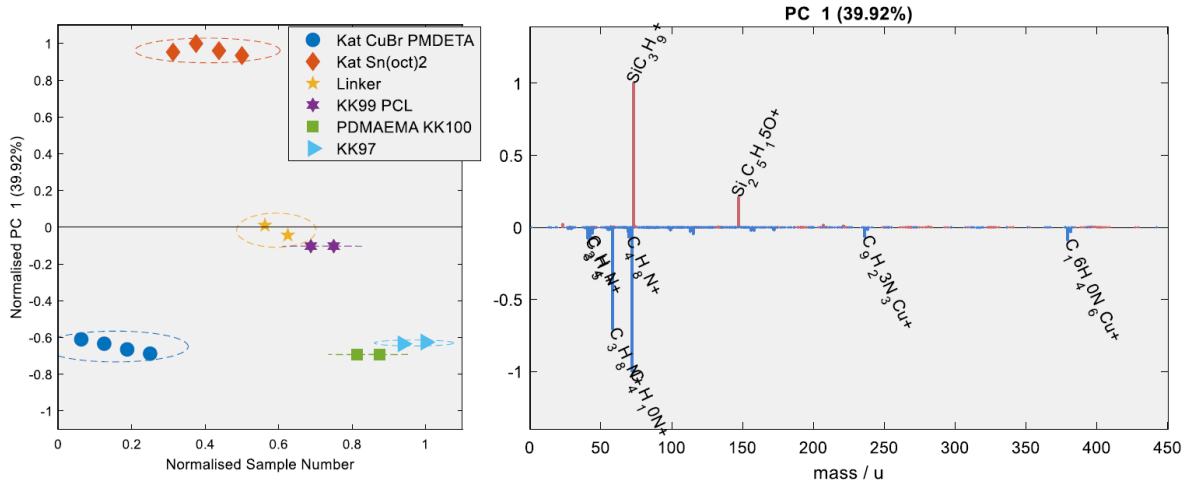

Figure 3-24: PC1 scores (left) and loadings (right) for catalyst CuBr/PMDETA (circle), catalyst $Sn(Oct)_2$ (diamonds), linker **98** (pentagrams), PCL reference **129** (stars), PDMAEMA reference **130** (squares) and sample **128** (triangles).

PC1 shows the greatest variance, separating signals based on PDMS signals ($SiC_3H_9^+$, $Si_2C_5H_{15}O^+$, etc.) and signals from the copper catalyst ($C_{16}H_{40}N_6Cu^+$, $C_9H_{23}N_3Cu^+$, $C_4H_8N^+$, $C_4H_{10}N^+$). These signals make up the loadings of PC1 (see Figure 3-24 right). The individual samples are plotted along the PC1 axis to yield the scores (Figure 3-24 left). Based on these principle components, the stannous catalyst $Sn(Oct)_2$ and the copper catalyst CuBr/PMDETA are separated the farthest. The PDMAEMA reference **130** and the sample **128** show notable scores for PC1 as some of the employed copper catalyst remained in the reference materials. Linker sample **98** and PCL reference **129** had no contact with the copper catalyst and therefore are found along the center.

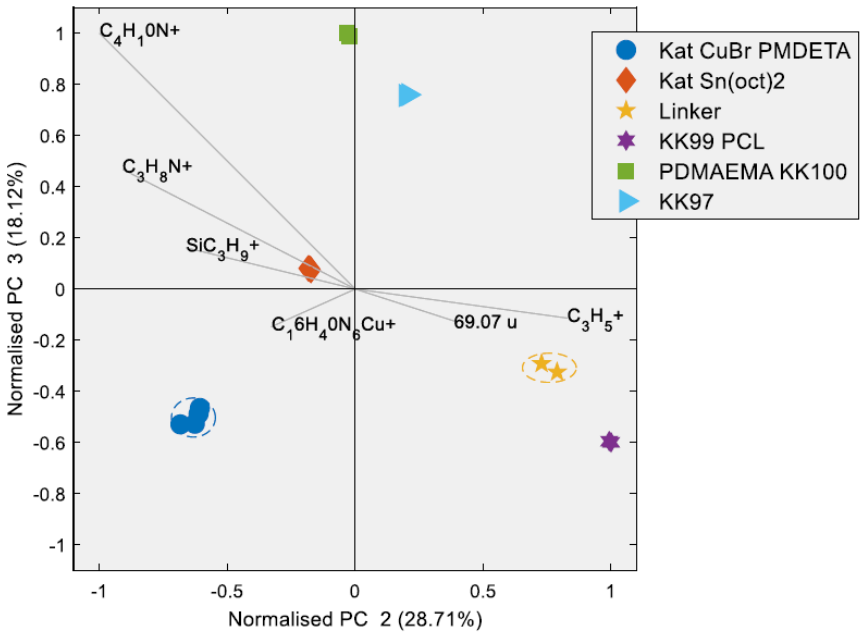

Figure 3-25: Biplot of scores in PC2 and PC3 for catalyst CuBr/PMDETA (circle), catalyst $Sn(Oct)_2$ (diamonds), linker **98**(pentagrams), PCL reference **129** (stars), PDMAEMA reference **130** (squares) and sample **128** (triangles) and on the same plot, noteworthy loadings.

In a similar manner, scores of two PC's can be plotted in a two-dimensional array to separate samples along these two axes. Figure 3-25 shows the score biplot of PC2 and PC3 for the simultaneously grafted sample **128** and the reference wafers PDMAEMA **130**, PCL **129**, linker **98** and the two catalysts CuBr/PMDETA $Sn(Oct)_2$. PC2 separates signals containing several aliphatic hydrocarbon species and a combination of copper catalyst signals and PDMS signals. A positive score in this component therefore indicates the presence of PCL. PC3 groups samples based on N-containing hydrocarbon species ($C_3H_8N^+$, $C_4H_{10}N^+$), and $SiC_3H_9^+$ as well as several copper catalyst species and some aliphatic hydrocarbons. A positive score in PC3 therefore reflects the presence of PDMAEMA on the surface. When analyzing the biplot, PDMAEMA reference **130** only shows a positive score in PC3 due to the significant presence of N-containing hydrocarbon species. The PCL reference **129**on the other hand shows a large positive score in the aliphatic hydrocarbon containing PC2. The stannous catalyst reference $Sn(Oct)_2$ is located close to the origin, indicating a low variance in either PC. The linker reference **98** shows a notable score in PC2 and a weak score in PC3 as some aliphatic hydrocarbons seem to correspond to linker fragments too. However this score is lower than for the PCL reference **129**. The copper catalyst shows a negative score in both axes. Most importantly, the simultaneously grafted wafer **128** is located in the top right quadrant, i.e. has a positive score in both PC3 and PC2, indicating the presence of both PDMAEMA and PCL

correlated signals. This finding is a strong indicator that the simultaneous grafting was successful.

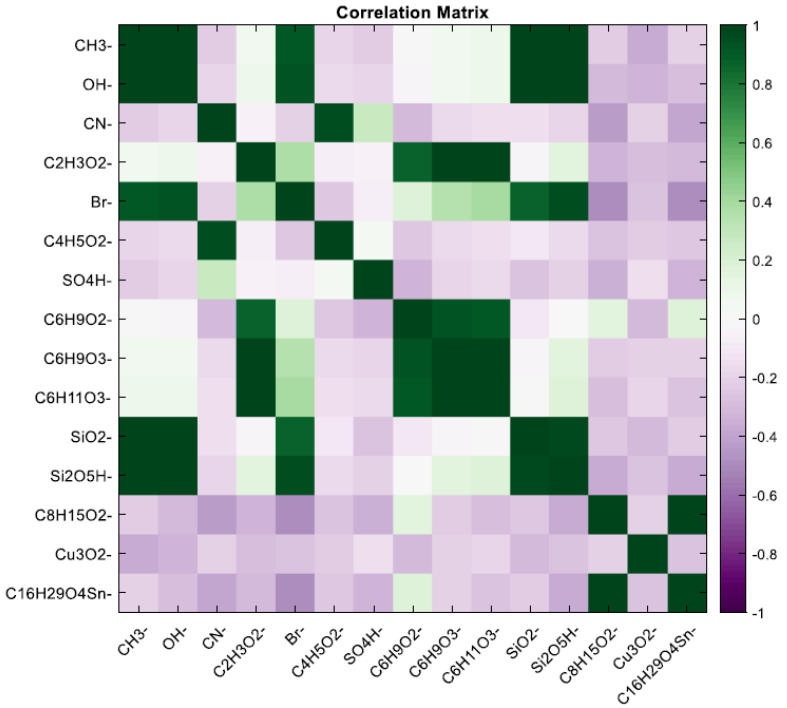

Figure 3-26: Correlation matrix between selected signals in the negative ion channel for MVA with positive (dark green) or negative (purple) correlation or uncorrelated (white).

The same approach as outlined above was repeated for the negative ion channel. First, a correlation matrix was produced summarizing positive, negative and zero correlations (see Figure 3-26). Notable correlations include: CH_3^-, OH^-, Br^-, SiO_2^- and $Si_2O_5H^-$; CN^- and $C_4H_5O_2$; $C_2H_3O_2^-$, $C_6H_9O_2^-$ and $C_6H_{11}O_3$; $C_8H_{15}O_2^-$ and $C_{16}H_{29}O_4Sn^-$ Notable anti-correlations were observed for: Br^- and $C_8H_{15}O_2^-$, $C_{16}H_{29}O_4Sn^-$ CN^- and $C_8H_{15}O_2^-$, $C_{16}H_{29}O_4Sn^-$.

Of course MVA should not serve as a method to blindly evaluate samples without critically assessing its findings. The method only reliably identifies the directions of greatest variance within the samples, it does not assess the pertinence of the sources of variance. If one sample is contaminated through sample handling and preparation, the maximal variance is most likely due to the contaminations. Hence, variances within the surface chemistry are suppressed by the much stronger variance originating from the contamination. A case in point is the variance shown in PC4 (see Figure 3-27). The previously identified sulfate contamination has the highest load in this principle component and therefore results in a large separation between simultaneously grafted wafer **128** and its reference spectra.

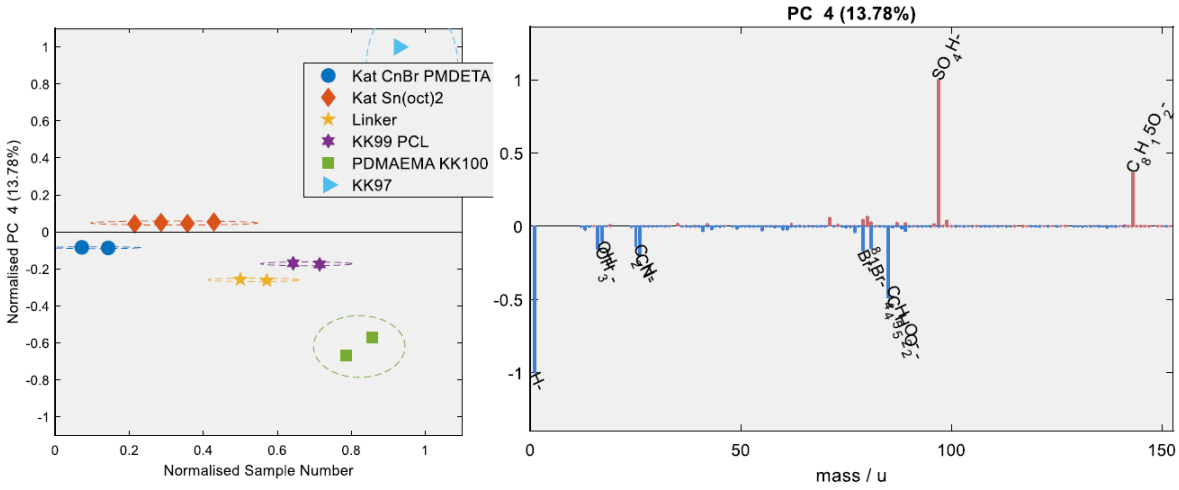

Figure 3-27: Negative ion channel PCA with scores (left) of PC 4 for catalyst CuBr/PMDETA (circle), catalyst $Sn(Oct)_2$ (diamonds), linker **98**(pentagrams), PCL reference **129** (stars), PDMAEMA reference **130** (squares) and sample **128** (triangles) and loadings (right).

Nevertheless, the biplot (see Figure 3-28) reveals a clear trend in the distribution of characteristic signals. The PCL reference wafer **129** shows a negative score in PC1, while the PDMAEMA reference wafer shows negative loadings in PC3. The simultaneously frafted wafer **128** on the other hand shows negative loading in both PC1 and PC3, indicating the presence of both signals on the wafer surface.

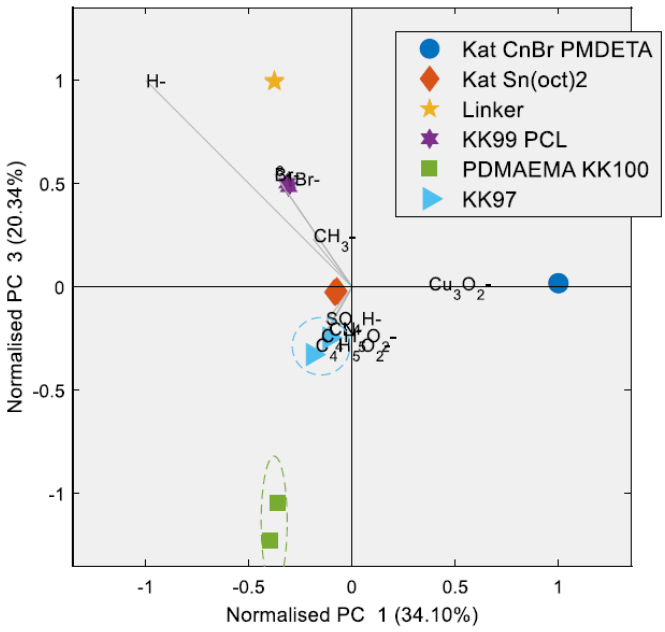

Figure 3-28: Biplot of scores in PC1 and PC3 for catalyst CuBr/PMDETA (circle), catalyst $Sn(Oct)_2$ (diamonds), linker **98** (pentagrams), PCL reference **129** (stars), PDMAEMA reference **130** (squares) and sample **128** (triangles) and on the same plot, noteworthy loadings.

The second multivariate analysis technique employed, (NMF) is a process whereby the original matrix consisting of spectra and their corresponding mass channels are factorized into two non-negative matrices. The advantage of this technique over PCA as outlined above is that it is free of bias. Whereas the selecting, picking and assigning of peaks prior to PCA allows for biases of the operator or else automatic binning and peak picking routines allows for algorithmic biases, NMF allows for the analysis of raw, un-binned datasets. The ToF-SIMS data in both positive and negative channels were subjected to NMF, establishing three factors each[305].

In the negative channel, the factorization was complicated by the previously mentioned sulfate ions that seem to dominate the simultaneously grafted wafer surface. The excellent ion yield of these fragments distort the statistically established distributions. As a consequence, factor one is dominated by the sulfate ion, resulting in a high separation of simultaneously grafted wafer **128** from the other samples. Factor two, bearing PDMAEMA related fragments is high for the PDMAEMA reference **130**, notable for the PCL reference **129** and low for all others. This distribution does not reflect the expected trend. Finally, the third factor that includes H^- and Br^- signals associated with the linker only reflects the high intensity of these signals on the linker sample **98** and notable loadings on the PCL reference **129**.

In the positive channel on the other hand, the insight gained through NMF is less ambiguous. The first factor included various oxygen containing hydrocarbons and was associated with PCL fragments. This factor showed the highest loadings for the PCL reference wafer **129**, notable loadings for the simultaneously grafted wafer **128** and very low loadings for all other samples. Such a distribution indicates the presence of PCL on the wafer of interest. Factor two contained signals associated with the linker and was therefore highest for the linker reference **98**, notable for the PCL reference **129** and the simultaneously grafted wafer **128**, and low for the PDMAEMA reference **130**. The final factor included nitrogen containing organic signals that were associated with PDMAEMA fragments. As a consequence, this factor was high for the PDMAEMA reference **130**, notable for the simultaneously grafted wafer **128** and low for all other samples. Such a distribution indicates that the two polymers grafted onto the wafer during the simultaneous grafting procedures are indeed present on the sample of interest.

Overall, the manual and statistical analysis and comparison of the reference spectra and the sample spectra strongly indicates the successful simultaneously grafting off wafer **128**. Further ToF-SIMS based methods were employed to assess the homogeneity of the grafted surface brushes.

ToF-SIMS Depth Profiles

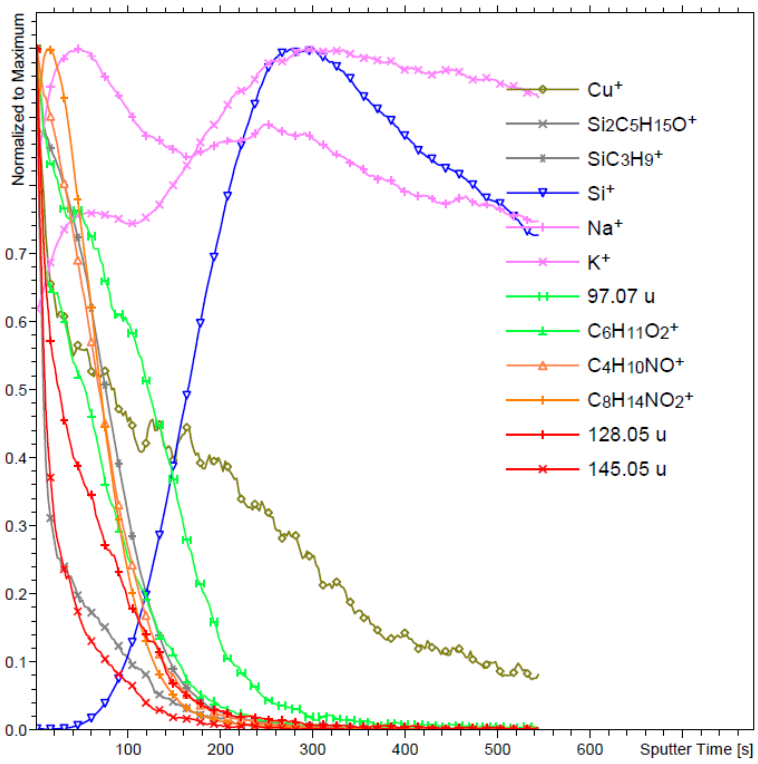

Figure 3-29: ToF-SIMS positive ions depth profile of **128** sputtered with 2.5 keV Ar_{1000} clusters and 30 keV Bi_3 primary ion source. All intensities normalized to maximum intensity.

The mixed brush wafer **128** was further analyzed with the aim to produce a depth profile of the relative polymer distributions. Through prolonged sputtering of the sample with argon clusters at 2.5 keV and 5 keV, the surface was slowly eroded away. After periodic intervals, higher energy (30 keV) Bi_3 ions were then employed as a primary ion source to eject characteristic secondary ions. By this approach, a depth profile can be constructed bearing information of elemental, isotopic and molecular composition, as the relative depth of secondary ion sources is dependent on sputtering time. Figure 3-29 plots the normalized intensities of various secondary ions that have previously been identified as characteristic for the individual reference samples against sputtering time. At low Ar_{1000} sputtering times, the normalized intensity of Si^+ ions (blue line) is zero and increases slowly, then more rapidly to yield a maximum after ca. 300 s sputtering time. The other observed ions, with the noteworthy exception of K^+, Na^+ and Cu^+ (see below) show a complementary trend to the Si^+ intensity. Green intensity traces are associated with PCL brushes and orange intensity traces are characteristic for PDMAEMA chains. Hence, PCL and PDMAEMA associated signals are most intense at low depths, decrease in intensity after eroding more material and are replaced by

substrate signals. These trends fit well with the model of polymeric material being removed from the surface until the argon clusters start eroding the silicon substrate.

One noteworthy caveat of this technique is that different erosion rates of sputtered samples are highly dependent on sample identity as well as primary ion source. Mono- or diatomic ion beams commonly used for depth profiling of inorganic materials often give poor results when applied on organic materials, just as the ion cluster sources used to characterize organic surfaces tend to give unsatisfactory results for inorganic materials[307]. Hence the depth profile of inorganic materials within an organic framework may be skewed by their relative erosion rates. It is with this caveat in mind that the intensities of K^+, Na^+ and Cu^+ ions should be compared to the intensities of organic fragments.

The presence of Cu^+ ions *per se* is expected despite the thorough washing procedures outlined above. ToF-SIMS is a highly sensitive technique and even trace amounts of copper ions trapped within (potentially entangled) polymer brushes are expected to yield noticeable intensities. Nonetheless, the vastly differing ion yields between metal ions and characteristic organic fragments do not allow a direct comparison between their relative intensities. This caveat has been accounted for by the normalization of each signal, making the depth profiles more useful for qualitative rather than quantitative interpretation. Cu^+ ion intensity decreases with increasing sputtering time but remains non-negligible even after the polymer brushes have fully eroded (their intensity has reached zero). Such a trend could either be explained by the normalization process or else by the formation of slowly eroding copper salt clusters on the wafer that continues to yield signals even when the surrounding (faster eroding) polymers have been removed completely.

The vertical distribution of potassium and sodium ions must also be interpreted with caution. Both alkali ions are a common contaminant and frequently observed by highly sensitive analytical approaches. Additionally, they are a very high yielding secondary ion source while at the same time portraying low erosion rates when present in salt clusters[302].

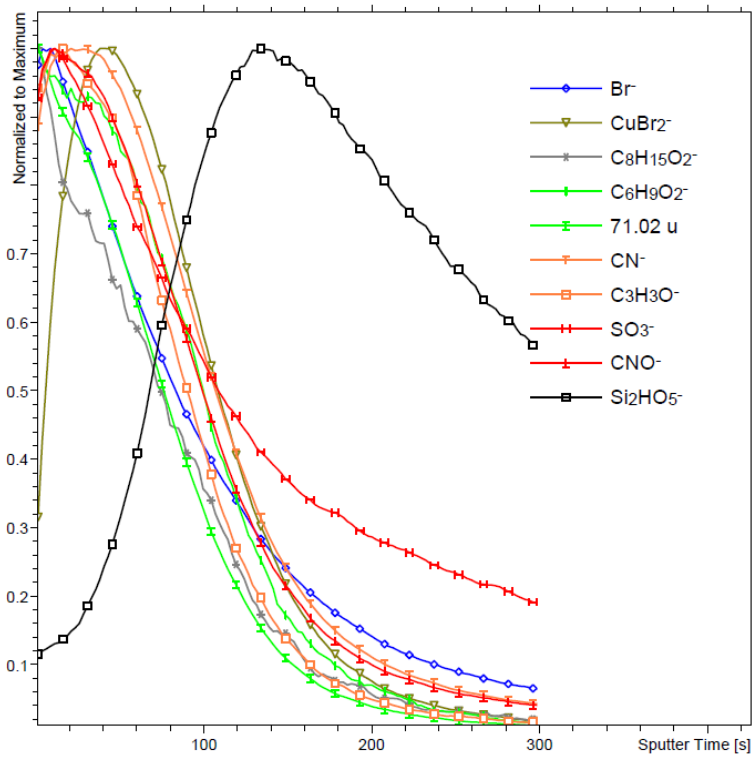

Figure 3-30: ToF-SIMS negative ions depth profile of binary brush **128** sputtered with 2.5 keV Ar_{1000} clusters and 30 keV Bi_3 primary ion source. All intensities normalized to maximum intensity.

Individual secondary ion fragments that have previously been identified to be characteristic for PCL and PDMAEMA samples were observed for the negative ion channel too. Figure 3-30 shows in green the depth profiles of $C_6H_9O_2^-$ secondary ions — fragments from the repeat unit of PCL and an unidentified but characteristic trace of 71.02 u also associated with PCL. These traces follow the pattern already observed for the positive ion channels: an intense peak is observed at low sputtering times and rapidly decreases as the surface brush is eroded away. The orange traces of CN^- and $C_3H_3O^-$ are both identified fragments of DMAEMA monomer and follow the same trend as the PCL fragments. These observation speak for the presence of both polymers at the surface of the wafer.

As previously discussed, the origin of the SO_3^- ion remains unclear but shows a somewhat similar trend to other inorganic ions observed: a lower intensity at the surface that first increases to a maximum at ca. 20 s sputter time and then levels off. In contrast to the other ions however, the sulfite ion intensity does not fall to zero at sputtering times of 300 s. Again, this effect is probably due to lower erosion rates of inorganic salts compared to the organic material surrounding it.

The vertical bromine distribution follows the patterns established by the PCL related fragments. The Br^- ion intensity is highest at the very surface and decreases with increasing sputtering time. Br^- signals may derive either from the linker, dormant chain ends, or from the catalyst. This distribution is in keeping with the assumption that growing PDMAEMA chains are terminated with Br^- due to the ATRP process. Hence, the chain ends furthest away from the surface should carry the highest intensity.

It is worth pointing out that the $CuBr_2^-$ signal diverges from the common trend of non-substrate signal intensities. The intensity of $CuBr_2^-$ ions at the very surface (sputtering time 0 s) is relatively low and then rapidly increases to a maximum to decrease according to the trend portrayed by the other signals too. Such an observation holds well with the hypothesis of copper catalysts remaining within the polymer brush sample despite washing procedures. The initial low intensity indicates that the washing step removed the catalyst from the very top of the surface (i.e. the chains with the highest degree of freedom and mobility) and consequently decreases within the thicker brush regimes. More importantly though, the high intensity of Br^- signals at the very surface with the low intensity of $CuBr_2^-$ signals at the air-brush interface may be taken as proof that the very surface Br^- signals indeed derive from dormant chain ends, as would be expected of ATRP-derived polymers. Still, another precautionary note should be added when interpreting ToF-SIMS patterns. Although the assignment of $CuBr_2^-$ ions to the secondary ion at 220.81 u is reliable due to the fine structure and isotope distribution, there is a certain degree of ambiguity as to whether the analyzed substrate does indeed contain $CuBr_2$ salts. In the high energy environment of primary ion sputtering, chemical reactions can indeed occur upon impact and in flight. For example, CuBr salt clusters present on the surface of the wafer may react with ejected chain-end derived Br^- ions to produce the observed secondary ion.

In contrast to the positive ion distribution, wafer derived signals (black) reach a maximum after only ca. 140 s sputtering time. The difference between the two secondary ions stems from the fact that only the first few nm of the wafer surface has been oxidized by ozone cleaning, (producing a layer of SiO_2) while the bulk material of the wafer is monocrystalline silicon. Hence the silicon oxide layer giving rise to the $Si_2HO_5^-$ signal intensity is depleted, while the Si^+ secondary ion is produced by sputtering of both silica as well as silicon substrate.

The depth profiles reveal a rather fast consumption of the layer with an increase in signals from the substrate starting at about 80 seconds of sputtering. No clear vertical separation of phases was resolved.

TOF-SIMS Lateral Distribution of Signals

ToF-SIMS further allows a lateral resolution of molecular, elemental and isotopic composition. For this technique, a region of interest is chosen and the primary ion beam focused towards a square of said area. Individual secondary ions of interest may then be selected from the ejected ions off the surface to produce a range of channels showing high and low intensities of said secondary ions. In this way an image with detailed elemental information may be reconstructed, achieving lateral resolutions of 100 nm. The maximal size is determined by the focus of the ion beam although larger areas may be surveyed by digitally connecting several smaller areas to produce one large area image. Interpretation of ToF-SIMS images is somewhat complicated by the incredible data load of this technique: a single 256 × 256 pixel image contains 65536 spectra. As a consequence, only ion channels of interest were identified and selected manually and therefore underlie operator bias.

Several areas of the wafer were surveyed. Figure 3-31 shows a large areal ToF-SIMS image of **128**, composed of several smaller negative ion channel signals, digitally aligned. Three secondary ion channels that were previously identified to be characteristic for the two polymer populations each (PCL and PDMAEMA respectively) were chosen to construct the image. Bright areas within the image represent high intensities of the fragments observed. Intensities may only be compared within each channel, the relative abundance between two populations cannot be established *via* this technique due to potentially large differences in secondary ion yield. However, on purely qualitative accounts, characteristic fragments for both polymers seem to coexist across the wafer. This finding is in line with the synthetic aim of producing mixed molecular brushes. Several dark areas can be seen on the image. These dark patches are some 10's to 100's of µm large and arose most likely from defect in the wafer substrate or from drying residues, mechanical abrasions from handling etc. It is worth pointing out that before, during and after wafer functionalization, care was taken to avoid direct contact with the wafer surface. However, even the commercially available monocrystalline silicon wafers used for these experiments are not perfectly flat surfaces.

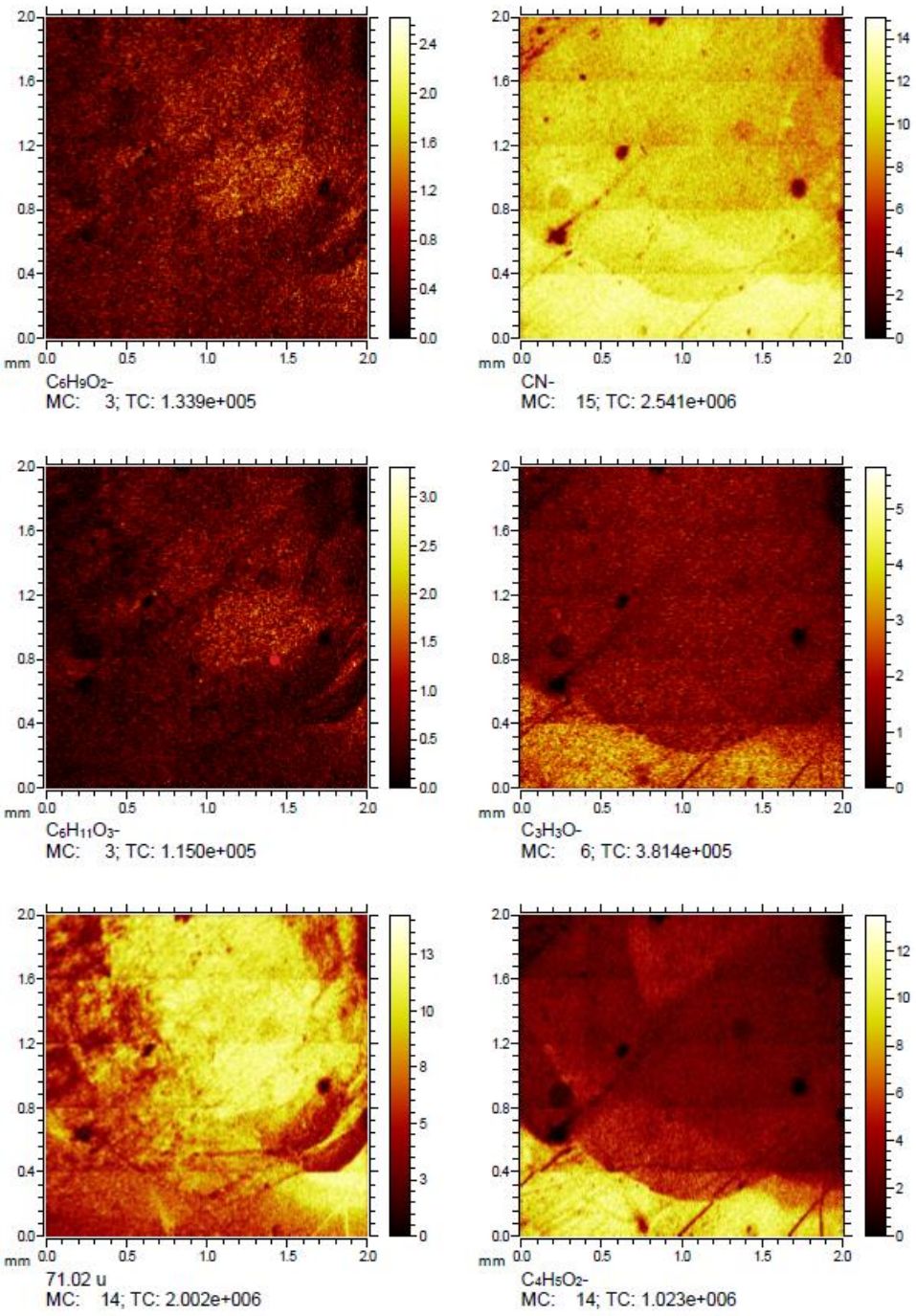

Figure 3-31: Negative ion channel, large areal ToF-SIMS image of binary brush wafer **128** showing lateral distribution of PCL typical secondary ions (left) and PDMAEMA typical fragments (right). The two populations seem to coincide. Dark spots on the surface arise from wafer defects and drying residue.

The positive ion channel of the same area (see Figure 3-32) shows the same trends and the same defects as observed in the negative ion channels.

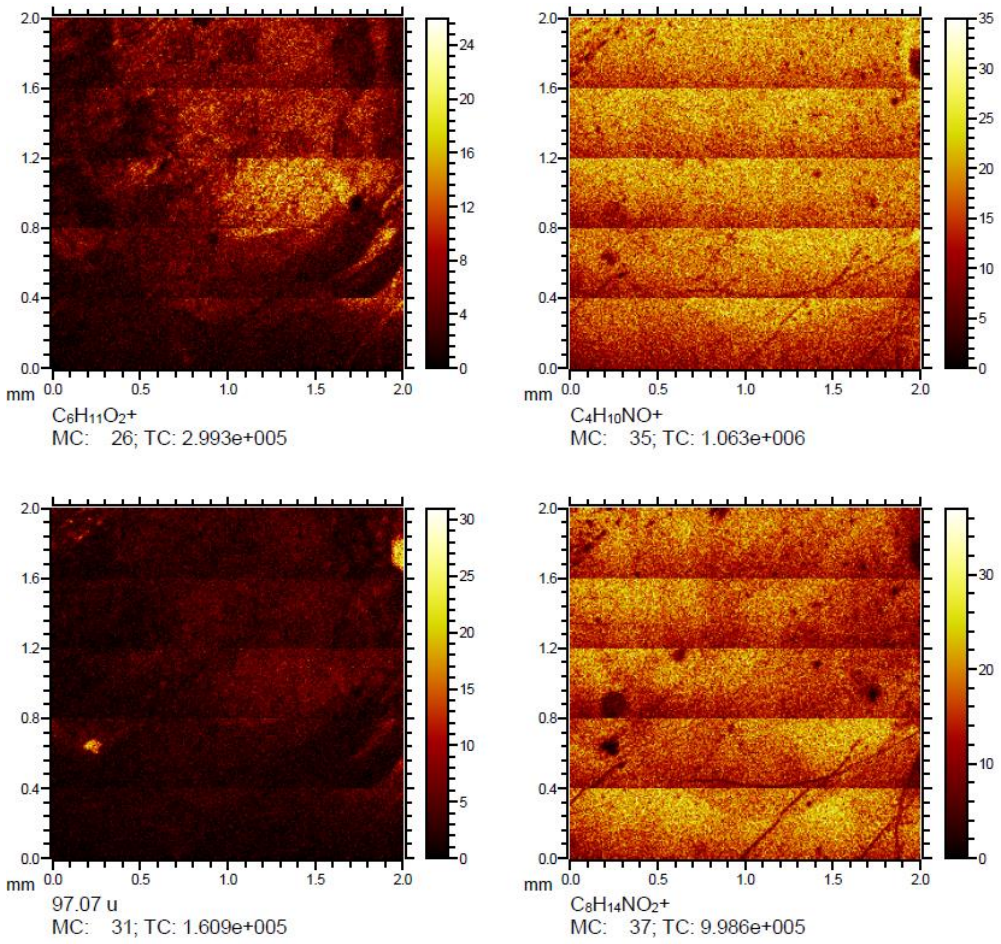

Figure 3-32: Positive ion channel, large areal ToF-SIMS image of binary brush wafer **128** showing lateral distribution of PCL typical secondary ions (left) and PDMAEMA typical fragments (right). The two populations seem to coincide. Dark spots on the surface arise from wafer defects and drying residue.

A smaller area within the large area survey is portrayed in Figure 3-33. Here, parallel curved "grooves" appear within several postitive ion channels. In the $C_8H_{14}NO_2^+$ channel, (a fragment associated with the DMAEMA monomer), the grooves are areas of lower intensity. In the 97.05 u channel, associated with PCL fragments, the grooves are areas of higher intensity, while also showing some brighter (i.e. more intense) circular structures. Hence, these grooves seem to be characterized by a complementary distribution of PCL and PDMAEMA fragments. The origin of the grooves is somewhat unclear. A range of origins may be envisioned. The grooves could be defects from the substrate wafer, caused by mechanical abrasion while handling for preparation. They could further represent defects within the linker distribution on the wafer, local differences in the polymerization, residues from washing and drying or else have occurred during transport and preparation for ToF-SIMS measurements. The size order of magnitude of these grooves seem to counter indicate self-assembled origins and speak more for the theory of mechanical abrasions. Interestingly, the

potassium channel shows a much increased intensity in the grooves structures contrasting with the rest of the wafer

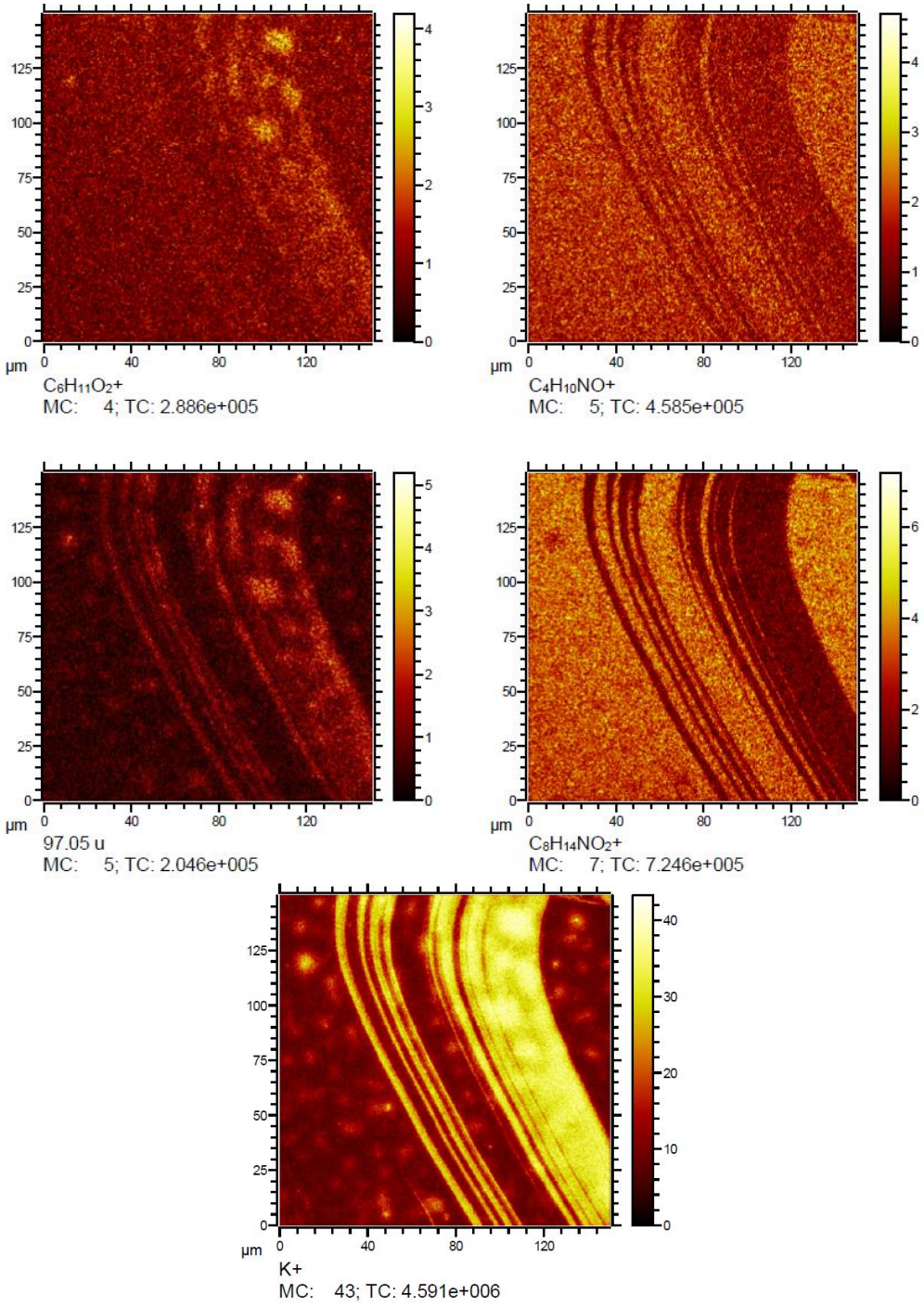

Figure 3-33: Positive ion channel ToF-SIMS image of binary brush wafer **128** showing lateral distribution of PCL typical secondary ions (top left and center left), PDMAEMA typical fragments (top right and center right) and potassium ion (bottom) in a smaller area. Groove-like curved structures appear on the surface: within the grooves, PCL and PDMAEMA signals are somewhat complementary.

The negative ion channels (see Figure 3-34) show a relatively homogeneous distribution of PCL and PDMAEMA derived fragments. The CN^- and $C_4H_5O_2^-$ ions, fragments from the PDMAEMA repeat unit have a high intensity across the entire surveyed area. These high intensities indicate that the PDMAEMA polymer is homogeneously distributed across the wafer. However, in one smaller image, several smaller spots (around 10 µm in diameter) were observed that portray a slight decrease in the CN^- channel and a marked decrease in $C_4H_5O_2^-$ fragment intensity. As for $C_6H_9O_2^-$ and $C_6H_{11}O_3^-$ channels, these PCL typical fragments have a lower intensity than the PDMAEMA signals, although direct comparisons are difficult to make without calibration. These signals, too are distributed with a homogeneous intensity across the wafer, with the conspicuous exception of a few higher intensity spots. These high intensity PCL and low intensity PDMAEMA spots coincide.

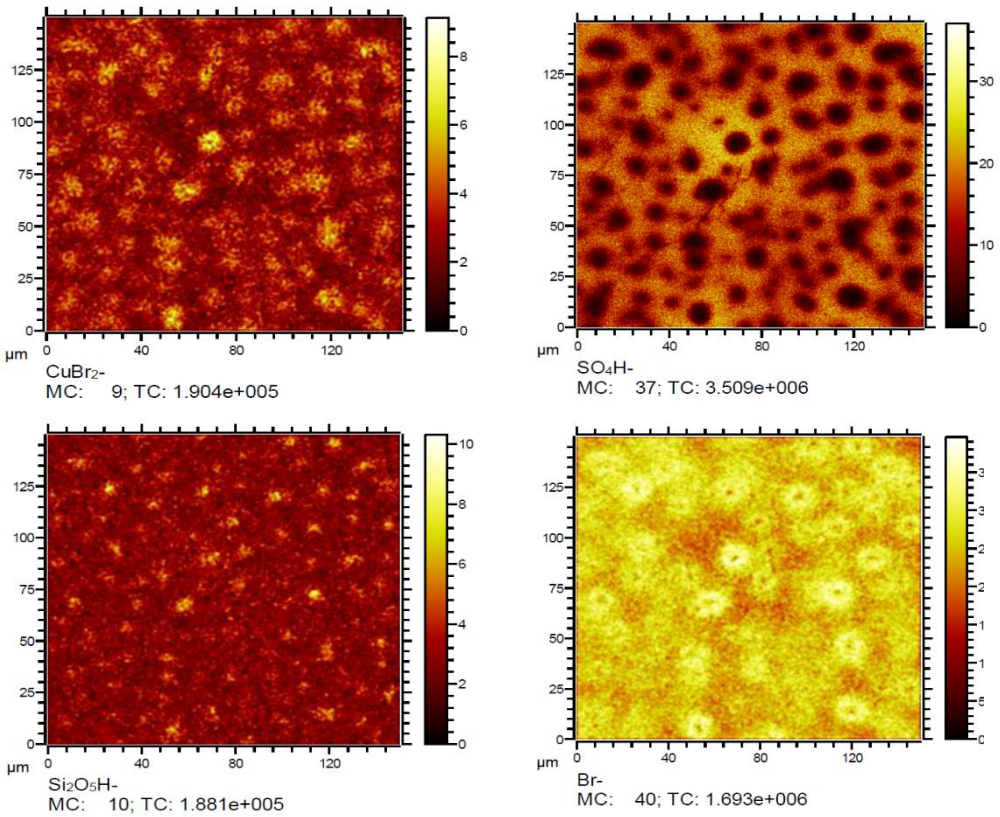

Figure 3-34: Negative ion channels of $CuBr_2^-$ (top left), SOH_4^- (top right), $Si_2O_5H^-$ (bottom left) and Br^- (bottom right) ions of binary brush wafer **128**.

When considering Figure 3-34 and the distribution of $CuBr_2^-$ and SOH_4^- these inorganic compounds closely match the distribution of the PCL and PDMAEMA variations respectively. As the sulfate ions were interpreted as impurities from washing steps earlier, there seems to be an affinity between the sulfate ions and the regions where PCL intensity is relatively lower and PDMAEMA intensities are relatively higher. The brushes having formed

first, the sulfate ions seem to attach to these outlined areas. Similarly, the $CuBr_2^-$ distribution seems to match that of the higher PCL intensities.

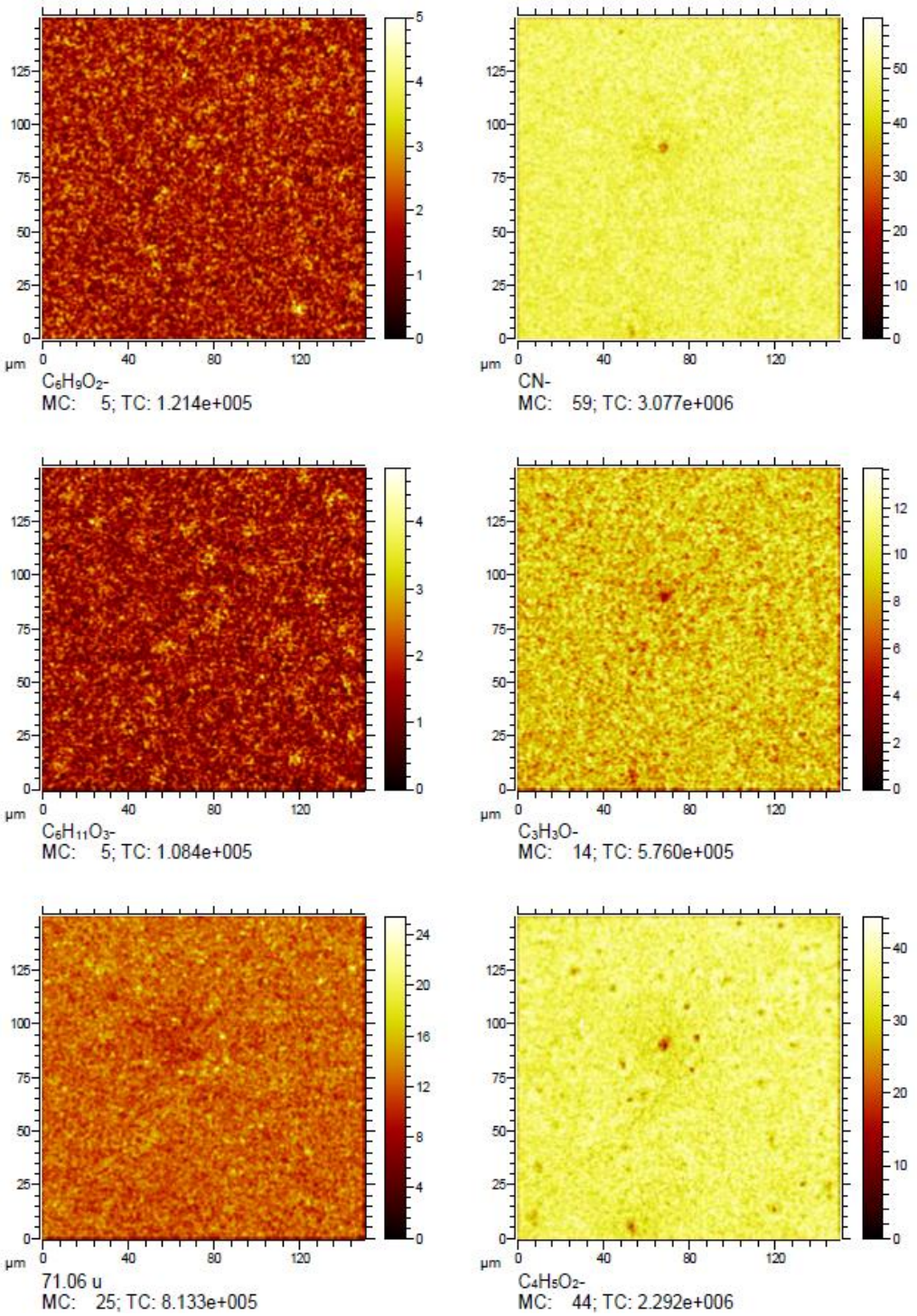

Figure 3-35: Negative ion channel image of small area. PCL derived fragments (left) and PDMAEMA fragments (right) show a distribution and coexistence across the entire surveyed area. Of note, small spots of higher intensity PCL fragments coincide with the same spots of slightly less intense PDMAEMA fragments.

These observations indicate that there seems to be a phase separation between PCL-only brushes and other PCL-PDMAEMA mixed areas. Contrasting the order of magnitude of the phase separations observed herein, with those observed in other Y-shaped mixed polymer systems, a spontaneous phase separation arising micelle formation seems unlikely. Theoretical calculations[308] and experimental results[104] of such systems predict a phase separation in the order of magnitude of a few nanometers. The lateral resolution of ToF-SIMS is around 100's of nanometers and the structures observed herein are several micrometers large. Hence the question of the molecular identity of these structures and their origins remains.

An alternative interpretation might be that the polymerization process itself led to a spatial resolution between the two monomer types. The large differences in polarity between the growing polymer chains, may have led to a preferential incorporation of DMAEMA monomer into regions where due to statistical distribution other PDMAEMA chains had already grown longer. The hydrophilic monomer might diffuse more rapidly into the hydrophilic chain than the hydrophobic CL monomer. Such an effect was previously stipulated by MINKO et al.[101] who described similar structural defects as a *nucleation* effect. This self-assembling behavior is highly interesting from a surface modification point of view, a type of covalently bonded two-dimensional polymerization-induced self-assembly (PISA). However, for the framework of this project, the self-assembling effect would be diametrically opposed to the synthetic aim of producing densely grafted brushes bearing a maximum of polarity frustration in sub-nanometer ranges. However, if indeed the polymerization induces phase separations, these periodic "islands" should be found across the whole wafer surface or at least in several regions. This was not found to be the case.

The most plausible origin of the observed defects might be defects present before or during SAM formation, while functionalizing the wafers with linker. If defects within the SAM of the linker persist, they will propagate and be amplified during the polymerization process. To assess this hypothesis, a wafer, functionalized only with the linker was measured in the image mode (see Figure 3-36, left). The most striking contrast between grafted wafer **128** and the linker-only wafer **98** is the absence of large scale defects. The "grooves" that were observed in grafted sample **128** do not appear on any region surveyed on the linker-only sample. This observation is in line with the hypothesis of such grooves originating from mechanical abrasions during handling of the grafted wafer sample. Importantly, the small-scale inhomogeneity in the Br^- distribution that were observed in the grafted sample also appears in the linker-only images. Small spots of low intensity Br^- signal appear on the linker-modified wafer. The order of magnitude and distribution of the low intensity spots are strongly reminiscent of the structures observed in the grafted sample. It is therefore likely that

the lower Br^- intensities observed in the grafted sample are an artefact from the linker preparation rather than arising from a poorly controlled polymerization. If Br^- signals on the linker-modified wafer are solely due to ATRP initiation moieties, the polymerization will therefore proceed to a lesser extend in these low Br^- regions. This absence of initiator thus further explains the lower intensity of PDMAEMA-derived signals in these regions. These low intensity spots hence have a lower grafting density. When sputtering areas with lower grafting densities with the same energy as the surrounding areas, the polymer layer is depleted more rapidly and substrate-derived signals occur more intensely. These effects are also observed in the grafted sample.

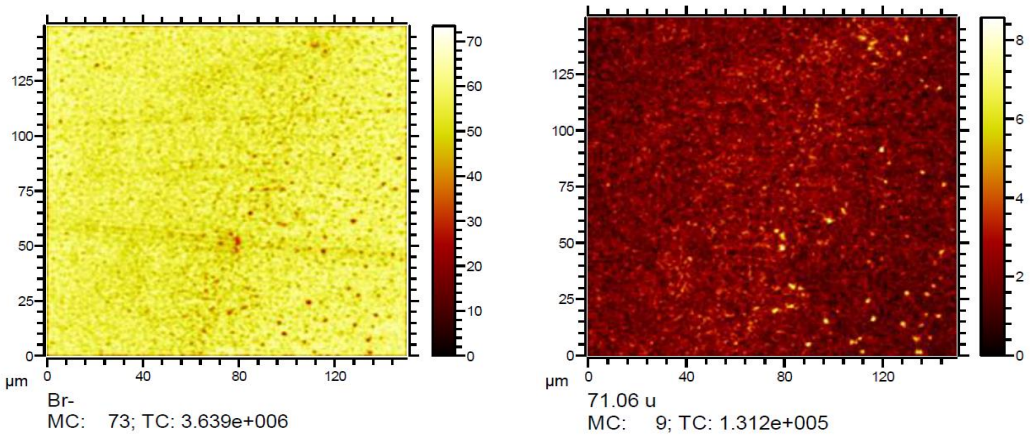

Figure 3-36: ToF-SIMS images of wafer functionalized only with linker **98**. The same inhomogeneities of Br^- (left) and 71.06 u (right) appear on the wafer surface.

The presence of lower intensity Br^- areas begs the question, why inhomogeneous distributions have formed and how to avoid them for future experiments. Analyzing the other channels in the ToF-SIMS images of the linker-modified wafer **98** revealed a possible cause. The 71.06 u channel portrays a complementary distribution to the Br^- channel. It is not altogether clear, how to assign this signal. A $C_3H_3O_2^-$ fragment would produce a 71.013 u signal. A hesitant assignment to $C_3H_7N_2^-$ does yield the observed mass of 71.06 u. This fragment may be matched to a deprotonated dimethyl carbodiimide fragment or else an ethyl carbodiimide fragment. The latter fragment may be rationalized as an EDC-related impurity derived from the first step in the linker synthesis. Despite the purification efforts for the synthesis, the high sensitivity of ToF-SIMS may easily explain the presence of such an impurity even after three columns. However, it remains unclear how this impurity was able to bond to the wafer surface to resists further washing steps. The 71.06 u signal also appears in the grafted sample, complementary to the Br^- distribution, despite hours of elevated temperatures and mechanical stirring.

Irrespective of the exact molecular structure of this fragment, it seems clear that some impurity with a polarity dissimilar enough to the linker as to cause a phase separation, bonded to the wafer and inhibited polymerization at these areas. The inhomogeneities observed in the grafted wafer are therefore not an indicator for polymerization induced phase separation but a linker-distribution difference. So disregarding the linker-derived defects, the ToF-SIMS image mode allowed to establish that the simultaneous grafting procedure produced homogeneously distributed binary mixed PDMAEMA-PCL brushes.

3.7.3 Surface Responsiveness

Contact angle (CA) measurements (see Table 3-12) were conducted on reference wafers and simultaneously gfrafted wafers, following immersion in THF as a good solvent for all polymers. CA measurements of reference wafers functionalized with PDMAEMA, wafer **130** showed a very low CA, as would be expected for a hydrophilic surface. The contact angle for PCL functionalized wafer **129** was much greater with measured angles between 60° and 70°. Interestingly, for the wafers functionalized *via* simultaneous tandem grafting of both polymers, the contact angles were around the same order of magnitude as the pure PCL reference sample, reflecting the longer PCL chains in contrast with PDMAEMA chains. Unfortunately, these low contact angles disqualified the combination of PDMAEMA and PCL for analysis *via* dynamic contact angle.

Table 3-12: Representative contact angle measurements under atmospheric conditions.

Entry	Surface	Good solvent	Contact angle
wafer	Clean wafer	N/A	79.9°
98	Linker modified	Toluene/THF	92.7°
130	PDMAEMA	Water /THF	< 20°
129	PCL	Toluene/THF	60° — 70°
128	$P(DMAEMA)_{15}$-$P(CL)_{33}$	THF	70° — 75°
134	$P(DMAEMA)_{22}$-$P(CL)_{44}$	THF	70° — 75°

Instead, Atomic Force Microscopy (AFM) measurements were conducted on the wafer surfaces in order to assess their responsiveness to selective solvents. The AFM measurements were conducted in tapping mode, allowing for direct interaction of the cantilever tip with the surface. This approach allows to directly measure the strength of interaction between the hydrophilic AFM cantilever tip and the substrate[309]. As a consequence, AFM measurements allow to assess surface topology, homogeneity and the adhesion force between cantilever and surface brushes. In a first step, a frame of reference was produced by measuring the linker modified wafer **98**, the PCL grafted wafer **129** and the PDMAEMA grafted wafer **130** (Figure 3-37).

The right column of Figure 3-37 shows the respective adhesion forces associated with the left hand topologies. The linker modified wafer **98** shows an overall homogeneous surface topology with low surface roughness. The micrograph shown in Figure 3-37 a) shows three spherical features with a height of 10 nm and a diameter of ~20 nm. When referring back to the inhomogeneities observed *via* ToF-SIMS, their size and shape are strongly reminiscent of the features observed by AFM. It stands to argue that the spherical topologies stem from the same carbodiimide impurity. The adhesion force is homogeneously low around 3-4 nN, with the exception of the impurity agglomerates.

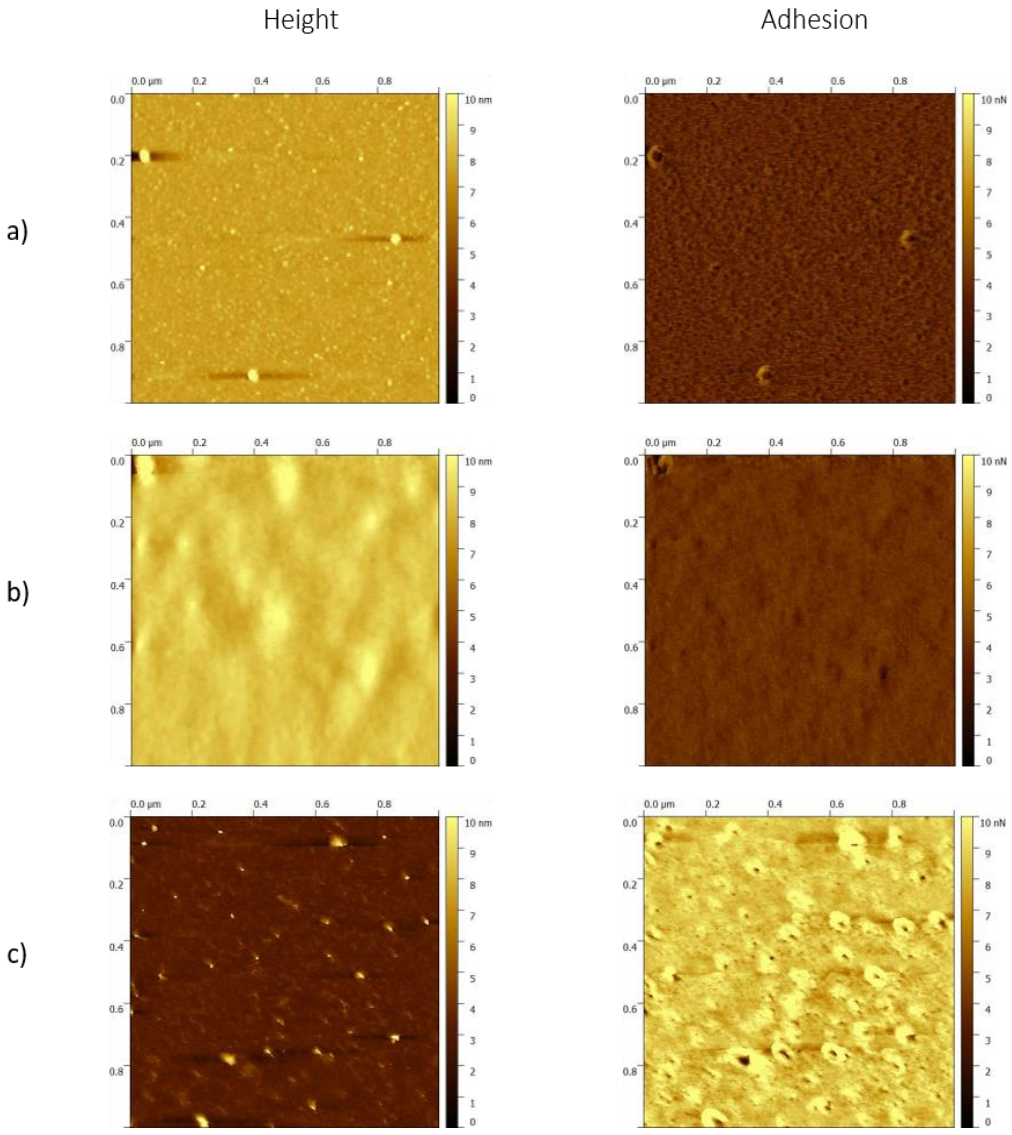

Figure 3-37: AFM micrographs (1000 nm x 1000 nm) in tapping mode showing the wafers in air: a) linker functionalized wafer **98**, surface topology and adhesion force between cantilever and surface, b) PDMAEMA reference **130**, c) PCL reference **129**

The PDMAEMA reference **130** (see Figure 3-37 c)) showed a smooth surface with only some gentle elevations (ca. 1 nm height difference). These height differences might represent differences in the substrate topology or else small differences in grafting density. Higher grafting density leads to greater steric crowding and hence a more fully extended brush regime. However, given the small amplitude, it is unclear whether these features warrant discussion. Overall, the smooth surface is indicative of an even grafting density and homogeneous chain length. The corresponding adhesion force is weak at ca. 3-4 nN. The cantilever tip has a hydrophilic silanol surface. As the interaction force measured *via* AFM is known to be sensitive to the substrate hydrophilicity[310], it was expected that the hydrophilic cantilever would interact more strongly with the hydrophilic PDMAEMA sample than the hydrophobic PCL sample or the linker. However this effect was not observed. Instead, the differences in adhesion force was due to differences in glass transition temperatures. While PDMAEMA was found to have a T_g around 8 °C, PCL has a T_g around -60 °C (*vide supra*). As a consequence, the PCL sample is softer and the cantilever therefore interacts more strongly with the polymer surface. Between the PDMAEMA brush and the linker functionalized surface, no significant change was perceived.

The PCL reference **129** showed the greatest inhomogeneities in surface topology. Several small (10-20 nm wide and 10 nm high) spots can be observed in the AFM micrograph Figure 3-37 e). With reference to the ToF-SIMS results, these could be catalyst derived impurities. Apart from these impurities, the surface appears very smooth, implying an even grafting density and chain length. When considering the adhesion force, a drastic difference to the other references can be observed. The adhesion force at the PCL references is around 10 nN and hence much higher than for the hydrophilic PDMAEMA, as expected for its low T_g.

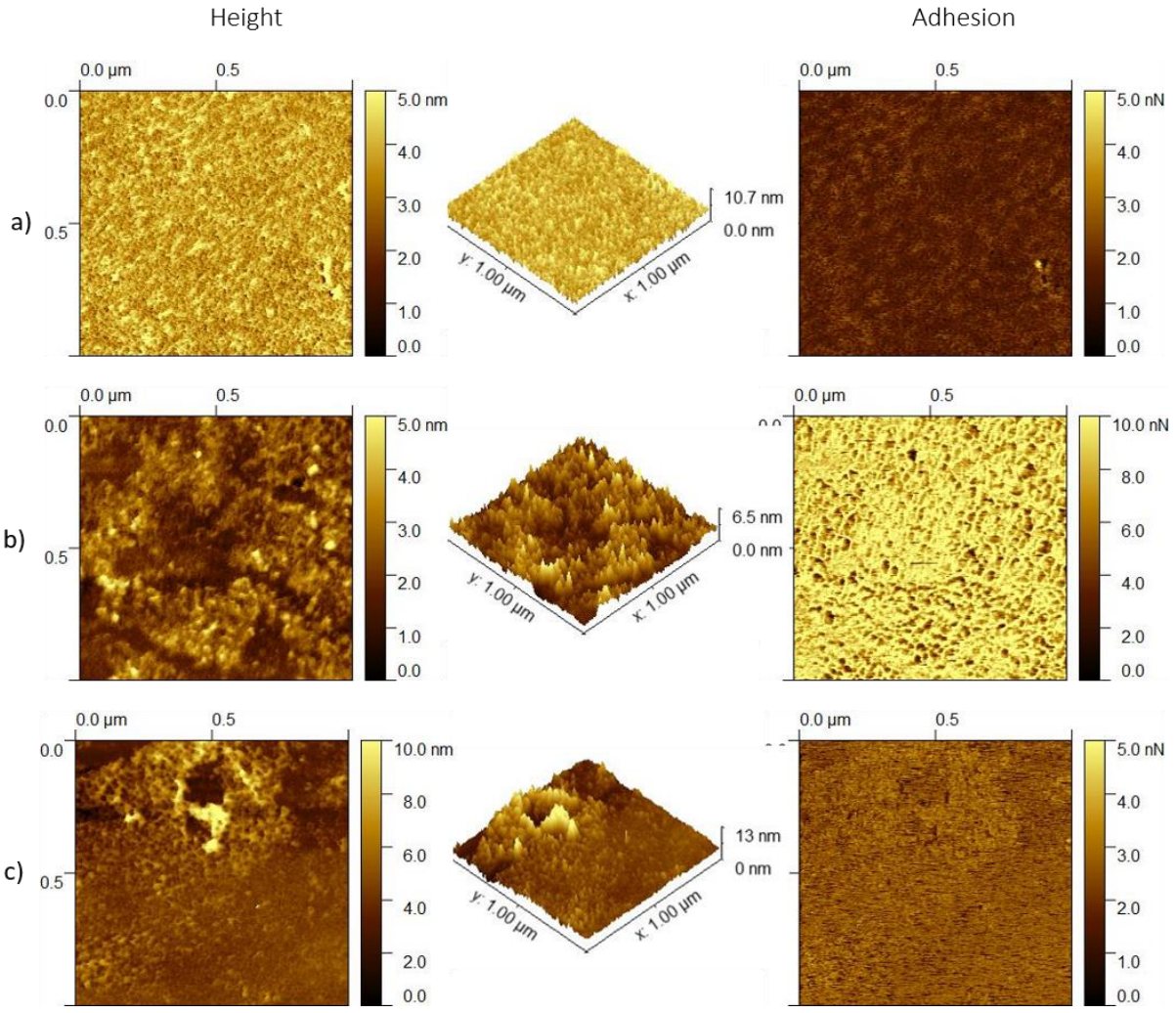

Figure 3-38: AFM microcraphs (1000 nm x 1000 nm) in tapping mode of simultaneously grafted silicon wafer **128** a) after immersion in THF b) after immersion in toluene for 10 min and c) after immersion in water for 15 min.

Figure 3-38 shows the simultaneously grafted wafer **128** after immersion in THF as a non-selective solvent (a), in toluene as a solvent selective for PCL (b) and after immersion in water, selective for PDMAEMA (c). The wafers were allowed to equilibrate for 15 min in each solvent to adopt their equilibrium morphologies. Binary brushes have been shown to adopt a topology that is solely dependent on the ultimate treatment, while all previous treatments are reversible[311]. However, as all measurements were conducted in air, the underlying assumption is that through rapid drying of the solvents the equilibrium morphology is locked in place. Indeed, previous studies have shown that the drying time frame is orders of magnitude faster than the time required to adopt equilibrium morphologies.[100] As THF is a good solvent for both polymer chains, any phase separation would therefore be expected to result exclusively from the incompatibility of the two polymers. The surface topology after immersion in AFM is rough, with textured morphologies rising around 10 nm above the surrounding surface. In addition to the raised chains, the topology is dominated by a periodic

array of small (ca. 10 nm diameter) indentations. These dimples are present both in the elevated structures as well as in the surface plane. When TSUKRUK et al.[104] investigated their Y-shaped PBA-PAA brushes, the same features were observed. The group interpreted these dimples as spontaneous phase separations based on the immiscibility of PBA with PAA. The indentations were due to the shorter chain length of PAA (see Figure 3-39). With the grafted wafers herein, the PDMAEMA chains are also shorter than the PCL chains. The high homogeneity of the observed dimples has several implications: the two polymers indeed undergo segregation and grafting density and chain length seem to be homogeneous based on the observed area. Adhesion force of the same area is very low at 0 nN - 3 nN.

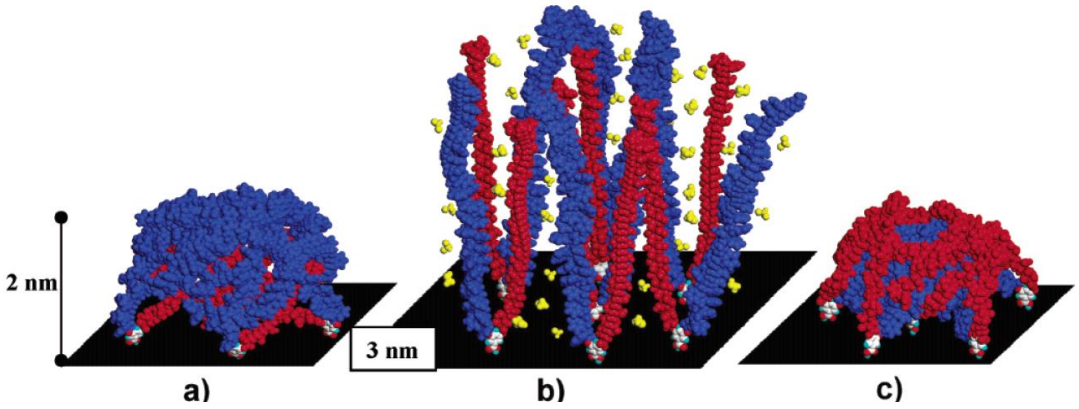

Figure 3-39: Molecular graphics representation of the proposed structural rearrangements in TSUKRUK'S Y-shaped brushes. (a) Internally segregated pinned micelle composed of seven grafted PS-PAA molecules. Upon treatment with toluene and subsequent drying, the PS arms (blue) form a corona covering the micelle's core consisting of PAA(red) arms. (b) Representation of the same seven molecules swelled in a nonselective solvent (yellow). (c) Top-open dimple structure containing collapsed PS arms partially covered by seven PAA chains. Reproduced with permission from [104] Copyright (c) 2003 American Chemical Society

The wafer was then placed in a beaker containing toluene — a solvent selective for PCL. The resulting surface morphology Figure 3-38 b) increased in roughness. The most notable change was found in the adhesion force. The average adhesion force increased from to ca. 10 nN. When contrasting these findings with the adhesion forces measured for the homopolymeric reference samples (see Figure 3-37), the cantilever interaction with the PCL reference (ca. 10 nN) closely resembles the cantilever interaction with the surface following toluene treatment. This implies that treatment with toluene allows to selectively bring PCL chains to the surface.

After immersing the same wafer in water for 15 min, the surface topology showed two regions: one of high surface roughness, surrounded by an area of lower surface roughness. Water is a selective solvent for PDMAEMA. As a result, PCL chains, immiscible with PDMAEMA chains and insoluble in water collapse as far as the steric crowding in the brush

allows. PDMAEMA chains on the other hand are fully extended. The adhesion force observed for the wafer after immersion in water decreased to 3-4 nN, as was observed for the PDMAEMA-only brush. Interestingly, the area showing higher topological features showed no adhesion interactions distinct from the surrounding area. The higher features might therefore represent PCL chains with higher DPs than the surrounding surface and could therefore explain the high intensity PCL signals observed in ToF-SIMS for some regions.

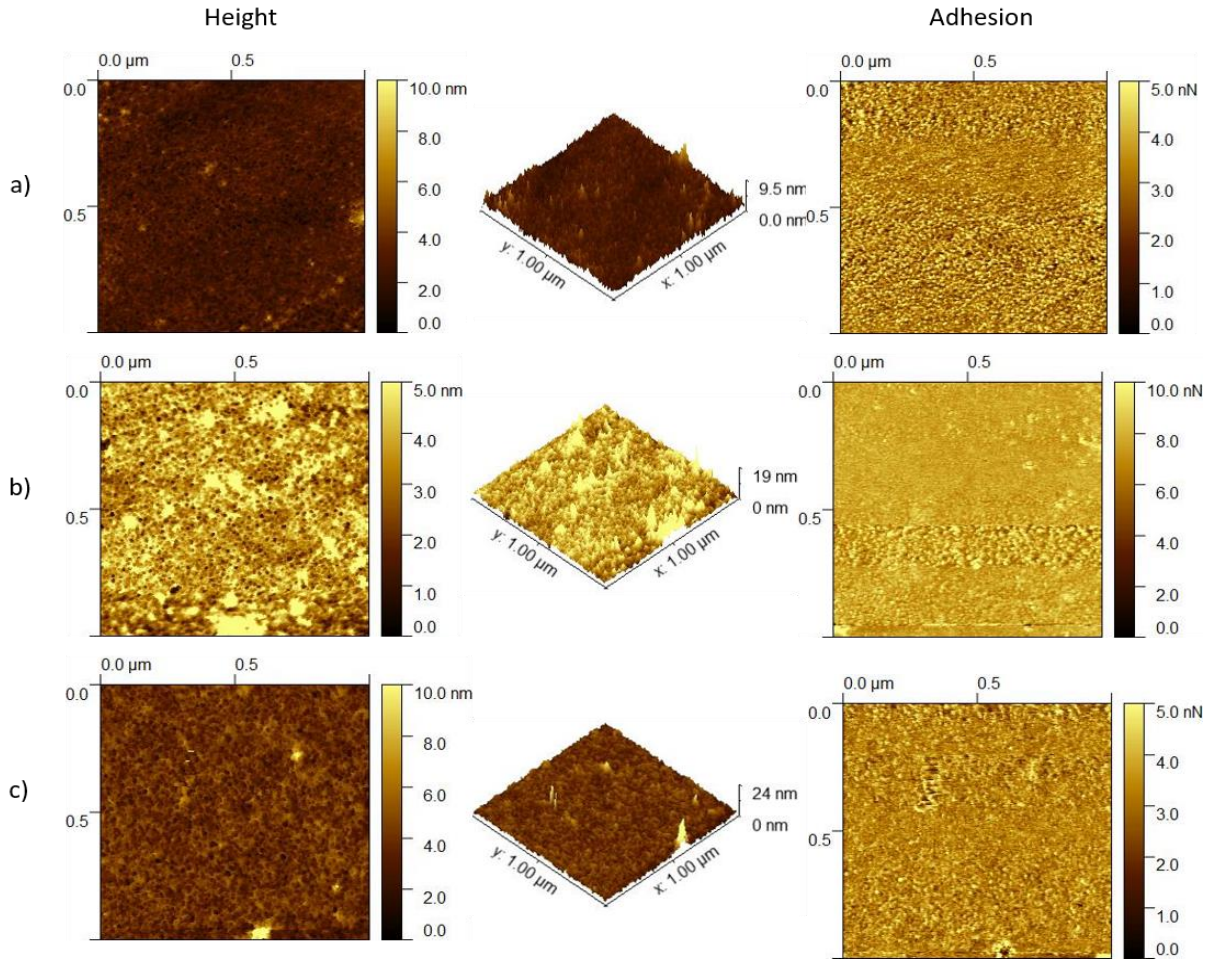

Figure 3-40: AFM microcraphs (1000 nm x 1000 nm) in tapping mode of simultaneously grafted silicon wafer **134** a) after immersion in water, b) after immersion in toluene for 10 min and c) after immersion in water for 15 min.

Further AFM measurements were conducted on wafers grafted with longer chains to assess whether chain length affects phase morphology and adaptability (see Figure 3-40). The mixed brush **134** with grafted $PDMAEMA_{22}$ and PCL_{44} had longer chains than mixed brush **128** with $PDMAEMA_{15}$ and PCL_{33} and a larger chain length difference. The topology of wafer **134** after immersion in THF (Figure 3-40 a)) was smooth. The adhesion force between cantilver and surface showed a distinct structure: small areas (ca. 10 nm) of high adhesion

(5 nN) interchanged with equally small regions of low interaction (2 nN). This pattern is indicative of PCL-PDMAEMA phase separation.

Immersion into toluene then led to a rearrangement of the topology with a concomitant increase in adhesion force (see Figure 3-40 b). The topological features show a distinct distribution of 10 nm dimples interpreted as PDMAEMA within a PCL phase. When the wafer was immersed into water (see Figure 3-40 c)), decreased to 3-4 nN. These longer chains therefore also show the stipulated adaptive behavior.

When contrasting the observations made through AFM topology and adhesion measurements with those made by TSUKRUK et al[104]. (see Figure 3-41), a few topological differences are striking. The dimples the group observed are surrounded by further, deep depressions. These contours give their AFM topologies the appearance of craters rather than dimples. In contrast, the surfaces produced herein show only the spherical or ellipsoid depressions arising from the shorter chains. The difference can be explained by dissimilar grafting densities. TSUKRUK et al. used a grafting-to approach. The steric bulk of the immobilized chains hinders a high grafting density and therefore the surface brushes do not

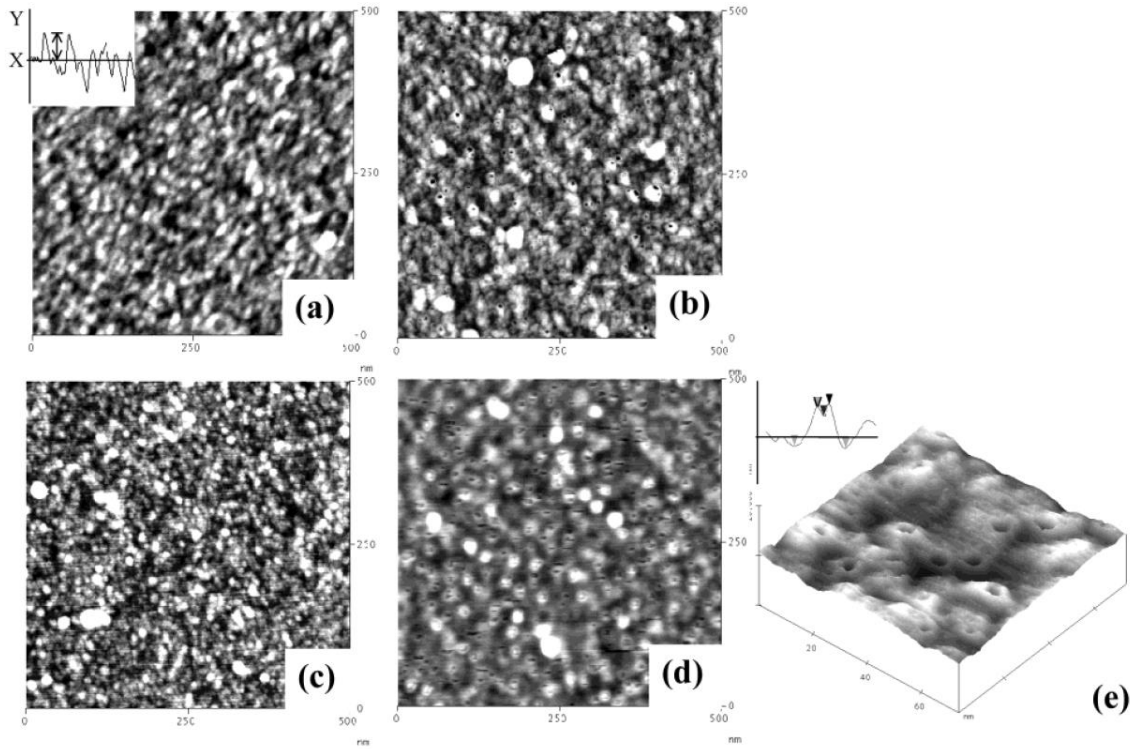

Figure 3-41: AFM topographical images (500x500 nm) of Y-shaped PS-PAA brushes treated with toluene (a, c) and water (b,d). The vertical scale is 5 nm. (e) High-resolution three-dimensional topographical image (70 _ 70 _ 10 nm) showing the craterlike (dimple) surface structures in the long-stem brush treated with water. Representative cross sections (30 _ 3 nm) are shown. Reproduced with permission from [104] Coyright © 2003 American Chemical Society.

form a continuous phase. The system presented herein evidently led to a much higher grafting density and hence only dimples within a continuous polymer phase are observed.

Simulations predict long-range order in the dimple phase[100]. The dimple domains observed above have narrowly distributed sizes and they are densely clustered. However no long-range order could be detected. Various groups have observed such a mismatch between theory and experiment.[312—314] Indeed, up to this date the predicted long-range order could not be observed experimentally. Simulations have shown that even minor differences in grafting distribution, concentration and composition disrupt the periodicity of ripple and dimple domains. FREDRICKSON et al.[313] simulated mixed polymer brushes while altering local grafting densities. They found that the long range order was sensitively dependent on the local grafting homogeneity. Simulations rely on the assumption that grafting sites are fully uncorrelated and uniformly distributed. In practice, the grafting sites are random, with fluctuations in grafting density and composition. Even small fluctuations in composition and grafting site lead to nucleation of domains within MPB. The ToF-SIMS measurements had shown the propagation of initiator defects onto the brush composition. So even when controlling for alternating polymer grafts, the inhomogeneous brush distribution remains subject to the grafting points of the Y-shaped initiator. This effect was also observed by contrasting randomly co-deposited immiscible brushes with Y-shape deposited brushes.[312]

3.8 Conclusion

The simultaneous surface grafting project was undertaken to design a synthetic pathway that reliably produces binary amphipolar mixed brushes in one single polymerization step. Employing orthogonal polymerization techniques is a rational necessity to retain control over such complex polymeric architectures. A particular focus was placed on the simultaneous nature of the two polymerizations while retaining spatial control (i.e. maximal molecular mixing) over the two polymers. In order to observe the characteristic phase transitions of amphipolar binary brushes, it was deemed necessary that the grafting density be as high as possible.

Y-shaped bi-functional initiators with anchoring functionality were identified as the only synthetic tool to enforce maximal mixing of polymer chains on a molecular level. The design motif was adopted and a trifunctional center was successfully equipped with two orthogonal initiating moieties. A primary alcohol on one arm allowed for initiation for ROP and a halo ester on the other arm initiated ATRP. A third functionality was introduced to enable covalent bonding with silica substrates. ^{1}H NMR, ^{13}C NMR, DOSY NMR, mass spectrometry and IR were used to confirm the successful Y-shaped linker synthesis. The silica wafers were easily functionalized with the linker through alcoholysis of the silyl ether anchoring group. The homogeneous SAM formation on the silica wafer was observed through AFM, XPS and ToF-SIMS measurements. The ease of functionalizing silica-based materials suggests that the synthetic approach chosen herein can easily be extended to other silica based systems and geometries.

The combination of two orthogonal polymerization techniques proved anything but trivial. The study started out with a previously reported tandem system connecting ATRP with DBU-catalyzed ROP. Although one-step, one-pot polymerizations of NIPAM and LLA could easily be conducted, the additional constraint of simultaneous polymerizations meant that the relative reaction kinetics had to be controlled. The true simultaneity of the two polymerizations was deemed necessary to avoid mutual steric hindrance. Monitoring relative rates of conversion as a function of reaction time allowed to assess whether the two polymeriaztions occur at comparable reaction rates. The DBU/ATRP proved kinetically mismatched to the extent that the ROP-derived chain would strongly impede the inbound monomers for ATRP like a stepwise synthesis. The kinetic differences remained in spite of a systematic altering of reaction temperature, UV irradiation, solvent and monomer. The findings herein pointed to a more general issue in simultaneous tandem systems. The use of

the term simultaneous should be restricted to those one-pot, one-step systems that occur at comparable timeframes.

The $Sn(Oct)_2$ catalytic system explored thereafter allowed to narrow the gap between the two polymerization rates by selecting adequate solvent, monomer combinations and temperature ranges. Non-interference between the two polymerizations and reliable initiation was proven though employing a bifunctional initiator. The resulting block copolymers were analyzed *via* GPC and DOSY NMR and showed covalent attachment between the two blocks. This covalent attachment meant that the polymerizations were reliably initiated by the dual initiator without detrimental interferences. It is important to point out that the conditions reported herein do not generalize to a straight forward protocol that can be applied to any combination of monomers. On the contrary, this study highlights the complexity of monomers, catalysts, solvents and temperature at interplay when conducting tandem reactions. Adjusting reactivity ratios of two polymerizations was shown to rely on careful tuning of reaction conditions and profound knowledge of monomers and catalysts involved. The systematic variation of the reaction parameters herein outline a methodology for independently adjusting reactivity ratios by exploring the available parameter space including solvents, monomers, temperatures and catalysts. The large range of adjustable parameters commends ATRP as a much more flexible polymerization technique than previously reported NMP.

The established system was then applied to the linker-modified wafers. Polymerization initiated by the wafers was tracked by employing a sacrificial dual initiator. Wafers with varying compositions of hydrophilic PDMAEMA and hydrophobic CL were grafted. Polymerizations were robust and work-ups were facile. The sacrificial initiator derived polymers were analyzed and also produced block copolymers as in the reactions without wafer present. The amphiphilicity of the resulting block copolymers was observed by DLS measurements.

Difficulties associated with analyzing chemical compositions on the wafers themselves were circumvented by applying surface-sensitive analysis techniques. XPS was employed to assess the success of the simultaneous grafting off linker functionalized wafers. Particularly the strong N1s signals observed exclusively on DMAEMA-grafted wafers clearly indicated the presence of PDMAEMA on the surface. The C1s and O1s peaks with their characteristic shoulders further helped to confirm the presence of the respective polymers (and their mixed combinations) on the surface. ToF-SIMS was shown to be particularly powerful in the context of characterizing brush surfaces. The combination of imaging techniques with depth profiling allowed to show the three-dimensional distribution of

polymer segments within the brush. It was shown that defects in the linker distribution propagated onto the grafting densities. Else, the brushes produced showed homogeneous polymer populations. AFM studies allowed to observe nanoscale phase separations in the brushes. Treatment of polymer brushes with selective solvents led to a collective rearrangement of the two polymer populations. A clear transition between a high adhesive phase and a low adhesive phase was observed as the surface adapted to the solvent. The changes in adhesive force were accompanied by distinct transitions in the surface morphology, proving the responsive nature of the synthesized brushes. The reversibility observed when cycling through selective solvents demonstrated the covalent attachment of the two polymers. The combination of various characterization techniques allowed to construct a complete picture of the grafted wafers.

4 SUMMARY AND OUTLOOK

The present thesis focused on the implementation of simultaneous tandem polymerizations for accessing challenging polymeric architectures. In Chapter 2, the synthesis of molecular bottlebrushes was explored, while Chapter 3 focused on establishing a synthetic pathway to afford binary mixed surface brushes.

The bottlebrush project investigated in Chapter 2 arose from a logical expansion of the work conducted by FREUDENSPRUNG[39] on the orthogonal combination of ROMP and ROP to yield linear block copolymers. A truly simultaneous approach to synthesize molecular bottlebrushes *via* two orthogonal polymerization processes had never before been achieved. The bottlebrush architecture was targeted by employing a backbone monomer with ROP initiating functionality. However, despite the preliminary NMR studies and homopolymerizations that indicated both orthogonality and polymerization control, it quickly transpired that mitigating the challenging architecture and complexity of two polymerizations was anything but trivial. It was shown that ROMP was impeded by the complex interaction of the inimer's hydroxyl group with the Grubbs catalyst. While in the absence of SIMes catalyst, ROMP proceeded smoothly with the inimer, the NHC led to deprotonation of the inimer and allowed for stable complexation with the metathesis catalyst. Complexation in turn resulted in a deactivated Grubbs catalyst. The ability of inimer complexation with the metathesis catalyst depends primarily on the inimer structure and spatial orientation of the hydroxyl functionality. Through rational monomer design, an inimer was synthesized that polymerized rapidly in the presence of Grubbs catalyst. Introducing a spacer between the olefin functionality and ROP initiating group allowed to avoid catalyst complexation, while the *exo*-orientation of norbornene-functionalization mitigated the steric demands of monomer coordination.

In addition to the polymerizability of both systems at the same time, defined by orthogonality and mutual compatibility, a second aspect of tandem polymerizations are the relative rates at which these transformations occur. It was stipulated that by carefully controlling the relative rates of side chain and backbone polymerizations, the challenging steric regimes that are intrinsic in molecular bottlebrush synthesis could be avoided or at least mitigated. In all established techniques (grafting to, grafting from and grafting through), the high steric crowding intrinsic to molecular bottlebrushes either lead to low grafting densities or incomplete conversion. The tandem approach was expected to circumvent the intense steric demands, only if the both polymerizations occur simultaneously. A scenario where one monomer reaches full conversion orders of magnitude before the second monomer would lead to the same dynamics as a step-wise approach, with the added difficulty of having to ensure mutual compatibility. In order to match the conversion rates of ROP and ROMP, polymerization conditions were adjusted and a ROP catalyst with slower turnover was selected. The NHC DTT was found to match the requirements concerning compatibility, orthogonality and tunable reaction rates. The combination of DTT temperature dependence, and LLA solubility in toluene allowed to match the relative polymerization rates of ROMP and ROP.

The simultaneous nature of the two polymerizations was proven by *in situ* kinetic NMR experiments. The kinetic curves thus established showed *pseudo* zero order kinetics for the ROP of LLA, while the first order kinetics of ROMP showed a distinct kink in reaction rate. The bimodal reaction rate of ROMP was interpreted as a result of the increasing steric demands towards the later stage of the polymerization or else a thermally induced instability of the Grubbs catalyst. Due to the decreasing polymerization rates towards the later stages of ROMP, only short molecular bottlebrushes could be synthesized with high fidelity, while longer targeted backbone DPs failed to reach high conversions of backbone monomer.

The molecular bottlebrushes produced *via* this tandem system were analyzed by NMR, GPC and AFM. NMR experiments were conducted for full assignment of all proton signals. DOSY NMR experiments showed the covalent attachment of the side chains and backbones. AFM micrographs showed the characteristic worm-like brush morphology. All short bottlebrushes were remarkably narrowly distributed. The bottlebrushes prepared in tandem were contrasted to those prepared *via* the grafting through approach, using the same monomer and catalyst combination. The grafting through bottlebrushes allowed to prepare longer backbones. However in direct comparison of brushes with the same DP in side chain and backbone, the tandem brushes were consistently more narrowly distributed. In order to assess the dispersity of the sidechains, the backbones of molecular bottlebrushes prepared by tandem grafting were depolymerized and the resulting side chains were characterized by

GPC and MALDI-ToF. It was found that the side chains were very narrowly distributed. In combination with the low overall dispersity, it could be shown that both polymerizations produced narrowly dispersed polymers. Overall, the presented synthetic strategy presents an extension for the synthetic toolbox to yield molecular bottlebrushes. The independent, simultaneous nature of this approach sets it apart from the commonly employed strategies of *grafting-from, grafting-to* and *grafting-through*.

The synthesis of binary mixed polymer brushes suffers from similar steric challenges as molecular bottlebrushes. A stepwise approach allows for good surface coverage with the first polymer but strongly impedes diffusion of the second monomer to the surface/initiators. Chapter 3 therefore explored how simultaneous tandem polymerization might benefit the synthesis of such systems. While simultaneous polymerization off a surface has previously been reported[209], there has not been any successful attempt towards combining simultaneous polymerization of non-miscible polymers with defined anchoring points. Control over the brush distribution, grafting density and grafting ratio was targeted through rational initiator design. A Y-shaped dual initiator was designed bearing an ATRP and a ROP initiating functionality. Additionally, a silyl ether group was chosen as anchoring functionality for immobilization on a silica surface. Successful synthesis was proved by help of ^{1}H, ^{13}C and 2D NMR techniques, as well as IR and mass spectrometry. Immobilization of the initiator on the silicon wafers was straightforward. The silicon wafers were treated in an ozone oven to afford a homogeneously oxidized surface. Immobilization of the linker was achieved by hydrolysis of the silyl ether anchoring group. The surface modification was assessed by help of XPS and contact angle measurements. XPS showed the presence of characteristic elements/groups (namely Br and carboxylic carbon peaks) in the functionalized samples that were absent in the unfunctionalized reference wafer.

With the successful surface modification of the wafers, an adequate combination of orthogonal polymerization methods was explored. ROP and ATRP were chosen due to the broad range of available catalytic systems that allows for a powerful platform to adjust initiation and polymerization rates. At first, a system combining DBU catalyzed ROP in combination with DBU-ligated standard ATRP catalyst was explored. ATRP homopolymerizations of a hydrophilic monomer (NIPAM) using DBU as ligand resulted in a relatively broadly distributed PNIPAM polymer. In a test tandem system however, it was quickly noted that the acrylamide's conversion remained low, even at a range of reaction temperatures. Replacing the DBU complexed ATRP catalyst for a more active catalyst complex did not lead to marked improvements. Due to the sensitive dependence of activation and deactivation rates in ATRP on solvent nature, a range of solvents were tested to afford better conversions of acrylic monomer. Toluene was found to produce the best polymerization

results. Initiation by UV light was employed I order to conduct the polymerization at lower temperatures. However no conversion of acrylic monomer was observed. The DBU-based tandem system was therefore assessed as unfit for the purposes of this project.

A second combination of ATRP and ROP was explored. The $Sn(Oct)_2$ catalyzed ROP of cyclic lactones was combined with a PMDETA-ligated ATRP catalyst (CuBr/PMDETA). The system was expected to produce more active ATRP catalysts due to the reducing nature of the stannous catalyst. Employing $Sn(Oct)_2$ led to better conversions of NIPAM and MMA as acrylic monomers, while ROP of cyclic lactones LLA and CL proceeded to full conversions. Choosing DMAEMA as monomer for ATRP allowed to harness the higher monomer activity of methacrylates of acrylamides. The $Sn(Oct)_2$ co-catalyzed ATRP of DMAEMA and ROP of CL was thus chosen for the simultaneous polymerization on the functionalized wafers.

A range of monomer ratios was targeted, including homopolymerizations of both monomers as a reference. In order to overcome the analytical challenges imposed by the heterogeneous system (*in-situ* NMR experiments are not feasible for the brushes growing at the interface), a sacrificial dual initiator was added to the polymerization solution. Conversions and degrees of polymerization were therefore indirectly determined through samples drawn from the reaction medium. The polymerizations were shown to proceed at comparable timeframes. Importantly, the dual initiator led to the formation of block copolymers, capable of forming supramolecular structures in water. The covalent attachment between the two blocks was evidenced by the single diffusion coefficient observed in DOSY NMR experiments. Molecular weight distributions were relatively narrow, ranging from 1.60 to 2.10. TGA measurements corresponded well to the theoretically expected weight ratios and showed a high percentage of head-to-tail additions in the PDMAEMA chains. Overall these results point towards a well-controlled tandem process.

The functionalized wafers were analyzed and compared to reference wafers by help of XPS, ToF-SIMS and AFM. The XPS spectra showed distinct differences from unfunctionalized wafers as well as from wafers functionalized with the linker only. The ratio of carbon to oxygen signal on the surface indicated the growth of an organic layer. Additionally, the presence of a high binding energy shoulder on the C1s region showed specific sp3 binding to oxygen and nitrogen. The nitrogen peak could be assigned to the DMAEMA monomer and was absent in both the linker functionalized wafer as well as wafers functionalized only with PCL. The XPS spectra were matched to the findings provided by ToF-SIMS analysis. The highly sensitive ToF-SIMS proved a powerful tool to assess both grafting success as well as distribution across the wafer surface. ToF-SIMS spectra were recorded for wafers functionalized with the tandem process, both homopolymers as well as

reference samples of catalysts. By assessment of the reference wafers, specific fragments could be allocated to the two monomers, as well as catalyst fragments. The spectra of tandem grafted binary mixed surface brushes showed the specific fragments of both polymers across the surface. Multivariate analyses supported the findings of manual selection analysis. Depth profiles showed the inverse distribution of polymer derived signals and substrate signals as expected. Finally, lateral distributions of various ions visualized for several areas on the tandem grafted wafers. Inhomogeneities in grafting density were associated with inhomogeneities in the linker distribution. Finally, the responsiveness of the tandem grafted brushes was proven by AFM measurements of the mixed binary brushes in air and following treatment of selective solvents. The brushes showed spontaneous phase separation to produce nanoscale arrays of surface patterns. The differences in glass transition temperature of the two polymers allowed to show that immersion of the wafers into selective solvents led to a solvophilic adaptation of the brushes.

The two projects discussed in chapters 2 and 3 showed that simultaneous tandem polymerizations can greatly simplify the synthesis of challenging polymeric architectures. The multistep syntheses that are usually required could be shortened to a single polymerization step, while retaining excellent control over both polymerization. However, the projects also showed that the complex interactions of both polymerizations requires precise control over all reaction parameters and necessitates detailed knowledge of catalysts and monomers. Despite the high demands on controlling reaction parameters, tandem polymerizations demonstrate the great potential in circumventing unfavorable steric regimes. As a consequence, these polymerizations are most useful in syntheses characterized by

Figure 4-1: Amphiphilic binary mixed brushes for stabilization of nanoparticle dispersions in media with various polarities.

challenging steric demands, such as those of molecular bottlebrushes or surface-initiated polymerizations.

The simultaneous surface grafting system explored herein could easily be expanded for a range of geometries. The linker described above is not limited for applications on planar surfaces but could be immobilized on concave, convex or porous substrates. The Y-shaped initiator used in chapter 3 could easily be immobilized on nanoparticles. The simultaneous tandem grafting approach could then leverage the difficult diffusion in between the nanoparticles and growing brushes to afford mixed binary brushes tethered covalently to the nanoparticles. If a hydrophilic and a hydrophobic monomer are selected for polymerization, amphiphilic mixed brushes can be synthesized on the surfaces. Such functionalizations have a range of applications. STEWART et al.[315] showed that by selective swelling and collapsing of amphiphilic surface brushes, nanoparticles could be loaded with hydrophobic molecules, followed by slow release. Such systems could then be used for controlled drug transport. ZHAO and coworkers[316] further demonstrated that such amphiphilic nanoparticles show excellent dispersibility in a range of solvents. Nanoparticle suspensions are liable to undergo agglomeration, leading to flocculation or sedimentation. Typically such agglomeration is prevented by functionalization with solvophilic polymer brushes[317]. Those brushes prevent agglomeration by sterics and osmotic pressure. However when transferring the dispersion from aqueous medium to an organic phase, these brushes collapse and the dispersed particles aggregate. For example sterically stabilized pigments in water based surface coatings, suffer from this drawback.[318] If however hydrophobic and hydrophilic polymer chains are used to stabilize the particles, excellent dispersion stability can be achieved in different media. In a non-selective solvent, both polymer chains are fully extended, resulting in a large steric barrier in between nanoparticles. When transferring the dispersed particles into a selective solvent, the solvophilic chains remain extended and allow of dispersion stability.

In a likewise manner, the simultaneous tandem system can be employed for porous materials, such as those used for filtration purposes. Functionalization of such porous materials with amphiphilic mixed polymer brushes allows for selective control over opening and closing of pores. In a good solvent, both brushes are fully extended and allow diffusion through the pores. In a selective solvent, one polymer collapses, blocking passage through the pores, while the second polymer chain remains extended. Such systems can be employed as nano valves for chemical gating[200], for drug delivery systems[319] or to remove buildup of material on filters[209].

A further interesting application for simultaneous tandem polymerizations to explore are syntheses of super-soft elastomers. As networks of highly grafted polymers, super-soft

elastomers derive their desirable macroscopic properties from the combination of side chain mobility and network stability[130]. In the synthesis of polymer networks, the crosslinking introduces a range of processing issues associated with solubility. If the network is synthesized first, followed by introduction of the side chains, the cross-linked “backbone” collapses when removed from its solvent. In the subsequent grafting step, accessibility of the telechelic side chains or side chain monomers is much lower inside the network than on its surface. As a consequence, homogeneous grafting is difficult to achieve. If, on the contrary, the polymers are grafted like molecular bottlebrushes, followed by crosslinking, the density of crosslinking points is concentration dependent and geometric considerations often lead to incomplete crosslinking or curing at a later stage. Simultaneous tandem polymerization offers the enticing option to produce homogeneously distributed grafts and cross-linking points. As all constituent of the later system are dissolved as monomers during initiation, the simultaneous approach allows for homogeneous dissolution of brushes and cross linkers. The orthogonal approach of simultaneous polymerization allows to independently address concentrations, rates and identity of crosslinking agent and brush regimes. Three approaches are conceivable. A reactive backbone ROMP inimer can be employed together with a fixed amount of cross-linking agent, building the scaffold of the network. ROMP-derived polymers are particularly suitable for this task due to their stiff structure. The inimer can simultaneously initiate the side chain polymerization. For this purpose, the system described in chapter 2 can be adopted with only the inclusion of crosslinking agents.

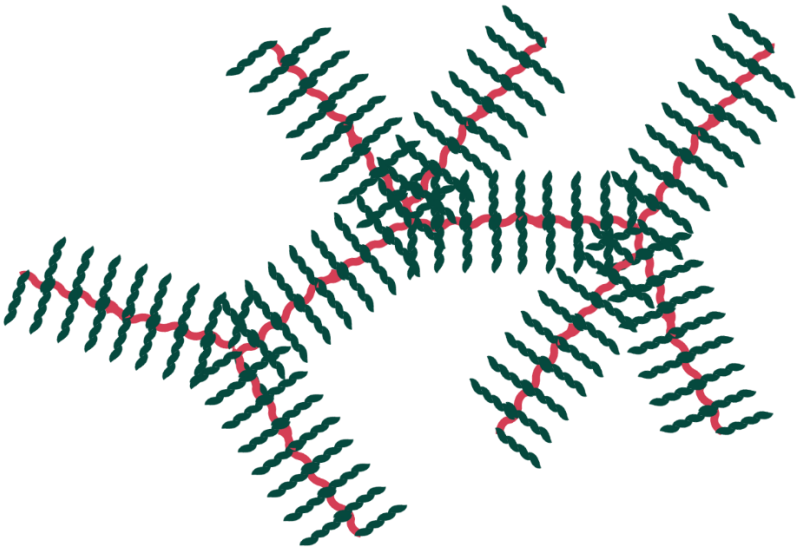

Figure 4-2: Crosslinked molecular bottlebrushes for supersoft elastomers

The simultaneous nature can also be exploited by synthesizing a brush network from PEGMA to form the brush regime and independently polymerize a crosslinking polymer chain orthogonal to the brush synthesis.

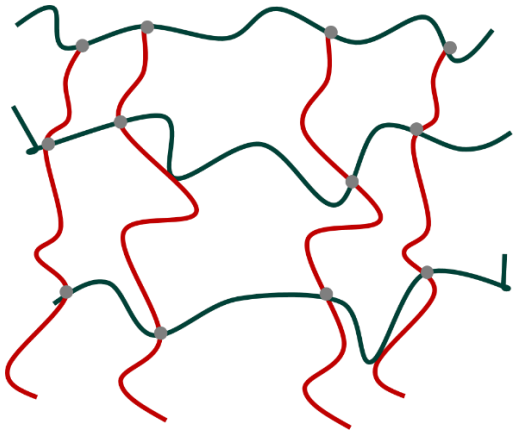

Figure 4-3: Amphiphilic co-network

Finally, an ATRP-ROMP system could be employed, with the side chains polymerized by ATRP[155,156]. The employment of ATRP allows to target a larger set of side chain functionalities. For example phosphoric acid containing monomers can be employed to synthesize proton conducting networks[320,321]. The grafting density can further be modulated by inclusion of unfunctionalized ROMP monomers. By this approach, amphiphilic co-networks can also be synthesized. Such co-networks are of interest for their various applications. Extended wear contact lenses for example require excellent wettability and ion conductivity, while they should retain their structure and allow for oxygen diffusion. Further uses include the production of semi-permeable membranes, slow release of pharmaceutical agents, nanoreactors or for touch-sensing[129].

5 EXPERIMENTAL

5.1 Characterization

5.1.1 Chromatography

Thin Layer Chromatography

Thin layer chromatography was performed on silica gel TLC-cards (layer thickness 0.20 mm, Fluka). Compounds were visualized by immersion in permanganate reagent ($KMnO_4$ (1.5 g), K_2CO_3 (10 g) and 10% NaOH in H_2O (200 mL) followed by heating with a heat gun (≤ 300 °C), ninhydrin stain (1.5 g of ninhydrin in 100 mL of n-butanol with 3.0 mL of acetic acid) or incubation in an iodine chamber or shining UV light (lamp filter 245 nm) as applicable.

Column chromatography

Column chromatography of crude products was conducted using silica gel 60 M with particle diameters of 0.040-0.053 mm purchased from MACHEREY-NAGEL as stationary phase. The elution was accelerated through the application of compressed air. Eluents are indicated in the experimental procedures as a ratio of A:B (with A and B the solvents). Crude products were exclusively dry loaded.

Gel permeation chromatography (GPC)

GPC was used to determine the molecular weight distributions (MWDs) using MZ-Gel SDplus 10E6, 10E4, and 500 columns with THF (at 30 °C) or DMF (at 60 °C with 1 $g.L^{-1}$ LiBr) as the eluent versus PSt, PMMA or PEO standards as indicated. MWD measurements were conducted at a concentration of 2 $g.L^{-1}$. Fractionations were conducted at concentrations of 10 $g.L^{-1}$. The Agilent Technologies 1260 Infinity setup was equipped with refractive index and UV detectors by WATERS, ERC, RHEODYNE and SOMA. All samples were dissolved in the eluent, equilibrated for several minutes and then filtered through a syringe driven TEFLON filter (MILLIPORE). The elution rate was set to 1 $mL.min^{-1}$.

5.1.2 Nuclear Magnetic Resonance Spectroscopy (NMR)

Solution NMR

Solution ^{1}H NMR and ^{13}C NMR spectra were recorded using BRUKER DPX-250, DPX-300, DPX-500, DPX-700 and DPX-850 spectrometers. Two-dimensional spectra (DOSY, COSY, HMBC, HSQC, NOESY etc.), ^{19}F NMR, ^{31}P NMR spectra were recorded using BRUKER DRX-500, DRX-700 and DRX-850 spectrometers. For solution NMR experiments, deuterated solvents were employed. The residual proton signals of the deuterated solvent was used as an internal reference[196]. For $CDCl_3$ the residual proton $CHCl_3$ (δ = 7.26 ppm), for CD_2Cl_2 residual $CDHCl_2$ (δ = 5.32 ppm) and THF-d_8 residual THF-d_7 (δ = 1.72 and 3.58 ppm) was used for calibration. For ^{13}C-NMR-Spektren the resonance of $CDCl_3$ (δ = 77.16 ppm), of C_6D_6 (δ = 128.06 ppm), of CD_2Cl_2 (δ = 53.84 ppm) and of THF-d_6 (67.21 und 25.31 ppm) were used for calibration. Unless otherwise stated, all experiments were conducted at 300 K. The temperature was defined with a standard 1H methanol NMR sample. The control of the temperature was realized with a VTU (variable temperature unit) and an accuracy of +/- 0,1K, which was checked with the standard BRUKER Topspin 3.5 software. Spectra were processed using BRUKER TopSpin 3.6 and MESTRENOVA x64 software. Chemical shifts δ were read off the centers of the multiplets and are reported in ppm. Multiplet patterns were reported using the abbreviations s = singulet, d = doublet, t = triplet m = multiplet and br = broad. Diffusion-ordered spectroscopy (DOSY NMR) experiments were conducted to investigate the covalent attachment of individual polymer blocks. In DOSY NMR, proton signals are resolved according to their diffusion coefficient and gives hence an idea of the prevailing molecular weights as well as indicating whether different polymer blocks are connected together or exist as separate homopolymers.

In-situ ^{1}H NMR Kinetic Experiments

For a ROP- ROMP Tandem in situ ^{1}H NMR kinetic experiment, HONDC-triazol adduct (15 mg, 0.03 mmol) was stirred in dry toluene-d8 (0.6 mL) for 20min in a glovebox. The yellow solution was transferred into a dry NMR tube equipped with a Teflon cap, containing L-lactide (85 mg, 0.6mmol, 20 eq.). The NMR tube was sealed and taken out of the glovebox. A reference spectrum was recorded on a BRUKER 500 MHz spectrometer at room temperature, using the residual proton peaks of the deuterated solvent as internal reference. The NMR tube was then taken out of the spectrometer, which was set to 80 °C and in a glovebox, the Grubbs-III catalyst (0.01 eq., 0.1 mL, 0.01 M in toluene-d8) was added to the reaction mixture. The green catalyst immediately turned orange upon mixing. The NMR tube was inserted into the spectrometer. The ^{1}H kinetic measurements were performed on a 500 MHz (Avance III) and 700 MHz NMR (Avance III) system at 298K. At the 500 MHz magnet 440 experiments were performed with a relaxation delay of D1 of 15s, a sweep width of 7500 Hz (15ppm), number of scans of 8 for each experiment and a 90° pulse for protons of 10,6 µs on a 5 mm BBFO ^{1}H/^{19}F X with z-gradient. A similar kinetic experiment on the 700 MHz spectrometer with 640 runnings were accomplished with a relaxation delay of 15s, a width of 12,600 Hz (18 ppm) and a 90° pulse of 13,8 µs on a QXI probe ^{1}H/^{13}C/^{15}N/^{19}F with z-gradient. The temperature was defined with a standard ^{1}H methanol NMR sample. The control of the temperature was realized with a VTU (variable temperature unit) and an accuracy of +/- 0,1K, which was checked with the standard Bruker Topspin 3.5 software.

5.1.3 Mass Spectrometry

Matrix Assisted Laser Desorption/Ionization-Time of Flight Mass Spectrometry (MALDI-ToF MS)

MALDI ToF MS spectra were recorded on a BRUKER Reflex II ToF Spectrometer equipped with a 337 nm N_2-laser. The samples for MALDI-ToF MS were prepared according to standard procedures. In brief, 5 µL of the sample solution (in THF, ca. 1 g. L^{-1}) were mixed with 15 µL of a saturated dithranol solution. 1 µL of the resulting mixture was placed on the sample holder. Functionalized Si surfaces were fixed on a topmount sample holder and introduced without any further treatment. 0.5 µL of the catalysts was deposited onto a Si wafer on a topmount sample holder and introduced into the instrument after drying.

Time of Flight — Secondary Ion Mass Spectrometry (ToF SIMS)

ToF-SIMS spectra were recorded on a BRUKER ION TOF TOF.SIMS^5 NCS instrument. The analyzer had a cycle time of 150 µs with a mass range of 1-2070 u. The analysis gun used Bi_3 at 30 keV and a current of 0.13 pA. The analyzed surfaced for each spectrum was 100x100 µm^2 to 200x200 µm^2. Surface spectra of the samples were acquired using Bi_3^+ ions at 30 keV energy with a cycle time of 150 µs and 0.10 pA, recording a mass range of 1-2070 u from an area of 200x200 µm^2.

Surface Spectra were acquired from:

- **128** Si with linker and PDMAEMA + PCL brushes (B660-B666)
- **98** Si with heterofunctional dual initiator (B648-B651, B714)
- **129** Si with linker + PCL brush (B652-B655)
- **130** Si with linker + PDMAEMA brush (B656-B659)
- **CuBr/PMDETA** catalyst in toluene (0.1 M, B632-B637)
- **$Sn(Oct)_2$** Tin octoate catalyst in toluene (0.4 M, B638-B647)

Large overviews of surface images were acquired using Bi_3^+ ions at 30 keV energy with a cycle time of 150 µs, recording a mass range of 1-2070 u from an area of 200x200 µm^2. Detailed spectral images were recorded at a mass range of 1-900 u, with a cycle time of 100 µs and 0.05 pA, using 30 keV Bi_3^+ ions from 150x150 µm^2. Surface images (overview and detail) were acquired from:

- **128** Si with linker and PDMAEMA + PCL brushes (B667-B670)
- **98** Si wafer with only linker-functionalization (B715-B716)

Depth Profiles were acquired with a cycle time of 150 µs (mass Range: 1-2070 u), using an analysis gun with 30 keV Bi_3^+ ions with a current of 0.10 pA at a 150x150 µm^2 area. The sputter gun used Ar_{1000} clusters with an energy of 2.5-5 keV at an area of 400x400 µm^2. Depth profiles were recorded for

- **128** (Si w linker and PDMAEMA + PCL brushes) (B671-B673)

ToF-SIMS Multivariate Analysis

For the MVA, spectra for all samples were acquired in replicate. From these spectra, a global peaks list was created, from mass intervals lists of 200-250 signals. Peaks with the highest intensity and further noteworthy peaks were assigned to empirical formulae. The

peaks list was then imported into the MATLAB simsMVA plugin, POISSON scaled and mean-centered before executing the MVA. For NMF, the data was POISSON-scaled but not mean-centered.

ExpressIon Compact Mass Spectrometry

Mass Spectrometry of small molecules was conducted using an ADVION expression compact mass spectrometer. Analytes were either applied on a glass capillary for use with the ADVION atmospheric solids analysis probe or else sampled off a TLC plate using the ADVION TLC plate reader. Spectra were recorded in the range between 10 to 2 000 u.

5.1.4 Fourier-Transform Infra-Red spectroscopy (FTIR)

FTIR spectra were recorded using a PERKIN ELMER BX spectrometer, equipped with a single reflection attenuated total reflection probe head by THERMO-SPECTRA-TECH. The laser was a He/Ne source with an emission wavelength of 633 nm. The analytes were spread on the ATR crystal as a powder or else as a liquid. The reported signals were normalized from zero to one, as signal intensity varies with penetration depth.

5.1.5 Thermal Analysis

Thermogravimetric Analysis

Thermogravimetric Analysis was conducted with a TGA-851 by METTLER-TOLEDO under nitrogen atmosphere. The heating rate was constant at 10 $K.min^{-1}$ between room temperature to 500 K. The thermal decomposition temperature was recorded off the point of inflection in the heating curve.

Differential Scanning Calorimetry

Differential scanning calorimetry measurements were performed using a DSC-822 by METTLER-TOLEDO. The temperature sweeps were conducted between -100 °C and 200 °C at a constant heating rate of 10 $K.min^{-1}$ under nitrogen atmosphere. The glass transition temperature and the melting points were determined from the second heating curve.

5.1.6 Atomic Force Microscopy (AFM)

AFM micrographs of the molecular bottlebrushes were recorded using a Dimension Icon with ScanAsyst. Measurements were performed in tapping mode under air with an

OPUS microcantilever with a resonance frequency of 300 kHz and spring constant of 26 N/m. A 1 mg/mL samlple of the brushes in THF was purified by preparative HPLC and immediately dropped on a freshly cleaved mica wafer. The solvent was allowed to evaporate at RT. These measurements were conducted by Helma Burg.

For the AFM measurements of modified silicon wafers, the wafers were cleaned with THF and allowed to dry at RT before submitting to AFM measurements. Measurements in tapping mode were conducted using a VTESPA-300 tip with a resonance frequency of 300 kHz and a spring constant of 42 N/m and a back of reflective Al. The wafers were tempered or dipped into selective solvents for the selected amount of time and allowed to dry on air at RT. For the adhesion force measurements, an OLTESPA 240 TS tip was used with a resonance frequency of 70 kHz and a spring constant of 2 N/m with a back of reflective Al. These measurements were conducted by [redacted]

5.1.7 Dynamic Light Scattering (DLS)

Hydrodynamic radii of micelles and nanoparticles were determined using a MALVERN Zetasizer 3000. A He/Ne-laser with emission wavelength of 633 nm was employed and scattering intensity was determined at a 90° angle. The measurements were performed with five repetitions, with the reported radius being an average of the five measurements. The dispersions were diluted with the appropriate solvent to the point where only a slight turbidity could be observed.

5.1.8 X-ray Photoelectron Spectroscopy (XPS)

XPS spectra were recorded using a KRATOS Axis Ultra DLD device with an aluminium anode as X-ray source and a delayline detector. Measurements were conducted in hybrid mode with a s spot sze of 300x700 μm^2. Survey spectra were recorded with a resolution of 80 pass energy, whle high resolution spectra were recorded with 20 pass energy. Measurement angles were fixed at 0° relative to the sample's normal.

5.2 General Procedures

All Syntheses were conducted under standard SCHLENK conditions. Glassware was dried in an oven at 110 °C for at least 24 h before they were transferred into a glovebox antechamber, where they were allowed to cool down to room temperature under full vacuum for at least three hours or overnight. Alternatively, clean glassware was washed out with the reaction solvent and dried by blow torch or heat gun for several minutes under high vacuum and allowed to cool to room temperature while maintaining the vacuum. Solvents and liquid reagents were transferred *via* air tight syringes that were flushed with argon or else *via* cannula. Solid reagents were added in a glovebox or else against a stream of argon, followed by evacuation cycles. Low temperature reactions were conducted by cooling with an ice bath or with dry-ice in acetone baths.

5.3 Materials

SIMes catalyst was purchased from ABCR GMBH (Karlsruhe, Germany) and stored in a glovebox. Toluene was refluxed over Na/benzophenone for four hours before condensing under Argon and were stored in a glovebox over molecular sieves. THF and triglyme were freshly distilled from Sodium/benzophenone into the reaction vessel. Solvents dried by this approach were considered free of oxygen and were not further degassed before polymerization. All other reaction solvents were purchased commercially dried from ARCOS or SIGMA ALDRICH. Commercially dried solvents were degassed *via* three consecutive freeze-pump-thaw cycles before application in a polymerization or before producing stock solutions. L-lactide, Second and Third Generation Grubbs catalysts were purchased from SIGMA ALDRICH, stored in a glovebox and used as received without further purification. Their stock solutions were always freshly prepared on the day of their employment. *Exo*-norborneol and *exo*-norbornenemethanol were purchased from Sigma Aldrich and distilled over CaH_2 under reduced pressure and stored in a glovebox at room temperature. St, MMA, DMAEMA were distilled over CaH_2 under reduced pressure and then stored in an ampule under argon in a freezer at -22 °C. NIPAM was recrystallized three times from a mixture of toluene/hexane (60/40) and stored in a fridge at 4 °C. All other chemicals were purchased from SIGMA ALDRICH and used as received.

Monomers were purified by distillation under reduced pressure to remove stabilizers and other impurities. After purification, they were stored in a SCHLENK flask under argon atmosphere in a freezer at -22 °C or in a dry box under nitrogen atmosphere.

5.4 Syntheses

5.4.1 Simultaneous Bottlebrush Polymerizations

Synthesis of 5-norbornene-*exo*-2-methanol

The synthesis of *exo*-enriched 5-norbornene-2-methanol was conducted according to a procedure established by KANAO et al.[172].

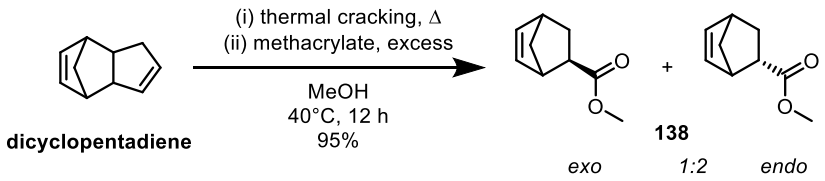

Scheme 5-1: Synthesis of 5-norbornene-2-carobxylate **138** from freshly cracked dicyclopentadiene through DIELS-ALDER cycloaddition with methacrylate.

Dicyclopentadiene (5.00g, 31.8mmol) was heated to 170°C and distilled off directly into a three necked flask charged with excess methacrylate (3.91g, 45.4mmol) and methanol (10mL) at 40°C. The reaction mixture was left to stir for 12h at 40°C. The excess Methyl Acrylate and methanol were removed under reduced pressure to yield 5-Norbornene-2-carboxylate (5.50g, 95% yield) as an orange oil that smelled pungently fruity. The reaction yielded a ratio of roughly 2:1 endo:*exo* isomers as established via ^{1}H NMR

^{1}H NMR (300 MHz, Chloroform-d) δ 6.10 (dd, J = 5.7, 3.1 Hz, 1H), 5.84 (dd, J = 5.8, 2.8 Hz, 1H), 3.60 (s, 1H), 3.54 (s, 3H), 2.93 — 2.67 (m, 2H), 1.83 (tt, J = 9.1, 3.4 Hz, 1H), 1.40 — 1.26 (m, 2H). 13C NMR (75 MHz, Chloroform-d) δ 174.87, 137.45, 132.15, 51.16, 49.37, 45.42, 42.92, 42.29, 29.00.

Synthesis of *exo*-5-norbornene-2-carboxylic acid

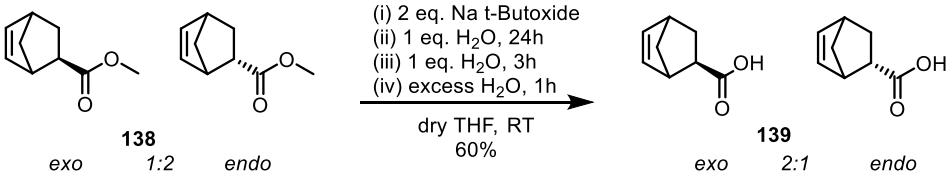

Scheme 5-2: Isomerization and *exo*-selective hydrolysis of norbornene-carboxylate **138** to yield *exo*-enriched 5-norbornene-2-carboxylix acid **139**.

Sodium tert-Butoxide (8.45g, 87.9mmol) and anhydrous THF (100mL) were placed in a dry 205mL Schlenck flask equipped with stirrer and addition funnel under Argon. Over a 20min timeframe, MNBC (KK34) (6.08g, 40.0mmol) were added via addition funnel under Argon, while cooled with an ice bath. Over 20 minutes. 720µl of DI water diluted in fry THF were added to the reaction vessel and eft to stir over night. Then, another 720µL of DI water, diluted in anhydrous THF (40mL) were added via addition funnel and left to stir for another 3h at RT. Finally, an excess amount of DI water was added directly to the reaction vessel to drive the hydrolysis to completion and after another 1h, reaction mixture was subjected to a standard work up to afford target molecule **139** (3.00g, 60% yield) as a pale yellow oil with a faint fruity smell.

^{1}H NMR (250 MHz, Chloroform-*d*) δ 11.56 (s, 1H), 6.30 — 6.00 (m, 3H), 3.03 (dt, *J* = 2.9, 1.4 Hz, 1H), 2.89 — 2.64 (m, 2H), 2.18 (ddd, *J* = 8.6, 4.4, 1.7 Hz, 1H), 1.86 (ddt, *J* = 9.4, 7.9, 4.7 Hz, 1H), 1.57 — 1.41 (m, 1H), 1.39 — 1.26 (m, 4H).

Synthesis of *exo*-5-norbornene-2-methanol

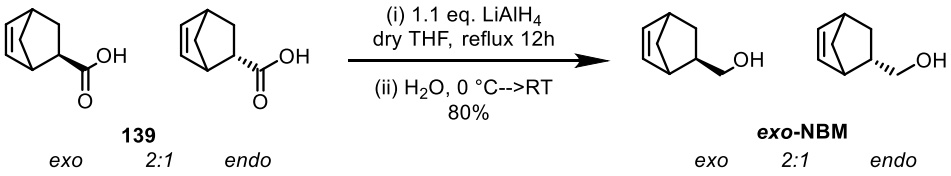

Scheme 5-3: $LiAlH_4$ reduction of carboxylic acid substrate **139** to yield the *exo*-enriched target molecule *exo*-NBM.

1.2 eq. Of LiAlH4 (1g, 26mmol) was added under nitrogen to a 250 mL RBF. The RBF was then placed into an ice bath. Dry THF (40 mL) was added dropwise into the flask, followed by a solution of *exo*-5-norbornene-2-carboxylic acid (3.00 g, 21 mmol) dissolved in dry THF (10 mL). The flask was then placed into an oil bath, and the reaction mixture was refluxed for

12 h. Next, the reaction mixture was cooled in an ice bath, then 1 mL of water was added dropwise to the flask, followed by 1 mL of 10% sodium hydroxide solution and finally 3mL of water. The flask was allowed to warm to room temperature and diluted with diethyl ether (200 mL). The solids were removed by filtering through celite, and the filtrate was washed with brine and dried over sodium sulfate. The solvent was removed to afford the product as a colorless oil (2.24g, 80% yield).

^{1}H NMR (300 MHz, Chloroform-*d*) δ 6.08 (m, 2H), 3.70-3.54 (m, 2H), 2.82 (s, 1H), 2.74 (s, 1H), 1.64 (m, 1H), 1.30 (m, 4H), 1.12 (m,1H).

Synthesis of pyridine analogue to Grubbs-III

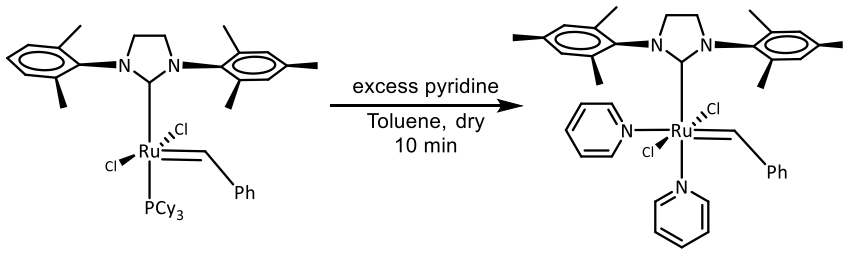

The Grubbs-III derivative (Grubbs-IIIP) was synthesized according to a method reported by GRUBBS and coworkers[179]. In brief, Grubbs-II (0.40 g, 0.47 mmol) was dissolved in toluene (dry, 5 mL), and pyridine (3 mL, 0.037 mol) was added. The reaction was stirred for 10 min during which time a color change from red to bright green was observed. The reaction mixture was cannula transferred into 100 mL of cold (-10 °C) pentane, and a green solid precipitated. The precipitate was filtered, washed with 4 × 5 mL of pentane, and dried under vacuum to afford Grubbs-IIIP as a green powder (0.21 g, 70% yield).

^{1}H NMR (300 MHz, $CDCl_3$) δ 7.54 (s, 1H), 6.91 (s, 3H), 6.68 (d, *J* = 14.1 Hz, 3H), 4.94 (s, 2H), 3.69 (d, *J* = 6.8 Hz, 2H), 2.71 (s, 5H), 2.46 (s, 4H), 2.20 (s, 4H), 2.06 (d, *J* = 17.1 Hz, 2H), 1.94 (s, 2H), 1.36 (s, 29H).

Synthesis of N-(hydroxyl ethyl)-cis-5-norbornene-*exo*-2,3-dicarboximide

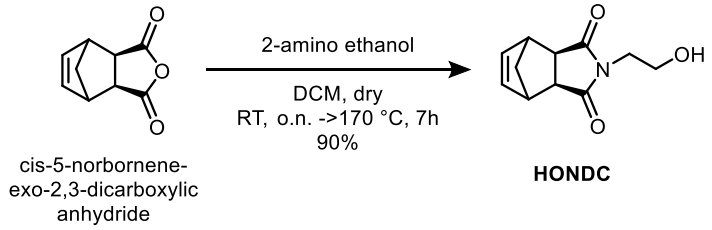

Scheme 5-4: One-pot synthesis of inimer molecule N-(hydroxyl ethyl)-cis-5-norbornene-*exo*-2,3-dicarboximide (HONDC) from cis-5-norbornene-*exo*-2,3-dicarboxylicanhydride.

N-(hydroxyl ethyl)-cis-5-norbornene-*exo*-2,3-dicarboximide (HONDC) was synthesized according to a method known in literature[186]. In brief, cis-5-norbornene-*exo*-2,3-dicarboxylicanhydride (4.00 g, 24.36 mmol) and 2-amino ethanol (1.42 mL, 24.36 mmol) was dissolved in 50 mL of DCM, and charged into a 100 mL round bottom flask with a stir bar. The reaction mixture was allowed to stir overnight at room temperature. After evaporating the solvent, the solid was reacted at 120°C for 7 hours. Then the reaction mixture was dissolved in DCM, and the insoluble impurities were removed by passing through a short neutral alumina column. After evaporating the solvent and being dried in vacuum, pure product (HONDC) was obtained as a white solid in 90% yield. The solid was dried azeotropically in high vacuum and stored in a glovebox.

Elemental Analysis Calculated for $C_{11}H_{13}NO_3$ C, 63.76; H, 6.32; N, 6.76; Found: C, 62.85; H, 6.41; N, 6.54.

^{1}H NMR (700 MHz, Tol) δ 5.77 (d, *J* = 2.0 Hz, 2H), 3.44 (q, *J* = 5.6 Hz, 2H), 3.35 (t, *J* = 5.3 Hz, 2H), 2.96 — 2.93 (m, 2H), 2.13 (dt, *J* = 4.6, 2.2 Hz, 2H), 1.59 (t, *J* = 5.9 Hz, 1H), 1.22 (d, *J* = 9.7 Hz, 1H), 1.17 — 1.13 (m, 1H).

^{13}C NMR (176 MHz, Tol) δ 177.43, 137.32, 60.11, 47.44, 45.08, 42.54, 40.97.

Synthesis of Latent Inimer-adduct

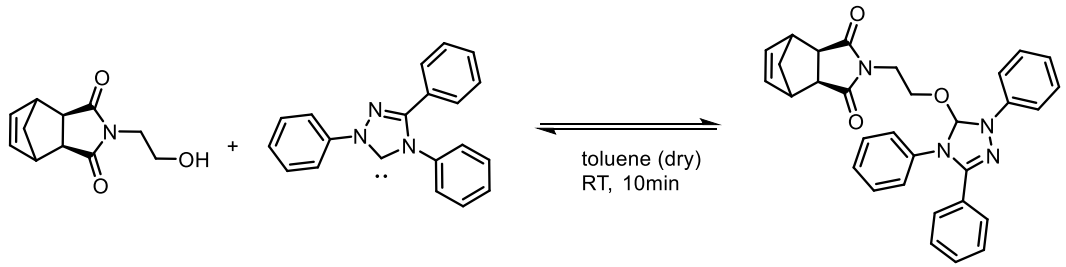

\{HONDC} DTT \{HONDCadduct}

active latent

Backbone monomer HONDC (50 mg, 0.24 mmol) was suspended together with DTT (73 mg, 0.24 mmol, 1 eq.) in toluene (1mL) in a vial equipped with a magnetic stir bar in a glove box and left to stir for 20 min. The pale yellow suspension turned into a bright yellow solution within this time to produce the latent catalyst HONDC-adduct. A sample of this solution was diluted with deuterated toluene-d_8 and submitted for characterization by NMR.

^{1}H NMR: 700 MHz, Tol) δ 7.69 — 7.64 (m, 1H), 7.51 — 7.47 (m, 1H), 6.85 (tt, *J* = 7.5, 1.1 Hz, 1H), 5.83 — 5.75 (m, 2H), 3.70 (dt, *J* = 10.2, 5.2 Hz, 1H), 3.62 — 3.57 (m, 0H), 3.52 (t, *J* = 5.3 Hz, 1H), 3.50 — 3.45 (m, 0H), 3.43 (t, *J* = 5.3 Hz, 1H), 3.35 (dd, *J* = 5.9, 4.8 Hz, 1H), 3.08 — 2.96 (m, 0H), 2.94 (p, *J* = 1.8 Hz, 1H), 2.06 (d, *J* = 1.6 Hz, 2H), 1.53 (s, 1H), 1.23 — 1.19 (m, 1H), 1.18 — 1.12 (m, 1H).

^{13}C NMR: (176 MHz, Tol) δ 177.23, 140.29, 137.30, 137.11, 129.06, 128.63, 128.50, 128.36, 127.90, 127.73, 127.59, 127.45, 125.06, 124.89, 124.75, 124.62, 122.68, 113.20, 60.00, 56.68, 47.43, 45.08, 45.03, 42.63, 42.41, 40.97, 38.05, 20.38, 20.27, 20.16, 20.05, 19.94, 19.83, 19.72.

Tandem Polymerization with SIMes Catalyst and Grubbs-II Initiator

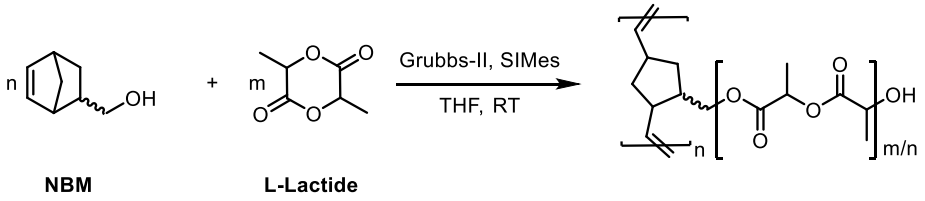

Scheme 5-5: Simultaneous tandem grafting of norbornene derivative NBM and L-lactide (LLA) catalyzed by SIMes and metathesis catalyst (either Grubbs-II or Grubbs-III).

Exemplified for tandem polymerization **27.** In a glovebox, SIMes (7.8 mg, 0.02 mmol, 1 eq.) and Norbornene methanol (2.5 mg, 0.02 mmol, 1 eq.) were weighed out into a vial equipped with stirring bar, septum and molecular sieves (to ward of adventitious water) and dissolved in THF (1mL). L-lactide (290 mg, 2 mmol, 100 eq.) and Grubbs-II (0.01M, 100 µL, 0.001 mmol, 0.005 eq.) were added into a separate sample vial, dissolved in THF (2.5 mL) and added into the sample vial containing catalyst and initiator to start polymerization. After 10 min, an excess of ethyl vinyl ether (200 µL) and TFA (200 µL, 0.1 M in THF) was added to terminate the metathesis polymerization. The vial was then removed from the glovebox and immediately precipitated in ice cold methanol after 10 minutes.

Table 5-1 Monomer equivalents and metathesis catalysts used for tandem polymerizations of NBM and LLA

Entry	Side chain targeted DP[a]	Backbone Targeted DP[b]	Metathesis Catalyst
5	100 eq LLA	100 eq NBM	Grubbs-II
6	100 eq LLA	50 eq NBM	Grubbs-II
7	100 eq LLA	20 eq NBM	Grubbs-II
9	20 eq LLA	100 eq NBM	Grubbs-II
10	20 eq LLA	100 eq NBM +50 eq NBE	Grubbs-II
11	20 eq LLA	100 eq NBM + 100 eq NBE	Grubbs-II
12	20 eq LLA	100 eq NBM + 200 eq NBE	Grubbs-II
19	50 eq LLA	100 eq NBM	Grubbs-IIIP
20	50 eq LLA	100 eq NBM	Grubbs-IIIP
21	20 eq LLA	100 eq NBM	Grubbs-III
22	45 eq LLA	100 eq NBM	Grubbs-III
23	50 eq LLA	20 eq *exo*-NBM	Grubbs-II
24	50 eq LLA	20 eq *exo*-NBM	Grubbs-II
25	80 eq LLA	10 eq *exo*-NBM	Grubbs-II
26	80 eq LLA	10 eq *exo*-NBM	Grubbs-II
27	100 eq LLA	200 eq *exo*-NBM	Grubbs-II
28	100 eq LLA	200 eq *exo*-NBM }	Grubbs-II
29	200 eq LLA	5 eq *exo*-NBM	Grubbs-II
30	200 eq LLA	5 eq *exo*-NBM	Grubbs-II

[a]with respect to backbone monomer. [b]with respect to metathesis catalyst

GPC (in THF, *vs* MMA standards) Mn 13 500 g.mol^{-1} Mw 17600 g.mol^{-1} PDI 1.30

^{1}H NMR: (300 MHz, $CDCl_3$) δ 5.09 (q, *J* = 7.1 Hz, 323H), 4.28 (d, *J* = 6.8 Hz, 1H), 2.23 (s, 1H), 1.50 (d, *J* = 7.1 Hz, 1279H).

Table 5-2: Reaction times, molecular weights (theoretical and experimental) of tandem polymerizations above.

Entry	Time	Mn_{theo} [a] (side chain) /g.mol^{-1}	Mn_{theo} [b] (brush) /g.mol^{-1}	Mn_{exp} [c] /g.mol^{-1}	PDI[c]
5	60 min	14 500	1 450 000	3 500	1.31
6	60 min	14 500	725 000	6 700	1.35
7	60 min	14 500	290 000	3 500	1.33
9	60 min	3 000	300 000	4 600	1.51
10	60 min	3 000	300 000	11 000	1.65
11	60 min	3 000	300 100	10 900	1.53
12	60 min	3 000	300 200	9 400	1.57
19	15 min	7 300	730 000	10 500	1.35
20	60 min	7 300	730 000	12 700	1.23
21	60 min	3 000	300 000	4 800	1.60
22	15 min	6 600	660 000	4 500	1.22
23	15 min	7 300	146 000	3 500	2.24
24	45 min	7 300	146 000	8 000	4.57
25	15 min	11 700	117 000	12 500	2.06
26	45 min	11 700	117 000	14 600	2.94
27	15 min	14 500	2 900 000	13 500	1.30
28	45 min	14 500	2 900 000	10 500	1.37
29	15 min	29 000	145 000	14 800	1.25
30	45 min	29 000	145 000	16 400	1.80

[a] theoretical molecular weight of side chains assuming 100% conversion of LLA monomer deriving exclusively from NBM initiated chains. [b] theoretical molecular weight assuming 100% conversion of NBM monomer and 100% conversion of LLA monomer. [c] determined *via* GPC against PSt standards.

ROMP with Grubbs-III Initiator

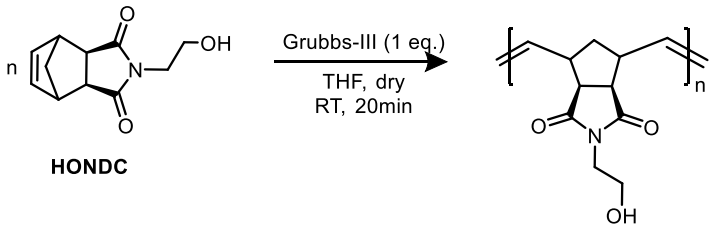

Exemplified for P(HONDC) homopolymer **31**. HONDC (100 mg, 48 mmol, 100 eq.) was dissolved in dry THF (3 mL) in a vial equipped with stir bar in a glovebox. Grubbs Third Generation catalyst (4 mg, 0.005 mmol, 1 eq.) was added to the vial in one batch and the green catalyst immediately turned orange upon dissolution. After 20 min stirring, the vial was taken out of the glovebox and the reaction was terminated with addition of ethylvinyl ether (0.2 mL). The solution was precipitated in ice-cold methanol, centrifuged and decanted. The polymer was dried under vacuum over night. The dry polymer **31** was isolated as a brittle off-white film (80 mg) and dissolved only in DMF with a few drops of HFIP, indicating strong hydrogen bonding interactions.

GPC (in DMF, *vs* PSt standards) Mn 15800 g.mol-1; Mw 18300 PDI 1.16

^{1}H NMR (700 MHz, DMF) δ 5.78 (t, *J* = 19.1 Hz, 1H), 5.56 (ddt, *J* = 19.6, 14.7, 8.1 Hz, 1H), 5.23 (hept, *J* = 6.4 Hz, 1H, HFIP), 4.85 — 4.74 (m, 1H), 3.65 — 3.58 (m, 2H), 3.52 (d, *J* = 12.9 Hz, 2H), 3.14 (dq, *J* = 21.2, 14.1, 10.4 Hz, 2H), , 2.80 — 2.71 (m, 2H), 2.08 (s, 1H), 1.60 — 1.51 (m, 1H).

ROP with NHC DTT

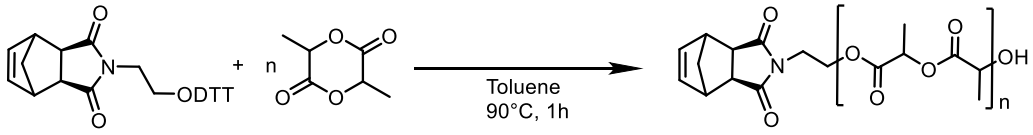

Exemplified for macromonomer **35**. Backbone monomer HONDC (50 mg, 0.24 mmol) was suspended together with DTT (73 mg, 0.24 mmol, 1 eq.) in toluene (1mL) in a vial equipped with a magnetic stir bar in a glove box and left to stir for 20 min. The pale yellow suspension turned into a bright yellow solution. L-lactide (700 mg, 4.8 mmol, 20 eq.) was placed in a dry SCHLENK tube equipped with a stir bar and suspended in dry Toluene (2 mL). The initiator solution was taken out of the glove box, added to the SCHLENK flask under Argon

atmosphere and lowered in an oil bath at 80 °C under positive Argon pressure. After 1 h, the reaction mixture, which had become viscous, was cooled to room temperature. A sample was drawn via an air tight syringe, diluted with DMF and submitted to GPC in DMF versus polystyrene standard. Another sample was drawn for ^{1}H NMR analysis, the solvent evaporated and redissolved in $CDCl_3$. The remaining reaction mixture was precipitated into ice cold methanol (100 mL), filtered and dried, then dissolved in a minimal amount of THF and re-precipitated into ice cold methanol. The polymer was filtered and dried under high vacuum to afford a white product (650 mg).

GPC (in THF, *vs* PSt standards) Mn 7500 g.mol^{-1}, Mw 9800 g.mol^{-1}, PDI 1.30.

^{1}H NMR (300 MHz, $CDCl_3$) δ 6.22 (d, *J* = 2.3 Hz, 2H), 5.09 (q, *J* = 7.2 Hz, 48H), 4.25 (m, 2H), 3.70 (m, 2H), 3.20 (s, 2H), 2.65 (d, *J* = 9.5 Hz, 3H), 1.81 — 1.11 (m, 151H).

Table 5-3: Monomer equivalents, conversions and molecular weights of PLLA by ROP

Entry	$[LLA]_0$/ $[HONDC]_0$	Conv.	Mn $_{theo}$ /g.mol^{-1}	Mn $_{exp}$ ^{1}H NMR /g.mol^{-1}	[a]Mn $_{exp}$ GPC /g.mol^{-1}	[a]PDI
34	5	98%	900	900	1300	1.20
36	10	99%	1600	1800	2200	1.21
37	20	97%	3100	3400	3800	1.23
35	30	98%	4500	4400	7500	1.30

[a]Determined *via* GPC using PSt as standards and THF as eluent.

One-pot-two-step Polymerization with DTT and Grubbs-III

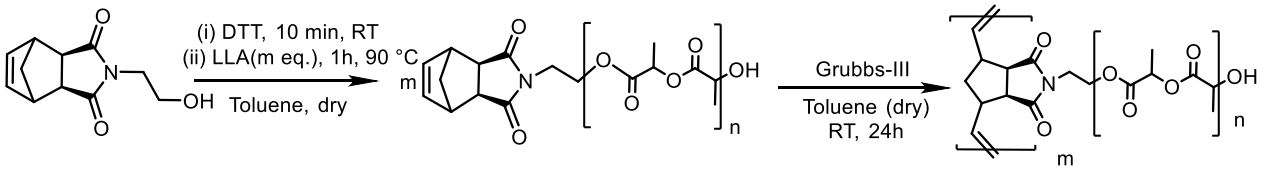

Exemplified for bottle brush **42**. HONDC (50 mg, 0.24 mmol) was suspended together with the triazol NHC (73 mg, 0.24 mmol, 1 eq.) in Toluene (5 mL) in a vial equipped with a magnetic stir bar in a glove box and left to stir for 20 min. The pale yellow suspension turned into a bright yellow solution. L-lactide (0.34 g, 2.4 mmol, 10 eq.) was placed in a dry SCHLENK

tube equipped with a stir bar and suspended in dry toluene (2 mL). The initiator solution was taken out of the glove box, added to the SCHLENK flask under Argon atmosphere and lowered in an oil bath at 80 °C under positive Argon pressure. After 1 h, the reaction mixture, which had become viscous, was cooled to room temperature. A sample was drawn via an air tight syringe, diluted with DMF and submitted to GPC in DMF versus polystyrene standard. Another sample was drawn for ^{1}H NMR analysis, the solvent evaporated and re-dissolved in $CDCl_3$. A sample (1 mL, 0.048 mmol MM) was removed and added to a SCHLENK flask containing a stir bar and G III stock solution in dry toluene (0.01 M, 0.1 mL, 0.02 eq) and left to stir under Argon for 24h. A sample was drawn via an air tight syringe, diluted with DMF and submitted to GPC in DMF versus polystyrene standard. Another sample was drawn for ^{1}H NMR analysis, mixed with ethyl vinyl ether (0.1 mL) to quench the ROMP, the solvent evaporated and redissolved in $CDCl_3$. The remaining reaction mixture was precipitated into ice cold methanol (100 mL), filtered and dried, then dissolved in a minimal amount of THF and re-precipitated into ice cold methanol. The polymer was filtered and dried under high vacuum to afford a white product.

GPC (in DMF, *vs* PSt standards) Mn 116000 g.mol$^-$ g.mol^{-1}; Mw 147300 g.mol^{-1}; PDI 1.27

^{1}H NMR (300 MHz, $CDCl_3$) δ 5.71 (d, *J* = 18.5 Hz, 1H), 5.44 (s, 1H), 5.09 (q, *J* = 7.2 Hz, 22H), 4.41 — 4.00 (m, 3H), 3.67 - 3.08 (m, 4H), 2.67 (s, 2H), 1.50 (t, *J* = 7.2 Hz, 68H), 0.81 (s, 1H).

Table 5-4. Stepwise bottlebrush synthesis (grafting through approach)

Entry	MM /g.mol^{-1}	Eq. MM	$M_{n\ theo}$ /g.mol^{-1}	Conversion [a] /%	$M_{n\ exp}$[a] ^{1}H NMR /g.mol^{-1}	$M_{n\ exp}$ [b] GPC /g.mol^{-1}	PDI [b]
38	1 300	25	32 500	100%	22 800	28 200	1.20
39	1 300	50	65 000	100%	45 700	50 900	1.28
40	1 300	100	130 000	99%	90 400	95 900	1.26
41	2 200	25	55 000	100%	40 900	43 500	1.24
42	2 200	50	110 000	100%	81 700	64 500	1.31
43	2 200	100	220 000	100%	163 400	116 700	1.27
44	3 400	25	85 000	100%	75 100	56 000[c]	1.21 [c]
45	3 400	50	170 000	100%	150 200	103 100 [c]	1.23 [c]
46	3 400	100	340 000	98%	294 300	162 900 [c]	1.27 [c]

Conducted in toluene at RT for 24h at an initial concentration of 0.04 M. [a]Determined by ^{1}H NMR [b]Determined *via* GPC using PSt standards and DMF as eluent. [c]small amount of late-eluting polymer population.

Tandem ROMP-ROP with DTT and Grubbs-III

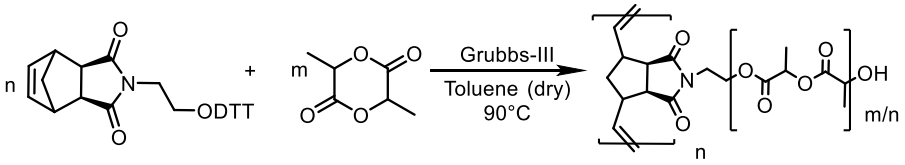

Exemplified for tandem BB **63**, see Table 5-5 for all polymerizations. HONDC (50mg, 0.24 mmol) and triazol (72 mg, 0.24 mmol, 1 eq.) were suspended in dry toluene (1mL) in a vial in a glovebox and left to stir for 20 min. The beige suspension turned into a bright yellow solution. L-lactide (360 mg, 2.4 mmol, 10 eq.) was placed in a in SCHLENK tube and Grubbs-III stock solution (600 µL, 0.01 M in toluene, 0.025 eq.), as well as dry toluene (1.7 mL) were added. The two monomer/initiator solutions were combined in the SCHLENK tube and sealed, taken out of the glovebox and attached to a SCHLENK line. Under slight positive Argon pressure, the SCHLENK tube was lowered into an oilbath set to 80 °C. After 2 h, the reaction was quenched with the addition of one drop of trifluoro acetic acid and 0.2 mL of ethyl vinyl ether. After 10min of stirring, the reaction solution was exposed to air and a sample was drawn, diluted with THF and submitted to GPC in THF versus polystyrene standard. The remaining reaction mixture was precipitated into ice cold methanol (100 mL) and filtered to produce a sticky brown product. The polymer was dried under high vacuum, dissolved in 0.5mL of THF and precipitated again into ice cold methanol to afford the off-white, flakey product **63**. (320 mg).

GPC (in DMF, vs PSt standards) Mn 62300 g.mol-1; Mw 66700 g.mol-1; PDI 1.07

1H NMR (700 MHz, Tol) δ 5.87 (s, 1H), 5.59 (s, 1H), 5.43 — 4.81 (m, 23H), 4.33 (s, 3H), 3.95 — 3.21 (m, 4H), 2.90 (s, 3H), 1.78 — 1.09 (m, 76 H), 0.75 (s, 1H).

Table 5-5. Tandem polymerizations of bottlebrushes with various chain lengths.

Polymerization	Equivalents		time /min	Conversion [a] /%	
	$[LLA]_0$/ $[HONDC]_0$	$[HONDC]_0$/ $[Grubbs\text{-}III]_0$		LLA	HONDC
47	5	25	60 min	95%	100%
48	9	25	60 min	94%	100%
49	5	50	20 min	99%	95%
50	10	40	60 min	94%	97%
51	10	50	60 min	99%	96%
52	20	40	60 min	95%	99%
54	5	25	30 min	100%	100%
55	5	25	60 min	95%	100%
56	5	25	3 h	95%	100%
57	5	25	20 h	100%	100%
58	9	25	30 min	94%	100%
59	9	25	60 min	94%	100%
60	9	25	3 h	94%	100%
61	9	25	20 h	100%	100%
62	10	40	60 min	94%	97%
63	10	40	120 min	95%	98%
64	10	40	39 h	96%	99%
65	20	40	60 min	95%	99%
66	20	40	120 min	96%	98%
67	20	40	17 h	97%	98%
68	20	40	23 h	96%	98%
69	5	100	30 min	94%	70%
70	5	100	60 min	94%	70%
71	5	100	3 h	90%	68%
72	11	100	30 min	82%	63%
73	11	100	60 min	100%	63%
74	11	100	20 h	100%	63%
75	11	100	70 h	98%	59%
76	5	200	30 min	95%	38%
77	5	200	60 min	93%	40%
78	10	200	20 min	98%	42%
79	10	200	60 min	98%	41%
80	10	200	16 h	97%	41%
81	10	200	24 h	97%	38%
82	20	200	20 min	98%	41%
83	20	200	60 min	98%	45%
84	20	200	16 h	98%	45%
85	20	200	24 h	96%	36%

Conducted in toluene at 90°C for $[HONDC]_0$ 0.04 M. [a] Determined by ^1H NMR

Table 5-6: Theoretical and experimental number average molecular weights of bottlebrushes.

Polymerization	M_n /g.mol^{-1}				PDI[a]
	Side chains theo	BB theo	^{1}H NMR exp	GPC[a] exp	
47	900	22 500	22 300	24 200	1.12
48	1 500	37 500	35 700	34 600	1.15
49	900	45 000	43 700	38 700	1.15
50	1 600	64 000	60 600	59 900	1.07
51	1 600	80 000	78 400	73 600	1.15
52	3 100	124 000	116 600	85 300	1.08
54	900	23 200	23 200	23 100	1.12
55	900	23 200	22 300	24 200	1.12
56	900	23 200	22 300	23 000	1.15
57	900	23 200	23 200	24 700	1.18
58	1 500	37 600	35 700	32 100	1.14
59	1 500	37 600	35 700	34 600	1.15
60	1 500	37 600	35 700	34 800	1.15
61	1 500	37 600	37 600	35 800	1.18
62	1 600	63 200	60 600	59 900	1.07
63	1 600	63 200	61 800	62 300	1.07
64	1 600	63 200	63 000	54 100	1.11
65	3 100	117 000	116 600	85 300	1.08
66	3 100	117 000	116 600	89 100	1.09
67	3 100	117 000	117 700	74 700	1.16
68	3 100	117 000	116 600	75 700	1.17
69	900	92 800	61 900	56 300*	1.33*
70	900	92 800	61 900	58 400*	1.32*
71	900	92 800	58 200	55 900*	1.35*
72	1 800	179 300	95 000	89 200*	1.38*
73	1 800	179 300	112 900	95 400*	1.42*
74	1 800	179 300	112 900	91 200*	1.41*
75	1 800	179 300	103 900	93 600*	1.40*
76	900	185 600	67 800	84 900*	1.16*
77	900	185 600	70 200	86 500*	1.18*
78	1 600	329 700	136 100	85 200*	1.20*
79	1 600	329 700	132 800	102 700*	1.19*
80	1 600	329 700	131 600	95 900*	1.23*
81	1 600	329 700	122 000	94 100*	1.23*
82	3 100	618 000	248 600	101 300*	1.15*
83	3 100	618 000	272 900	127 500*	1.19*
84	3 100	618 000	272 900	133 600*	1.20*
85	3 100	618 000	214 200	131 200*	1.20*

[a] Determined by GPC using PS as standards and DMF as eluent.

Backbone depolymerization of molecular bottlebrushes

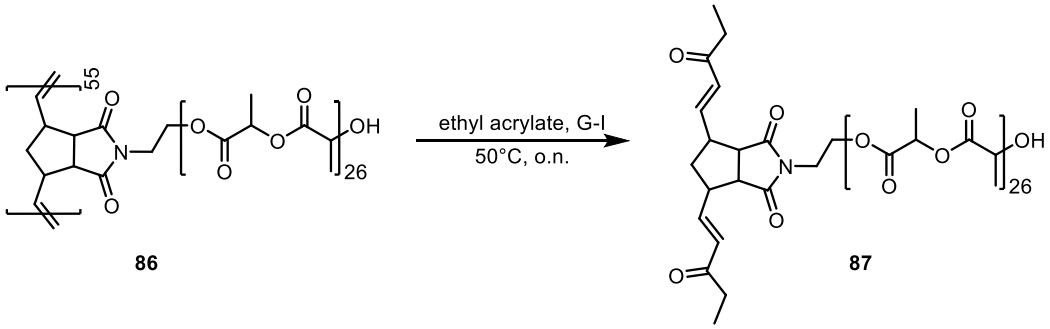

86 **87**

Insertion metathesis depolymerization of molecular bottlebrush **86** was conducted according to a protocol reported by WAGENER et al.[199] In brief, a flame-dried SCHLENK tube was charged with polymer **86** (500 mg, 0.167 mmol of side chain units), copper (I) iodide (0.1 mg, 0.01 eq.) and Grubbs-I (1.4 mg, 0.01 eq.) under argon atmosphere. Ethyl acrylate (180 µL, 2.1 eq. relative to the side chain unit of the polymer) was then injected and the reaction mixture was degassed by three freeze-pump-thaw cycles. Following the final degassing cycle, the reaction was heated to 50 °C with an oil bath. After 16 h, the metathesis catalyst was quenched by addition of excess ethyl vinyl ether (200 µL), the reaction was exposed to air and the extent of depolymerization was determined by NMR. The reaction mixture was diluted with THF (1 mL) and passed through a syringe driven Teflon filter (0.45 µm) to remove solid copper catalyst. A sample of the crude depolymerized bottlebrush **87** solution was submitted to GPC and MALDI-ToF.

GPC (in DMF, *vs* PSt standards) Mn 6000 g.mol^{-1} Mw 6900 g.mol^{-1} PDI 1.15

^{1}H NMR: (^{1}H NMR (300 MHz, $CDCl_3$) δ 6.33 (dd, *J* = 17.3, 1.6 Hz, 61H), 6.05 (dd, *J* = 17.3, 10.4 Hz, 60H), 5.75 (dd, *J* = 10.4, 1.6 Hz, 65H), 5.10 (p, *J* = 5.7 Hz, 76H), 4.15 (q, *J* = 7.1 Hz, 117H), 3.68 (s, 1H), 2.65 (s, 2H), 1.51 (d, *J* = 7.2 Hz, 208H), 1.24 (t, *J* = 7.1 Hz, 181H).

Table 5-7: Molecular weights of molecular bottlebrush **86** and after depolymerization (**87**)

Entry	$DP_{side\ chain}$	$DP_{backbone}$	Mn_{theo}	Mn_{exp}	PDI[c]
86	26	55	220 000	224 000	1.42
87	26	1	4 000	6 000	1.15

5.4.2 Simultaneous Surface Grafting

Esterification of undecenoic acid with tris(hydroxymethyl) ethane

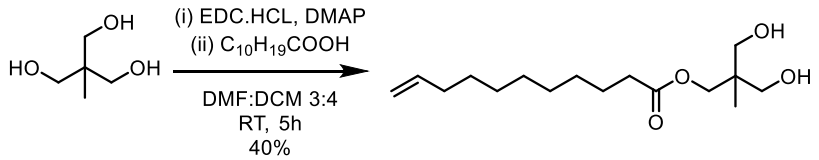

89 **90**

Tris(hydroxymethyl) ethane (**89**, 10 g, 83 mmol), undecenoic acid (3.8 g, 20 mmol), DMAP (3 g, 25 mmol) and EDC HCl (7.9 g, 25 mmol) were dissolved in a mixed solvent of DMF/DCM (30 mL/40 mL) under SCHLENK conditions. The reaction mixture was stirred for 5 h under Argon. Then, the reaction mixture was rigorously washed with 2N HCl (50 mL). The aqueous phase was extracted 3 times with DCM (3x30 mL). The organic layers were combined, washed with brine and dried over $NaSO_4$. The dried organic layers were filtered and the DCM was removed with reduced pressure. The crude product was purified via column chromatography (Silica gel, EtOAc: cy-H 1:3, R_f 0.25) to afford compound **90** as a light yellow oil (2.29 g, yield 40%).

ESI-MS: needed 286.41, found 287.5 $[M+H]^+$

^{1}H NMR (700 MHz, DMSO) δ 5.79 (ddt, *J* = 16.9, 10.2, 6.7 Hz, 1H), 4.99 (dq, *J* = 17.0, 1.7 Hz, 1H), 4.93 (ddt, *J* = 10.0, 2.5, 1.2 Hz, 1H), 4.45 (t, *J* = 5.4 Hz, 2H), 3.86 (s, 2H), 3.33 (s, 2H), 3.24 (h, *J* = 5.4 Hz, 4H), 2.27 (t, *J* = 7.4 Hz, 2H), 2.03 — 1.97 (m, 2H), 1.51 (p, *J* = 7.3 Hz, 2H), 1.33 (t, *J* = 7.2 Hz, 2H), 1.25 (s, 7H), 0.77 (s, 3H).

^{13}C NMR (176 MHz, DMSO) δ 172.94, 138.85 114.62, 65.86, 63.44, 40.54, 33.59, 33.14, 28.64 (d, *J* = 9.6 Hz), 28.21, 24.47, 16.45

FTIR: ν max/cm^{-1} 3479 (br.medium, alcohol), 3076, (weak) ,2924 s, med. Alkane CH) , 2853 (s, med.alkane CH stretching), 1724 (s, strong, ester carbonyl stretch), 1638, 1621 (s, w, terminal olefin CH stretching), 1467 (s, med.alkane stretching), 1382, 1158 (s, strong, ester stretching), 1052 (alcohol stretching), 1016, 992 (monosubstituted alkene bending), 909 (monosubstituted alkene bending), 723

Introduction of haloester to product 90

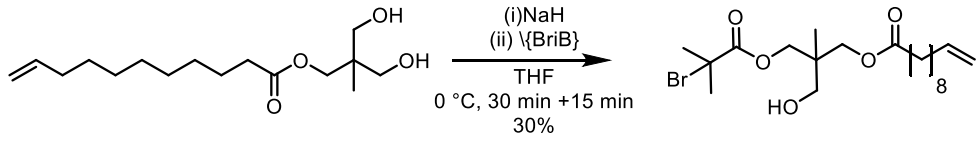

90 **92**

To a dry SCHLENK flask (500 mL) equipped with a large stir bar was added 0.44 g of NaH (11 mmol, 0.9 eq., 60% in paraffin oil) under argon atmosphere. The paraffin oil was removed from the NaH suspension by suspending in dry heptane (20 mL). The suspension was allowed to precipitate and by tilting the SCHLENK flask, the supernatant heptane was removed via air tight syringe and deposed off in a beaker containing 200 mL isopropanol. This procedure was repeated three times. In a second dry 250 mL SCHLENK flask, ester **90** (3.5 g, 12.2 mmol) was dissolved in dry THF (50 mL) and slowly transferred into the NaH-containing SCHLENK flask, cooled by an ice bath. The hydrogen gas was washed out through the argon inlet. After the addition was complete, a solution of bromo iso butyryl bromide (1.4 mL in 50 mL THF, 11 mmol) was added very slowly, still cooled by an ice bath. The reaction mixture was allowed to stir for 20 minutes and was then quenched slowly (cooled by an ice bath) by very slow addition of saturated NH4Cl (wait between each drop until fuzzing subsides) until no more effervescence was observed. The reaction mixture was then exposed to air and the precipitated salts were filtered off through a Büchner funnel equipped with filter paper. The THF was removed by help of a rotary evaporator and a crude NMR was recorded. Flash column chromatography (silica gel, Ethyl Acetate: cy-Hexane, 1:10, R_f 0.32) yielded product **92** as a clear oil (1.43 g, yield 30%)

ESI-MS: 434.17 needed. Found: 435.2 $[M+H]^+$

^{1}H NMR (700 MHz, DMSO) δ 5.79 (ddt, *J* = 18.2, 9.6, 6.6 Hz, 1H), 4.99 (d, *J* = 17.2 Hz, 1H), 4.93 (d, *J* = 10.2 Hz, 1H), 4.79 (s, 1H), 4.00 (s, 2H), 3.92 (p, *J* = 11.3 Hz, 3H), 3.33 (d, *J* = 8.3 Hz, 5H), 2.32 — 2.26 (m, 3H), 2.01 (q, *J* = 7.2 Hz, 3H), 1.91 — 1.88 (m, 7H), 1.51 (q, *J* = 7.0 Hz, 3H), 1.33 (q, *J* = 7.2 Hz, 3H), 1.25 (s, 11H), 0.91 (s, 3H).

^{13}C NMR (176 MHz, DMSO) δ 172.72, 170.51, 138.78, 114.59, 67.13, 65.28, 63.00, 57.30, 39.94, 33.12, 28.37, 28.19, 16.51.

FTIR: ν max/cm^{-1} 3518 (br.medium, alcohol), 2976 (alkane CH) ,2927(s, med. Alkane CH) , 2855 (s, med.alkane CH stretching), 1731(s, strong, ester carbonyl stretch), 1640 (s, w,

terminal olefin CH stretching), 1463 (s, med.alkane stretching), 1388 and 1371 (s, med. Geminal dimethyl bending), 1272, (s, medium ester stretching), 1158 (s, strong, ester stretching), 1108 (s, med.), 1055 (alcohol stretching), 1011, 992 (monosubstituted alkene bending), 908 (monosubstituted alkene bending), 759, 722,

Hydrosilylation of ester 92

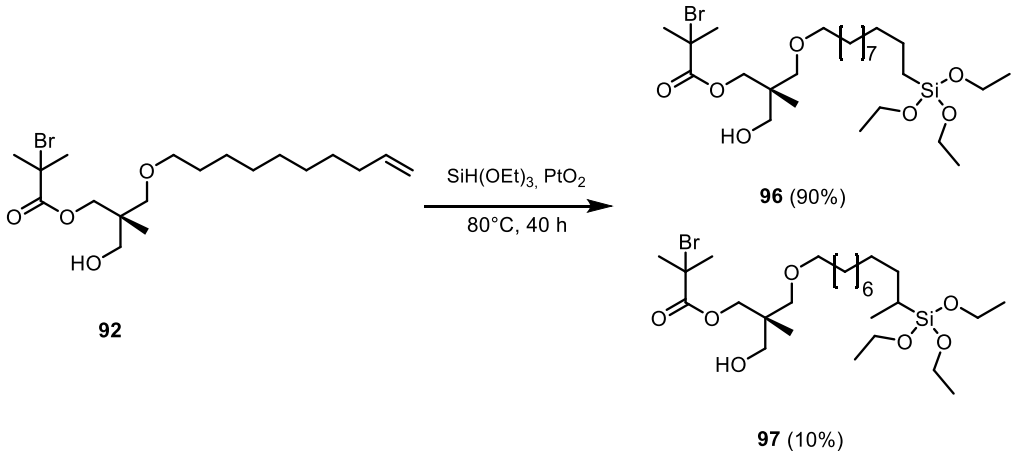

Haloester **92** (1.00 g, 2.46 mmol) and triethoxysilane (0.68 mL, 3.68 mmol) were added to a dry SCHLENK flask under argon. PtO_2 (2.8 mg, 0.0012 mmol) were added in one portion under a stream of argon and the mixture was heated to 80 °C with stirring. After 12 h, the flask was cooled to room temperature and 10 mL hexane was added. The solution was filtered through a plug of activated charcoal over a teflon filter paper to afford pure product **96** as a clear oil (1.47 g, quant.)

ESI-MS: needed: 598.25, found 553.3 [M-C_2H_5O]

^{1}H NMR: ^{1}H NMR (700 MHz, CD_2Cl_2) δ 4.15 — 4.09 (m, 2H), 4.05 — 3.98 (m, 2H), 3.90 — 3.79 (m, 8H), 3.73 (s, 1H), 3.69 (q, *J* = 6.8 Hz, 1H), 2.39 — 2.31 (m, 3H), 1.97 (d, *J* = 4.5 Hz, 6H), 1.68 — 1.60 (m, 3H), 1.32 (d, *J* = 15.0 Hz, 18H), 1.24 (dt, *J* = 10.9, 6.9 Hz, 14H), 1.05 (s, 2H), 0.92 (t, *J* = 7.0 Hz, 2H), 0.69 — 0.57 (m, 1H).

^{13}C NMR (176 MHz, CD_2Cl_2) δ 67.20, 65.28 (d, *J* = 41.5 Hz), 59.22, 34.13, 30.64, 29.27, 24.94, 17.85.

FTIR: ν max/cm^{-1} 3499 (br.medium, alcohol), 2971 (alkane CH) ,2928(s, med. Alkane CH) , 2854 (s, med., alkane CH stretching), 1739(s, strong, ester carbonyl stretch), , 1465 (s, med., alkane stretching), 1388 and 1368 (s, med., geminal dimethyl bending), 1269, (s, medium ester stretching), 1161 (s, strong, ester stretching), 1101 (s, strong) 1076 (alcohol stretching), 1013, 963, 855, 792

ATRP of NIPAM with DBU as ligand

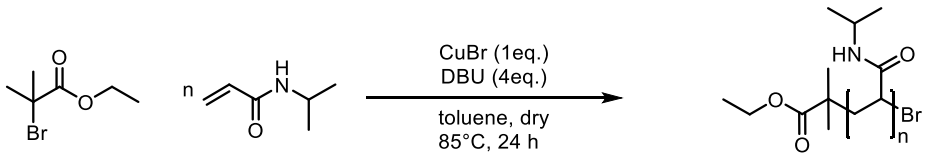

NIPAM monomer was dried azeotropically with toluene and stored in a glovebox. DBU and CuBr were purchased from Sigma Aldrich and stored in a glove box. In a glove box, NIPAM (788 mg, 7 mmol, 100 eq.) and ethyl α-bromoisobutyrate (14 mg, 0.07 mmol, 1 eq.), dry toluene (3 mL) and a stir bar were placed in a SCHLENK tube and sealed. The SCHLENK tube was taken out of the glovebox, attached to SCHLENK line and immersed in an oil bath set to 85 °C. After five minutes, the catalyst stock solution (700 µL, CuBr 0.1M, DBU 0.4 M in toluene) was added to the SCHLENK flask via syringe. The very pale green solution turned slightly brown over the span of one day and the solution remained homogeneous. A sample was drawn for recording a ^{1}H NMR spectrum. ^{1}H NMR showed that only negligible amounts of unreacted NIPAM remained in the reaction mixture. The reaction mixture was then purified by passing through a short alumina column and precipitated into ice cold methanol to yield the white powdery polymer **100** (yield 600 mg).

GPC (in THF, *vs* PSt standards) Mn 2400 g.mol^{-1} Mw 8000 g.mol^{-1} 3.33

^{1}H NMR ^{1}H NMR (300 MHz, $CDCl_3$) δ 6.72 — 5.67 (m, 5H), 5.54 (d, *J* = 10.2 Hz, 2H), 3.96 (s, 117H), 3.67 (d, *J* = 6.3 Hz, 96H), 3.47 (s, 31H), 1.39 — 1.04 (m, 751H).

ROP of L-lactide with DBU

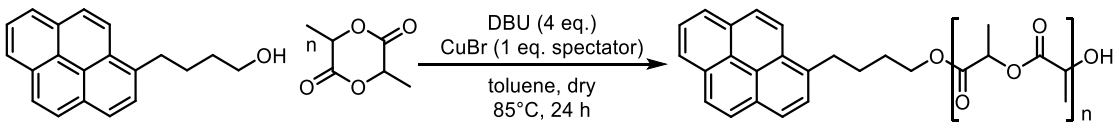

In a glovebox, L-lactide (500 mg, 3.5 mmol, 100 eq.) and pyrene butanol (10 mg, 0.035 mmol, 1 eq.), dry toluene (3 mL) and a stir bar were placed in a SCHLENK tube and sealed. The SCHLENK tube was taken out of the glovebox, attached to SCHLENK line and immersed in an oil bath set to 85 °C. After five minutes, the catalyst stock solution (700 µL, CuBr 0.1M, DBU 0.4M in toluene) was added to the SCHLENK flask via syringe. The very pale green solution turned slightly brown over the span of one day and the solution remained homogeneous. A sample was drawn for recording a ^{1}H NMR spectrum. The reaction mixture was purified by precipitation into ice cold methanol to yield the white flakey polymer **101** (yield 450 mg)

GPC (in THF *vs* PSt standards) Mn 4500, Mw 12600 PDI 2.81

^{1}H NMR ^{1}H NMR (300 MHz, $CDCl_3$) δ 8.26 — 7.70 (m, 9H), 5.22 — 5.07 (m, 194H), 1.49 (q, J = 6.5 Hz, 615H).

Tandem polymerization of NIPAM and LLA with DBU as ligand and catalyst

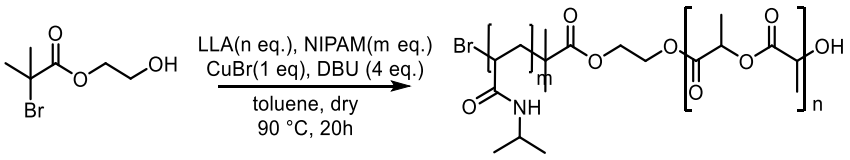

Exemplified for polymer **103**. For all solvents and monomer equivalents, see summary Table 5-8) In a glovebox, CuBr (1 eq.) and DBU (4 eq.) were combined in dry toluene to make a 0.1M stock solution (with respect to CuBr). The stock solution was stored over molecular sieves to ward off adventitious water and stored in a glovebox in darkness. NIPAM (135 mg, 1.0 mmol, 50 eq.), LLA (200 mg, 1.0 mmol, 50 eq.), initiator HBIB(200 µL of 0.1 M in toluene, 0.02 mmol, 1 eq) and toluene (3 mL) were combined in a SCHLENK flask equipped with a stir bar. The SCHLENK flask was sealed, taken out of the glovebox and degassed via three freeze-pump-thaw cycles. The reaction mixture was then frozen again and the catalyst stock solution (200 µL of 0.1 M in toluene, 0.02 mmol, 1 eq.) was added onto the frozen solution and submitted to another cycle of vacuum pumping. The monomer solution turned green upon addition of the catalyst. The SCHLENK tube was then lowered into an oil bath set at the required reaction temperature. After the prescribed time intervals, samples were drawn via degassed syringe and a portion was set aside for ^{1}H NMR analysis. The remaining portion was diluted with THF and filtered through a syringe equipped with a 0.45 µm Teflon filter

and containing a plug of neutral alumina gel to be submitted to GPC. After the determined reaction time, the reaction vessel was submerged into a liquid nitrogen bath. The solution was then diluted with THF, filtered through a pad of alumina gel, precipitated into ice cold methanol, and dried over a sintered glass filter and under reduced pressure to yield of a white powdery polymer (240 mg).

GPC (in THF *vs* PSt standards) Mn 16800 g.mol^{-1}; Mw 62400 g.mol^{-1}; PDI 3.71

^{1}H NMR: ^{1}H NMR (300 MHz, $CDCl_3$) δ 6.20 (d, *J* = 17.0 Hz, 2H), 6.02 — 5.84 (m, 1H), 5.55 (d, *J* = 10.1 Hz, 2H), 5.09 (q, *J* = 7.1 Hz, 120H), 3.69 (d, *J* = 6.2 Hz, 22H), 1.79 (q, *J* = 4.1 Hz, 21H), 1.51 (d, *J* = 7.1 Hz, 346H), 1.21 — 1.08 (m, 21H).

Table 5-8: Overview of reaction conditions for polymerizations **102-108**

Entry	Monomer 1	Monomer 2	Ligand	Solvent	Temp.
102[a]	100 eq LLA	100 eq NIPAM	DBU 3 eq	toluene	85 °C
103	100 eq LLA	100 eq NIPAM	DBU 3 eq	toluene	85 °C
104	100 eq LLA	100 eq NIPAM	DBU 3 eq	toluene	90 °C
105	50 eq LLA	50 eq NIPAM	DBU 3 eq	toluene	75 °C
106	100 eq LLA	100 eq NIPAM	DBU 3 eq	MeCN	75 °C
107	100 eq LLA	100 eq NIPAM	PMDETA 1 eq	toluene	90 °C
108	100 eq LLA	100 eq NIPAM	DBU 3 eq	DMF	90 °C

[a]ATRP inititiator: **EBIB** and ROP initiator pyrenebutanol, 1 eq. each

Table 5-9: Overview over molecular weights and conversions for polymerizations above

Entry	Time	Conversion[a] Monomer 1	Conversion[a] Monomer 2	Mn theo /g.mol^{-1}	Mn exp[b] /g.mol^{-1}	Mw exp[b] /g.mol^{-1}	PDI[b]
102[b]	20 h	100%	71%	15000, 6000	5300	16400	3.11
103	24 h	99%	44%	27 000	6700	20000	2.98
104	18 h	97%	77%	27 000	4900	17200	3.50
105	20 h	99%	14%	13 500	16800	62400	3.71
106	24 h	86%	58%	27 000	10300	14200	1.37
107	23 h	100%	31%	27 000	9900	26700	2.70
108	20 h	75%	16%	27 000	4300	15700	3.65

ATRP-ROP Tandem Polymerization with DBU as catalyst and PMDETA as ligand

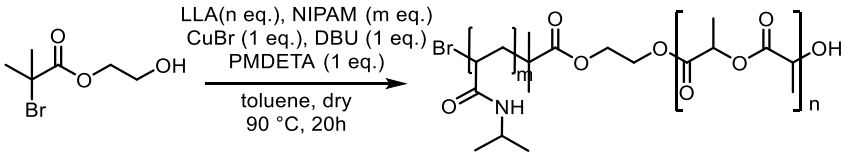

Exemplified for polymer **107**. In a glovebox, CuBr (1 eq.) and PMDETA (1 eq.) were combined in dry solvent to form the catalyst complex as 0.1M stock solution in toluene. The stock solution was stored over molecular sieves to ward off adventitious water and stored in a glovebox in darkness. Monomers LLA (500 mg, 3.5 mmol,100 eq.) and MMA (400 mg, 3.5 mmol,100 eq.), sacrificial linker (350 µL, 0.1 M in toluene, 1 eq.), DBU (350 µL, 0.1M in toluene, 1 eq.) and toluene (dry, 7 mL) were combined in a SCHLENK flask equipped with a stir bar. The SCHLENK flask was sealed, taken out of the glovebox and degassed via three freeze-pump-thaw cycles. The reaction mixture was then frozen again and the catalyst stock solution (350 µL, 0.1M, 1 eq.) was added onto the frozen solution and submitted to another cycle of vacuum pumping. The monomer solution turned green upon addition of the catalyst. The SCHLENK tube was then lowered into an oil bath set at the required reaction temperature. After the prescribed time intervals, samples were drawn via degassed syringe and a portion was set aside for ^{1}H NMR analysis. The remaining portion was diluted with THF and filtered through a syringe equipped with a 0.45 µm Teflon filter and containing a plug of neutral alumina gel to be submitted to GPC. After the determined reaction time, the reaction vessel was submerged into a liquid nitrogen bath. The solution was then diluted with THF, filtered through a pad of alumina gel, precipitated into ice cold methanol, and dried over a sintered glass filter and under reduced pressure to yield the powdery, off-white polymer **107** (yield 700 mg).

GPC (in THF *vs* PSt standards) Mn 9900 g.mol^{-1}, Mw 26700 g.mol^{-1}, PDI 2.70

^{1}H NMR (300 MHz, $CDCl_3$) δ 6.52 (d, *J* = 16.8 Hz, 23H), 6.25 (dd, *J* = 17.0, 10.2 Hz, 22H), 5.90 (s, 25H), 5.79 (d, *J* = 10.1 Hz, 21H), 5.42 (p, *J* = 7.2 Hz, 59H), 4.41 (h, *J* = 6.7 Hz, 22H), 3.68 — 3.35 (m, 5H), 3.13 (s, 2H), 1.86 — 1.74 (m, 177H), 1.39 (d, *J* = 6.6 Hz, 137H).

ATRP-ROP with DBU as catalyst and ligand at RT with UV irradiation

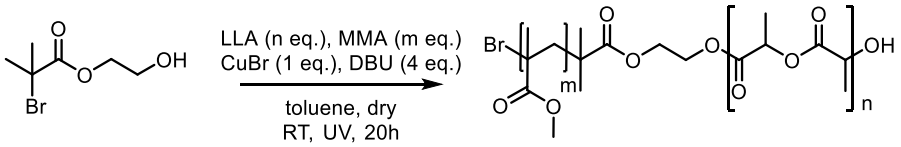

Polymerizations with UV-irradiations were conducted according to a procedure reported by WANG et al.[284], exemplified for polymer **110**. For all solvents and monomer equivalents, see Table 5-10. LLA (300 mg, 2.0 mmol, 100 eq.), MMA (200 mg, 2.0 mmol, 100 eq.) sacrificial linker (200 µL, 0.1M in toluene, 0.02 mmol, 1 eq.) and toluene (3 mL) were combined in a SCHLENK flask equipped with a stir bar. The SCHLENK flask was sealed, taken out of the glovebox and degassed via three freeze-pump-thaw cycles. The reaction mixture was then frozen again and the catalyst stock solution of (200 µL, 0.1M w.r.t. CuBr in toluene, 0.02 mmol, 1 eq.) was added onto the frozen solution and submitted to another cycle of vacuum pumping. The monomer solution turned pale green upon addition of the catalyst. The SCHLENK tube was placed inside the UV reaction chamber equipped with a stirring plate and a window for a UV lamp (365 nm, 6 W). The reaction mixture turned highly viscous within 3 h and within 8 h, the lower portion of the reaction mixture had solidified. After the prescribed time intervals, samples were drawn via degassed syringe and a portion was set aside for ^{1}H NMR analysis. The remaining portion was diluted with THF and filtered through a syringe equipped with a 0.45 µm teflon filter and containing a plug of neutral alumina gel for GPC. After the determined reaction time, the reaction vessel was submerged into a liquid nitrogen bath. The solution was then diluted with THF, filtered through a pad of alumina gel, precipitated into ice cold methanol, and dried over a sintered glass filter and under reduced pressure to yield a sticky polymer (350 mg)

GPC (in THF, *vs* MMA standards) Mn 9900 g.mol^{-1} Mw 16800 g.mol^{-1} PDI 1.69

^{1}H NMR (300 MHz, CDCl3) δ 5.09 (q, J = 7.1 Hz, 80H), 3.53 (s, 104H), 1.81 (s, 58H), 1.74 (s, 26H), 1.50 (d, J = 7.0 Hz, 227H), 1.18 (s, 8H), 0.95 (s, 29H), 0.77 (s, 69H).

Table 5-10: Summary table for UV-initiated polymerizations.

Entry	Monomer 1	Monomer 2	Solvent	Temperature
109[a]	100 eq LLA	100 eq MMA	toluene	90 °C
110	100 eq LLA	100 eq MMA	toluene	RT, UV
111	100 eq LLA	200 eq MMA	DMF	RT, UV
112	100 eq LLA	200 eq MMA	toluene	RT, UV
113	100 eq LLA	100 eq MMA	THF	RT, UV
114	100 eq LLA	100 eq MMA	toluene	95 °C

[a]ATRP inititiator: **EBIB** and ROP initiator pyrenebutanol

Tandem $Sn(Oct)_2$ (co-)catalyzed ATRP and ROP

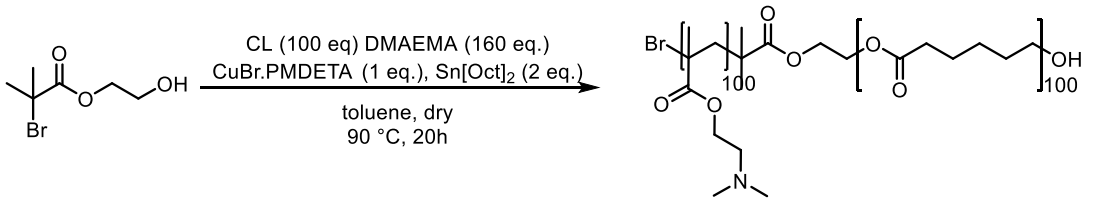

Exemplified for polymerization **127**, for reaction conditions and monomer equivalents, see Table 5-11. In a glovebox, a stock solution was made up for the PMDETA-complexed CuBr catalyst (0.1 M, in dry toluene), linker HBIB(0.1 M, in dry toluene) and stannous octoate catalyst (0.2 M, in dry toluene). Also in a glovebox, a dry SCHLENK flask equipped with a stir bar was loaded with monomers CL (240 mg, 2.0 mmol, 100 eq.) and DMAEMA (530 mg, 3.4 mmol,160 eq.), linker HBIB(200 µL, 0.1M, 0.02 mmol, 1 eq.) and toluene (2 mL). The SCHLENK flask was sealed, taken out of the glovebox and degassed via three freeze-pump-thaw cycles. The reaction mixture was then frozen again and stannous octoate solution (200µL, 0.1 M, 0.04 mmol, 2 eq.) and copper catalyst (200 µL, 0.1 M, 0.02 mmol, 1 eq.) were added onto the frozen solution and submitted to another cycle of vacuum pumping. The clear copper complex solution turned moss green upon freezing in the SCHLENK tube. The SCHLENK tube was then lowered into an oil bath set at 90 °C, upon which the solution turned bright blue. After a few minutes, the reaction mixture faded to a pale green. After the prescribed time intervals, samples were drawn via degassed syringe and a portion was set aside for ^{1}H NMR analysis. The remaining portion was diluted with THF and filtered through a syringe equipped with a 0.45 µm Teflon filter and containing a plug of neutral alumina gel to be submitted to GPC. After the determined reaction time, the reaction vessel was submerged into a liquid nitrogen bath. The solution was then diluted with THF, filtered through a pad of alumina gel, precipitated into ice cold methanol or hexanes (as applicable), and dried over a sintered glass filter and under reduced pressure. The polymer was isolated as a white powder (500 mg).

GPC: (in THF, *vs* MMA standards) Mn 7300 g.mol^{-1} Mw 11600 g.mol^{-1} PDI 1.59

^{1}H NMR: (300 MHz, $CDCl_3$) δ 4.07 (t, *J* = 6.6 Hz, 40H), 2.61 (d, *J* = 6.9 Hz, 20H), 2.32 (dt, *J* = 7.3, 3.7 Hz, 77H), 1.88 (d, *J* = 27.3 Hz, 8H), 1.67 (ddq, *J* = 13.5, 8.5, 4.9 Hz, 53H), 1.40 (q, *J* = 8.2 Hz, 27H), 1.07 (s, 8H), 0.91 (s, 15H).

Table 5-11: reaction conditions and monomer equivalents for tandem ATRP-ROP with $Sn(Oct)_2$.

Entry	Monomer 1	Monomer 2	Temperature	Solvent
115	LLA 100 eq	MMA 100 eq	90 °C	toluene
116	LLA 100 eq	MMA 400 eq	90 °C	toluene
117	CL 100 eq	MMA 200 eq	90 °C	bulk
118	LLA 100 eq	NIPAM 100 eq	90 °C	toluene
119	CL 100 eq	MMA 200 eq	90 °C	bulk
120	CL 100 eq	NIPAM 100 eq	90 °C	toluene
122	CL 100 eq	-	90 °C	bulk
123	-	DMAEMA 100 eq	90 °C	bulk
124	CL 100 eq	DMAEMA 100 eq	90 °C	bulk
125[*]	CL 100 eq	DMAEMA 100 eq	90 °C	bulk
126	CL 200 eq	DMAEMA 160 eq	90 °C	bulk
127	CL 100 eq	DMAEMA 160 eq	90 °C	bulk

*4 eq. $Sn(Oct)_2$

Table 5-12: Reaction times, conversions and polymer molecular weights of tandem polymerizations with $Sn(Oct)_2$

Entry	Time	Conversion Monomer 1	Conversion Monomer 2	Mn GPC g.mol^{-1}	Mw GPC g.mol^{-1}	PDI GPC
115	20h	100%	26%	N.D.	N.D.	N.D.
	4 d	100%	48%	N.D.	N.D.	N.D.
116	2 h	66%	32%	9 800	13600	4.39
	3 h	81%	37%	10 600	40400	3.81
	6 h	87%	38%	10 500	38600	3.68
117	1 h	5%	31%	5 700	14300	2.50
	3 h	86%	35%	10 000	17300	1.73
	6 h	100%	38%	8 800	17300	1.94
118	2 h	8%	8%	8 900	19300	2.17
	3 h	9%	7%	900	1000	1.09
	4 h	15%	14%	900	1000	1.14
119	2 h	8%	37%	850	950	1.14
	3 h	31%	39%	3 500	9600	2.73
	4 h	63%	41%	4 100	9100	2.22
120	2 h	6%	18%	2 200	3200	1.45
	3 h	10%	18%	4 100	5500	1.35
	4 h	19%	19%	7500	10100	1.35
122	1 h	42%	-	5 500	6100	1.10
	20 h	98%	-	10 700	22600	2.11
140	1 h	-	44%	3 000	6400	2.12
	20 h	-	64%	4 600	12700	2.75
	26 h	-	74%	6 000	14700	2.45
124	1 h	15%	52%	2 700	4700	1.72
	3 h	72%	53%	6 800	9500	1.39
	20 h	90%	72%	6 700	10700	1.60
125[d]	1 h	22%	58%	2 000	3700	1.87
	2 h	34%	58%	2 600	4400	1.69
	3 h	54%	58%	4 100	5800	1.41
126	2 h	21%	57%	9800	21600	2.20
	6 h	46%	61%	11100	20500	1.85
	20 h	85%	80%	9500	21800	2.29
127	2 h	37%	51%	6000	8600	1.43
	6 h	58%	56%	7700	11100	1.44
	20 h	74%	88%	7300	11600	1.59

Tandem ATRP-ROP with additional ATRP deactivator

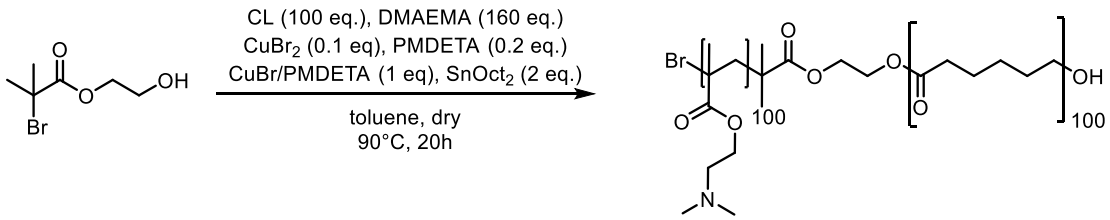

In a glovebox, the monomers CL (1.6 g, 14 mmol, 100 eq) and DMAEMA (3.5 g, 22 mmol, 160 eq.) initiator HBIB(1.4 mL, 0.1 M, 0.14 mmol, 1 eq.), $CuBr_2$ (2.1 mg, 0.014 mmol, 0.1 eq.) and toluene (7mL) were combined in a SCHLENK flask equipped with a stir bar. The SCHLENK flask was sealed, taken out of the glovebox and degassed via three freeze-pump-thaw cycles. The reaction mixture was then frozen again and the stannous catalyst solution (100 µL, 0.28 mmol, 2 eq.) , CuBr/PMDETA (140 µL, 1M in toluene, 0.14 mmol, 1 eq.) and PMDETA stock solution (280 µL, 0.1 M in toluene, 0.28 mmol, 0.2 eq.) were added onto the frozen solution and submitted to another cycle of vacuum pumping. The SCHLENK tube was then lowered into an oil bath set at 90 °C. After a few minutes, the reaction mixture took on an intense green hue. After the prescribed time intervals, samples were drawn via degassed syringe and a portion was set aside for ^{1}H NMR analysis. The remaining portion was diluted with THF and filtered through a syringe equipped with a 0.45 µm Teflon filter and containing a plug of neutral alumina gel to be submitted to GPC. After the determined reaction time, the reaction vessel was submerged into a liquid nitrogen bath. The solution was then diluted with THF, filtered through a pad of alumina gel, precipitated into ice cold methanol and dried over a sintered glass filter and under reduced pressure to yield the faintly green powdery polymer **141** (3.50 g).

GPC (in THF, *vs* MMA standards) Mn 18600 g.mol^{-1} Mw 28900 g.mol^{-1} PDI 1.56

^{1}H NMR (300 MHz, $CDCl_3$) δ 6.06 (s, 1H), 5.51 (d, *J* = 1.9 Hz, 1H), 4.28 — 4.07 (m, 7H), 4.06 — 3.95 (m, 3H), 2.56 (dt, *J* = 12.8, 5.6 Hz, 8H), 2.32 — 2.17 (m, 17H), 1.89 (s, 3H), 1.83 — 1.74 (m, 6H), 1.74 — 1.67 (m, 8H), 1.58 (dd, *J* = 10.6, 4.9 Hz, 1H), 1.33 (h, *J* = 7.2 Hz, 1H), 1.02 (s, 20H).

Functionalization of Wafers

Silicone wafers with a 0.7x0.7 cm^2 square geometry were cleaned with acetone, ethanol and THF by immersion in a beaker, covering with the respective solvent and placing in an ultrasound bath. The slides were then placed in an ozone oven for 30 min, after which they were transferred into a glovebox. In the glovebox, the wafers were immersed into a vial

containing the stock linker solution (0.2 M in dry, degassed toluene). The wafers were not dried themselves so as to allow the adsorbed water monolayers to catalyze the condensation reaction. The wafers were allowed to rest in the solution for 24 h, while making sure that they were fully submerged. After the prescribed time, the WAFERS were removed from the linker solution and washed with dry toluene. The functionalized wafers were stored in a glass vial covered with aluminum foil, in a glovebox.

ATRP-ROP on wafer

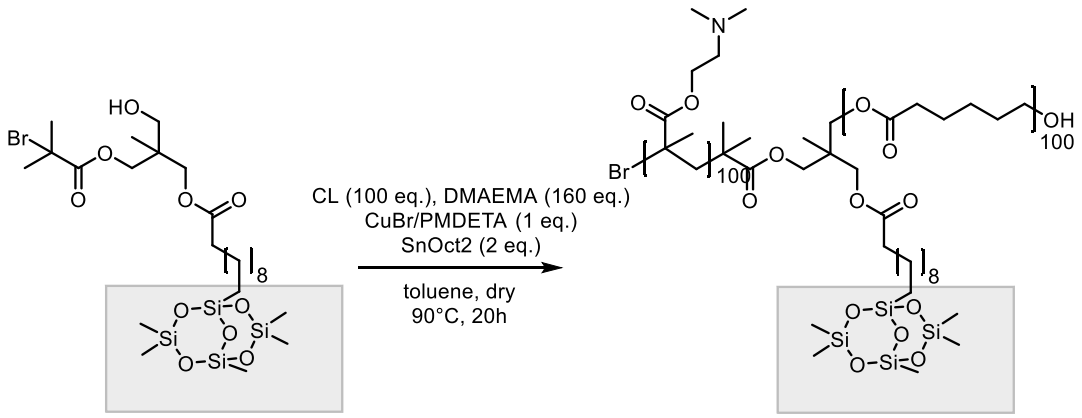

Exemplified for polymerization **137**. In a glovebox, monomers DMAEMA (520 mg, 3.2 mmol, 160 eq.), CL (240 mg, 2.0 mmol, 100 eq.), functionalized wafer (1 piece, 0.7x0.7 cm^2), sacrificial linker (200 µL. 0.02 mmol,1 eq.) and toluene (3mL) were combined in a SCHLENK flask equipped with a small stir bar. The SCHLENK flask was sealed, taken out of the glovebox and degassed via three freeze-pump-thaw cycles. The reaction mixture was then frozen again and the stannous catalyst solution (200 µL, 0.2 M in toluene, 0.04 mmol, 2 eq.) and CuBr/PMDETA stock solution (200 µL, 0.1 M in toluene, 0.02 mmol, 1 eq.) were added onto the frozen solution and submitted to another cycle of vacuum pumping. The SCHLENK tube was then lowered into an oil bath set at 90 °C. After a few minutes, the reaction mixture took on a pale green hue. After the prescribed time intervals, samples were drawn via degassed syringe and a portion was set aside for ^{1}H NMR analysis. The remaining portion was diluted with THF and filtered through a syringe equipped with a 0.45 µm Teflon filter and containing a plug of neutral alumina gel to be submitted to GPC. After the determined reaction time, the reaction vessel was submerged into a liquid nitrogen bath. The solution was then diluted with THF, filtered through a pad of alumina gel, precipitated into ice cold methanol or hexanes (as applicable), and dried over a sintered glass filter and under reduced pressure. The wafer was taken out of the reaction vessel and placed in a beaker containing THF and a small stir bar. Care was taken to avoid direct contact of the wafer with the stir bar. After 1 h, the THF was replaced and the wafer was allowed to wash for another hour. This cycle was performed three

times, with the final rinsing cycle conducted overnight. The wafer was then taken out of the THF and allowed to dry on air at RT, ready for analyses. The dried polymer **137** was isolated as fine white powder. (560 mg).

GPC (in THF, *vs* MMA standards) Mn 14000 g.mol^{-1} Mw 28000 g.mol^{-1} PDI 2.00

^{1}H NMR: (300 MHz, $CDCl_3$) δ 5.02 (s, 73H), 4.21 — 4.05 (m, 323H), 3.99 (t, *J* = 6.6 Hz, 21H), 3.56 (t, *J* = 6.7 Hz, 20H), 3.19 — 2.65 (m, 85H), 2.63 — 2.53 (m, 238H), 2.39 (d, *J* = 7.0 Hz, 47H), 1.81 — 1.73 (m, 180H), 1.61 — 1.47 (m, 63H), 1.40 — 1.26 (m, 46H), 1.00 (s, 22H), 0.91 — 0.78 (m, 74H).

Table 5-13: Monomer equivalents, molecular weights and molar fractions of tandem surface polymerizations

Entry	CL	DMAEMA	M_n[a]	Mw[a]	PDI[a]	f[b]
128	20	20	5 140	8600	1.68	0.40
129	100	-	15700	26800	1.71	0
130	-	100	6000	12600	2.10	1
131[c]	100	-	14400	28800	2.00	0
132[c]	-	100	17100	37800	2.21	1
133	200	160	11900	23600	1.98	0.3
134	30	30	9 000	18000	2.00	0.5
135	100	160	7000	10900	1.56	0.5
136[c]	200	200	10700	17800	1.66	0.4
137	100	160	14000	28000	2.00	0.5

6 BIBLIOGRAPHY

6.1 List of References

(1) Tajeddin, B.; Arabkhedri, M. Polymers and Food Packaging. *Polym. Sci. Innov. Appl.* **2020**, 525—543. https://doi.org/10.1016/B978-0-12-816808-0.00016-0.

(2) Giwa, A.; Ahmed, M.; Hasan, S. W. Polymers for Membrane Filtration in Water Purification. In *Polymeric Materials for Clean Water. Springer Series on Polymer and Composite Materials*; Springer: Cham, 2019; pp 167—190. https://doi.org/10.1007/978-3-030-00743-0_8.

(3) Park, J. B. Polymeric Implant Materials. In *Biomaterials Science and Engineering*; Springer: Boston, MA, 1984; pp 265—303. https://doi.org/10.1007/978-1-4613-2769-1_10.

(4) Elias, H.-G. *Macromolecules Vol. 1: Chemical Structures and Syntheses*, 1st ed.; Wiley-VCH Verlag: Weinheim, 2005.

(5) Odian, G. *Principles of Polymerization*, 2nd ed.; Wiley-Intersciene: New York, 1981. https://doi.org/10.1002/pol.1981.130191009.

(6) Jenkins, A. D.; Stepto, R. F. T.; Kratochvíl, P.; Suter, U. W. Glossary of Basic Terms in Polymer Science (IUPAC Recommendations 1996). *Pure Appl. Chem.* **1996**, *68* (12), 2287—2311. https://doi.org/10.1351/pac199668122287.

(7) Flory, P. J. Molecular Size Distribution in Linear Condensation Polymers. *J. Am. Chem.*

Soc. 1936, *58* (10), 1877—1885. https://doi.org/10.1021/ja01301a016.

(8) Jenkins, A. D.; Jones, R. G.; Moad, G. Terminology for Reversible-Deactivation Radical Polymerization Previously Called "Controlled" Radical or "Living" Radical Polymerization (IUPAC Recommendations 2010). *Pure Appl. Chem.* 2010, *82* (2), 483—491. https://doi.org/10.1351/PAC-REP-08-04-03.

(9) Chen, M.; Zhong, M.; Johnson, J. A. Light-Controlled Radical Polymerization: Mechanisms, Methods, and Applications. *Chem. Rev.* 2016, *116* (17), 10167—10211. https://doi.org/10.1021/acs.chemrev.5b00671.

(10) Nesvadba, P. Radical Polymerization in Industry. In *Encyclopedia of Radicals in Chemistry, Biology and Materials*; John Wiley & Sons, Ltd: Online, 2012. https://doi.org/10.1002/9781119953678.rad080.

(11) Matyjaszewski, K. Atom Transfer Radical Polymerization (ATRP): Current Status and Future Perspectives. *Macromolecules* 2012, *45* (10), 4015—4039. https://doi.org/10.1021/ma3001719.

(12) Grubbs, R. B.; Grubbs, R. H. 50th Anniversary Perspective: Living Polymerization—Emphasizing the Molecule in Macromolecules. *Macromolecules* 2017, *50* (18), 6979—6997. https://doi.org/10.1021/ACS.MACROMOL.7B01440.

(13) Jenkins, A. D.; Jones, R. G.; Moad, G. Terminology for Reversible-Deactivation Radical Polymerization Previously Called "Controlled" Radical or "Living" Radical Polymerization (IUPAC Recommendations 2010)*. *Pure Appl. Chem* 2010, *82* (2), 483—491. https://doi.org/10.1351/PAC-REP-08-04-03.

(14) Elias, H.-G. *Macromolecules Volume 1: Chemical Structures and Syntheses*; Wiley VCH: Weinheim, 2005; Vol. 1. https://doi.org/10.1002/macp.200600047.

(15) Harrisson, S. The Chain Length Distribution of an Ideal Reversible Deactivation Radical Polymerization. *Polymers (Basel).* 2018, *10* (8), 887. https://doi.org/10.3390/POLYM10080887.

(16) Guégain, E.; Guillaneuf, Y.; Nicolas, J. Nitroxide-Mediated Polymerization of Methacrylic Esters: Insights and Solutions to a Long-Standing Problem. *Macromol. Rapid Commun.* 2015, *36* (13), 1227—1247. https://doi.org/10.1002/marc.201500042.

(17) Leifert, D.; Studer, A. Der "Persistent Radical Effect" in Der Organischen Chemie. *Angew. Chemie* 2020, *132* (1), 74—110. https://doi.org/10.1002/ANGE.201903726.

(18) and, K. M.; Xia, J. Atom Transfer Radical Polymerization. *Chem. Rev.* 2001, *101* (9),

2921—2990. https://doi.org/10.1021/CR940534G.

(19) Davis, K. A.; Matyjaszewski, K. Effect of (Pseudo)Halide Initiators and Copper Complexes with Non-halogen Anions on the Atom Transfer Radical Polymerization. *J. Macromol. Sci. Part A* **2007**, *41 A* (5), 449—465. https://doi.org/10.1081/MA-120030918.

(20) Perrier, S. 50th Anniversary Perspective: RAFT Polymerization—A User Guide. *Macromolecules* **2017**, *50* (19), 7433—7447. https://doi.org/10.1021/ACS.MACROMOL.7B00767.

(21) Nuyken, O.; Pask, S. D. Ring-Opening Polymerization—An Introductory Review. *Polymers (Basel).* **2013**, *5* (2), 361—403. https://doi.org/10.3390/polym5020361.

(22) Ishii, R.; Nomura, N.; Kondo, T. Stereoselective Bulk Polymerization of Racemic Lactide for Stereoblock Poly(Racemic Lactide) Using an Achiral Aluminum Complex. *Polym. J.* **2004**, *36*, 261—264.

(23) Dorresteijn, R.; Haschick, R.; Klapper, M.; Müllen, K. Poly(L-Lactide) Nanoparticles via Ring-Opening Polymerization in Non-Aqueous Emulsion. *Macromol. Chem. Phys.* **2012**, *213* (19), 1996—2002. https://doi.org/10.1002/macp.201200345.

(24) Sosnowski, S.; Gadzinowski, M.; Slomkowski, S. Poly(L,L-Lactide) Microspheres by Ring-Opening Polymerization. *Macromolecules* **1996**, *29* (13), 4556—4564.

(25) Gadzinowski, M.; Sosnowski, S.; Slomkowski, S. Kinetics of the Dispersion Ring-Opening Polymerization of ϵ-Caprolactone Initiated with Diethylaluminum Ethoxide. *Macromolecules* **1996**, *29* (20), 6404—6407. https://doi.org/10.1021/ma9600466.

(26) Brown, J. M.; Conn, A. D.; Pilcher, G.; Leitão, M. L. P.; Meng-Yan, Y. On the Strain Energy of 5-Ring and 6-Ring Lactones. *J. Chem. Soc. Chem. Commun.* **1989**, No. 23, 1817—1819. https://doi.org/10.1039/C39890001817.

(27) du Pont, E. I.; Wallace Carothers, B. H.; Borough, G. L.; Van Natta, F. J. Studies of Polymerization and Ring Formation X. the Reversible Polymerization of Six-Membered Cyclic Esters. *J. AM. CHEM. SOC* **1932**, *54* (2), 761—772.

(28) Hofman, A.; Słomkowski, S.; Penczek, S. Structure of Active Centers and Mechanism of the Anionic Polymerization of Lactones. *Die Makromol. Chemie* **1984**, *185* (1), 91—101. https://doi.org/10.1002/macp.1984.021850110.

(29) Sipos, L.; Zsuga, M.; Kelen, T. Living Ring-Opening Polymerization of l,l-Lactide Initiated with Potassium t-Butoxide and Its 18-Crown-6 Complex. *Polym. Bull.* **1992**, *27* (5), 495—502. https://doi.org/10.1007/BF00300596.

(30) Cherdron, V. H.; Ohse, H.; Korte, F. Die Polymerisation von Lactonen. Teil 1: Homopolymerisation 4-, 6- Und 7-Gliedriger Lactone Mit Kationischen Initiatoren. *Die Makromol. Chemie* **1962**, *56* (1), 179—186. https://doi.org/10.1002/macp.1962.020560113.

(31) Sherck, N. J.; Kim, H. C.; Won, Y.-Y. Y. Elucidating a Unified Mechanistic Scheme for the DBU-Catalyzed Ring-Opening Polymerization of Lactide to Poly(Lactic Acid). *Macromolecules* **2016**, *46* (13), 4699—4713. https://doi.org/10.1021/acs.macromol.6b00621.

(32) Jones, G. O.; Chang, Y. A.; Horn, H. W.; Acharya, A. K.; Rice, J. E.; Hedrick, J. L.; Waymouth, R. M. N-Heterocyclic Carbene-Catalyzed Ring Opening Polymerization of ε-Caprolactone with and without Alcohol Initiators: Insights from Theory and Experiment. *J. Phys. Chem. B* **2015**, *119* (17), 5728—5737. https://doi.org/10.1021/acs.jpcb.5b01595.

(33) Brown, H. A.; Xiong, S.; Medvedev, G. A.; Chang, Y. A.; Abu-Omar, M. M.; Caruthers, J. M.; Waymouth, R. M. Zwitterionic Ring-Opening Polymerization: Models for Kinetics of Cyclic Poly(Caprolactone) Synthesis. *Macromolecules* **2014**, *47* (9), 2955—2963. https://doi.org/10.1021/ma500395j.

(34) Zhang, X.; Waymouth, R. M. Zwitterionic Ring Opening Polymerization with Isothioureas. *ACS Macro Lett.* **2014**, *3* (10), 1024—1028. https://doi.org/10.1021/mz500525n.

(35) Gowda, R. R.; Chen, E. Y. X. Organocatalytic and Chemoselective Polymerization of Multivinyl-Functionalized γ-Butyrolactones. *ACS Macro Lett.* **2016**, *5* (6), 772—776. https://doi.org/10.1021/acsmacrolett.6b00370.

(36) Nyce, G. W.; Lamboy, J. A.; Connor, E. F.; Waymouth, R. M.; Hedrick, J. L. Expanding the Catalytic Activity of Nucleophilic N-Heterocyclic Carbenes for Transesterification Reactions. *Org. Lett.* **2002**, *4* (21), 3587—3590. https://doi.org/10.1021/ol0267228.

(37) Connor, E. F.; Nyce, G. W.; Myers, M.; Möck, A.; Hedrick, J. L. First Example of N-Heterocyclic Carbenes as Catalysts for Living Polymerization: Organocatalytic Ring-Opening Polymerization of Cyclic Esters. *J. Am. Chem. Soc.* **2002**, *124* (6), 914—915. https://doi.org/10.1021/ja0173324.

(38) Brulé, E.; Guérineau, V.; Vermaut, P.; Prima, F.; Balogh, J.; Maron, L.; Slawin, A. M. Z.; Nolan, S. P.; Thomas, C. M. Polymerization of Cyclic Esters Using N-Heterocyclic Carbene Carboxylate Catalysts. *Polym. Chem.* **2013**, *4* (8), 2414—2423.

https://doi.org/10.1039/c3py00108c.

(39) Freudensprung, I.; Klapper, M.; Müllen, K. Triblock Terpolymers by Simultaneous Tandem Block Polymerization (STBP). *Macromol. Rapid Commun.* **2016**, *37* (3), 209—214. https://doi.org/10.1002/marc.201500568.

(40) Si, G.; Zhang, S.; Pang, W.; Wang, F.; Tan, C. Stereoselective Zwitterionic Ring-Opening Polymerization of Rac-Lactide. *Polymer (Guildf).* **2018**, *154*, 148—152. https://doi.org/10.1016/j.polymer.2018.09.004.

(41) Dove, A. P.; Li, H.; Pratt, R. C.; Lohmeijer, B. G. G.; Culkin, D. A.; Waymouth, R. M.; Hedrick, J. L. Stereoselective Polymerization of Rac- and Meso-Lactide Catalyzed by Sterically Encumbered N-Heterocyclic Carbenes. *Chem. Commun.* **2006**, No. 27, 2881—2883. https://doi.org/10.1039/b601393g.

(42) Jones, G. O.; Chang, Y. A.; Horn, H. W.; Acharya, A. K.; Rice, J. E.; Hedrick, J. L.; Waymouth, R. M. N-Heterocyclic Carbene-Catalyzed Ring Opening Polymerization of ε-Caprolactone with and without Alcohol Initiators: Insights from Theory and Experiment. *J. Phys. Chem. B* **2015**, *119* (17), 5728—5737. https://doi.org/10.1021/acs.jpcb.5b01595.

(43) Lohmeijer, B. G. G.; Dubois, G.; Leibfart, F.; Pratt, R. C.; Nederberg, F.; Nelson, A.; Waymouth, R. M.; Wade, C.; Hedrick, J. L. Organocatalytic Living Ring-Opening Polymerization of Cyclic Carbosiloxanes. *Org. Lett.* **2006**, *8* (21), 4683—4686. https://doi.org/10.1021/ol0614166.

(44) Enders, D.; Niemeier, O.; Henseler, A. Organocatalysis by N-Heterocyclic Carbenes. *Chem. Rev.* **2007**, *107* (12), 5606—5655. https://doi.org/10.1021/cr068372z.

(45) Nifant'ev, I.; Ivchenko, P. Coordination Ring-Opening Polymerization of Cyclic Esters: A Critical Overview of DFT Modeling and Visualization of the Reaction Mechanisms. *Molecules* **2019**, *24* (22), 4117. https://doi.org/10.3390/molecules24224117.

(46) Bielawski, C. W.; Grubbs, R. H. Living Ring-Opening Metathesis Polymerization. *Prog. Polym. Sci.* **2007**, *32*, 1—29. https://doi.org/10.1016/j.progpolymsci.2006.08.006.

(47) Schrock, R. R.; Murdzek, J. S.; Bazan, G. C.; Robbins, J.; Dimare, M.; O'Regan, M. Synthesis of Molybdenum Imido Alkylidene Complexes and Some Reactions Involving Acyclic Olefins. *J. Am. Chem. Soc.* **1990**, *112* (10), 3875—3886. https://doi.org/10.1021/ja00166a023.

(48) Schrock, R. R. Multiple Metal—Carbon Bonds for Catalytic Metathesis Reactions (Nobel

Lecture). *Angew. Chemie Int. Ed.* **2006**, *45* (23), 3748—3759. https://doi.org/10.1002/anie.200600085.

(49) Bielawski, C. W.; Grubbs, R. H. Living Ring-Opening Metathesis Polymerization. **2007**, *32*, 1—29. https://doi.org/10.1016/j.progpolymsci.2006.08.006.

(50) Choi, T.-L.; Grubbs, R. H. Controlled Living Ring-Opening-Metathesis Polymerization by a Fast-Initiating Ruthenium Catalyst. *Angew. Chemie Int. Ed.* **2003**, *42* (15), 1743—1746. https://doi.org/10.1002/anie.200250632.

(51) Walsh, D. J.; Lau, S. H.; Hyatt, M. G.; Guironnet, D. Kinetic Study of Living Ring-Opening Metathesis Polymerization with Third-Generation Grubbs Catalysts. *J. Am. Chem. Soc.* **2017**, *139* (39), 13644—13647. https://doi.org/10.1021/jacs.7b08010.

(52) Grubbs, R. H. Olefin-Metathesis Catalysts for the Preparation of Molecules and Materials (Nobel Lecture). *Angew. Chemie Int. Ed.* **2006**, *45* (23), 3760—3765. https://doi.org/10.1002/anie.200600680.

(53) Scholl, M.; Ding, S.; Lee, C. W.; Grubbs, R. H. Synthesis and Activity of a New Generation of Ruthenium-Based Olefin Metathesis Catalysts Coordinated with 1,3-Dimesityl-4,5-Dihydroimidazol-2-Ylidene Ligands. *Org. Lett.* **1999**, *1* (6), 953—956. https://doi.org/10.1021/ol990909q.

(54) Andrew Hejl; Oren A. Scherman, and; Grubbs*, R. H. Ring-Opening Metathesis Polymerization of Functionalized Low-Strain Monomers with Ruthenium-Based Catalysts. *Macromolecules* **2005**, *38* (17), 7214—7218. https://doi.org/10.1021/MA0501287.

(55) Sutthasupa, S.; Shiotsuki, M.; Sanda, F. Recent Advances in Ring-Opening Metathesis Polymerization, and Application to Synthesis of Functional Materials. *Polym. J.* **2010**, *42* (12), 905—915. https://doi.org/10.1038/pj.2010.94.

(56) Zhao, B.; Brittain, W. J. *Polymer Brushes: Surface-Immobilized Macromolecules*.

(57) Nakamura, Y. Intermolecular Interactions of Brush-like Polymers. *Polym. J. 2011 439* **2011**, *43* (9), 757—761. https://doi.org/10.1038/pj.2011.61.

(58) Nakamura, Y.; Wan, Y.; Mays, J. W.; Iatrou, H.; Hadjichristidis, N. Radius of Gyration of Polystyrene Combs and Centipedes in Solution. *Macromolecules* **2000**, *33* (22), 8323—8328. https://doi.org/10.1021/ma0007076.

(59) Wintermantel, M.; Gerle, M.; Fischer, K.; Schmidt, M.; Wataoka, I.; Urakawa, H.; Kajiwara, K.; Tsukahara, Y. Molecular Bottlebrushes †. *Macromolecules* **1996**.

https://doi.org/10.1021/ma950227s.

(60) Feng, H.; Böhmer, M.; Fokkink, R.; Sprakel, J.; Leermakers, F. Reentrant Stabilization of Grafted Nanoparticles in Polymer Solutions. *J. Phys. Chem. B* **2015**, *119* (40), 12938—12946. https://doi.org/10.1021/acs.jpcb.5b05504.

(61) Fernandes, N. J.; Koerner, H.; Giannelis, E. P.; Vaia, R. A. Hairy Nanoparticle Assemblies as One-Component Functional Polymer Nanocomposites: Opportunities and Challenges. *MRS Commun.* **2013**, *3* (1), 13—29. https://doi.org/10.1557/mrc.2013.9.

(62) Koch, K.; Geller, S.; Acar, K.; Bach, P.; Tsarenko, E.; Schmidt, A. Creation of a PDMS Polymer Brush on SiO2-Based Nanoparticles by Surface-Initiated Ring-Opening Polymerization. *Polymers (Basel).* **2020**, *12*, 787. https://doi.org/10.3390/POLYM12040787.

(63) Sperling, R. A.; Parak, W. J. Surface Modification, Functionalization and Bioconjugation of Colloidal Inorganic Nanoparticles. *Phil. Trans. R. Soc. A.* **2010**, *38*, 1333—1383. https://doi.org/10.1098/rsta.2009.0273.

(64) Parak, W. J. Controlled Interaction of Nanoparticles with Cells. *Science (80-.).* **2016**, *351* (6275), 814—815. https://doi.org/10.1126/science.aaf0751.

(65) Lau, K. H. A.; Ren, C.; Sileika, T. S.; Park, S. H.; Szleifer, I.; Messersmith, P. B. Surface-Grafted Polysarcosine as a Peptoid Antifouling Polymer Brush. *Langmuir* **2012**, *28* (46), 16099—16107. https://doi.org/10.1021/la302131n.

(66) Chen, W.-L.; Cordero, R.; Tran, H.; Ober, C. K. 50th Anniversary Perspective: Polymer Brushes: Novel Surfaces for Future Materials. *Macromolecules* **2017**, *50* (11), 4089—4113. https://doi.org/10.1021/acs.macromol.7b00450.

(67) Benetti, E. M.; Spencer, N. D. Using Polymers to Impart Lubricity and Biopassivity to Surfaces: Are These Properties Linked? *Helv. Chim. Acta* **2019**, *102* (5), e1900071. https://doi.org/10.1002/hlca.201900071.

(68) Yu, K.; Lo, J. C. Y.; Mei, Y.; Haney, E. F.; Siren, E.; Kalathottukaren, M. T.; Hancock, R. E. W.; Lange, D.; Kizhakkedathu, J. N. Toward Infection-Resistant Surfaces: Achieving High Antimicrobial Peptide Potency by Modulating the Functionality of Polymer Brush and Peptide. *ACS Appl. Mater. Interfaces* **2015**, *7* (51), 28591—28605. https://doi.org/10.1021/acsami.5b10074.

(69) Gao, G.; Lange, D.; Hilpert, K.; Kindrachuk, J.; Zou, Y.; Cheng, J. T. J.; Kazemzadeh-Narbat, M.; Yu, K.; Wang, R.; Straus, S. K.; Brooks, D. E.; Chew, B. H.; Hancock, R. E. W.;

Kizhakkedathu, J. N. The Biocompatibility and Biofilm Resistance of Implant Coatings Based on Hydrophilic Polymer Brushes Conjugated with Antimicrobial Peptides. *Biomaterials* **2011**, *32* (16), 3899—3909. https://doi.org/10.1016/j.biomaterials.2011.02.013.

(70) Buzzacchera, I.; Vorobii, M.; Kostina, N. Y.; De Los Santos Pereira, A.; Riedel, T.; Bruns, M.; Ogieglo, W.; Möller, M.; Wilson, C. J.; Rodriguez-Emmenegger, C. Polymer Brush-Functionalized Chitosan Hydrogels as Antifouling Implant Coatings. *Biomacromolecules* **2017**, *18* (6), 1983—1992. https://doi.org/10.1021/acs.biomac.7b00516.

(71) Skovdal, S. M.; Jørgensen, N. P.; Petersen, E.; Jensen-Fangel, S.; Ogaki, R.; Zeng, G.; Johansen, M. I.; Wang, M.; Rohde, H.; Meyer, R. L. Ultra-Dense Polymer Brush Coating Reduces Staphylococcus Epidermidis Biofilms on Medical Implants and Improves Antibiotic Treatment Outcome. *Acta Biomater.* **2018**, *76*, 46—55. https://doi.org/10.1016/j.actbio.2018.07.002.

(72) Schöttler, S.; Becker, G.; Winzen, S.; Steinbach, T.; Mohr, K.; Landfester, K.; Mailänder, V.; Wurm, F. R. Protein Adsorption Is Required for Stealth Effect of Poly(Ethylene Glycol)- and Poly(Phosphoester)-Coated Nanocarriers. *Nat. Nanotechnol.* **2016**, *11* (4), 372—377. https://doi.org/10.1038/nnano.2015.330.

(73) Simon, J.; Wolf, T.; Klein, K.; Landfester, K.; Wurm, F. R.; Mailänder, V. Hydrophilicity Regulates the Stealth Properties of Polyphosphoester-Coated Nanocarriers. *Angew. Chemie - Int. Ed.* **2018**, *57* (19), 5548—5553. https://doi.org/10.1002/anie.201800272.

(74) Nejadnik, M. R.; van der Mei, H. C.; Norde, W.; Busscher, H. J. Bacterial Adhesion and Growth on a Polymer Brush-Coating. *Biomaterials* **2008**, *29* (30), 4117—4121. https://doi.org/10.1016/j.biomaterials.2008.07.014.

(75) Roosjen, A.; Van Der Mei, H. C.; Busscher, H. J.; Norde, W. Microbial Adhesion to Poly(Ethylene Oxide) Brushes: Influence of Polymer Chain Length and Temperature. *Langmuir* **2004**, *20* (25), 10949—10955. https://doi.org/10.1021/la048469l.

(76) Buhl, K. B.; Agergaard, A. H.; Lillethorup, M.; Nikolajsen, J. P.; Pedersen, S. U.; Daasbjerg, K. Polymer Brush Coating and Adhesion Technology at Scale. *Polymers (Basel).* **2020**, *12* (7), 1475. https://doi.org/10.3390/polym12071475.

(77) Zhao, J.; Shang, Z.; Gao, L. Bonding Quartz Wafers by the Atom Transfer Radical Polymerization of the Glycidyl Methacrylate at Mild Temperature. *Sensors Actuators, A Phys.* **2007**, *135* (1), 257—261. https://doi.org/10.1016/j.sna.2006.06.070.

(78) Li Jeon, N.; Choi, I. S.; Whitesides, G. M.; Kim, N. Y.; Laibinis, P. E.; Harada, Y.; Finnie, K. R.; Girolami, G. S.; Nuzzo, R. G. Patterned Polymer Growth on Silicon Surfaces Using Microcontact Printing and Surface-Initiated Polymerization. *Appl. Phys. Lett* **1999**, *75* (26), 4203. https://doi.org/10.1063/1.125582.

(79) van der Waarden, M. Stabilization of Carbon-Black Dispersions in Hydrocarbons. *J. Colloid Sci.* **1950**, *5* (4), 317—325. https://doi.org/10.1016/0095-8522(50)90056-0.

(80) Striolo, A.; Egorov, S. A. Steric Stabilization of Spherical Colloidal Particles: Implicit and Explicit Solvent. *J. Chem. Phys.* **2007**, *126* (1), 014902. https://doi.org/10.1063/1.2409710.

(81) Kanazawa, H.; Okano, T. Temperature-Responsive Chromatography for the Separation of Biomolecules. *J. Chromatogr. A* **2011**, *1218* (49), 8736—8747. https://doi.org/10.1016/j.chroma.2011.04.015.

(82) Barbey, R.; Lavanant, L.; Paripovic, D.; Schüwer, N.; Sugnaux, C.; Tugulu, S.; Klok, A. Polymer Brushes via Surface-Initiated Controlled Radical Polymerization: Synthesis, Characterization, Properties, and Applications. *Chem. Rev.* **2009**, *109* (11), 5437—5527. https://doi.org/10.1021/cr900045a.

(83) Zhang, T.; Chen, T.; Amin, I.; Jordan, R. ATRP with a Light Switch: Photoinduced ATRP Using a Household Fluorescent Lamp. *Polym. Chem.* **2014**, *5*, 4790—4796. https://doi.org/10.1039/c4py00346b.

(84) Harris, B. P.; Metters, A. T. Generation and Characterization of Photopolymerized Polymer Brush Gradients. *Macromolecules* **2006**, *39* (8), 2764—2772. https://doi.org/10.1021/ma0512051.

(85) Bao, C.; Tang, S.; Horton, J. M.; Jiang, X.; Tang, P.; Qiu, F.; Zhu, L.; Zhao, B. Effect of Overall Grafting Density on Microphase Separation of Mixed Homopolymer Brushes Synthesized from Y-Initiator-Functionalized Silica Particles. *Macromolecules* **2012**, *45* (19), 8027—8036. https://doi.org/10.1021/ma301300k.

(86) Wu, T.; Efimenko, K.; Genzer, J. Combinatorial Study of the Mushroom-to-Brush Crossover in Surface Anchored Polyacrylamide. *J. Am. Chem. Soc.* **2002**, *124* (32), 9394—9395. https://doi.org/10.1021/ja027412n.

(87) Xu, F. J.; Yuan, Z. L.; Kang, E. T.; Neoh, K. G. Branched Fluoropolymer-Si Hybrids via Surface-Initiated ATRP of Pentafluorostyrene on Hydrogen-Terminated Si(100) Surfaces. *Langmuir* **2004**, *20* (19), 8200—8208. https://doi.org/10.1021/la048706k.

(88) Mori, H.; Böker, A.; Krausch, G.; Müller, A. H. E. Surface-Grafted Hyperbranched

Polymers via Self-Condensing Atom Transfer Radical Polymerization from Silicon Surfaces. *Macromolecules* **2001**, *34* (20), 6871—6882. https://doi.org/10.1021/ma0019048.

(89) Edmondson, S.; Huck, W. T. S. Quasi-2D Polymer Objects from Patterned, Crosslinked Polymer Brushes. *Adv. Mater.* **2004**, *16* (15), 1327—1331. https://doi.org/10.1002/adma.200400761.

(90) Comrie, J. E.; Huck, W. T. S. Formation of Hybrid 2D Polymer-Metal Microobjects. *Langmuir* **2007**, *23* (3), 1569—1576. https://doi.org/10.1021/la0619372.

(91) Bian, H.; Yang, J.; Zhang, N.; Wang, Q.; Liang, Y.; Dong, D. Ultrathin Free-Standing Polymer Membranes with Chemically Responsive Luminescence via Consecutive Photopolymerizations. *Polym. Chem.* **2016**, *7*, 1191—1196. https://doi.org/10.1039/c5py02013a.

(92) Kohri, M.; Shinoda, Y.; Kohma, H.; Nannichi, Y.; Yamauchi, M.; Yagai, S.; Kojima, T.; Taniguchi, T.; Kishikawa, K. Facile Synthesis of Free-Standing Polymer Brush Films Based on a Colorless Polydopamine Thin Layer. *Macromol. Rapid Commun.* **2013**, *34* (15), 1220—1224. https://doi.org/10.1002/marc.201300395.

(93) Kumar, S.; Dory, Y. L.; Lepage, M.; Zhao, Y. Surface-Grafted Stimuli-Responsive Block Copolymer Brushes for the Thermo-, Photo- and PH-Sensitive Release of Dye Molecules. *Macromolecules* **2011**, *44* (18), 7385—7393. https://doi.org/10.1021/ma2010102.

(94) Bernards, M. T.; Cheng, G.; Zhang, Z.; Chen, S.; Jiang, S. Nonfouling Polymer Brushes via Surface-Initiated, Two-Component Atom Transfer Radical Polymerization. *Macromolecules* **2008**, *41* (12), 4216—4219. https://doi.org/10.1021/ma800185y.

(95) Li, L.; Wu, J.; Gao, C. Surface-Grafted Block Copolymer Brushes with Continuous Composition Gradients of Poly(Poly(Ethylene Glycol)-Monomethacrylate) and Poly(N-Isopropylacrylamide). *Sci. China Chem.* **2011**, *54* (2). https://doi.org/10.1007/s11426-010-4192-8.

(96) Wang, Z.; Liu, T.; Zhao, Y.; Lee, J.; Wei, Q.; Yan, J.; Li, S.; Olszewski, M.; Yin, R.; Zhai, Y.; Bockstaller, M. R.; Matyjaszewski, K. Synthesis of Gradient Copolymer Grafted Particle Brushes by ATRP. *Macromolecules* **2019**, *52* (24), 9466—9475. https://doi.org/10.1021/acs.macromol.9b02157.

(97) Xu, C.; Barnes, S. E.; Wu, T.; Fischer, D. A.; Delongchamp, D. M.; Batteas, J. D.; Beers, K. L. Solution and Surface Composition Gradients via Microfluidic Confinement:

Fabrication of a Statistical-Copolymer-Brush Composition Gradient. *Adv. Mater.* **2006**, *18* (11), 1427—1430. https://doi.org/10.1002/adma.200502341.

(98) Wang, J.; Müller, M. Microphase Separation of Mixed Polymer Brushes: Dependence of the Morphology on Grafting Density, Composition, Chain-Length Asymmetry, Solvent Quality, and Selectivity. *J. Phys. Chem. B* **2009**, *113* (33), 11384—11402. https://doi.org/10.1021/jp903161j.

(99) Li, M.; Pester, C. W. Mixed Polymer Brushes for "Smart" Surfaces. *Polymers (Basel).* **2020**, *12* (7), 1—28. https://doi.org/10.3390/polym12071553.

(100) Minko, S.; Usov, D.; Froeck, C.; Stamm, M.; Müller, M.; Scholl, A. Lateral versus Perpendicular Segregation in Mixed Polymer Brushes. *Phys. Rev. Lett.* **2002**, *88* (3), 4. https://doi.org/10.1103/PhysRevLett.88.035502.

(101) Usov, D.; Gruzdev, V.; Nitschke, M.; Stamm, M.; Hoy, O.; Luzinov, I.; Tokarev, I.; Minko, S. Three-Dimensional Analysis of Switching Mechanism of Mixed Polymer Brushes. **2007**, *40*, 8774—8734. https://doi.org/10.1021/ma071090w.

(102) Sidorenko, A.; Minko, S.; Schenk-Meuser, K.; Duschner, H.; Stamm, M. Switching of Polymer Brushes. *Langmuir* **1999**, *15* (24), 8349—8355. https://doi.org/10.1021/la990869z.

(103) Sidorenko, A.; Minko, S.; Schenk-Meuser, K.; Duschner, H.; Stamm, M. Switching of Polymer Brushes. *Langmuir* **1999**, *15* (24), 8349—8355. https://doi.org/10.1021/la990869z.

(104) Julthongpiput, D.; Lin, Y. H.; Teng, J.; Zubarev, E. R.; Tsukruk, V. V. Y-Shaped Amphiphilic Brushes with Switchable Micellar Surface Structures. *J. Am. Chem. Soc.* **2003**, *125* (51), 15912—15921. https://doi.org/10.1021/ja038051u.

(105) Houbenov, N.; Minko, S.; Stamm, M. Mixed Polyelectrolyte Brush from Oppositely Charged Polymers for Switching of Surface Charge and Composition in Aqueous Environment. *Macromolecules* **2003**, *36* (16), 5897—5901. https://doi.org/10.1021/ma0341869.

(106) Bratek-Skicki, A.; Eloy, P.; Morga, M.; Dupont-Gillain, C. Reversible Protein Adsorption on Mixed PEO/PAA Polymer Brushes: Role of Ionic Strength and PEO Content. *Langmuir* **2018**, *34* (9), 3037—3048. https://doi.org/10.1021/acs.langmuir.7b04179.

(107) Bratek-Skicki, A.; Cristaudo, V.; Savocco, J.; Nootens, S.; Morsomme, P.; Delcorte, A.; Dupont-Gillain, C. Mixed Polymer Brushes for the Selective Capture and Release of

Proteins. *Biomacromolecules* **2019**, *20* (2), 778—789. https://doi.org/10.1021/acs.biomac.8b01353.

(108) Estillore, N. C.; Advincula, R. C. Stimuli-Responsive Binary Mixed Polymer Brushes and Free-Standing Films by LbL-SIP. *Langmuir* **2011**, *27* (10), 5997—6008. https://doi.org/10.1021/la200089x.

(109) Ionov, L.; Houbenov, N.; Sidorenko, A.; Stamm, M.; Minko, S. Smart Microfluidic Channels. *Adv. Funct. Mater.* **2006**, *16* (9), 1153—1160. https://doi.org/10.1002/adfm.200500562.

(110) Motornov, M.; Sheparovych, R.; Lupitskyy, R.; MacWilliams, E.; Hoy, O.; Luzinov, I.; Minko, S. Stimuli-Responsive Colloidal Systems from Mixed Brush-Coated Nanoparticles. *Adv. Funct. Mater.* **2007**, *17* (14), 2307—2314. https://doi.org/10.1002/adfm.200600934.

(111) Minko, S. *Smart Responsive Coatings from Mixed Polymer Brushes*, Vol. 957.; 2007. https://doi.org/10.1021/bk-2007-0957.ch006.

(112) Bratek-Skicki, A.; Eloy, P.; Morga, M.; Dupont-Gillain, C. Reversible Protein Adsorption on Mixed PEO/PAA Polymer Brushes: Role of Ionic Strength and PEO Content. *Langmuir* **2018**, *34* (9), 3037—3048. https://doi.org/10.1021/acs.langmuir.7b04179.

(113) Delcroix, M. F.; Huet, G. L.; Conard, T.; Demoustier-Champagne, S.; Du Prez, F. E.; Landoulsi, J.; Dupont-Gillain, C. C. Design of Mixed PEO/PAA Brushes with Switchable Properties toward Protein Adsorption. *Biomacromolecules* **2013**, *14* (1), 215—225. https://doi.org/10.1021/bm301637h.

(114) Chen, C.; Atif, M.; He, K.; Zhang, M.; Chen, L.; Wang, Y. A Binary Mixed Polymer Brush Coating with Adjusted Hydrophobic Property to Control Protein Adsorption. *Mater. Adv.* **2021**, *2* (6), 2120—2131. https://doi.org/10.1039/d0ma00932f.

(115) Huang, X.; Hauptmann, N.; Appelhans, D.; Formanek, P.; Frank, S.; Kaskel, S.; Temme, A.; Voit, B. Synthesis of Hetero-Polymer Functionalized Nanocarriers by Combining Surface-Initiated ATRP and RAFT Polymerization. *Small* **2012**, *8* (23), 3579—3583. https://doi.org/10.1002/smll.201201397.

(116) Gumus, B.; Herrera-Alonso, M.; Ramírez-Hernández, A. Kinetically-Arrested Single-Polymer Nanostructures from Amphiphilic Mikto-Grafted Bottlebrushes in Solution: A Simulation Study. *Soft Matter* **2020**, *16* (21), 4969—4979. https://doi.org/10.1039/d0sm00771d.

(117) Xie, G.; Martinez, M. R.; Olszewski, M.; Sheiko, S. S.; Matyjaszewski, K. Molecular Bottlebrushes as Novel Materials. *Biomacromolecules*. American Chemical Society January 14, 2019, pp 27—54. https://doi.org/10.1021/acs.biomac.8b01171.

(118) Haugan, I. N.; Maher, M. J.; Chang, A. B.; Lin, T. P.; Grubbs, R. H.; Hillmyer, M. A.; Bates, F. S. Consequences of Grafting Density on the Linear Viscoelastic Behavior of Graft Polymers. *ACS Macro Lett.* **2018**, *7* (5), 525—530. https://doi.org/10.1021/acsmacrolett.8b00116.

(119) Sheiko, S. S.; Sumerlin, B. S.; Matyjaszewski, K. Cylindrical Molecular Brushes: Synthesis, Characterization, and Properties. *Progress in Polymer Science (Oxford)*. Pergamon July 1, 2008, pp 759—785. https://doi.org/10.1016/j.progpolymsci.2008.05.001.

(120) Dalsin, S. J.; Hillmyer, M. A.; Bates, F. S. Linear Rheology of Polyolefin-Based Bottlebrush Polymers. *Macromolecules* **2015**, *48* (13), 4680—4691. https://doi.org/10.1021/acs.macromol.5b01153.

(121) Liang, H.; Cao, Z.; Wang, Z.; Sheiko, S. S.; Dobrynin, A. V. Combs and Bottlebrushes in a Melt. *Macromolecules* **2017**, *50* (8), 3430—3437. https://doi.org/10.1021/acs.macromol.7b00364.

(122) López-Barrón, C. R.; Brant, P.; Eberle, A. P. R.; Crowther, D. J. Linear Rheology and Structure of Molecular Bottlebrushes with Short Side Chains. *J. Rheol. (N. Y. N. Y).* **2015**, *59* (3), 865—883. https://doi.org/10.1122/1.4918977.

(123) Qian, Z.; Chen, D.; McKenna, G. B. Re-Visiting the "Consequences of Grafting Density on the Linear Viscoelastic Behavior of Graft Polymers." *Polymer (Guildf).* **2020**, *186*. https://doi.org/10.1016/j.polymer.2019.121992.

(124) Tsukahara, Y.; Kohjiya, S.; Tsutsumi, K.; Okamoto, Y. On the Intrinsic Viscosity of Poly(Macromonomer)S. *Macromolecules* **1994**, *27* (6), 1662—1664. https://doi.org/10.1021/ma00084a061.

(125) Sheiko, S. S.; Sun, F. C.; Randall, A.; Shirvanyants, D.; Rubinstein, M.; Lee, H. Il; Matyjaszewski, K. Adsorption-Induced Scission of Carbon-Carbon Bonds. *Nature* **2006**, *440* (7081), 191—194. https://doi.org/10.1038/nature04576.

(126) Xie, G.; Martinez, M. R.; Olszewski, M.; Sheiko, S. S.; Matyjaszewski, K. Molecular Bottlebrushes as Novel Materials. *Biomacromolecules* **2019**, *20* (1), 27—54. https://doi.org/10.1021/acs.biomac.8b01171.

(127) Schué, E.; Kopyshev, A.; Lutz, J.; Börner, H. G. Molecular Bottle Brushes with Positioned

Selenols: Extending the Toolbox of Oxidative Single Polymer Chain Folding with Conformation Analysis by Atomic Force Microscopy. *J. Polym. Sci.* **2020**, *58* (1), 154—162. https://doi.org/10.1002/pola.29496.

(128) Neugebauer, D.; Zhang, Y.; Pakula, T.; Sheiko, S. S.; Matyjaszewski, K. Densely-Grafted and Double-Grafted PEO Brushes via ATRP. A Route to Soft Elastomers. *Macromolecules* **2003**, *36*, 6746—6755. https://doi.org/10.1021/ma0345347.

(129) Reynolds, V.; Mukherjee, S.; Xie, R.; Levi, A.; Atassi, A.; Uchiyama, T.; Wang, H.; Chabinyc, M.; Bates, C. Super-Soft Solvent-Free Bottlebrush Elastomers for Touch Sensing. **2020**, *7*, 181. https://doi.org/10.1039/c9mh00951e.

(130) Zhang, Y.; Costantini, N.; Mierzwa, M.; Pakula, T.; Neugebauer, D.; Matyjaszewski, K. Super Soft Elastomers as Ionic Conductors. *Polymer (Guildf).* **2004**, *45* (18), 6333—6339. https://doi.org/10.1016/j.polymer.2004.06.045.

(131) Zhou, B.; He, D.; Hu, J.; Ye, Y.; Peng, H.; Zhou, X.; Xie, X.; Xue, Z. A Flexible, Self-Healing and Highly Stretchable Polymer Electrolyte: Via Quadruple Hydrogen Bonding for Lithium-Ion Batteries. *J. Mater. Chem. A* **2018**, *6*, 11725—11733. https://doi.org/10.1039/c8ta01907j.

(132) Banquy, X.; Burdyńska, J.; Lee, D. W.; Matyjaszewski, K.; Israelachvili, J. Bioinspired Bottle-Brush Polymer Exhibits Low Friction and Amontons-like Behavior. *J. Am. Chem. Soc.* **2014**, *136* (17), 6199—6202. https://doi.org/10.1021/ja501770y.

(133) Neugebauer, D.; Theis, M.; Pakula, T.; Wegner, G.; Matyjaszewski, K. Densely Heterografted Brush Macromolecules with Crystallizable Grafts. Synthesis and Bulk Properties. *Macromolecules* **2006**, *39* (2), 584—593. https://doi.org/10.1021/ma051702h.

(134) Sun, G.; Cho, S.; Clark, C.; Verkhoturov, S. V.; Eller, M. J.; Li, A.; Pavía-Jiménez, A.; Schweikert, E. A.; Thackeray, J. W.; Trefonas, P.; Wooley, K. L. Nanoscopic Cylindrical Dual Concentric and Lengthwise Block Brush Terpolymers as Covalent Preassembled High-Resolution and High-Sensitivity Negative-Tone Photoresist Materials. *J. Am. Chem. Soc.* **2013**, *135* (11), 4203—4206. https://doi.org/10.1021/ja3126382.

(135) Bhattarai, N.; Ramay, H. R.; Gunn, J.; Matsen, F. A.; Zhang, M. PEG-Grafted Chitosan as an Injectable Thermosensitive Hydrogel for Sustained Protein Release. *J. Control. Release* **2005**, *103*, 609—614. https://doi.org/10.1016/j.jconrel.2004.12.019.

(136) Johnson, J. A.; Lu, Y. Y.; Burts, A. O.; Lim, Y. H.; Finn, M. G.; Koberstein, J. T.; Turro, N. J.; Tirrell, D. A.; Grubbs, R. H. Core-Clickable PEG-Branch-Azide Bivalent-Bottle-Brush Polymers by ROMP: Grafting-through and Clicking-To. *J. Am. Chem. Soc.* **2011**, *133* (3),

559—566. https://doi.org/10.1021/ja108441d.

(137) Johnson, J. A.; Lu, Y. Y.; Burts, A. O.; Xia, Y.; Durrell, A. C.; Tirrell, D. A.; Grubbs, R. H. Drug-Loaded, Bivalent-Bottle-Brush Polymers by Graft-through ROMP. *Macromolecules* **2010**, *43* (24), 10326—10335. https://doi.org/10.1021/ma1021506.

(138) Zou, J.; Jafr, G.; Themistou, E.; Yap, Y.; Wintrob, Z. A. P.; Alexandridis, P.; Ceacareanu, A. C.; Cheng, C. PH-Sensitive Brush Polymer-Drug Conjugates by Ring-Opening Metathesis Copolymerization. *Chem. Commun.* **2011**, *47* (15), 4493—4495. https://doi.org/10.1039/c0cc05531j.

(139) Kuepfert, M.; Cohen, A. E.; Cullen, O.; Weck, M. Shell Cross-Linked Micelles as Nanoreactors for Enantioselective Three-Step Tandem Catalysis. *Chem. — A Eur. J.* **2018**, *24* (70), 18648—18652. https://doi.org/10.1002/chem.201804956.

(140) Freudensprung, I.; Joe, D.; Nietzel, S.; Vollmer, D.; Klapper, M.; Müllen, K. Spherical Polyolefin Particles from Olefin Polymerization in the Confined Geometry of Porous Hollow Silica Particles. *Macromol. Rapid Commun.* **2016**, *37* (20), 1651—1656. https://doi.org/10.1002/marc.201600295.

(141) Spange, S.; Grund, S. Nanostructured Organic-Inorganic Composite Materials by Twin Polymerization of Hybrid Monomers. *Adv. Mater.* **2009**, *21* (20), 2111—2116. https://doi.org/10.1002/adma.200802797.

(142) Nese, A.; Li, Y.; Sheiko, S. S.; Matyjaszewski, K. Synthesis of Molecular Bottlebrushes by Atom Transfer Radical Polymerization with Ppm Amounts of Cu Catalyst. *ACS Macro Lett.* **2012**, *1* (8), 991—994. https://doi.org/10.1021/mz3002484.

(143) Binder, K.; Butt, H.-J.; Floudas, G.; Frey, H.; Hsu, H.-P.; Landfester, K.; Kolb, U.; Kühnle, A.; Maskos, M.; Müllen, K.; Paul, W.; Schmidt, M.; Spiess, H. W.; Virnau, P. Structure Formation of Polymeric Building Blocks: Complex Polymer Architectures; Springer, Cham, 2013; pp 115—210. https://doi.org/10.1007/12_2013_230.

(144) Yamauchi, Y.; Horimoto, N. N.; Yamada, K.; Matsushita, Y.; Takeuchi, M.; Ishida, Y. Two-Step Divergent Synthesis of Monodisperse and Ultra-Long Bottlebrush Polymers from an Easily Purifiable ROMP Monomer. *Angew. Chemie - Int. Ed.* **2021**, *60* (3), 1528—1534. https://doi.org/10.1002/anie.202009759.

(145) Czelusniak, I.; Khosravi, E.; Kenwright, A. M.; Ansell, C. W. G. Synthesis, Characterization, and Hydrolytic Degradation of Polylactide-Functionalized Polyoxanorbornenes. *Macromolecules* **2007**, *40*, 1444—1452. https://doi.org/10.1021/ma061900o.

(146) Radzinski, S. C.; Foster, J. C.; Matson, J. B. Preparation of Bottlebrush Polymers via a One-Pot Ring-Opening Polymerization (ROP) and Ring-Opening Metathesis Polymerization (ROMP) Grafting-Through Strategy. *Macromol. Rapid Commun.* **2016**, *37* (7), 616—621. https://doi.org/10.1002/marc.201500672.

(147) Foster, J. C.; Radzinski, S. C.; Matson, J. B. Graft Polymer Synthesis by RAFT Transfer-To. **2017**, 2865—2876. https://doi.org/10.1002/pola.28621.

(148) Chen, C.; Wunderlich, K.; Mukherji, D.; Koynov, K.; Heck, A. J.; Raabe, M.; Barz, M.; Fytas, G.; Kremer, K.; Ng, D. Y. W.; Weil, T. Precision Anisotropic Polymers by Sequence Controlled. *J. Am. Chem. Soc.* **2020**, *142* (3), 1340. https://doi.org/10.1021/JACS.9B10491.

(149) Liska, J.; Borsig, E. Polymer-Analogous Reactions on Poly(2,6-Dimethyl-1,4-Phenylene Oxide). *J. Macromol. Sci. Part C* **1995**, *35* (3), 517—529. https://doi.org/10.1080/15321799508014597.

(150) Alaboalirat, M.; Qi, L.; Arrington, K. J.; Qian, S.; Keum, J. K.; Mei, H.; Littrell, K. C.; Sumpter, B. G.; Carrillo, J. M. Y.; Verduzco, R.; Matson, J. B. Amphiphilic Bottlebrush Block Copolymers: Analysis of Aqueous Self-Assembly by Small-Angle Neutron Scattering and Surface Tension Measurements. *Macromolecules* **2019**, *52* (2), 465—476. https://doi.org/10.1021/acs.macromol.8b02366.

(151) Sumerlin, B. S.; Neugebauer, D.; Matyjaszewski, K. Initiation Efficiency in the Synthesis of Molecular Brushes by Grafting from via Atom Transfer Radical Polymerization. *Macromolecules* **2005**, *38* (3), 702—708. https://doi.org/10.1021/ma048351b.

(152) Zhang, M.; Breiner, T.; Mori, H.; Müller, A. H. E. Amphiphilic Cylindrical Brushes with Poly(Acrylic Acid) Core and Poly(n-Butyl Acrylate) Shell and Narrow Length Distribution. *Polymer (Guildf).* **2003**. https://doi.org/10.1016/S0032-3861(02)00774-7.

(153) Radzinski, S. C.; Foster, J. C.; Matson, J. B. Preparation of Bottlebrush Polymers via a One-Pot Ring-Opening Polymerization (ROP) and Ring-Opening Metathesis Polymerization (ROMP) Grafting-Through Strategy. *Macromol. Rapid Commun.* **2016**, *37* (7), 616—621. https://doi.org/10.1002/marc.201500672.

(154) Ireland, B. J.; Dobigny, B. T.; Fogg, D. E. Decomposition of a Phosphine-Free Metathesis Catalyst by Amines and Other Bronsted Bases: Metallacyclobutane Deprotonation as a Major Deactivation Pathway. *ACS Catal.* **2015**, *5* (8), 4690—4698. https://doi.org/10.1021/acscatal.5b00813.

(155) Charvet, R.; Novak, B. M. One-Pot, One-Catalyst Synthesis of Graft Copolymers by Controlled ROMP and ATRP Polymerizations. *Macromolecules* **2004**, *37* (23), 8808—

8811. https://doi.org/10.1021/ma049244k.

(156) Ding, L.; Qiu, J.; Wei, J.; Zhu, Z. Facile Synthesis of Brush Poly(Phosphoamidate)s via One-Pot Tandem Ring-Opening Metathesis Polymerization and Atom Transfer Radical Polymerization. *Macromol. Rapid Commun.* **2014**, *35* (17), 1509—1515. https://doi.org/10.1002/marc.201400050.

(157) Cheng, C.; Khoshdel, E.; Wooley, K. L. One-Pot Tandem Synthesis of a Core-Shell Brush Copolymer from Small Molecule Reactants by Ring-Opening Metathesis and Reversible Addition-Fragmentation Chain Transfer (Co)Polymerizations. *Macromolecules* **2007**, *40* (7), 2289—2292. https://doi.org/10.1021/ma0627525.

(158) Bielawski, C. W.; Morita, T.; Grubbs, R. H. Synthesis of ABA Triblock Copolymers via a Tandem Ring-Opening Metathesis Polymerization: Atom Transfer Radical Polymerization Approach. *Macromolecules* **2000**, *33* (3), 678—680. https://doi.org/10.1021/ma990625l.

(159) Kluthe, K. E. I.; Wagner, M.; Klapper, M. Simultaneous Bottlebrush Polymerization. *Macromolecules* **2021**. https://doi.org/10.1021/acs.macromol.0c01724.

(160) Carafa, M.; Mesto, E.; Quaranta, E. DBU-Promoted Nucleophilic Activation of Carbonic Acid Diesters. *European J. Org. Chem.* **2011**, No. 13, 2458—2465. https://doi.org/10.1002/ejoc.201001725.

(161) Gimferrer, M.; Salvador, P.; Poater, A.; Metathesis Catalysis, O. Computational Monitoring of Oxidation States in Olefin Metathesis Scheme 1. Accepted Mechanism for Ruthenium-Based. *Organometallics* **2019**, *38*, 34. https://doi.org/10.1021/acs.organomet.9b00591.

(162) Freudensprung, I. Tandempolymerisationen an Polymeren Und Anorganischen Trägermaterialien, Johannes Gutenberg Universität Mainz, 2016.

(163) Coulembier, O.; Dove, A. P.; Pratt, R. C.; Sentman, A. C.; Culkin, D. A.; Mespouille, L.; Dubois, P.; Waymouth, R. M.; Hedrick, J. L. Latent, Thermally Activated Organic Catalysts for the on-Demand Living Polymerization of Lactide. *Angew. Chemie - Int. Ed.* **2005**, *44* (31), 4964—4968. https://doi.org/10.1002/anie.200500723.

(164) Nelson, D. J.; Nolan, S. P. N-Heterocyclic Carbenes. In *N-Heterocyclic Carbenes: Effective Tools for Organometallic Synthesis*; Nolan, S. P., Ed.; Viley VCH Verlag GmbH & Co KGaA: Weinheim, 2014; Vol. N-Heterocyclic Carb..., pp 1—24.

(165) Smith, E. M.; Dogra, K.; Older, C. M. METHOD FOR PREPARING DEUTERATED

AROMATIC COMPOUNDS. WO 2011/053334 Al, May 5, 2011.

(166) Hyatt, M. G.; Walsh, D. J.; Lord, R. L.; Andino Martinez, J. G.; Guironnet, D. Mechanistic and Kinetic Studies of the Ring Opening Metathesis Polymerization of Norbornenyl Monomers by a Grubbs Third Generation Catalyst. *J. Am. Chem. Soc.* **2019**, *141* (44), 17918—17925. https://doi.org/10.1021/jacs.9b09752.

(167) Gowda, R. R.; Chen, E. Y. X. Organocatalytic and Chemoselective Polymerization of Multivinyl-Functionalized γ-Butyrolactones. *ACS Macro Lett.* **2016**, *5* (6), 772—776. https://doi.org/10.1021/acsmacrolett.6b00370.

(168) Gowda, R. R.; Y-X Chen, E. Organocatalytic and Chemoselective Polymerization of Multivinyl-Functionalized γ-Butyrolactones. *ACS Macro Lett.* **2016**, *5* (6), 772—776. https://doi.org/10.1021/acsmacrolett.6b00370.

(169) Hlil, A. R.; Balogh, J.; Moncho, S.; Su, H. L.; Tuba, R.; Brothers, E. N.; Al-Hashimi, M.; Bazzi, H. S. Ring Opening Metathesis Polymerization (ROMP) of Five- to Eight-Membered Cyclic Olefins: Computational, Thermodynamic, and Experimental Approach. *J. Polym. Sci. Part A Polym. Chem.* **2017**, *55* (18), 3137—3145. https://doi.org/10.1002/pola.28695.

(170) Sonoda, T.; Kobayashi, S.; Tanaka, M. Periodically Functionalized Linear Polyethylene with Tertiary Amino Groups via Regioselective Ring-Opening Metathesis Polymerization. *Macromolecules* **2021**, *13*, 35. https://doi.org/10.1021/acs.macromol.0c02611.

(171) Choi, T. L.; Grubbs, R. H. Controlled Living Ring-Opening-Metathesis Polymerization by a Fast-Initiating Ruthenium Catalyst. *Angew. Chemie - Int. Ed.* **2003**, *42* (15), 1743—1746. https://doi.org/10.1002/anie.200250632.

(172) Kanao, M.; Otake, A.; Tsuchiya, K.; Ogino, K. Stereo-Selective Synthesis of Exo-Norbornene Derivatives for Resist Materials. *J. Photopolym. Sci. Technol.* **2009**, *22* (3), 365—370. https://doi.org/10.2494/photopolymer.22.365.

(173) Schulz, M. D.; Wagener, K. B. Solvent Effects in Alternating ADMET Polymerization. *ACS Macro Lett.* **2012**, *1* (4), 449—451. https://doi.org/10.1021/mz200236r.

(174) Pal, S.; Alizadeh, M.; Kong, P.; Kilbinger, A. F. M. Oxanorbornenes: Promising New Single Addition Monomers for the Metathesis Polymerization. *Chem. Sci.* **2021**, *12*, 6705—6711. https://doi.org/10.1039/d1sc00036e.

(175) Thiel, V.; Hendann, M.; Wannowius, K. J.; Plenio, H. On the Mechanism of the Initiation Reaction in Grubbs-Hoveyda Complexes. *J. Am. Chem. Soc.* **2012**, *134* (2), 1104—1114.

https://doi.org/10.1021/ja208967h.

(176) Vougioukalakis, G. C.; Grubbs, R. H. Ruthenium-Based Heterocyclic Carbene-Coordinated Olefin Metathesis Catalysts. *Chem. Rev.* **2010**, *110* (3), 1746—1787. https://doi.org/10.1021/cr9002424.

(177) Scholl, M.; Ding, S.; Lee, C. W.; Grubbs, R. H. Synthesis and Activity of a New Generation of Ruthenium-Based Olefin Metathesis Catalysts Coordinated with 1,3-Dimesityl-4,5-Dihydroimidazol-2-Ylidene Ligands. *Org. Lett.* **1999**, *1* (6), 953—956. https://doi.org/10.1021/ol990909q.

(178) Dalsin, S. J.; Rions-Maehren, T. G.; Beam, M. D.; Bates, F. S.; Hillmyer, M. A.; Matsen, M. W. Bottlebrush Block Polymers: Quantitative Theory and Experiments. *ACS Nano* **2015**, *9* (12), 12233—12245. https://doi.org/10.1021/acsnano.5b05473.

(179) Sanford, M. S.; Love, J. A.; Grubbs, R. H. A Versatile Precursor for the Synthesis of New Ruthenium Olefin Metathesis Catalysts. *Organometallics* **2001**, *20* (25), 5314—5318. https://doi.org/10.1021/om010599r.

(180) Neary, W. J.; Fultz, B. A.; Kennemur, J. G. Well-Defined and Precision-Grafted Bottlebrush Polypentenamers from Variable Temperature ROMP and ATRP. *ACS Macro Lett.* **2018**, *7* (9), 1080—1086. https://doi.org/10.1021/acsmacrolett.8b00576.

(181) Pietrasik, J.; Sumerlin, B. S.; Lee, H. il; Gil, R. R.; Matyjaszewski, K. Structural Mobility of Molecular Bottle-Brushes Investigated by NMR Relaxation Dynamics. *Polymer (Guildf).* **2007**, *48* (2), 496—501. https://doi.org/10.1016/j.polymer.2006.11.057.

(182) Radzinski, S. C.; Foster, J. C.; Chapleski, R. C.; Troya, D.; Matson, J. B. Bottlebrush Polymer Synthesis by Ring-Opening Metathesis Polymerization: The Significance of the Anchor Group. *J. Am. Chem. Soc.* **2016**, *138* (22), 6998—7004. https://doi.org/10.1021/jacs.5b13317.

(183) Radzinski, S. C.; Foster, J. C.; Chapleski, R. C.; Troya, D.; Matson, J. B. Bottlebrush Polymer Synthesis by Ring-Opening Metathesis Polymerization: The Significance of the Anchor Group. *J. Am. Chem. Soc.* **2016**, *138* (22), 6998—7004. https://doi.org/10.1021/jacs.5b13317.

(184) Radzinski, S. C.; Foster, J. C.; Scannelli, S. J.; Weaver, J. R.; Arrington, K. J.; Matson, J. B. Tapered Bottlebrush Polymers: Cone-Shaped Nanostructures by Sequential Addition of Macromonomers. *ACS Macro Lett.* **2017**, *6* (10), 1175—1179. https://doi.org/10.1021/acsmacrolett.7b00724.

(185) Pal, S.; Alizadeh, M.; Kong, P.; Kilbinger, A. F. M. Oxanorbornenes: Promising New Single Addition Monomers for the Metathesis Polymerization. *Chem. Sci.* **2021**, *12*, 6705—6711. https://doi.org/10.1039/d1sc00036e.

(186) Qiao, Y.; Zhao, Y.; Yuan, X.; Zhao, Y.; Ren, L. One-Dimensional Photonic Crystals Prepared by Self-Assembly of Brush Block Copolymers with Broad PDI. *J. Mater. Sci.* **2018**, *53* (23), 16160—16168. https://doi.org/10.1007/s10853-018-2754-x.

(187) Schulz, M. D.; Wagener, K. B. Solvent Effects in Alternating ADMET Polymerization. *ACS Macro Lett.* **2012**, *1* (4), 449—451. https://doi.org/10.1021/mz200236r.

(188) Rufh, S. A.; Goudreault, A. Y.; Foscato, M.; Jensen, V. R.; Fogg, D. E. Rapid Decomposition of Olefin Metathesis Catalysts by a Truncated N-Heterocyclic Carbene: Efficient Catalyst Quenching and n-Heterocyclic Carbene Vinylation. *ACS Catal.* **2018**, *8* (12), 11822—11826. https://doi.org/10.1021/acscatal.8b03123.

(189) Gerle, M.; Fischer, K.; Roos, S.; Müller, A. H. E.; Schmidt, M.; Sheiko, S. S.; Prokhorova, S.; Möller, M. Main Chain Conformation and Anomalous Elution Behavior of Cylindrical Brushes as Revealed by GPC/MALLS, Light Scattering, and SFM. *Macromolecules* **1999**, *32* (8), 2629—2637. https://doi.org/10.1021/ma9816463.

(190) Flook, M. M.; Ng, V. W. L.; Schrock, R. R. Synthesis of Cis,Syndiotactic ROMP Polymers Containing Alternating Enantiomers. *J. Am. Chem. Soc.* **2011**, *133* (6), 1784—1786. https://doi.org/10.1021/JA110949F.

(191) Nakamura, Y.; Wan, Y.; Mays, J. W.; Iatrou, H.; Hadjichristidis, N. Radius of Gyration of Polystyrene Combs and Centipedes in Solution. *Macromolecules* **2000**, *33* (22), 8323—8328. https://doi.org/10.1021/ma0007076.

(192) Viel, S.; Mazarin, M.; Giordanengo, R.; Phan, T. N. T.; Charles, L.; Caldarelli, S.; Bertin, D. Improved Compositional Analysis of Block Copolymers Using Diffusion Ordered NMR Spectroscopy. *Anal. Chim. Acta* **2009**, *654* (1), 45—48. https://doi.org/10.1016/j.aca.2009.06.049.

(193) Hiller, W. Quantitative Studies of Block Copolymers and Their Containing Homopolymer Components by Diffusion Ordered Spectroscopy. *Macromol. Chem. Phys.* **2019**, *220* (17), 1900255. https://doi.org/10.1002/macp.201900255.

(194) Runge, M. B.; Dutta, S.; Bowden, N. B. Synthesis of Comb Block Copolymers by ROMP, ATRP, and ROP and Their Assembly in the Solid State. *Macromolecules* **2006**, *39*, 498. https://doi.org/10.1021/ma052012g.

(195) Blümich, B. *Essential NMR - For Scientists and Engineers*, 2nd ed.; Springer International Publishing: Cham, 2019. https://doi.org/10.1007/978-3-030-10704-8.

(196) Fulmer, G. R.; M Miller, A. J.; Sherden, N. H.; Gottlieb, H. E.; Nudelman, A.; Stoltz, B. M.; Bercaw, J. E.; Goldberg, K. I.; Beckman, M. NMR Chemical Shifts of Trace Impurities: Common Laboratory Solvents, Organics, and Gases in Deuterated Solvents Relevant to the Organometallic Chemist. *Organometallics* **2010**, *29* (9), 2176—2179. https://doi.org/10.1021/om100106e.

(197) Hong, S. H.; Wenzel, A. G.; Salguero, T. T.; Day, M. W.; Grubbs, R. H. Decomposition of Ruthenium Olefin Metathesis Catalysts. *J. AM. CHEM. SOC* **2007**, *129*, 7961—7968. https://doi.org/10.1021/ja0713577.

(198) Walsh, D. J.; Wade, M. A.; Rogers, S. A.; Guironnet, D. Challenges of Size-Exclusion Chromatography for the Analysis of Bottlebrush Polymers. *Macromolecules* **2020**, *53* (19), 8610—8620. https://doi.org/10.1021/acs.macromol.0c01357.

(199) Schulz, M. D.; Ford, R. R.; Wagener, K. B. Insertion Metathesis Depolymerization. *Polym. Chem.* **2013**, *4* (13), 3656—3658. https://doi.org/10.1039/c3py00531c.

(200) Motornov, M.; Sheparovych, R.; Katz, E.; Minko, S. Chemical Gating with Nanostructured Responsive Polymer Brushes: Mixed Brush versus Homopolymer Brush. *ACS Nano* **2008**, *2* (1), 41—52. https://doi.org/10.1021/nn700214f.

(201) Motornov, M.; Sheparovych, R.; Tokarev, I.; Roiter, Y.; Minko, S. Nonwettable Thin Films from Hybrid Polymer Brushes Can Be Hydrophilic. *Langmuir* **2007**, *23* (1), 13—19. https://doi.org/10.1021/la061737q.

(202) Jackson, A. M.; Myerson, J. W.; Stellacci, F. Spontaneous Assembly of Subnanometre-Ordered Domains in the Ligand Shell of Monolayer-Protected Nanoparticles. *Nat. Mater.* **2004**, *3*, 330—336. https://doi.org/10.1038/nmat1116.

(203) Stirling, J.; Lekkas, I.; Sweetman, A.; Djuranovic, P.; Guo, Q.; Pauw, B.; Granwehr, J.; Lé Vy, R. L.; Moriarty, P. Critical Assessment of the Evidence for Striped Nanoparticles. *PLoS One* **2014**, *9* (11), e108482. https://doi.org/10.1371/journal.pone.0108482.

(204) Lemieux, M.; Usov, D.; Minko, S.; Stamm, M.; Shulha, H.; Tsukruk, V. V. Reorganization of Binary Polymer Brushes: Reversible Switching of Surface Microstructures and Nanomechanical Properties. *Macromolecules* **2003**, *36* (19), 7244—7255. https://doi.org/10.1021/ma034634c.

(205) Thiessen, W.; Wolff, T. NMRP and ATRP Double Initiators for the Formation of Binary

Polymer Brushes via Grafting-from Methods. *Des. Monomers Polym.* **2011**, *14*(3), 287—302. https://doi.org/10.1163/138577211X557567.

(206) Wang, Y.; Brittain, W. J. Simultaneous Binary Mixed Homopolymer Brush Formation by Combining Nitroxide-Mediated Radical Polymerization and Living Cationic Ring-Opening Polymerization. *Macromol. Rapid Commun.* **2007**, *28* (7), 811—815. https://doi.org/10.1002/marc.200600915.

(207) Li, W.; Bao, C.; Wright, R. A. E.; Zhao, B. Synthesis of Mixed Poly(ε-Caprolactone)/Polystyrene Brushes from Y-Initiator-Functionalized Silica Particles by Surface-Initiated Ring-Opening Polymerization and Nitroxide-Mediated Radical Polymerization. *RSC Adv.* **2014**, *4* (36), 18772—18781. https://doi.org/10.1039/c4ra02429j.

(208) Weimer, M. W.; Scherman, O. A.; Sogah, D. Y. Multifunctional Initiators Containing Orthogonal Sites. One-Pot, One-Step Block Copolymerization by Simultaneous Free Radical and Either Cationic Ring-Opening or Anionic Ring-Opening Polymerization. *Macromolecules* **1998**, *31* (23), 8425—8428. https://doi.org/10.1021/ma980949u.

(209) Priftis, D.; Sakellariou, G.; Baskaran, D.; Mays, J. W.; Hadjichristidis, N. Polymer Grafted Janus Multi-Walled Carbon Nanotubes. *Soft Matter* **2009**, *5* (21), 4272—4278. https://doi.org/10.1039/b908100c.

(210) Braunecker, W. A.; Tsarevsky, N. V; Gennaro, A.; Matyjaszewski, K. Thermodynamic Components of the Atom Transfer Radical Polymerization Equilibrium: Quantifying Solvent Effects. *Macromolecules* **2009**, *42*, 6348—6360. https://doi.org/10.1021/ma901094s.

(211) Alba, A.; Du Boullay, O. T.; Martin-Vaca, B.; Bourissou, D. Direct Ring-Opening of Lactide with Amines: Application to the Organo-Catalyzed Preparation of Amide End-Capped PLA and to the Removal of Residual Lactide from PLA Samples. *Polym. Chem.* **2015**, *6* (6), 989—997. https://doi.org/10.1039/c4py00973h.

(212) Wolf, F. F.; Friedemann, N.; Frey, H. Poly(Lactide)-Block-Poly(HEMA) Block Copolymers: An Orthogonal One-Pot Combination of ROP and ATRP, Using a Bifunctional Initiator. *Macromolecules* **2009**, *42* (15), 5622—5628. https://doi.org/10.1021/ma900894d.

(213) Zoppe, J. O.; Ataman, C.; Mocny, P.; Wang, J.; Moraes, J.; Klok, A. Surface-Initiated Controlled Radical Polymerization: State-of-the-Art, Opportunities, and Challenges in Surface and Interface Engineering with Polymer Brushes. *Chem. Rev.* **2017**, *117* (3), 1105—1318. https://doi.org/10.1021/acs.chemrev.6b00314.

(214) Tang, W.; Matyjaszewski, K. Effects of Initiator Structure on Activation Rate Constants in ATRP. 2007. https://doi.org/10.1021/ma062897b.

(215) Gillies, M. B.; Matyjaszewski, K.; Norrby, P.-O.; Pintauer, T.; Poli, R.; Richard, P. A DFT Study of R-X Bond Dissociation Enthalpies of Relevance to the Initiation Process of Atom Transfer Radical Polymerization. *Macromolecules* 2003, *36* (22), 8551—8559. https://doi.org/10.1021/ma0351672.

(216) Lane, J. R.; Contreras-García, J.; Piquemal, J. P.; Miller, B. J.; Kjaergaard, H. G. Are Bond Critical Points Really Critical for Hydrogen Bonding? *J. Chem. Theory Comput.* 2013, *9* (8), 3263—3266. https://doi.org/10.1021/ct400420r.

(217) Karas, L. J.; Batista, P. R.; Viesser, R. V.; Tormena, C. F.; Rittner, R.; De Oliveira, P. R. Trends of Intramolecular Hydrogen Bonding in Substituted Alcohols: A Deeper Investigation. *Phys. Chem. Chem. Phys.* 2017, *19* (25), 16904—16913. https://doi.org/10.1039/c7cp03572a.

(218) Sabourault, N.; Mignani, G.; Wagner, A.; Mioskowski, C. Platinum Oxide (PtO 2): A Potent Hydrosilylation Catalyst. *Org. Lett.* 2002, *4* (13), 2117—2119. https://doi.org/10.1021/ol025658r.

(219) Anamaria Moldovan; Frank Feldman; Georg Krugel; Martin Zimmer; Jochen Rentsch; Martin Hermle; Angelika Roth-Fölsch; Kai Kaufmann; Christian Hagendorf. Simple Cleaning and Conditioning of Silicon Surfaces with UV/Ozone Sources . *Energy Procedia* 2014, *55*, 834—844. https://doi.org/10.1016/j.egypro.2014.08.067.

(220) Miller, D. J.; Biesinger, M. C.; McIntyre, N. S. Interactions of CO2 and CO at Fractional Atmosphere Pressures with Iron and Iron Oxide Surfaces: One Possible Mechanism for Surface Contamination? *Surf. Interface Anal.* 2002, *33* (4), 299—305. https://doi.org/10.1002/sia.1188.

(221) Noonuruk, R.; Sritharathikhun, J.; Pecharapa, W. Surface Wettability of Silica Films Modified by UV/Ozone Treatment. *KMITL Sci. Tech. J* 2016, *16* (2), 46—51.

(222) Fournier, D.; Romagné, M. L.; Pascual, S.; Montembault, V.; Fontaine, L. 1,8-Diazabicyclo[5.4.0]Undec-7-Ene (DBU) as Ligand for Atom Transfer Radical Polymerization (ATRP). *Eur. Polym. J.* 2005, *41* (7), 1576—1581. https://doi.org/10.1016/j.eurpolymj.2005.01.013.

(223) Song, J.; Xu, J.; Pispas, S.; Zhang, G. One-Pot Synthesis of Poly(L-Lactide)-b-Poly(Methyl Methacrylate) Block Copolymers. *RSC Adv.* 2015, *5* (48), 38243—38247. https://doi.org/10.1039/c4ra17202g.

(224) Matyjaszewski, K. Atom Transfer Radical Polymerization (ATRP): Current Status and Future Perspectives. *Macromolecules* **2012**, *45* (10), 4015—4039. https://doi.org/10.1021/ma3001719.

(225) Jakubowski, W.; Matyjaszewski, K. New Segmented Copolymers by Combination of Atom Transfer Radical Polymerization and Ring Opening Polymerization. *Macromol. Symp.* **2006**, *240* (1), 213—223. https://doi.org/10.1002/masy.200650826.

(226) Matyjaszewski, K.; Miller, P. J.; Shukla, N.; Immaraporn, B.; Gelman, A.; Luokala, B. B.; Siclovan, T. M.; Kickelbick, G.; Valiant, T.; Hoffmann, H.; Pakula, T. Polymers at Interfaces: Using Atom Transfer Radical Polymerization in the Controlled Growth of Homopolymers and Block Copolymers from Silicon Surfaces in the Absence of Untethered Sacrificial Initiator. *Macromolecules* **1999**, *32* (26), 8716—8724. https://doi.org/10.1021/ma991146p.

(227) Kryuchkov, M. A.; Detrembleur, C.; Bazuin, C. G. Linear Amphiphilic Diblock Copolymers of Lactide and 2-Dimethylaminoethyl Methacrylate Using Bifunctional-Initiator and One-Pot Approaches. *Polymer (Guildf).* **2014**, *55* (10), 2316—2324. https://doi.org/10.1016/j.polymer.2014.04.007.

(228) Chen, R.; Feng, W.; Zhu, S.; Botton, G.; Ong, B.; Wu, Y. Surface-Initiated Atom Transfer Radical Polymerization Grafting of Poly(2,2,2-Trifluoroethyl Methacrylate) from Flat Silicon Wafer Surfaces. *J. Polym. Sci. Part A Polym. Chem.* **2006**, *44* (3), 1252—1262. https://doi.org/10.1002/pola.21232.

(229) Matyjaszewski, K.; Jakubowski, W.; Min, K.; Tang, W.; Huang, J.; Braunecker, W. A.; Tsarevsky, N. V. Diminishing Catalyst Concentration in Atom Transfer Radical Polymerization with Reducing Agents. *Proc. Natl. Acad. Sci. U. S. A.* **2006**, *103* (42), 15309—15314. https://doi.org/10.1073/pnas.0602675103.

(230) Ashford, E. J.; Naldi, V.; O'Dell, R.; Billingham, N. C.; Armes, S. P. First Example of the Atom Transfer Radical Polymerisation of an Acidic Monomer: Direct Synthesis of Methacrylic Acid Copolymers in Aqueous Media. *Chem. Commun.* **1999**, No. 14, 1285—1286. https://doi.org/10.1039/a903773j.

(231) Jakubowski, W.; Lutz, J.-F.; Slomkowski, S.; Matyjaszewski, K. Block and Random Copolymers as Surfactants for Dispersion Polymerization. I. Synthesis via Atom Transfer Radical Polymerization and Ring-Opening Polymerization. *J. Polym. Sci. Part A Polym. Chem.* **2005**, *43* (7), 1498—1510. https://doi.org/10.1002/pola.20629.

(232) Fu, Y. H.; Madrahimov, S. T.; Bergbreiter, D. E. Block Copolymers Derived from

Polyisobutylene Oligomers. *J. Polym. Sci. Part A Polym. Chem.* **2018**, *56* (16), 1860—1867. https://doi.org/10.1002/pola.29069.

(233) Yang, H.; Zhao, X.; Zhang, X.; Ma, L.; Wang, B.; Wei, H. Optimization of Bioreducible Micelles Self-Assembled from Amphiphilic Hyperbranched Block Copolymers for Drug Delivery. *J. Polym. Sci. Part A Polym. Chem.* **2018**, *56* (13), 1383—1394. https://doi.org/10.1002/pola.29019.

(234) Kagawa, Y.; Minami, H.; Okubo, M.; Zhou, J. Preparation of Block Copolymer Particles by Two-Step Atom Transfer Radical Polymerization in Aqueous Media and Its Unique Morphology. *Polymer (Guildf).* **2005**, *46* (4), 1045—1049. https://doi.org/10.1016/j.polymer.2004.11.040.

(235) Weaver, J. V. M.; Bannister, I.; Robinson, K. L.; Bories-Azeau, X.; Armes, S. P.; Smallridge, M.; McKenna, P. Stimulus-Responsive Water-Soluble Polymers Based on 2-Hydroxyethyl Methacrylate. *Macromolecules* **2004**, *37* (7), 2395—2403. https://doi.org/10.1021/ma0356358.

(236) Li, Y.; Tang, Y.; Narain, R.; Lewis, A. L.; Armes, S. P. Biomimetic Stimulus-Responsive Star Diblock Gelators. *Langmuir* **2005**, *21* (22), 9946—9954. https://doi.org/10.1021/la050356u.

(237) Yamamoto, S. I.; Pietrasik, J.; Matyjaszewski, K. Temperature- and PH-Responsive Dense Copolymer Brushes Prepared by ATRP. *Macromolecules* **2008**, *41* (19), 7013—7020. https://doi.org/10.1021/ma8011366.

(238) Shemper, B. S.; Mathias, L. J. Syntheses and Characterization of Statistical and Block Fluorinated Copolymers with Linear and Star-like Architectures via ATRP. *Eur. Polym. J.* **2004**, *40* (4), 651—665. https://doi.org/10.1016/j.eurpolymj.2003.12.010.

(239) Yamamoto, S. I.; Pietrasik, J.; Matyjaszewski, K. The Effect of Structure on the Thermoresponsive Nature of Well-Defined Poly(Oligo(Ethylene Oxide) Methacrylates) Synthesized by ATRP. *J. Polym. Sci. Part A Polym. Chem.* **2008**, *46* (1), 164—202. https://doi.org/10.1002/pola.22371.

(240) Luis de la Fuente, J.; Fernández-García, M.; Fernández-Sanz, M.; Madruga, E. L. Sequence Distribution and Stereoregularity of Methyl Methacrylate and Butyl Acrylate Statistical Copolymers Synthesized by Atom Transfer Radical Polymerization. *Macromolecules* **2001**, *34* (17), 5833—5837. https://doi.org/10.1021/ma010428y.

(241) Oh, J. K.; Bencherif, S. A.; Matyjaszewski, K. Atom Transfer Radical Polymerization in Inverse Miniemulsion: A Versatile Route toward Preparation and Functionalization of

Microgels/Nanogels for Targeted Drug Delivery Applications. *Polymer (Guildf).* **2009**, *50* (19), 4407—4423. https://doi.org/10.1016/j.polymer.2009.06.045.

(242) Johnson, J. A.; Lewis, D. R.; Díaz, D. D.; Finn, M. G.; Koberstein, J. T.; Turro, N. J. Synthesis of Degradable Model Networks via ATRP and Click Chemistry. *J. Am. Chem. Soc.* **2006**, *128* (20), 6564—6565. https://doi.org/10.1021/ja0612910.

(243) Bencherif, S. A.; Washburn, N. R.; Matyjaszewski, K. Synthesis by AGET ATRP of Degradable Nanogel Precursors for in Situ Formation of Nanostructured Hyaluronic Acid Hydrogel. *Biomacromolecules* **2009**, *10* (9), 2499—2507. https://doi.org/10.1021/bm9004639.

(244) Sun, Y.; Zhou, C.; Zhang, A.; Xu, L.; Yao, F.; Cen, L.; Fu, G. D. The Synthesis of Hydrogels with Controlled Distribution of Polymer Brushes in Hydrogel Network. *Appl. Surf. Sci.* **2014**, *320*, 818—828. https://doi.org/10.1016/j.apsusc.2014.09.085.

(245) Matyjaszewski, K.; Miller, P. J.; Shukla, N.; Immaraporn, B.; Gelman, A.; Luokala, B. B.; Siclovan, T. M.; Kickelbick, G.; Valiant, T.; Hoffmann, H.; Pakula, T. Polymers at Interfaces: Using Atom Transfer Radical Polymerization in the Controlled Growth of Homopolymers and Block Copolymers from Silicon Surfaces in the Absence of Untethered Sacrificial Initiator. *Macromolecules* **1999**, *32* (26), 8716—8724. https://doi.org/10.1021/ma991146p.

(246) Zhao, J.; Shang, Z.; Gao, L. Bonding Quartz Wafers by the Atom Transfer Radical Polymerization of the Glycidyl Methacrylate at Mild Temperature. *Sensors Actuators, A Phys.* **2007**, *135* (1), 257—261. https://doi.org/10.1016/j.sna.2006.06.070.

(247) Dong, H.; Huang, J.; Koepsel, R. R.; Ye, P.; Russell, A. J.; Matyjaszewski, K. Recyclable Antibacterial Magnetic Nanoparticles Grafted with Quaternized Poly(2-(Dimethylamino)Ethyl Methacrylate) Brushes. *Biomacromolecules* **2011**, *12* (4), 1305—1311. https://doi.org/10.1021/bm200031v.

(248) Lee, S. H.; Dreyer, D. R.; An, J.; Velamakanni, A.; Piner, R. D.; Park, S.; Zhu, Y.; Kim, S. O.; Bielawski, C. W.; Ruoff, R. S. Polymer Brushes via Controlled, Surface-Initiated Atom Transfer Radical Polymerization (ATRP) from Graphene Oxide. *Macromol. Rapid Commun.* **2010**, *31* (3), 281—288. https://doi.org/10.1002/marc.200900641.

(249) Mulvihill, M. J.; Rupert, B. L.; He, R.; Hochbaum, A.; Arnold, J.; Yang, P. Synthesis of Bifunctional Polymer Nanotubes from Silicon Nanowire Templates via Atom Transfer Radical Polymerization. *J. AM. CHEM. SOC* **2005**, *127*, 16040—16041. https://doi.org/10.1021/ja056242m.

(250) Burdyńska, J.; Daniel, W.; Li, Y.; Robertson, B.; Sheiko, S. S.; Matyjaszewski, K. Molecular Bottlebrushes with Bimodal Length Distribution of Side Chains. *Macromolecules* **2015**, *48* (14), 4813—4822. https://doi.org/10.1021/acs.macromol.5b00795.

(251) Rzayev, J. Synthesis of Polystyrene-Polylactide Bottlebrush Block Copolymers and Their Melt Self-Assembly into Large Domain Nanostructures. *Macromolecules* **2009**, *42* (6), 2135—2141. https://doi.org/10.1021/ma802304y.

(252) Burdyńska, J.; Li, Y.; Aggarwal, A. V.; Höger, S.; Sheiko, S. S.; Matyjaszewski, K. Synthesis and Arm Dissociation in Molecular Stars with a Spoked Wheel Core and Bottlebrush Arms. *J. Am. Chem. Soc.* **2014**, *136* (36), 12762—12770. https://doi.org/10.1021/ja506780y.

(253) Bolton, J.; Rzayev, J. Tandem RAFT-ATRP Synthesis of Polystyrene - Poly(Methyl Methacrylate) Bottlebrush Block Copolymers and Their Self-Assembly into Cylindrical Nanostructures. *ACS Macro Lett.* **2012**, *1* (1), 15—18. https://doi.org/10.1021/mz200003j.

(254) Jing, J.; Jiang, B.; Liang, F.; Yang, Z. Bottlebrush-Colloid Janus Nanoparticles. *ACS Macro Lett.* **2019**, *8* (6), 737—742. https://doi.org/10.1021/acsmacrolett.9b00234.

(255) Pal, D.; Miao, Z.; Garrison, J. B.; Veige, A. S.; Sumerlin, B. S. Ultra-High-Molecular-Weight Macrocyclic Bottlebrushes via Post-Polymerization Modification of a Cyclic Polymer. *Macromolecules* **2020**, *53* (22), 9717—9724. https://doi.org/10.1021/acs.macromol.0c01797.

(256) Fantin, M.; Isse, A. A.; Gennaro, A.; Matyjaszewski, K. Understanding the Fundamentals of Aqueous ATRP and Defining Conditions for Better Control. *Macromolecules* **2015**. https://doi.org/10.1021/acs.macromol.5b01454.

(257) Jakubowski, W.; Min, K.; Matyjaszewski, K. Activators Regenerated by Electron Transfer for Atom Transfer Radical Polymerization of Styrene. *Macromolecules* **2006**, *39* (1), 39—45. https://doi.org/10.1021/ma0522716.

(258) Li, Q.; Zhang, L.; Bai, L.; Miao, J.; Cheng, Z.; Zhu, X. Atom Transfer Radical Polymerization. *Prog. Chem.* **2010**, *22* (11), 2079—2088. https://doi.org/10.1002/9783527809080.cataz01278.

(259) Simakova, A.; Averick, S. E.; Konkolewicz, D.; Matyjaszewski, K. Aqueous ARGET ATRP. *Macromolecules* **2012**, *45* (16), 6371—6379. https://doi.org/10.1021/ma301303b.

(260) Matyjaszewski, K.; Hongchen, D.; Jakubowski, W.; Pietrasik, J.; Kusumo, A. Grafting from Surfaces for "Everyone": ARGET ATRP in the Presence of Air. *Langmuir* **2007**, *23*

(8), 4528—4531. https://doi.org/10.1021/la063402e.

(261) Karkare, P.; Kumar, S.; Murthy, C. N. ARGET-ATRP Using β-CD as Reducing Agent for the Synthesis of PMMA-b-PS-b-PMMA Triblock Copolymers. *J. Appl. Polym. Sci.* **2019**, *136* (9), 47117. https://doi.org/10.1002/app.47117.

(262) Oh, J. K.; Dong, H.; Zhang, R.; Matyjaszewski, K.; Schlaad, H. Preparation of Nanoparticles of Double-Hydrophilic PEO-PHEMA Block Copolymers by AGET ATRP in Inverse Miniemulsion. *J. Polym. Sci. Part A Polym. Chem.* **2007**, *45* (21), 4764—4772. https://doi.org/10.1002/pola.22230.

(263) Li, W.; Matyjaszewski, K. AGET ATRP of Oligo(Ethylene Glycol) Monomethyl Ether Methacrylate in Inverse Microemulsion. *Polym. Chem.* **2012**, *3*, 1813—1819. https://doi.org/10.1039/c1py00431j.

(264) Rolland, M.; Whitfield, R.; Messmer, D.; Parkatzidis, K.; Truong, N. P.; Anastasaki, A. Effect of Polymerization Components on Oxygen-Tolerant Photo-ATRP. *ACS Macro Lett.* **2019**, *8* (12), 1546—1551. https://doi.org/10.1021/acsmacrolett.9b00855.

(265) Kütahya, C.; Wang, P.; Li, S.; Liu, S.; Li, J.; Chen, Z.; Strehmel, B. Carbon Dots as a Promising Green Photocatalyst for Free Radical and ATRP-Based Radical Photopolymerization with Blue LEDs. *Angew. Chemie - Int. Ed.* **2020**, *59* (8), 3166—3171. https://doi.org/10.1002/anie.201912343.

(266) Konkolewicz, D.; Schröder, K.; Buback, J.; Bernhard, S.; Matyjaszewski, K. Visible Light and Sunlight Photoinduced ATRP with Ppm of Cu Catalyst. *ACS Macro Lett.* **2012**, *1* (10), 1219—1223. https://doi.org/10.1021/mz300457e.

(267) Pan, X.; Fantin, M.; Yuan, F.; Matyjaszewski, K. Externally Controlled Atom Transfer Radical Polymerization. *Chem. Soc. Rev.* **2018**, *47*, 5457—5490. https://doi.org/10.1039/c8cs00259b.

(268) Konkolewicz, D.; Wang, Y.; Krys, P.; Zhong, M.; Isse, A. A.; Gennaro, A.; Matyjaszewski, K. SARA ATRP or SET-LRP. End of Controversy? *Polym. Chem.* **2014**, *5*, 4396—4417. https://doi.org/10.1039/c4py00149d.

(269) Konkolewicz, D.; Wang, Y.; Zhong, M.; Krys, P.; Isse, A. A.; Gennaro, A.; Matyjaszewski, K. Reversible-Deactivation Radical Polymerization in the Presence of Metallic Copper. A Critical Assessment of the SARA ATRP and SET-LRP Mechanisms. *Macromolecules* **2013**, *46* (22), 8749—8772. https://doi.org/10.1021/ma401243k.

(270) Chmielarz, P.; Krys, P.; Park, S.; Matyjaszewski, K. PEO-b-PNIPAM Copolymers via SARA

ATRP and EATRP in Aqueous Media. *Polymer (Guildf).* **2015**, *71*, 143—147. https://doi.org/10.1016/j.polymer.2015.06.042.

(271) Bortolamei, N.; Isse, A. A.; Magenau, A. J. D.; Gennaro, A.; Matyjaszewski, K. Controlled Aqueous Atom Transfer Radical Polymerization with Electrochemical Generation of the Active Catalyst. *Angew. Chemie - Int. Ed.* **2011**, *50* (48), 11391—11394. https://doi.org/10.1002/anie.201105317.

(272) Lohmeijer, B. G. G.; Pratt, R. C.; Leibfarth, F.; Logan, J. W.; Long, D. A.; Dove, A. P.; Nederberg, F.; Choi, J.; Wade, C.; Waymouth, R. M.; Hedrick, J. L. Guanidine and Amidine Organocatalysts for Ring-Opening Polymerization of Cyclic Esters. *Macromolecules* **2006**, *39* (25), 8547—8583. https://doi.org/10.1021/ma0619381.

(273) Lohmeijer, B. G. G.; Pratt, R. C.; Leibfarth, F.; Logan, J. W.; Long, D. A.; Dove, A. P.; Nederberg, F.; Choi, J.; Wade, C.; Waymouth, R. M.; Hedrick, J. L. Guanidine and Amidine Organocatalysts for Ring-Opening Polymerization of Cyclic Esters. *Macromolecules* **2006**, *39* (25), 8574—8583. https://doi.org/10.1021/ma0619381.

(274) Gandhi, A.; Paul, A.; Sen, S. O.; Sen, K. K. Studies on Thermoresponsive Polymers: Phase Behaviour, Drug Delivery and Biomedical Applications. *Asian J. Pharm. Sci.* **2015**, *10* (2), 99—107. https://doi.org/10.1016/j.ajps.2014.08.010.

(275) Szczepaniak, G.; Łagodzińska, M.; Dadashi-Silab, S.; Gorczyński, A.; Matyjaszewski, K. Fully Oxygen-Tolerant Atom Transfer Radical Polymerization Triggered by Sodium Pyruvate. *Chem. Sci.* **2020**, *11* (33), 8809—8816. https://doi.org/10.1039/d0sc03179h.

(276) Zhang, B. Y.; He, W. D.; Li, W. T.; Li, L. Y.; Zhang, K. R.; Zhang, H. Preparation of Block-Brush PEG-b-P(NIPAM-g-DMAEMA) and Its Dual Stimulus-Response. *Polymer (Guildf).* **2010**, *51* (14), 3039—3046. https://doi.org/10.1016/j.polymer.2010.05.012.

(277) Ye, J.; Narain, R. Water-Assisted Atom Transfer Radical Polymerization of N-Isopropylacrylamide: Nature of Solvent and Temperature. *J. Phys. Chem. B* **2009**, *113* (3), 676—681. https://doi.org/10.1021/jp808905s.

(278) Wu, T.; Zhang, Y.; Wang, X.; Liu, S. Fabrication of Hybrid Silica Nanoparticles Densely Grafted with Thermoresponsive Poly(N-Isopropylacrylamide) Brushes of Controlled Thickness via Surface-Initiated Atom Transfer Radical Polymerization. *Chem. Mater.* **2008**, *20* (1), 101—109. https://doi.org/10.1021/cm702073f.

(279) Silvestro, G. Di; Yuan, C. M.; Mussini, P. R. Competitive Complexation by Ligand and Solvent: Polarographic Characterization of ATRP Catalyst Polyamine-Copper Complexes in Acetonitrile + Water Mixed Solvents. *J. Solution Chem.* **2004**, *33* (8), 923—

940. https://doi.org/10.1023/B:JOSL.0000048045.72710.9a.

(280) Tashrifi, Z.; Khanaposhtani, M. M.; Larijani, B.; Mahdavi, M. Dimethyl Sulfoxide: Yesterday's Solvent, Today's Reagent. *Adv. Synth. Catal.* **2020**, *362* (1), 65—86. https://doi.org/10.1002/adsc.201901021.

(281) Tang, W.; Kwak, Y.; Braunecker, W.; Tsarevsky, N. V; Coote, M. L.; Matyjaszewski, K. Understanding Atom Transfer Radical Polymerization: Effect of Ligand and Initiator Structures on the Equilibrium Constants. *J. Am. Chem. Soc.* **2008**, *130* (32), 10702—10713. https://doi.org/10.1021/ja802290a.

(282) Janczak, J.; Kubiak, R.; Lisowski, J. Structural Evidence of the Formation of ZnPc-DBU Complex during Recrystallisation of Commercially Available ZnPc Dye. *Polyhedron* **2011**, *30* (2), 253—258. https://doi.org/10.1016/j.poly.2010.10.011.

(283) Gurr, P. A.; Mills, M. F.; Qiao, G. G.; Solomon, D. H. Initiator Efficiency in ATRP : The Tosyl Chloride / CuBr / PMDETA System. **2005**, *46*, 2097—2104. https://doi.org/10.1016/j.polymer.2005.01.015.

(284) Lei, L.; Li, F.; Zhao, H.; Wang, Y. One-Pot Synthesis of Block Copolymers by Ring-Opening Polymerization and Ultraviolet Light-Induced ATRP at Ambient Temperature. *J. Polym. Sci. Part A Polym. Chem.* **2018**, *56* (7), 699—704. https://doi.org/10.1002/pola.28940.

(285) Storey, R. F.; Sherman, J. W. Kinetics and Mechanism of the Stannous Octoate-Catalyzed Bulk Polymerization of ε-Caprolactone. *Macromolecules* **2002**, *35* (5), 1504—1512. https://doi.org/10.1021/ma010986c.

(286) Kricheldorf, H. R. Tin-Initiated Polymerizations of Lactones: Mechanistic and Preparative Aspects. *Macromol. Symp.* **2000**, *135*, 55—65. https://doi.org/10.1002/1521-3900(200003)153:1<55::AID-MASY55>3.0.CO;2-T.

(287) Greszta, D.; Mardare, D.; Matyjaszewski, K. "Living" Radical Polymerization. 1. Possibilities and Limitations. *Macromolecules* **1994**, *27* (3), 638—644. https://doi.org/10.1021/ma00081a002.

(288) Jakubowski, W.; Lutz, J.-F.; Slomkowski, S.; Matyjaszewski, K. Block and Random Copolymers as Surfactants for Dispersion Polymerization. I. Synthesis via Atom Transfer Radical Polymerization and Ring-Opening Polymerization. *J. Polym. Sci. Part A Polym. Chem.* **2005**, *43* (7), 1498—1510. https://doi.org/10.1002/pola.20629.

(289) Glaied, O.; Delaite, C.; Dumas, P. Synthesis of A2B Star Block Copolymers from a

Heterotrifunctional Initiator. *J. Polym. Sci. Part A Polym. Chem.* **2005**, *44* (6), 1796—1806. https://doi.org/10.1002/pola.21283.

(290) Weidner, S. M.; Kricheldorf, H. R. The Role of Transesterification in SnOct 2 -Catalyzed Polymerizations of Lactides. *Macromol. Chem. Phys.* **2017**, *218* (3), 1600331. https://doi.org/10.1002/macp.201600331.

(291) Zheng, J. Y.; Tan, M. J.; Thoniyot, P.; Loh, X. J. Unusual Thermogelling Behaviour of Poly[2-(Dimethylamino)Ethyl Methacrylate] (PDMAEMA)-Based Polymers Polymerized in Bulk. *RSC Adv.* **2015**, *5* (76), 62314—62318. https://doi.org/10.1039/c5ra12816a.

(292) Li, D.; Sheng, X.; Zhao, B. Environmentally Responsive "Hairy" Nanoparticles: Mixed Homopolymer Brushes on Silica Nanoparticles Synthesized by Living Radical Polymerization Techniques. *J. Am. Chem. Soc.* **2005**, *127* (17), 6248—6256. https://doi.org/10.1021/ja0422561.

(293) Sidorenko, A.; Minko, S.; Schenk-Meuser, K.; Duschner, H.; Stamm, M. Switching of Polymer Brushes. *Langmuir* **1999**, *15* (24), 8349—8355. https://doi.org/10.1021/la990869z.

(294) Luzinov, I.; Voronov, A.; Minko, S.; Kraus, R.; Wilke, W.; Zhuk, A. Encapsulation of Fillers with Grafted Polymers for Model Composites. *J. Appl. Polym. Sci.* **1996**, *61* (7), 1101—1109. https://doi.org/10.1002/(sici)1097-4628(19960815)61:7<1101::aid-app5>3.0.co;2-q.

(295) Aoyagi, Y.; Yamashita, K.; Doi, Y. Thermal Degradation of Poly[(R)-3-Hydroxybutyrate], Poly[ε-Caprolactone], and Poly[(S)-Lactide]. *Polym. Degrad. Stab.* **2002**. https://doi.org/10.1016/S0141-3910(01)00265-8.

(296) Stawski, D.; Nowak, A. Thermal Properties of Poly(N,N-Dimethylaminoethyl Methacrylate). *PLoS One* **2019**, *14* (6), e0217441. https://doi.org/10.1371/journal.pone.0217441.

(297) Takashi Kashiwagi; Atsushi Inaba; James E. Brown; Koichi Hatada; Tatsuki Kitayama; Eiji Masuda. Effects of Weak Linkages on the Thermal and Oxidative Degradation of Poly(Methyl Methacrylates). *Macromolecules* **1986**, *19*, 2160—2168.

(298) Zhuravlev, E.; Schmelzer, J. W. P.; Wunderlich, B.; Schick, C. Kinetics of Nucleation and Crystallization in Poly(ε-Caprolactone) (PCL). *Polymer (Guildf).* **2011**, *52* (9), 1983—1990. https://doi.org/10.1016/j.polymer.2011.03.013.

(299) Trindade, G. F.; Abel, M. L.; Watts, J. F. Non-Negative Matrix Factorisation of Large Mass

Spectrometry Datasets. *Chemom. Intell. Lab. Syst.* **2017**, *163*, 76—85. https://doi.org/10.1016/j.chemolab.2017.02.012.

(300) Honigfort, M. E.; Brittain, W. J.; Bosanac, T.; Wilcox, C. S. Use of Precipitons for Copper Removal in Atom Transfer Radical Polymerization [1]. *Macromolecules* **2002**, *35* (13), 4849—4851. https://doi.org/10.1021/ma020155m.

(301) Ydens, I.; Moins, S.; Botteman, F.; Degée, P.; Dubois, P. Removal of Copper-Based Catalyst in Atom Transfer Radical Polymerization Using Different Extraction Techniques. *e-Polymers* **2014**, *4* (1), 39. https://doi.org/10.1515/epoly.2004.4.1.414.

(302) Yang, L.; Shirahata, N.; Saini, G.; Zhang, F.; Pei, L.; Asplund, M. C.; Kurth, D. G.; Ariga, K.; Sautter, K.; Nakanishi, T.; Smentkowski, V.; Linford, M. R. Effect of Surface Free Energy on PDMS Transfer in Microcontact Printing and Its Application to ToF-SIMS to Probe Surface Energies. *Langmuir* **2009**, *25* (10), 5674—5683. https://doi.org/10.1021/la804272n.

(303) Graham, D. J.; Price, D. D.; Ratner, B. D. Solution Assembled and Microcontact Printed Monolayers of Dodecanethiol on Gold: A Multivariate Exploration of Chemistry and Contamination. *Langmuir* **2002**, *18* (5), 1518—1527. https://doi.org/10.1021/la010059z.

(304) Mabe, A. N.; Perez Perez, L. X.; Wu, A. S.; Wilson, T. S. *Effects of Varying Composition and Kinetics on the Microstructural and Mechanical Properties of Polysiloxane Foams*; Livermore, CA (United States), 2018. https://doi.org/10.2172/1438809.

(305) Graham, D. J.; Castner, D. G. Multivariate Analysis of ToF-SIMS Data from Multicomponent Systems: The Why, When, and How. *Biointerphases* **2012**, *7*(1—4), 1—12. https://doi.org/10.1007/s13758-012-0049-3.

(306) Wold, S.; Esbensen, K.; Geladi, P. Principal Component Analysis. *Chemom. Intell. Lab. Syst.* **1987**, *2* (1—3), 37—52. https://doi.org/10.1016/0169-7439(87)80084-9.

(307) Noël, C.; Houssiau, L. Hybrid Organic/Inorganic Materials Depth Profiling Using Low Energy Cesium Ions. *J. Am. Soc. Mass Spectrom.* **2016**, *27* (5), 908—916. https://doi.org/10.1007/s13361-016-1353-9.

(308) Zhulina, E.; Balazs, A. C. Designing Patterned Surfaces by Grafting Y-Shaped Copolymers. *Macromolecules* **1996**, *29* (7), 2667—2673.

(309) Piontek, M. C.; Roos, W. H. *Atomic Force Microscopy: An Introduction*; Humana Press, New York, NY, 2018; Vol. 1665. https://doi.org/10.1007/978-1-4939-7271-5_13.

(310) Lai, T.; Shi, K.; Huang, P. Adhesion Force Behaviors between Two Silica Surfaces with

Varied Water Thin Film Due to Substrate Temperature Studied by AFM. *J. Adhes.* **2020**, *96* (9), 855—872. https://doi.org/10.1080/00218464.2018.1523725.

(311) Minko, S.; Usov, D.; Goreshnik, E.; Stamm, M. Environment-Adopting Surfaces with Reversibly Switchable Morphology. *Macromol. Rapid Commun.* **2001**, *22* (3), 206—211. https://doi.org/10.1002/1521-3927(200102)22:3<206::aid-marc206>3.0.co;2-%23.

(312) Santer, S.; Kopyshev, A.; Donges, J.; Rühe, J.; Jiang, X.; Zhao, B.; Müller, M. Memory of Surface Patterns in Mixed Polymer Brushes: Simulation and Experiment. *Langmuir* **2007**, *23* (1), 279—285. https://doi.org/10.1021/la0629577.

(313) Hur, S. M.; Frischknecht, A. L.; Huber, D. L.; Fredrickson, G. H. Self-Assembly in a Mixed Polymer Brush with Inhomogeneous Grafting Density Composition. *Soft Matter* **2013**, *9* (22), 5341—5354. https://doi.org/10.1039/c3sm50173f.

(314) Minko, S.; Müller, M.; Usov, D.; Scholl, A.; Froeck, C.; Stamm, M. Lateral versus Perpendicular Segregation in Mixed Polymer Brushes. *Phys. Rev. Lett.* **2002**, *88* (3), 4. https://doi.org/10.1103/PhysRevLett.88.035502.

(315) Fox, T. L.; Tang, S.; Zhang, G.; Horton, J. M.; Zhao, B.; Zhu, L.; Stewart, P. L. Loading and Delivery Characteristics of Binary Mixed Polymer Brush-Grafted Silica Nanoparticles. *Macromol. Chem. Phys.* **2016**, *217* (16), 1767—1776. https://doi.org/10.1002/MACP.201600143.

(316) Zhou, J.; Wang, L.; Yang, Q.; Liu, Q.; Yu, H.; Zhao, Z. Novel Thermoresponsive and PH-Responsive Aggregates from Self-Assembly of Triblock Copolymer PSMA- b -PNIPAAm- b -PSMA. **2007**, 5573—5580. https://doi.org/10.1021/jp070480h.

(317) Tadros, T. Dispersion Stability. *Encycl. Colloid Interface Sci.* **2013**, 249—250. https://doi.org/10.1007/978-3-642-20665-8_67.

(318) Wicks, Z. W.; Jones, F. N.; Peter Pappas, S.; Wicks, D. A. *Organic Coatings : Science and Technology*, Edition 3.; Wiley Interscience: Weinheim, 2006.

(319) Huang, X.; Hauptmann, N.; Appelhans, D.; Formanek, P.; Frank, S.; Kaskel, S.; Temme, A.; Voit, B. Synthesis of Hetero-Polymer Functionalized Nanocarriers by Combining Surface-Initiated ATRP and RAFT Polymerization. *Small* **2012**, *8* (23), 3579—3583. https://doi.org/10.1002/smll.201201397.

(320) Głowińska, A.; Trochimczuk, A. W. Polymer-Supported Phosphoric, Phosphonic and Phosphinic Acids—From Synthesis to Properties and Applications in Separation Processes. *Molecules* **2020**, *25* (18), 4236. https://doi.org/10.3390/molecules25184236.

(321) Markova, D.; Opper, K. L.; Wagner, M.; Klapper, M.; Wagener, K. B.; Müllen, K. Synthesis of Proton Conducting Phosphonic Acidfunctionalized Polyolefins by the Combination of ATRP and ADMET. *Polym. Chem* **2013**, *4*, 1351. https://doi.org/10.1039/c2py20886e.

6.2 Index of Figures

6.3 Index of Schemes

6.4 Index of Tables

7 APPENDIX

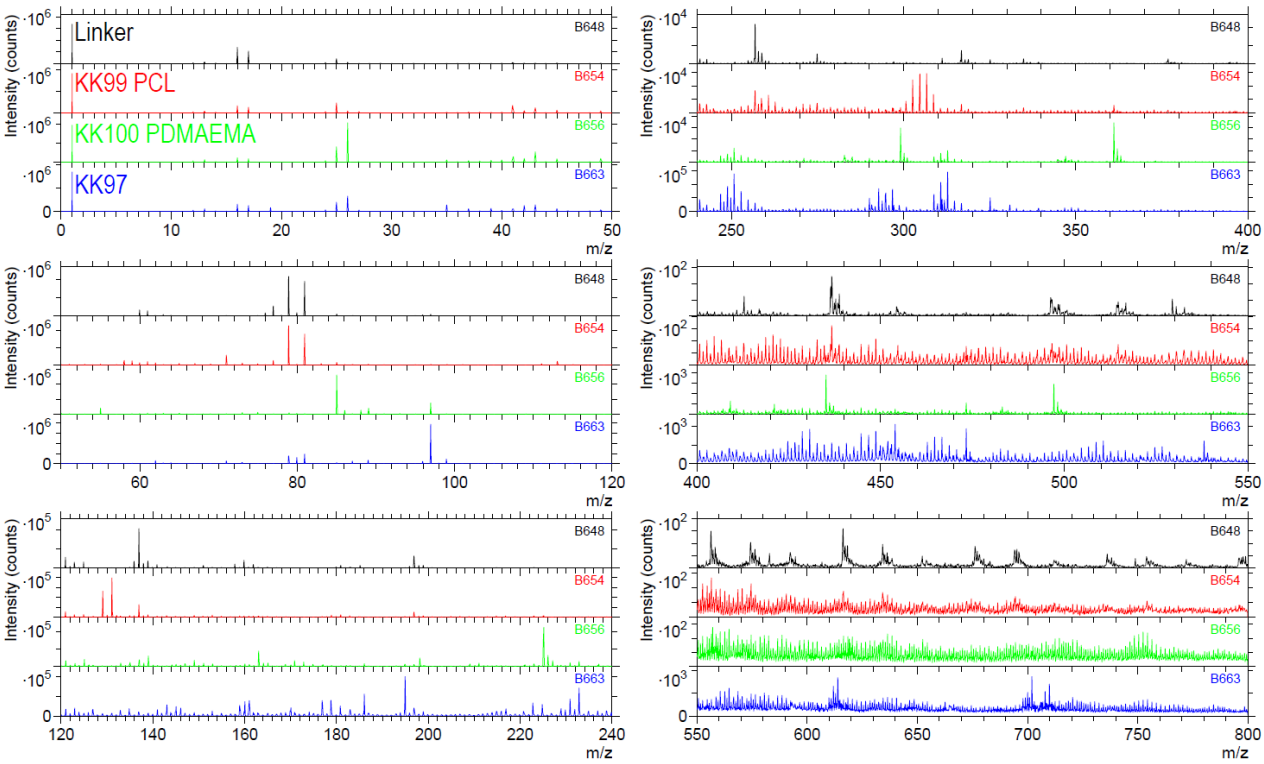

Figure 7-1: Negative ion channel ToF-SIMS spectra of sample wafer **128** (blue) and reference wafer **129** (red), **130** (green) and **98** (black) from 0-800 u.

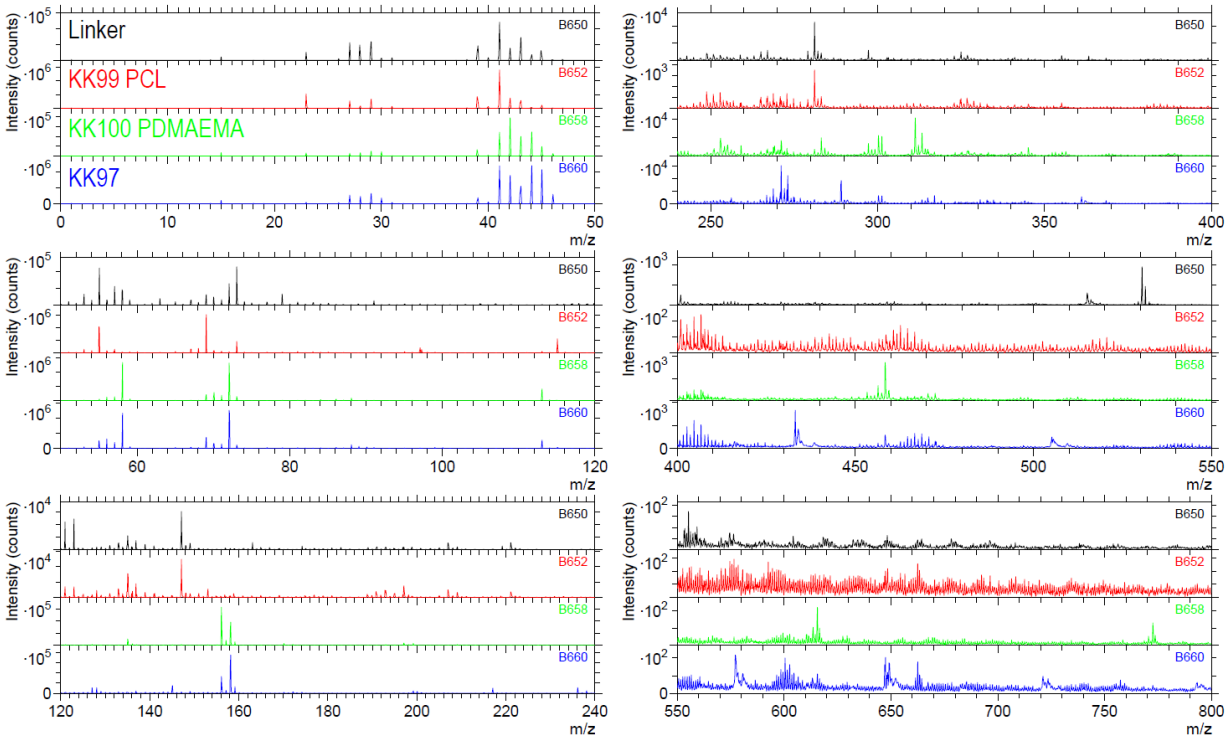

Figure 7-2: Positive ion channel ToF-SIMS spectra of sample wafer **128** (blue) and reference wafer **129** (red), **130** (green) and **98** (black) from 0-800 u.

Rights and Permissions

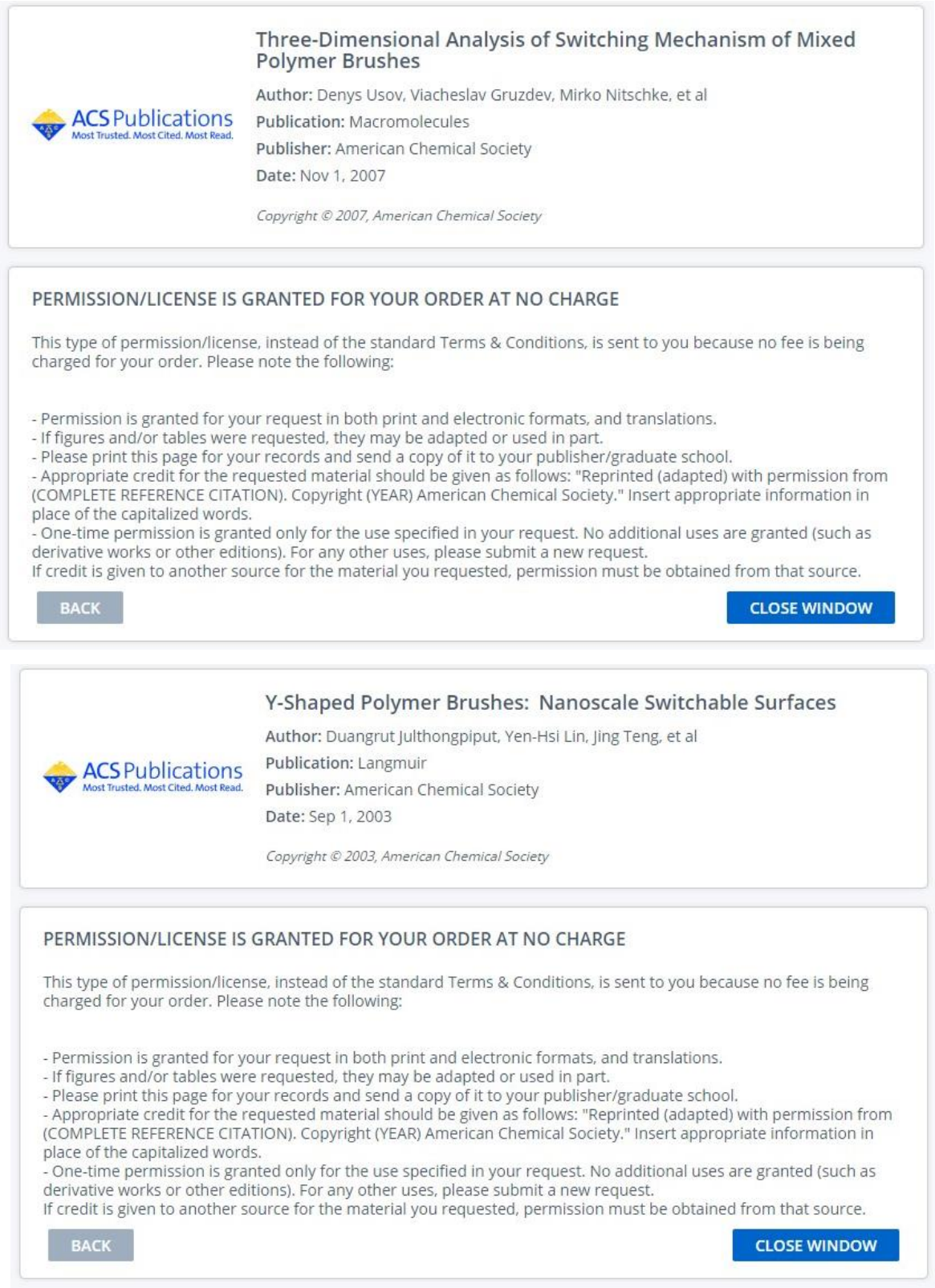

ACS Publications
Most Trusted. Most Cited. Most Read.

Three-Dimensional Analysis of Switching Mechanism of Mixed Polymer Brushes

Author: Denys Usov, Viacheslav Gruzdev, Mirko Nitschke, et al
Publication: Macromolecules
Publisher: American Chemical Society
Date: Nov 1, 2007

Copyright © 2007, American Chemical Society

PERMISSION/LICENSE IS GRANTED FOR YOUR ORDER AT NO CHARGE

This type of permission/license, instead of the standard Terms & Conditions, is sent to you because no fee is being charged for your order. Please note the following:

- Permission is granted for your request in both print and electronic formats, and translations.
- If figures and/or tables were requested, they may be adapted or used in part.
- Please print this page for your records and send a copy of it to your publisher/graduate school.
- Appropriate credit for the requested material should be given as follows: "Reprinted (adapted) with permission from (COMPLETE REFERENCE CITATION). Copyright (YEAR) American Chemical Society." Insert appropriate information in place of the capitalized words.
- One-time permission is granted only for the use specified in your request. No additional uses are granted (such as derivative works or other editions). For any other uses, please submit a new request.

If credit is given to another source for the material you requested, permission must be obtained from that source.

BACK CLOSE WINDOW

ACS Publications
Most Trusted. Most Cited. Most Read.

Y-Shaped Polymer Brushes: Nanoscale Switchable Surfaces

Author: Duangrut Julthongpiput, Yen-Hsi Lin, Jing Teng, et al
Publication: Langmuir
Publisher: American Chemical Society
Date: Sep 1, 2003

Copyright © 2003, American Chemical Society

PERMISSION/LICENSE IS GRANTED FOR YOUR ORDER AT NO CHARGE

This type of permission/license, instead of the standard Terms & Conditions, is sent to you because no fee is being charged for your order. Please note the following:

- Permission is granted for your request in both print and electronic formats, and translations.
- If figures and/or tables were requested, they may be adapted or used in part.
- Please print this page for your records and send a copy of it to your publisher/graduate school.
- Appropriate credit for the requested material should be given as follows: "Reprinted (adapted) with permission from (COMPLETE REFERENCE CITATION). Copyright (YEAR) American Chemical Society." Insert appropriate information in place of the capitalized words.
- One-time permission is granted only for the use specified in your request. No additional uses are granted (such as derivative works or other editions). For any other uses, please submit a new request.

If credit is given to another source for the material you requested, permission must be obtained from that source.

BACK CLOSE WINDOW

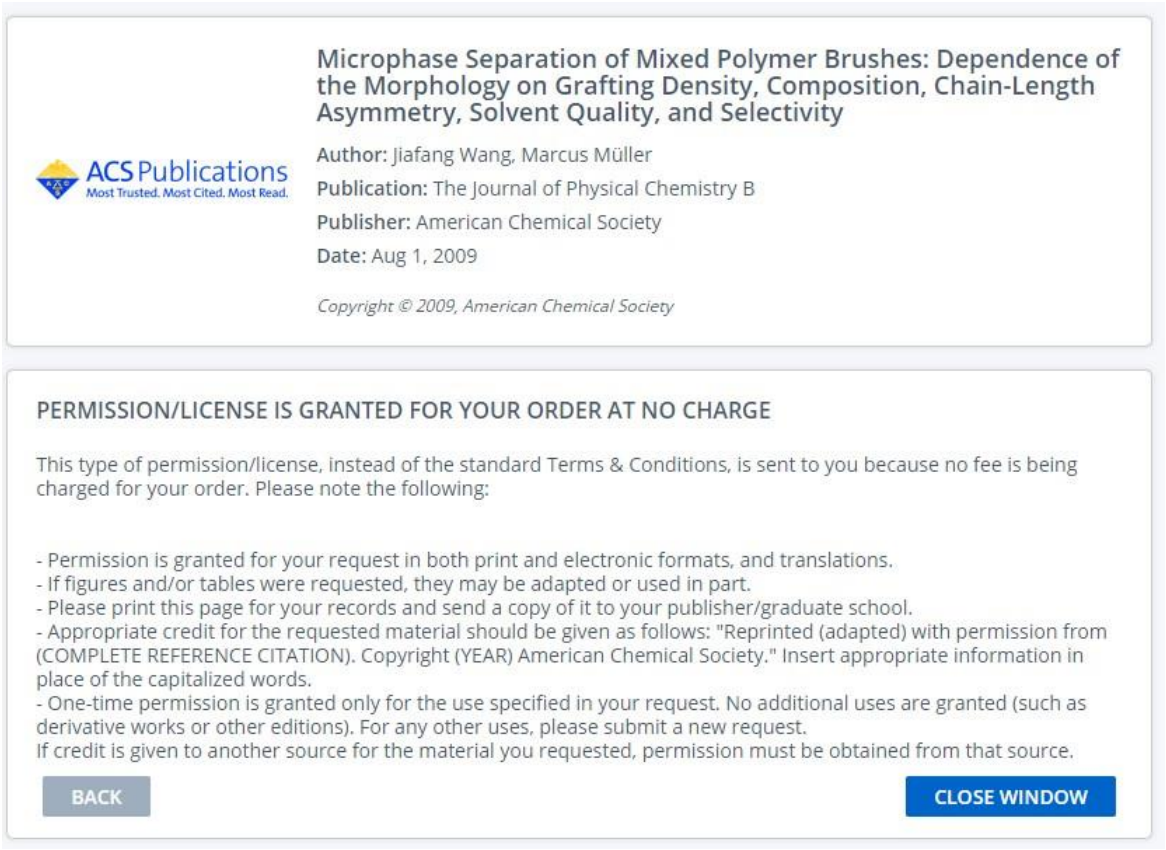

ACS Publications
Most Trusted. Most Cited. Most Read.

Microphase Separation of Mixed Polymer Brushes: Dependence of the Morphology on Grafting Density, Composition, Chain-Length Asymmetry, Solvent Quality, and Selectivity

Author: Jiafang Wang, Marcus Müller

Publication: The Journal of Physical Chemistry B

Publisher: American Chemical Society

Date: Aug 1, 2009

Copyright © 2009, American Chemical Society

PERMISSION/LICENSE IS GRANTED FOR YOUR ORDER AT NO CHARGE

This type of permission/license, instead of the standard Terms & Conditions, is sent to you because no fee is being charged for your order. Please note the following:

- Permission is granted for your request in both print and electronic formats, and translations.
- If figures and/or tables were requested, they may be adapted or used in part.
- Please print this page for your records and send a copy of it to your publisher/graduate school.
- Appropriate credit for the requested material should be given as follows: "Reprinted (adapted) with permission from (COMPLETE REFERENCE CITATION). Copyright (YEAR) American Chemical Society." Insert appropriate information in place of the capitalized words.
- One-time permission is granted only for the use specified in your request. No additional uses are granted (such as derivative works or other editions). For any other uses, please submit a new request.

If credit is given to another source for the material you requested, permission must be obtained from that source.

BACK CLOSE WINDOW

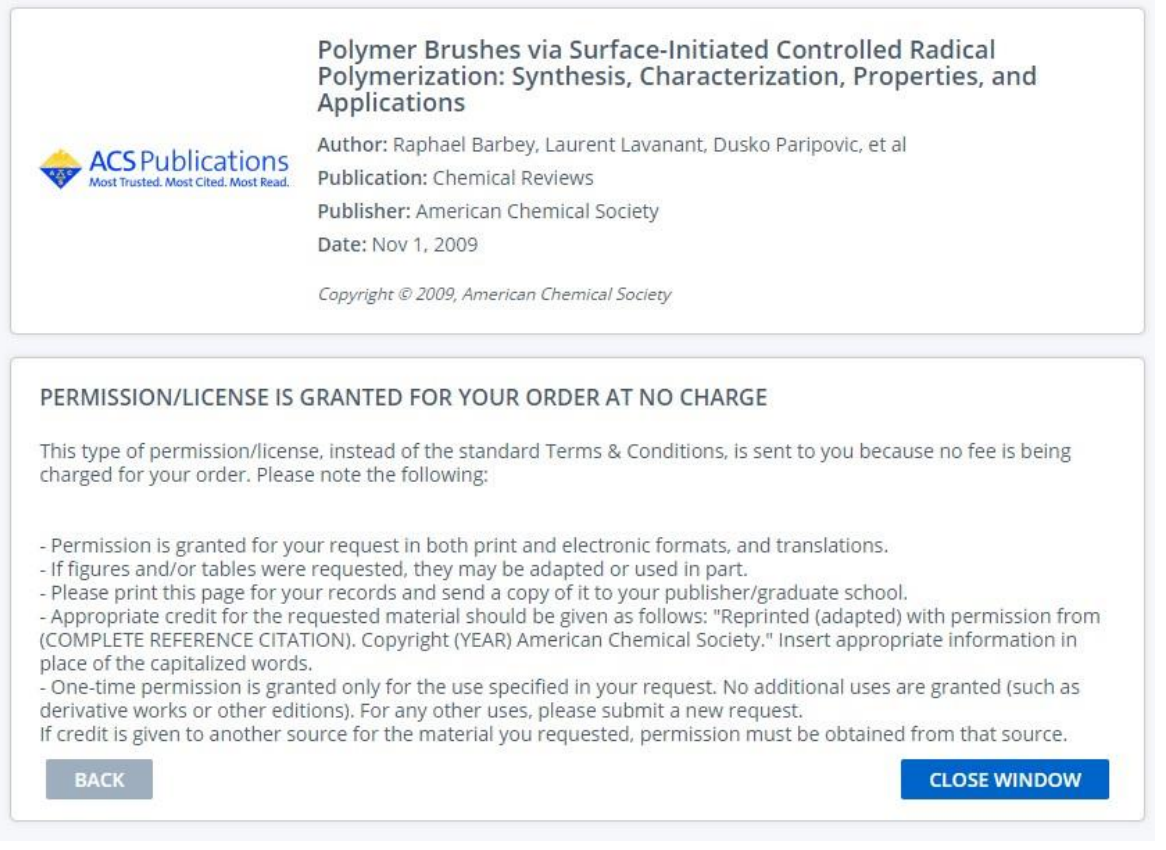

ACS Publications
Most Trusted. Most Cited. Most Read.

Polymer Brushes via Surface-Initiated Controlled Radical Polymerization: Synthesis, Characterization, Properties, and Applications

Author: Raphael Barbey, Laurent Lavanant, Dusko Paripovic, et al

Publication: Chemical Reviews

Publisher: American Chemical Society

Date: Nov 1, 2009

Copyright © 2009, American Chemical Society

PERMISSION/LICENSE IS GRANTED FOR YOUR ORDER AT NO CHARGE

This type of permission/license, instead of the standard Terms & Conditions, is sent to you because no fee is being charged for your order. Please note the following:

- Permission is granted for your request in both print and electronic formats, and translations.
- If figures and/or tables were requested, they may be adapted or used in part.
- Please print this page for your records and send a copy of it to your publisher/graduate school.
- Appropriate credit for the requested material should be given as follows: "Reprinted (adapted) with permission from (COMPLETE REFERENCE CITATION). Copyright (YEAR) American Chemical Society." Insert appropriate information in place of the capitalized words.
- One-time permission is granted only for the use specified in your request. No additional uses are granted (such as derivative works or other editions). For any other uses, please submit a new request.

If credit is given to another source for the material you requested, permission must be obtained from that source.

BACK CLOSE WINDOW

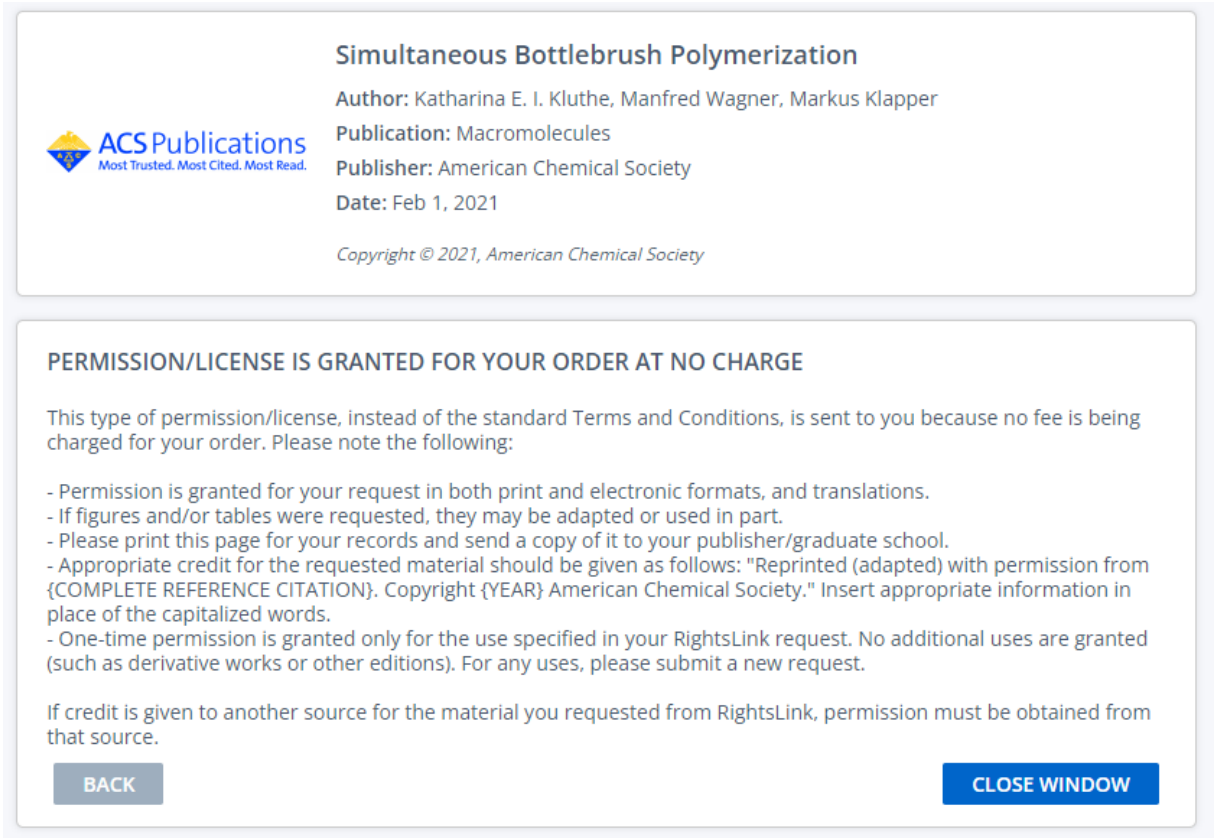

ACS Publications
Most Trusted. Most Cited. Most Read.

Simultaneous Bottlebrush Polymerization

Author: Katharina E. I. Kluthe, Manfred Wagner, Markus Klapper
Publication: Macromolecules
Publisher: American Chemical Society
Date: Feb 1, 2021

Copyright © 2021, American Chemical Society

PERMISSION/LICENSE IS GRANTED FOR YOUR ORDER AT NO CHARGE

This type of permission/license, instead of the standard Terms and Conditions, is sent to you because no fee is being charged for your order. Please note the following:

- Permission is granted for your request in both print and electronic formats, and translations.
- If figures and/or tables were requested, they may be adapted or used in part.
- Please print this page for your records and send a copy of it to your publisher/graduate school.
- Appropriate credit for the requested material should be given as follows: "Reprinted (adapted) with permission from {COMPLETE REFERENCE CITATION}. Copyright {YEAR} American Chemical Society." Insert appropriate information in place of the capitalized words.
- One-time permission is granted only for the use specified in your RightsLink request. No additional uses are granted (such as derivative works or other editions). For any uses, please submit a new request.

If credit is given to another source for the material you requested from RightsLink, permission must be obtained from that source.

BACK CLOSE WINDOW

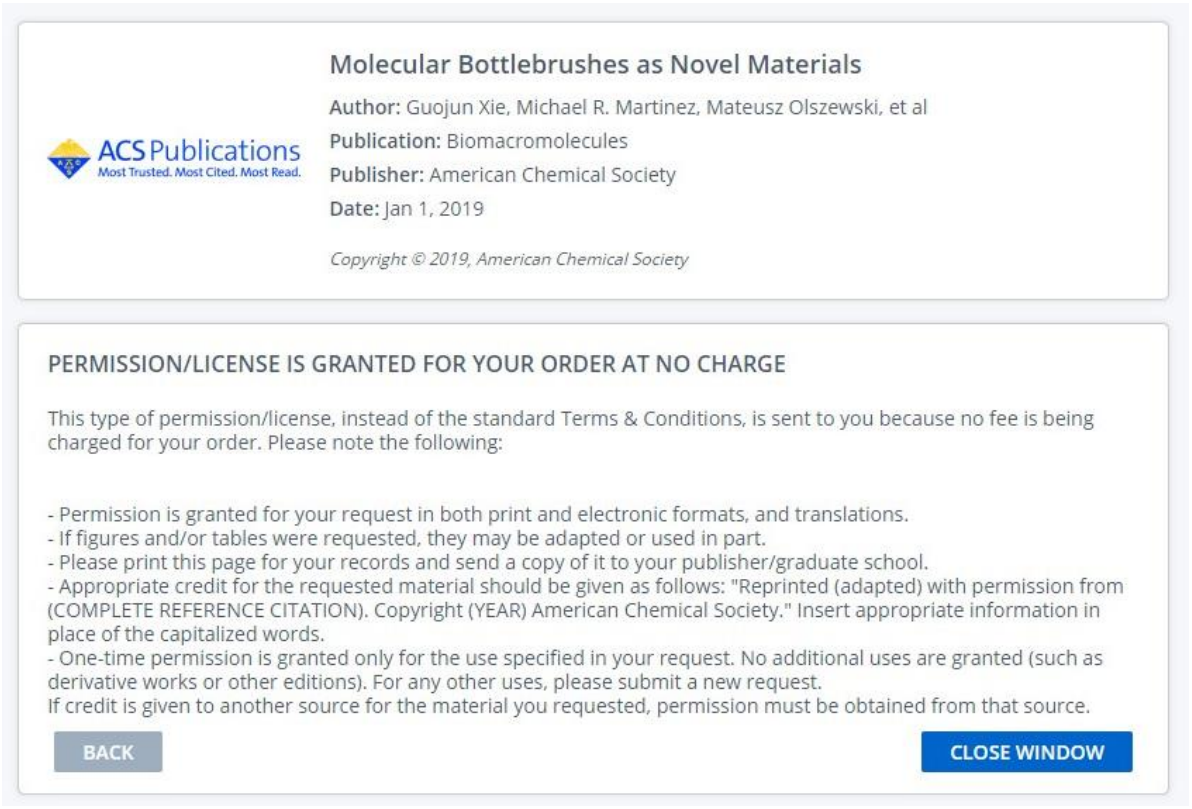

ACS Publications
Most Trusted. Most Cited. Most Read.

Molecular Bottlebrushes as Novel Materials

Author: Guojun Xie, Michael R. Martinez, Mateusz Olszewski, et al
Publication: Biomacromolecules
Publisher: American Chemical Society
Date: Jan 1, 2019

Copyright © 2019, American Chemical Society

PERMISSION/LICENSE IS GRANTED FOR YOUR ORDER AT NO CHARGE

This type of permission/license, instead of the standard Terms & Conditions, is sent to you because no fee is being charged for your order. Please note the following:

- Permission is granted for your request in both print and electronic formats, and translations.
- If figures and/or tables were requested, they may be adapted or used in part.
- Please print this page for your records and send a copy of it to your publisher/graduate school.
- Appropriate credit for the requested material should be given as follows: "Reprinted (adapted) with permission from (COMPLETE REFERENCE CITATION). Copyright (YEAR) American Chemical Society." Insert appropriate information in place of the capitalized words.
- One-time permission is granted only for the use specified in your request. No additional uses are granted (such as derivative works or other editions). For any other uses, please submit a new request.

If credit is given to another source for the material you requested, permission must be obtained from that source.

BACK CLOSE WINDOW

Licensed Content Information

License Number:	**RNP/21/APR/038348**
License date:	01-Apr-2021
DOI:	10.1103/PhysRevLett.88.035502
Title:	Lateral versus Perpendicular Segregation in Mixed Polymer Brushes
Author:	S. Minko et al.
Publication:	Physical Review Letters
Publisher:	American Physical Society
Cost:	USD $ 0.00